

Cellular mechanisms of carbon concentration and pH
regulation in the calcifying cells of the sea urchin
(*Strongylocentrotus purpuratus*) larva

Dissertation

Zur Erlangung des akademischen Grades

Dr. rer. nat.

der Mathematisch-Naturwissenschaftlichen Fakultät

der Christian-Albrechts-Universität zu Kiel

vorgelegt von

Ann-Sophie Matt

Kiel, Mai 2024

Erster Gutachter: Dr. Marian Yong-An Hu
Zweiter Gutachter: Prof. Dr. Thomas Roeder

Tag der Einreichung: 23.05.2024
Tag der mündlichen Prüfung: 24.07.2024
Zum Druck genehmigt am: 24.07.2024

Unterschrift

Prof. Dr. Frank Kempken

Summary

Biom mineralization represents an evolutionary ancient process utilized across taxa spanning the five kingdoms, to enable hardening of their tissues for protection and mechanical support. Within the marine ecosystem, a predominant fraction of organisms engages in the synthesis of calcium carbonate (CaCO_3) minerals, such as calcite and aragonite, to construct their skeletal structures and protective shells. The calcification process is an intricate and sophisticated mechanism relying on acquisition of Ca^{2+} ions and dissolved inorganic carbon (DIC) (i.e., CO_2 , HCO_3^- , CO_3^{2-}), as well as regulation of pH homeostasis to facilitate CaCO_3 precipitation. The mechanisms underlying the calcification process have fascinated researchers since over a century, but detailed information regarding the cellular physiology of calcifying systems remains scarce. Especially, in consideration of the ongoing phenomenon of climate change, including increasing anthropogenic CO_2 emissions leading to increased atmospheric $p\text{CO}_2$ and consequently decreases in ocean surface pH, termed as ocean acidification (OA), the calcification process in different marine calcifying species has received considerable attention. Deeper understanding of the mechanisms underlying the calcification process would be helpful to make better predictions how future ocean conditions, like a decreased oceanic pH can influence calcifying organisms in marine ecosystems. The present study aimed to characterize the cellular carbon concentration mechanism (CCM) in the calcifying primary mesenchyme cells (PMCs) of the sea urchin (*Strongylocentrotus purpuratus*) larva. Furthermore, this work addressed the important question of intracellular pH regulation and water transport to support the mineralization process.

Using molecular approaches, such as *in situ* hybridization and gene expression analyses, this work identified one cytosolic (iCA) and another extracellular membrane-bound carbonic anhydrase (eCA), located exclusively in the PMCs that dynamically respond with changes in expression levels during re-mineralization. Intracellular pH measurements in combination with CO_2 -pulse experiments demonstrated iCA activity in the PMCs, whereas pharmacological inhibition revealed an opposing contribution of iCA and eCA on the CCM. Knock-down of the eCA *Cara7* induced impaired formation of specific skeleton segments. Moreover, H^+ -selective electrode measurements showed eCA-catalyzed CO_2 hydration rates at the PMC surface that were abolished by pharmacological inhibition of knock-down of *Cara7*. Finally, a role of eCA in the cellular HCO_3^-

uptake process was demonstrated by reduced pH_i regulatory capacities during inhibition and knock-down of *Cara7*. These results provide a strong line of evidence for a CA mediated CCM in calcifying cells. The extracellular hydration of metabolic CO_2 , catalyzed by eCA *Cara7*, coupled with HCO_3^- uptake mechanisms mitigates the loss of carbon and reduces the cellular proton load during the calcification process, by leaving the accrued H^+ outside the cell.

This work also identified a new participant in controlling the intracellular pH homeostasis during the calcification process. The otopetrin-like *Otop2l* codes for a proton channel, also exclusively expressed in the PMCs of the sea urchin larva. During re-mineralization the expression level of *Otop2l* were increased and knock-down revealed impaired skeleton formation. Intracellular pH measurements identified Zn^{2+} -sensitive H^+ fluxes, which regulate intracellular pH in a $\text{Na}^+/\text{HCO}_3^-$ -independent manner. Moreover, the outwardly directed H^+ flux mediated by *Otop2l* is activated by extracellular $\text{pH} > 8.0$, which indicates optimum functionality of this proton channel under oceanic pH conditions. However, this pH dependency of the main exit route for protons from the calcifying cell and the altered proton gradients across the plasma membrane may make the calcification process vulnerable for the predicted decrease in oceanic pH. Since *Otop2l* is the main exit route for H^+ during calcification and shows decreased activity during OA conditions, alternative intracellular pH regulatory mechanisms that are energetically more costly may explain the increased energy metabolism under acidified conditions. Given the deep evolutionary association of otopetrins with calcifying systems in metazoans, our results may have strong implications for the cellular physiology of other marine calcifiers and their responses to future OA conditions.

Additionally, this study presents evidence for an involvement of the aquaglyceroporin *spAQP9* in the cellular calcification process of sea urchin larvae. *In situ* hybridization and molecular analyses revealed exclusive expression of *spAQP9* expressed in the PMCs, reaching peak expression levels during skeleton formation and re-mineralization, implying its pivotal role in skeletogenesis initiation and spicule elongation. This observation is underpinned by pharmacological approaches targeting *spAQP9* function that resulted in impaired spicule formation. Using heterologous expression in *Xenopus laevis* oocytes, a dual function of *spAQP9* as H_2O and CO_2 channel could be demonstrated. Immunohistological staining localized *spAQP9* in intracellular vesicular structures, coinciding with Ca^{2+} -rich vesicles where amorphous calcium carbonate (ACC) precipitation for the

calcification process potentially takes place. Antibody staining combined with a re-calcification assay identified two distinct types of PMCs based on spAQP9 sub-cellular distribution, that correspond to actively calcifying vs. resting PMCs. These findings highlight a role of spAQP9's role in the cellular calcification process by mediating H₂O and potentially also CO₂ transport across vesicular membranes.

The present thesis unveiled a novel cellular carbon concentration mechanism, underscored by the central role of an extracellular carbonic anhydrase Cara7, alongside the characterization of a proton channel Otop2l and an aquaporin spAQP9 in PMCs, elucidating central aspects of the intricate calcification process in the sea urchin larva. These discoveries provide significant knowledge of a more profound mechanistic understanding of the calcification process in marine organisms and offer valuable perspectives into their responses to past, present and future oceanic conditions.

Zusammenfassung

Biominalisation ist ein evolutionär alter Prozess, der von Organismen aus allen fünf Tierreichen genutzt wird, um ihre Gewebe zum Schutz und zur mechanischen Unterstützung zu verfestigen. Ein Großteil der im marinen Ökosystem lebenden Organismen synthetisiert Calciumcarbonat (CaCO_3) - Mineralien, wie Calcit und Aragonit, um ihre Skelettstrukturen und Schalen aufzubauen. Für den komplexen Kalzifizierungs-Prozess wird die Aufnahme von Ca^{2+} -Ionen und gelöstem anorganischem Kohlenstoff (DIC) (d. h. CO_2 , HCO_3^- , CO_3^{2-}), sowie die Regulation des pH-Haushalts benötigt, um die CaCO_3 -Präzipitation zu ermöglichen. Dieser Prozess steht seit langem im Mittelpunkt der marinen Forschung, aber detaillierte Informationen zur zugrundeliegenden Physiologie bleibt größtenteils unbekannt. Insbesondere vor dem Hintergrund der zunehmenden anthropogenen CO_2 -Emissionen, die zu einem Anstieg des atmosphärischen $p\text{CO}_2$ und ebenfalls zu einem Abfall des pH-Werts der Ozeane führt, was als Ozeanversauerung (OA) bezeichnet wird, haben Forschende bereits Auswirkungen auf die Kalzifikation bei verschiedenen marinen kalzifizierenden Arten feststellen können. Ein tieferes Verständnis der Kalzifizierungs-Mechanismen wäre daher hilfreich, um bessere Vorhersagen über die Auswirkungen von zukünftige Ozeanbedingungen auf das marine Ökosystem erteilen zu können. Die vorliegende Studie beabsichtigt den zellulären Kohlenstoffkonzentrationsmechanismus (KKM) in den kalzifizierenden primären Mesenchymzellen (PMZ) der Larve des Seeigels (*Strongylocentrotus purpuratus*) zu charakterisieren. Darüber hinaus definiert diese Arbeit die intrazelluläre pH-Regulierung und den Wassertransport in den PMCs während der Skelettbildung der Larve.

Mit Hilfe von molekularen Analysen wie *in situ* Hybridisierung und Genexpressions-Analysen wurden eine zytoplasmatische (iCA) und eine extrazelluläre membrangebundene Carboanhydrase (eCA) identifiziert, die ausschließlich in den PMCs vorhanden sind und deren Expression während der Re-Mineralisierung erhöht war. Intrazelluläre pH-Messungen in Kombination mit CO_2 -Puls-Experimenten zeigten eine iCA-Aktivität in den PMCs, während pharmakologische Inhibierungs-Versuche einen gegensätzlichen Beitrag von iCA und eCA zum KKM darlegten. Knock-down de eCA Cara7 führte zu beeinträchtiger Bildung von spezifischen Skelettsegmente. Darüber hinaus demonstrierten H^+ -selektive Elektrodenmessungen CO_2 -Hydratisierungsraten an der PMC-

Oberfläche, welche durch eCA katalysiert wurde. Die vorhergesagte Beteiligung von eCA bei der zellulären HCO_3^- -Aufnahme wurde durch eine verringerte pH_i -Regulationskapazität bei Hemmung und Knock-down von *Cara7* nachgewiesen. Daher schlagen wir einen neuartigen CA-vermittelten KKM in kalzifizierenden Zellen vor. Die extrazelluläre Hydratisierung von metabolischem CO_2 , katalysiert durch eCA *Cara7*, gekoppelt mit HCO_3^- -Aufnahmemechanismen, mindert den Kohlenstoffverlust. Zusätzlich wird die zelluläre Protonenlast während des Kalzifizierungs-Prozesses reduziert, indem die H^+ außerhalb der Zelle entstehen.

Zusätzlich konnte in dieser Studie ein neuer Mechanismus identifiziert werden, welcher an der intrazellulären pH-Homöostase während des Kalzifizierungs-Prozesses der Larve beteiligt ist. Das Otopetrin-ähnliche *Otop2l* kodiert einen Protonenkanal, der ebenfalls ausschließlich in den PMZs der Seeigel-Larve exprimiert wird. Eine gesteigerte Expression von *Otop2l* konnte während der Re-Mineralisierung festgestellt werden, und der Knock-down führte zu beeinträchtigter Skelettbildung. Intrazelluläre pH-Messungen identifizierten Zn^{2+} -sensitive H^+ Permeabilität, die den intrazellulären pH in einer $\text{Na}^+/\text{HCO}_3^-$ -unabhängigen Weise regulieren. Darüber hinaus war der nach außen gerichtete H^+ -Transport durch *Otop2l* stark aktiv bei einem extrazellulären $\text{pH} > 8,0$, was auf eine Anpassung an den relativ stabilen Ozean-pH hinweist. Dieses pH abhängige Aktivitäts-Optimum und ein reduzierter Protonen-Transport durch *Otop2l* macht den Kalzifizierungs-Prozess anfällig für die voranschreitende Erniedrigung des ozeanischen pH-Werts. Da *Otop2l* aber der Hauptaustrittsweg für H^+ ist, die während der Kalzifizierung anfallen, muss wahrscheinlich eine Verlagerung der intrazellulären pH-Regulierung zu den alternativen energieaufwändigeren Mechanismen erfolgen, was den erhöhten Energie-Metabolismus während OA-Bedingungen erklärt. Angesichts der tiefgründigen evolutionären Assoziation von Otopetrinen und den kalzifizierenden Systemen bei Metazoa haben unsere Ergebnisse große Bedeutung für die zelluläre Physiologie von anderen marinen kalzifizierenden Organismen und deren Reaktionen auf zukünftige OA-Bedingungen.

Weitere Ergebnisse dieser Studie identifizierten die Präsenz eines Aquaglyceroporins *spAQP9*, welches am zellulären Kalzifizierungs-Prozess von Seeigel-Larven beteiligt ist. *In situ* Hybridisierung und molekulare Analysen zeigen die Expression von *spAQP9* ausschließlich in den PMZ, wobei die Expression während der Skelettbildung und Re-Mineralisierung ihren Höhepunkt erreicht und damit ihre wichtige Rolle bei der Initiierung der Skeletogenese und der Skelettwachstums impliziert. Diese Beobachtung wird untermauert durch pharmakologische

Ansätze, welche die Funktionsweise von spAQP9 hemmen und zu einer Beeinträchtigung der Skelettbildung führt. Heterologen Expression in *Xenopus laevis* Oozyten konnte die duale Funktion von spAQP9 als H₂O- und CO₂-Kanal zeigen. Immunohistologische Untersuchung lokalisierte spAQP9 in intrazellulären vesikulären Strukturen, vergleichbar mit den Ca²⁺-reichen Vesikeln in PMCs, in denen die Amorphe Calcium Carbonat (ACC) - Präzipitation für den Kalzifizierungs-Prozesses potenziell stattfindet. Antikörperfärbung in Kombination mit einem Re-Mineralisierungstest identifizierte zwei verschiedene Arten von PMCs basierend auf der subzellulären Verteilung von spAQP9, die aktive und ruhende PMCs entsprechen. Diese Ergebnisse verdeutlichen die Rolle von spAQP9 bei dem zellulären Kalzifizierungs-Prozess durch den H₂O und potenziellen CO₂-Transport über Vesikelmembranen.

Die vorliegende Studie enthüllte einen neuartigen zellulären Kohlenstoffkonzentrationsmechanismus, unterstrichen durch die zentrale Rolle einer extrazellulären Carboanhydrase Cara7, neben der Charakterisierung eines Protonenkanals Otop21 und eines Aquaporins spAQP9 in den PMZ. Diese Funde beleuchten die zentralen Aspekte des komplexen Kalzifizierungs-Prozesses in der Seeigel-Larve. Diese Entdeckungen liefern bedeutende Erkenntnisse für ein tieferes mechanistisches Verständnis des Kalzifizierungs-Prozesses bei marinen Organismen und bieten wertvolle Einblicke in ihre Reaktionen auf vergangene, derzeitige und zukünftige ozeanische Bedingungen.

Contents

| | |
|---|----|
| Summary..... | I |
| Zusammenfassung..... | V |
| 1 Introduction..... | 1 |
| 1.1 Biocalcification / Biomineralization | 1 |
| 1.1.1 Marine calcification: general information / process | 1 |
| 1.1.2 Seawater carbonate chemistry and ocean acidification OA | 2 |
| 1.1.3 Principles of calcification in organisms..... | 3 |
| 1.2 Purple Sea urchin <i>Strongylocentrotus purpuratus</i> | 4 |
| 1.2.1 Model organism: the sea urchin larva..... | 4 |
| 1.2.2 Larval development..... | 5 |
| 1.2.3 Primary mesenchyme cells (PMCs) | 7 |
| 1.2.4 Calcification in the sea urchin larvae..... | 8 |
| 1.2.5 Ion transport and pH homeostasis in PMCs..... | 9 |
| 1.3 Otopetrin family of proton channels..... | 10 |
| 1.4 Carbonic Anhydrases..... | 12 |
| 1.5 Aquaporins | 13 |
| 1.6 Objectives | 15 |
| 2 Methods | 16 |
| 2.1 Maintenance of adult sea urchins and larval cultures | 16 |
| 2.2 In silico analysis | 16 |
| 2.2.1 Gene mining and structural analysis | 16 |
| 2.2.2 Phylogenetic analysis..... | 17 |
| 2.2.3 Single cell transcriptome database analysis..... | 17 |
| 2.3 Molecular Techniques | 18 |
| 2.3.1 Molecular cloning..... | 18 |
| 2.3.2 Whole mount in situ hybridization..... | 19 |
| 2.3.3 RT-qPCR | 20 |
| 2.3.4 Immunocytochemistry | 20 |
| 2.3.5 Western blot analysis | 20 |
| 2.3.6 Morpholino injection..... | 21 |
| 2.4 In vivo experimental Techniques..... | 22 |
| 2.4.1 Re-calcification assay..... | 22 |

| | | |
|---------|--|-----|
| 2.4.2 | Determination of calcification and re-calcification rate under pharmacological inhibition/different pH conditions (ocean acidification experiment) | 22 |
| 2.4.3 | Intracellular pH (pH _i) measurements | 23 |
| 2.4.3.1 | Characterization of H ⁺ fluxes in PMCs | 24 |
| 2.4.3.2 | Determination of Carbonic Anhydrase Activity | 24 |
| 2.4.3.3 | Determination of pH _i regulatory capacities | 25 |
| 2.4.3.4 | pH _i measurements and transfection of HEK-293 cells | 25 |
| 2.4.4 | Oocyte preparation, coding RNA synthesis and cRNA injection | 26 |
| 2.4.5 | Oocyte swelling experiment | 26 |
| 2.4.6 | Oocyte CO ₂ excretion experiment | 27 |
| 2.4.7 | Water flux measurements in PMCs | 28 |
| 2.5 | Electrophysiology | 29 |
| 2.5.1 | H ⁺ selective micro-electrode preparation | 29 |
| 2.5.2 | Two-electrode voltage-clamp (TEVC) recordings | 30 |
| 2.5.3 | Membrane potential measurements | 30 |
| 2.5.4 | Micro-electrode measurements at the PMC surface | 31 |
| 2.5.5 | CO ₂ conductivity measurements in Oocytes | 32 |
| 2.6 | Statistics | 32 |
| 3 | Publications and Manuscript | 33 |
| I | An otopetrin family proton channel promotes cellular acid efflux critical for biomineralization in a marine calcifier | 33 |
| II | Extracellular carbonic anhydrase activity promotes a carbon concentration mechanism in metazoan calcifying cells | 64 |
| III | Dual role of an aquaglyceroporin mediating water and CO ₂ conductance identified in the calcifying cells of the sea urchin embryo | 107 |
| 4 | unpublished data | 133 |
| 5 | Discussion | 135 |
| 5.1 | Carbon concentration mechanisms | 135 |
| 5.1.1 | Extracellular carbonic anhydrase activity supports a HCO ₃ ⁻ uptake mechanism in calcifying cells | 136 |
| 5.1.2 | A potential role of extracellular carbonic anhydrase in sub-cellular compartments | 139 |
| 5.1.3 | A potential function of the aquaglyceroporin spAQP9 in vesicular carbon concentration | 140 |
| 5.2 | Cellular pH regulation (buffer import) & H ⁺ export | 141 |
| 5.2.1 | Anionic buffer import of HCO ₃ ⁻ | 142 |
| 5.2.2 | H ⁺ export | 144 |
| 5.2.3 | pH _i differences | 146 |

| | | |
|-------|---|-----|
| 5.3 | Water transport in PMCs..... | 146 |
| 5.4 | Effect of Ocean Acidification | 149 |
| 5.4.1 | Impact of Global Warming | 152 |
| 5.5 | Evolutionary aspects of Biomineralization mechanisms..... | 153 |
| 6 | Conclusion | 155 |
| 7 | References..... | 157 |
| | Acknowledgements | i |
| | Eidesstattliche Erklärung..... | ii |

1 Introduction

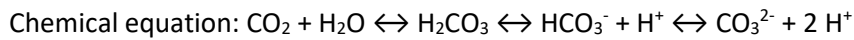
1.1 Biocalcification / Biomineralization

1.1.1 Marine calcification: general information / process

Biomineralization is the formation mechanism and deposition of minerals, used by organisms to harden their tissues and skeletons for a great variety of biological functions (Gilbert et al., 2022). Biomineralization is found in organisms of the five kingdoms and has evolved independently many times during evolution (Knoll, 2003). The major classes of biominerals comprise calcium carbonates, calcium phosphates and silica, that occur widely but discontinuously across the tree of life (Knoll, 2003). In the marine realm, calcium carbonate (CaCO_3) accounts for the largest fraction of mineral type created by marine organisms. Calcium carbonate can occur in three major forms, including calcite, aragonite and vaterite of which the first two are the major forms used by organisms (Addadi et al., 2003). Fossil records suggest that calcium carbonate skeletons evolved even before the Cambrian explosion in the Neoproterozoic more than 600 million years ago (Knoll, 2003; Oates, 2010; Steele et al., 2020). Furthermore, small marine organisms are responsible for the creation of large geological structures, like chalk mountains and limestone, coral reefs and deep-sea sediment that bind carbon over long geological timescales and therefore play a pivotal role in the global carbon cycle (Van Cappellen, 2003). For instance, limestone consists of crystalline forms of CaCO_3 , calcite and aragonite, primarily formed through biological processes involving coccolithophores and foraminifera. Additionally, it contains silica, derived from siliceous skeleton fragments of sponges and diatoms (Oates, 2010; Taylor et al., 2011). Coral reefs, such as the Great Barrier Reef, are constructed by colonies of corals that produce a skeletal framework mainly composed of aragonite (Clark, 2020; Stanley, 2008).

1.1.2 Seawater carbonate chemistry and ocean acidification OA

The ocean, being the largest reservoir of carbon, relies on the dynamic equilibrium between CaCO_3 formation and dissolution. The seawater CO_2 carbonate system encompasses four dissolved inorganic carbon species (DIC), namely CO_2 , H_2CO_3 , HCO_3^- , CO_3^{2-} , whose concentration are contingent upon pH (Tanhua et al., 2013).



Over the past 250 years of industrialization, there has been a continual rise in anthropogenic CO_2 emission, as well as other greenhouse gases (Fig. 1.1 A left). Given the ocean's role as a carbon sink, it absorbs the increased influx of anthropogenic CO_2 through persistent atmospheric exchange (Martins Medeiros & Souza, 2023).

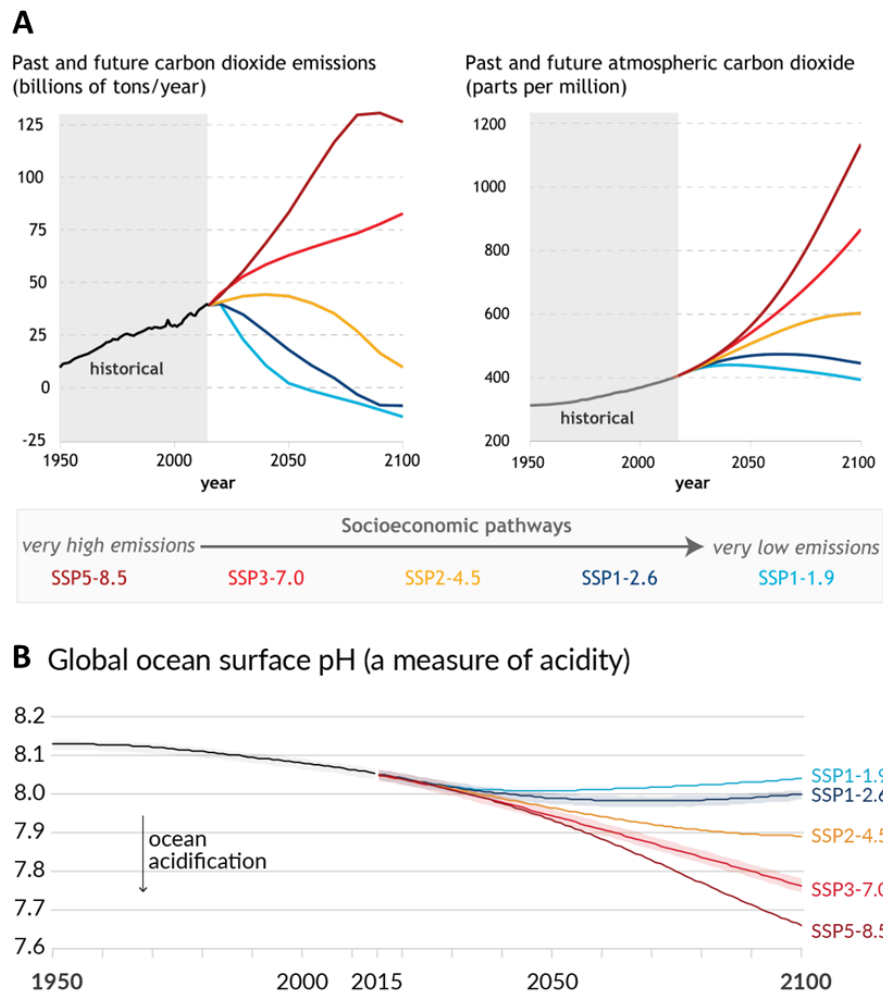


Fig. 1.1: (A) Predicted anthropogenic CO_2 emission (left) and subsequent predicted atmospheric CO_2 (ppm) (right). The projections for each of the five scenarios are shown in colour (2015 – 2100), the black curve represents the historical simulations (1950 – 2014). (light blue curve) SSP1-1.19 = very low emissions

(GtCO₂/year); (dark red curve) SSP5-8.5 = very high emissions (GtCO₂/year). (B) Predicted change of the global ocean surface pH. The projections for each of the five scenarios are shown in colour (2015 – 2100), the black curve represents the historical simulations (1950 – 2014). (light blue curve) very low emissions (GtCO₂/year); (dark red curve) very high emissions (GtCO₂/year). Adapted from IPCC 2021

Furthermore, atmospheric $p\text{CO}_2$ has already increased from pre-industrial levels of ~350 ppm to currently 423.31 ppm (Global Monitoring Laboratory – Carbon Cycle Greenhouse Gases (gml.noaa.gov/ccgg/); Fig. 1.1 A right). This increase in CO₂ levels results in its dissolution in seawater, leading to the release of additional protons (H⁺), ultimately causing a reduction in oceanic pH, commonly referred to as ocean acidification. The current high $p\text{CO}_2$ level already led to a decrease of 0.1 pH unit in the ocean surface pH since industrialization (Jiang et al., 2019). Projected scenarios based on various future anthropogenic CO₂ emission trajectories, as outlined in the Intergovernmental Panel on Climate Change (IPCC) Reports, suggests a potential pH decline of up to 0.5 units by the end of this century, with further CO₂ emissions leading to ~1000 ppm by the end of the century (SSP5-8.5) (Fig. 1.1 B) (Intergovernmental Panel on Climate Change IPCC, 2023; IPCC, 2021). These shifts in pH and $p\text{CO}_2$ levels pose significant implications for the physiology, health and survival of marine life (Fabry et al., 2008; Melzner et al., 2009). Consequently, the saturation states of calcite and aragonite, the prevailing CaCO₃ polymorphs used by calcifying organisms, are anticipated to diminish. Additionally, the reduction in the direct availability of carbonate ions, crucial for the construction of calcareous structures, will impact calcifying marine organisms adversely (Caldeira & Wickett, 2003; Wittmann & Pörtner, 2013).

1.1.3 Principles of calcification in organisms

Marine calcifying organisms encompass a wide range of species, including corals, mollusks, echinoderms, coccolithophores, algae and sponges. They utilize CaCO₃ as a building material to create biomineralized structures, which serve essential functional roles, such as tissue support, protection against predators, reproduction, locomotion, detection of gravity, to name a few (P. Gilbert et al., 2022; Song et al., 2019). Mineral deposition occurs in a regulated process within isolated spaces and in close association with organic matrix (Towe, 1990). Different models for the calcification process exist, mainly separating between intra- and extracellular calcification mechanisms. Intracellular calcification, mainly by the generation of an metastable amorphous

CaCO₃ (ACC) precursor in subcellular compartments has been demonstrated in several calcifying species including sea urchins, corals and mollusks (Mass et al., 2017; Mount et al., 2004; Sun et al., 2020). In addition, extracellular calcifying environments like the calcifying fluid in corals or the extrapallial fluid in bivalves, that lies between the calcifying cells and the skeleton, has been demonstrated to be critically involved in mineral formation (Crenshaw, 1972; Sevilgen et al., 2019). Recent advances propose that calcification in many calcifying systems likely comprises a combination of both processes (P. Gilbert et al., 2022). However, in both systems a chemically complex aqueous solution, termed calcifying fluid (CF) has to be created, from where carbonate biominerals or amorphous precursors grow from. For this seawater or seawater-like fluids, containing 10 mM Ca²⁺, 0.1 – 0.3 mM CO₃²⁻, 2 mM HCO₃⁻ and CO₂ are endocytosed into the biologically controlled isolated compartments, termed as “privileged space”, and further utilized for the calcification process (P. Gilbert et al., 2022). Due to ocean acidification, the changing ocean conditions, such as less availability of CO₃²⁻ ions, decreasing surface pH and increase in temperature, could have serious impact on marine calcifiers (Caldeira & Wickett, 2003; Melzner et al., 2009).

1.2 Purple Sea urchin *Strongylocentrotus purpuratus*

1.2.1 Model organism: the sea urchin larva

The overall definition of a model organism is: “to extensively study a non-human species to understand a range of biological phenomena or to generate data, which can be transferred on other organisms” (Fields & Johnston, 2005; Paredes, 2016). For over 150 years, the purple sea urchin *Strongylocentrotus purpuratus*, first discovered and named by William Stimpson in 1875 (Stimpson, 1857) has been studied considerably and used as a model organism for many scientific areas. In particular the sea urchin larva has been used by biologists to study the development and morphogenesis of an early deuterostome, because of its properties, which are listed below: The larva exhibits a small size from about 300 μM, it is transparent and has a simple body plan consisting of a three partite digestive tract, an ectoderm, a simple nervous system, a calcitic endoskeleton and a limited spectrum of 15-20 distinct cell types (Fig. 1.2).

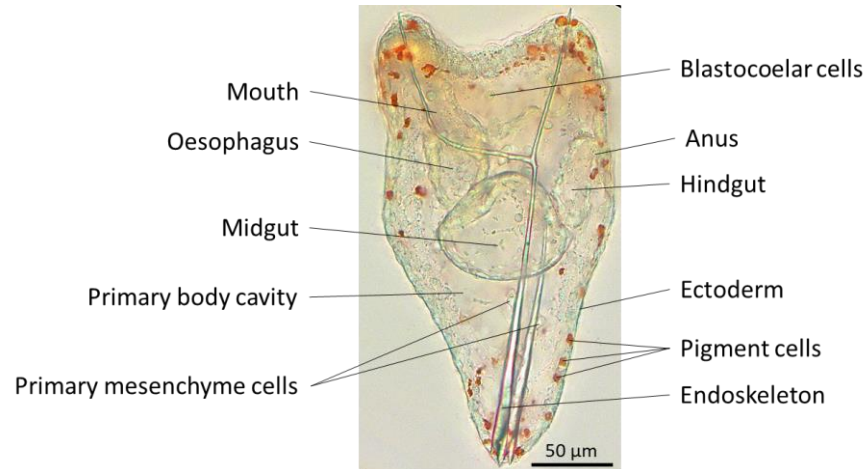


Fig. 1.2: Morphology of a larvae of the purple sea urchin *Strongylocentrotus purpuratus*, lateral view, 4 dpf (days post fertilization).

The genome of the purple sea urchin is fully sequenced, tools for analyzation and manipulation of the gene expression are available and sea urchins and their larvae are relatively easy to maintain under laboratory conditions. Larval cultures can be produced by obtaining eggs from females and sperm from males by gently shaking the animal. The fertilized eggs undergo a rapid embryogenesis within only four days until development of the pluteus larvae. Depending on the number of eggs, a large number (ten thousand to millions) of synchronously developing embryos, can be obtained (Adonin et al., 2021; Ettensohn, 2017). Currently the purple sea urchin *S. purpuratus* has limitations when it comes to the generation of genetically modified strains due to the long generation times of approximately five years from egg to egg. Here species with a shorter generations time (i.e. *Lytechinus pictus*) of one year are promising sea urchin models to promote genetically modified strains.

1.2.2 Larval development

S. purpuratus reproduce by external fertilization by releasing their eggs and sperm into the seawater. After ten hours post fertilization (hpf), in the cleavage stage, the embryo consists of macromeres, mesomeres and micromeres, with four cells for each cell type. Following the next cleavage, the micromeres will divide into four small and four large micromeres. The four large micromeres will further differentiate into the primary mesenchyme cells (PMCs), which give rise

to the skeletogenic cell line of the larva. After 24 hpf the embryo transforms into the blastula, which forms the blastocoel cavity. Further, cilia appear and the embryo hatches from its fertilization envelope and starts to swim. After 48 hpf the PMC ingression starts, followed by the invagination of the archenteron, which is initiated by the changing shape of the mesoderm and cell rearrangement. This stage is called gastrula and in the mid-gastrula stage at 48-52 hpf the skeletogenesis initiates. During this phase the secondary mesenchyme cells form filopodia, migrate to the blastocoel wall and help connecting the archenteron with the blastocoel wall. After 72 hpf the larva reaches the prism stage, with a fully formed intestine consisting of a mouth, a three partite gut and an anus. After 96 hpf the larva drastically changed its shape due to high growth rates of the skeleton and develops to the swimming and feeding pluteus larva with four arms (S. E. Gilbert, 2000; McClay, 2011). Later during development, the larva will transform into eight-armed pluteus larva. Further the rudiment growths in the coelomic pouch, that will metamorphose into the juvenile sea urchin after 50 - 60 days post fertilization (dpf) (Smith et al., 2008) (Fig. 1.3).

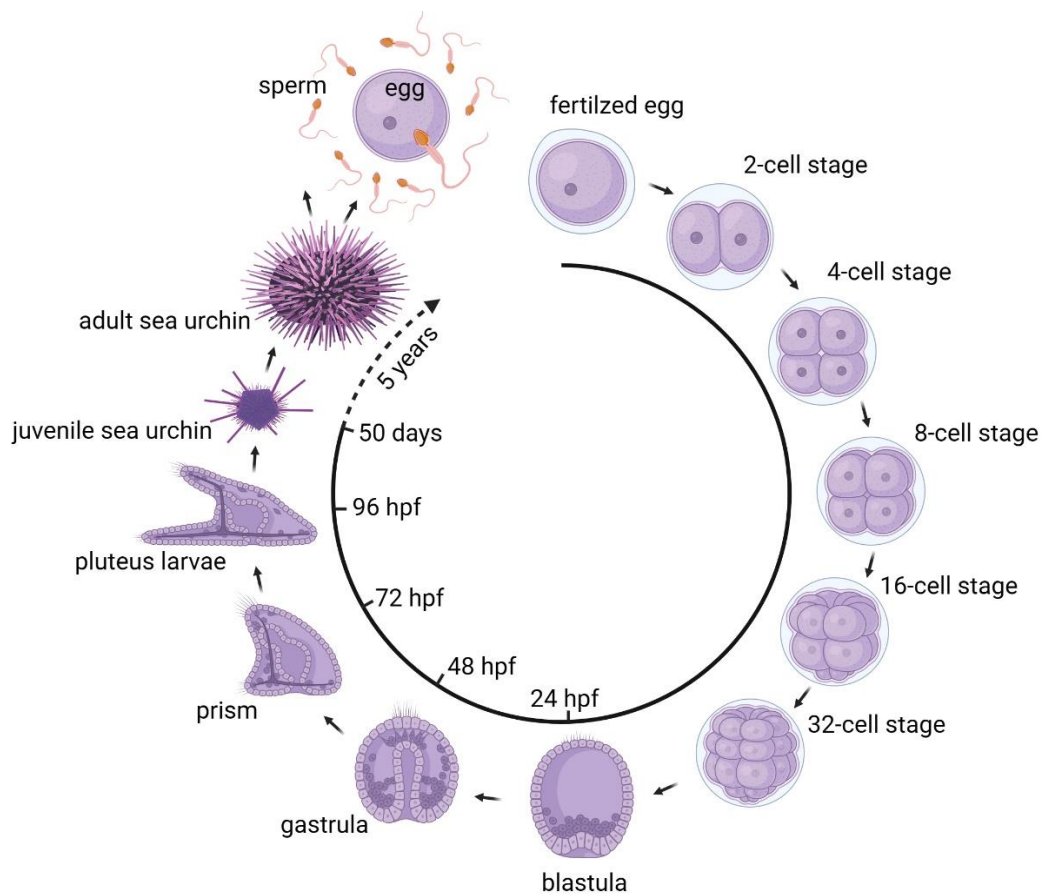


Fig. 1.3: Illustration of the life cycle of the purple sea urchin *Strongylocentrotus purpuratus* from egg to egg. hpf: hours post fertilization. Image created with BioRender.com, with permission.

1.2.3 Primary mesenchyme cells (PMCs)

In the 12-cell stage of the sea urchin embryo, the four micromeres divide unequally into four large and four small micromeres. These four large micromeres (32-cell stage) give rise to the cellular lineage that forms the larval skeleton. In the blastula stage these cells start to ingest into the blastocoel close to the blastocoel wall and form the mesenchyme. The mesenchyme is divided into primary and secondary mesenchyme cells. The primary mesenchyme cells (PMCs) are the calcifying cells of the larva, are motile, actively form filopodia and are arranged in a defined pattern on the blastocoel wall. A ring of PMCs is formed around the invagination of the archenteron with two triangular cell clusters on the side, where ventro-lateral branches of cells extend towards the animal pole. This is followed by the fusion of the filopodia of the PMC population to form a syncytial cord. In the mid-gastrula stage at six – eight hours after ingress of the mesenchyme cells, the skeleton formation begins in the triangular PMC clusters, creating a triradiate spicule rudiment on the oral side of the embryo (Fig. 1.4 A). Further, the elongation of the skeleton continues along the PMC cords to form the body rod, the postoral rod and the anterolateral rod, which dictate the position and shape of the skeleton (Fig. 1.4 B). The syncytial cord of PMCs surrounds the skeleton, creating a sheath between the skeleton and the extracellular matrix (Wilt, 1999; Wolpert & Gustafson, 1961).

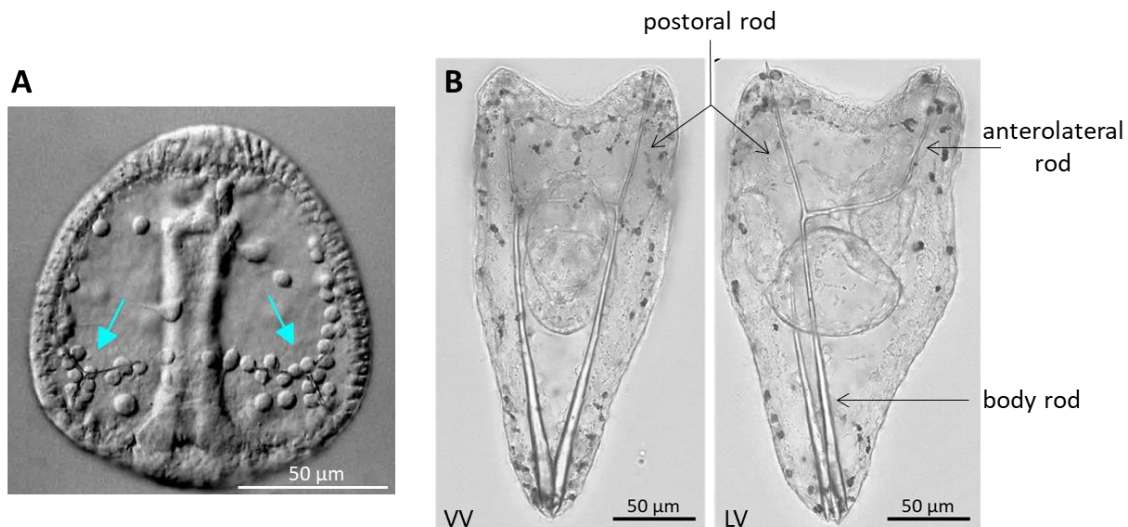


Fig. 1.4: (A) Late gastrula with PMC ring. Blue arrows indicate the triradiate spicule rudiment on the oral side of the embryo. (adapted from (Morrill & Marcus, 2005)) (B) Four dpf larva with a fully developed skeleton showing the different spicule parts, including postoral rod, anterolateral rod and body rod. VV: ventral view; LV: lateral view

1.2.4 Calcification in the sea urchin larvae

The spicules of the sea urchin larva consist of high magnesium calcite containing 5% MgCO_3 (Wilt, 2002). Analyses of the spicule composition demonstrated the incorporation of glycoproteins that comprise 0.1% of the total mass. To name a few, the most abundant spicule matrix proteins are msp120, SM50, SM30, SM37, Lectins, matrix metallo-proteases, collagen and carbonic anhydrases. These matrix proteins have an important role in regulating the growth and the physical properties of the biomineral, regarding its special texture, flexibility and hardness of the spicule (Mann et al., 2010). Additionally, some of these genes are exclusively expressed in the PMCs and therefore act as marker genes for PMCs. In the sea urchin larva mineralization is initiated inside the PMCs as a metastable transient amorphous calcium carbonate (ACC) precursor that is exocytosed to generate the crystalline calcitic endoskeleton (Beniash et al., 1997; Politi et al., 2006; Raz et al., 2003). ACC is accumulated and stored in vesicles inside the PMCs, transported to the syncytial cord membrane and secreted to the spicule (Winter et al., 2021). ACC is characterized by its disordered, non-crystalline structure and high solubility, in contrast to its more crystalline counterparts, calcite and aragonite. The lack of structure gives it distinct and very dynamic properties, however making it less stable and more difficult to detect using light microscopic methods (Addadi et al., 2003). The mature spicule of the larva still contains more than 40% ACC, to further maintain flexibility and avoid brittleness of the spicule (Emlet, 1982; Kahil et al., 2021). The sea urchin larva, and also other marine calcifiers evolved sophisticated cellular mechanisms to control the abiotic conditions in the calcification vesicles to promote the formation and stabilization of ACC (Raz et al., 2003). The calcium used for biomineralization derives from the seawater, which contains only 10 mM Ca^{2+} . Early studies by Nakano and Okazaki using radioactive Ca^{45} could demonstrate, that calcium is transported from the seawater through the PMC to the spicule (Nakano et al., 1963). Recent studies using cryo-transmission electron microscopy techniques coupled with elemental analyses confirmed this observation and could identify vesicles containing high amounts of calcium, that are transported inside the cell and potentially contribute to the calcification process (Kahil et al., 2020; Winter et al., 2021).

Therefore, the seawater-like fluid inside the vesicles must undergo a change in composition to concentrate Ca^{2+} up to 15 M and elimination of other ions (i.e. NaCl) and water. Moreover, for maturation of ACC and its crystallization at the spicule, water must be eliminated from the vesicles as well as from the syncytial cord (Kahil et al., 2020, 2021).

1.2.5 Ion transport and pH homeostasis in PMCs

To produce ACC in sub-cellular compartments and to generate the calcitic endoskeleton the calcifying cells must exhibit transport mechanisms to promote the concentration of calcification substrates and eliminate protons that are liberated during CaCO_3 formation (Hu et al., 2018; Sikes et al., 1981; Taylor et al., 2017; Vidavsky et al., 2016). Recent studies have shed light on the largely unknown membrane transport processes in PMCs but many knowledge gaps are still remaining to fully understand the cellular and sub-cellular mechanisms of CaCO_3 formation.

It is currently believed that the major pathway for calcium uptake is achieved by endocytosis of seawater-like fluids from the blastocoel. These conclusions were drawn from several lines of evidences. First the route of calcium transport was characterized using the membrane-impermeable fluorescent dye calcein, that specifically binds to Ca^{2+} ions. Calcein pulse-chase experiments showed emitted fluorescence within endocytosed vesicles of PMCs as well as in newly formed spicules (Bentov et al., 2009; Vidavsky et al., 2016). Cryo-TEM analyses in combination with elemental analyses demonstrated that PMCs contain more than 100 vesicles with a diameter of 100 - 500 nm that are often connected by a vesicular network, which have a high calcium concentration up to ~ 15 M (Kahil et al., 2020; Vidavsky et al., 2015, 2016). These Ca^{2+} -rich vesicles contain mineral particles of 20 – 200 nm of ACC (Kahil et al., 2020, 2023). Very recently, researchers detected phosphate in Ca^{2+} -rich vesicles, which could play a role in the stabilization of ACC (Kahil et al., 2023). In addition, pharmacological studies suggest, that besides the vesicular uptake of Ca^{2+} , there is also an energy dependent pathway for Ca^{2+} uptake potentially involving Ca^{2+} -ATPases, that mediates Ca^{2+} transport between cell organelles (Kahil et al., 2021). While the source and transport of Ca^{2+} is understood to some extent, the transport and concentration of carbon in PMCs remained mainly unknown. Sikes *et al.* demonstrated that up to 60% of carbon, which is deposited in the larval skeleton, derives from metabolic CO_2 , while the

remaining 40% are absorbed from the environment (Sikes et al., 1981). Here it has been demonstrated that PMCs exhibit a Na^+ -dependent HCO_3^- uptake mechanism, that mediates the import of bicarbonate from the seawater/blastocoel (Hu et al., 2018; Stumpff et al., 2012). HCO_3^- transport by the $\text{Na}^+/\text{HCO}_3^-$ cotransporter (NBC) Sp-Slc4a10 was stimulated in actively calcifying PMCs leading to an increase in the cellular bicarbonate pool of PMCs (Hu et al., 2020). The conversion of metabolic CO_2 to form HCO_3^- depends on the pH and is catalyzed by carbonic anhydrases. In fact, pharmacological studies using the specific carbonic anhydrase inhibitor acetazolamide could detect reductions in calcification rates in the presence of this small molecule inhibitor (De Goeyse et al., 2021; Karakostis et al., 2016; Livingston et al., 2006; Mitsunaga et al., 1986). The formation of CO_3^{2-} from CO_2 or HCO_3^- will liberate protons that must be removed from the cell to maintain acid-base homeostasis and to further promote calcification. Thus, PMCs must have pH regulatory mechanisms that enable the export of protons from the site of calcification. Na^+/H^+ -exchangers (NHE) were proposed as an elimination route for H^+ and therefore plays an important role in the pH homeostasis during skeleton maintenance, but not necessarily for the removal of protons during high rates of mineralization (Hu et al., 2020). A third potential exit route is the energy consuming *V-type* H^+ -ATPase (VHA) that has been detected in large vacuoles of secondary mesenchyme cells that appear in large numbers during high calcification activity (Hu et al., 2020). It has been speculated that protons liberated by PMCs are absorbed into these vesicles and thereby removed from the calcification front. However, the exit route for protons from PMCs remains highly speculative but represents a key element in the calcification machinery not only in the sea urchin larva, but many other calcifying organisms.

1.3 Otopetrin family of proton channels

Otopetrins are a newly discovered family of proton selective channels, which promote proton transport across cell membranes (Saotome et al., 2019). They are named after their first discovery in the formation process of otoliths/otoconia in the vertebrate inner ear (Hughes et al., 2004). Knock-down and mutations of otopetrins lead to agenesis of statolith and otoliths in the vertebrate inner ear (Hughes et al., 2004; Hurlle et al., 2003). There are only three genes related to the otopetrin family in animals, Otop1, Otop2 and Otop3 (Hughes et al., 2008) and otopetrins have no structural similarities with other transporters or ion channels (Tu et al., 2018). They all

share the structure of 12 transmembrane helices, and one single otopetrin subunit is divided into two domains, the amino-terminal (N) domain and the carboxy-terminal (C) domain. Two subunits form the homo-dimeric architecture to assemble the pseudo-tetrameric organization of the protein (Saotome et al., 2019). Otop1 was detected to induce sour-sensing in the taste system in mice. This Otop1 is sensitive to changes in pH by sensing the H^+ in acidic stimuli and induce an inwards directed proton current in the taste receptor cells, which further leads to an action potential cascade (Teng et al., 2019; J. Zhang et al., 2019). An Otop1-like proton channel was also found in the sour sensing receptor cells of the fruit fly *Drosophila melanogaster* (Ganguly et al., 2021). Otop1 was not only detected in the taste buds, but also in the vestibular system in the inner ear. There it is involved in the formation of vertebrate otoconia in mice or bigger otoliths in zebra fish, which are composed of polymorphs of calcium carbonate ($CaCO_3$) crystals precipitated around extracellular matrix proteins (Hughes et al., 2004; Hurle et al., 2003). Using heterologous expression systems, a highly zinc-sensitive proton conductance was detected (Tu et al., 2018). Otopetrins are not voltage gated but rather $[H^+]$ gated by extracellular protons and exhibit their optimum working spectrum under different pH conditions. For example, Otop2 is active under alkaline conditions from pH 8-8.5 and is mostly inhibited under acidic conditions $pH < 7$, however, Otop1 and Otop3 are very active under acidic conditions (Teng et al., 2022).

An otopetrin homologue was detected in the sea urchin genome that is exclusively expressed in PMCs of the sea urchin larva (Rafiq et al., 2014). Due to their association with calcifying tissues and the fact, that otopetrins conduct protons and their pH dependent activation and H^+ gating, they may represent a key player in pH regulatory mechanisms underlying the calcification process. PMCs of sea urchin larvae need to export protons to maintain intracellular pH and to promote mineralization (Stumpp et al., 2012). Especially during high calcification rates during the rapid early formation of the larval skeleton, PMCs may be challenged by a substantial acid load. Calculations suggest, the generation of 1 mole of calcium carbonate liberates 1.6 moles of protons (Sikes et al., 1981) that must be removed from the cell. Here the present work addressed the role of otopetrins as a potential exit route for protons in calcifying cells.

1.4 Carbonic Anhydrases

Carbonic anhydrase (CA) is an enzyme, which was first discovered and purified in 1933 from erythrocytes by Meldrum and Roughton (Meldrum & Roughton, 1933). Carbonic anhydrase catalyzes the reversible interconversion of CO_2 and H_2O to HCO_3^- and H^+ by interacting with CO_2 and H_2O or $\text{H}_2\text{CO}_3/\text{HCO}_3^-$. CAs were demonstrated to speed up this reaction by 1 million-fold (Jackson et al., 2007). This simple reaction catalyzed by CAs is involved in many physiological processes of fundamental importance and occurs ubiquitously in organism of the five kingdoms (Supuran, 2008; Tripp et al., 2001; Zebal et al., 2019), while the uncatalyzed hydration of CO_2 itself is too slow to accomplish these functions in biological systems (Bertucci et al., 2013). For example, CAs are essentially involved in a number of biological processes including osmoregulation, blood gas transport, CO_2 concentration for photosynthesis, respiration, regulation of the acid/base homeostasis as well as biomineralization (Supuran, 2008). CAs are metalloenzymes, which bind zinc as their cofactor in their active side (Lindskog, 1997; Tripp et al., 2001). The reaction cycle starts by binding of water to zinc that creates a very reactive hydroxide ion and releases a proton. This results in a nucleophilic attack of CO_2 , leading to zinc-bound bicarbonate, which is instable and as a consequence bicarbonate is released and replaced by another water molecule (Christianson & Fierke, 1996; Le Roy et al., 2015; Zebal et al., 2019). In general, CAs can be divided into five subfamilies, α -CA, β -CA, γ -CA, δ -CA and ζ -CA, where α -CAs are the most abundant and best studied group of CAs. They occur cytosolic, secreted, mitochondrial or membrane bound (Supuran, 2008; Tripp et al., 2001; Zebal et al., 2019). Depending on their localization CAs can have very different functions. For example, intracellular CAs, are involved in CO_2 transport in the blood (Geers & Gros, 2000) and cellular carbon supply and increase the CO_2 concentration for photosynthesis in plants or marine algae (Burlacot et al., 2022; H. Zhang et al., 2020). Extracellular or membrane-bound CAs were demonstrated to be involved in pH homeostasis in osteoclasts (Riihonen et al., 2007). Another example are marine invertebrates, which rely on the availability of DIC species for synthesis of their CaCO_3 skeleton. Some studies proposed the usage of external HCO_3^- as well as metabolic CO_2 as the main DIC supply (Furla et al., 2000; ter Kuile et al., 1989). Accordingly, CO_2 must be converted to bicarbonate, where carbonic anhydrases were proposed to play a key role in this process. Recent research described such involvement of CAs in the calcification process in mollusks (Wang, Wang, Jia, Song, et al., 2017), sponges (Jackson et al., 2007; Jones & Ledger, 1986), corals (Bertucci et al.,

2013), coccolithophores (H. Zhang et al., 2020) or foraminifera (De Goeysse et al., 2021). However, the exact mechanisms by which Cas contribute to the calcification process in the living animal is yet unknown, largely due to the lack of functional data. Nevertheless, the sea urchin larva has a long-standing association with the study of CAs. Impressively, the first CA activity in the sea urchin embryo was already measured in 1933 by Brinkman (Brinkman, 1933). Following this, Benson and Chow showed highly increased CA activity in the beginning of the development at 24 hpf, mid-blastula stage, which is exactly the time point when skeletogenesis initiates (Benson, C. & Chow, 1979). This was the first evidence for the potential contribution of CAs to the calcification process. Pharmacological approaches using the CA specific inhibitor acetazolamide (AZM) (Maren, 1977; Miller et al., 1950) on whole larvae (in vivo) as well as micromere cell cultures (in vitro) showed reduction in spicule growth in the presence of the inhibitor (Benson, C. & Chow, 1979; Mitsunaga et al., 1986). After genome sequencing and gene annotation of the sea urchin *Strongylocentrotus purpuratus*, 19 genes coding for CAs were found, but only very few were detected in PMC specific databases (Livingston et al., 2006). Despite their strong association with calcifying systems, the exact functions of CAs remained enigmatic in the calcification process. Thus, the present work aimed at better understanding the function of CAs in the calcification process using the calcifying PMCs of the sea urchin larva as a model system.

1.5 Aquaporins

Channels and transporters situated within the cell membrane enable the selective movement of molecules, ions, and also water through the lipid bilayer. Aquaporins (AQPs) are a distinct family of transmembrane proteins that facilitate the transport of water in response to osmotic gradients across membranes (Dix & Solomon, 1984). AQPs were first discovered by Peter Agre in 1988 (Denker et al., 1988), and in the course of further research they have been associated to a wide range of biological functions, including osmotic regulation, acid-base homeostasis and gas transport in cells and across epithelia (Brown et al., 2012; Endeward et al., 2006; Hu et al., 2014; MacIver et al., 2009; Todgham & Hofmann, 2009; Tsukaguchi et al., 1999; Weiner & Verlander, 2017). AQPs share an evolutionarily conserved structure, consisting of six transmembrane α -helices and two half-helices, connected by extracellular and intracellular loops, with cytoplasmatic C- and N-termini (Verkman, 2000). This structure forms a hydrophobic pore,

and the specific arrangement of amino acid sequences, like the NPA signature motif and aromatic arginine (ar/R), determines the selectivity of the channel (Hedfalk et al., 2006; Hub & De Groot, 2008). Four of these monomers form a homo-tetramer, integrated in the cell membrane, allowing the functional aquaporin to transport four water molecules concurrently (Verkman, 2011).

AQPs have been demonstrated to selectively conduct water while excluding other solutes and gases (Verkman & Mitra, 2000). However, in addition to water, some AQPs were demonstrated to also conduct gases including CO₂ and NH₃ (Cooper et al., 2015; Geyer et al., 2013). Within the aquaporin family, aquaglyceroporins constitute a subfamily, that differ in their pore composition and size, resulting in distinct selectivity properties. They not only transport water but also permit the movement of other small, uncharged solutes like glycerol, NH₃, CO₂, urea and H₂O₂ (Aharon & Bar-Shavit, 2006; Hub & De Groot, 2008; Ishibashi et al., 2002; Li et al., 2020; Tsukaguchi et al., 1999). In humans, aquaglyceroporins (AQP3, 7, 9, 10) play essential roles in various processes, including skin hydration, cell proliferation, and kidney water permeability (AQP3) (Rojek et al., 2008; Verkman, 2011), adipocyte glycerol metabolism and urine concentration in the kidney (AQP7) (Rojek et al., 2008; Verkman, 2013), gluconeogenesis and glycolysis in the liver and osteoclast differentiation (AQP9) (Aharon & Bar-Shavit, 2006; Carbrey et al., 2003; Rojek et al., 2008), as well as water and nutrient absorption in the intestine (AQP10) (Ishibashi et al., 2002).

While their primary function has long been associated with water transport, an increasing attention has been dedicated to their role as gas channels, facilitating the passage of CO₂ through the cell membrane (Cooper et al., 2015; Endeward et al., 2006). For instance, CO₂ transport via AQPs has been observed in various organisms, such as the tobacco plant (Uehlein et al., 2003), red blood cells (Endeward et al., 2006), and marine diatoms (Matsui et al., 2018). These observations underscore the diverse array of physiological processes in which AQPs are involved, extending beyond their fundamental role as water channels (Verkman, 2011).

In the calcification process within PMCs of the sea urchin larva, water or CO₂ transport potentially plays a significant role. For example, concentration of calcification substrates in the calcification vesicles is potentially associated with the removal of water similar to the situation observed in macropinosome shrinkage (Zeziulia et al., 2022). Furthermore, concentration of carbon in the calcification compartment may be associated with the CO₂ conductivity of AQPs as well. But AQPs may be also involved in a range of other calcification-relevant processes including filopodia formation, regulation of cell volume and cell migration (Loitto et al., 2007; Verkman, 2000, 2011, 2013). Previous reports and databases (echinobase.org database) provided evidence primarily at

the gene and transcriptome levels for the presence of AQPs in the sea urchin (Ishibashi, 2006; Ishibashi et al., 2020; Rafiq et al., 2014; Todgham & Hofmann, 2009). Interestingly some AQPs are exclusively expressed in the calcifying primary mesenchyme cells (Rafiq et al., 2014). However, the physiological functions of AQPs in PMCs remain unclear. Thus, a core task of the present work will be dedicated to decipher their role in the calcification process.

1.6 Objectives

The aim of this work was to elucidate the following research hypotheses to further unravel the cellular mechanisms of the calcification process taking place in the PMCs of the sea urchin larva.

- I. The role of an otopetrin-like proton channel in the PMCs of the sea urchin larva as a potential proton exit route during the calcification process.
- II. Understanding the function of carbonic anhydrases in the PMCs of the sea urchin larva and their involvement in the carbon concentration mechanisms for the calcification process.
- III. The role of aquaporins in the PMCs of the sea urchin larva and their potential contribution in the calcification process.

2 Methods

2.1 Maintenance of adult sea urchins and larval cultures

Adult purple sea urchins (*Strongylocentrotus purpuratus*) were collected at the coast of California (Ja Jolla, USA) and shipped to the Helmholtz Centre for Ocean Research Kiel (GEOMAR). The sea urchins were kept in a climate chamber at 12°C at the GEOMAR. The animals were maintained in a re-circulating natural seawater system, using fresh Baltic seawater with an adjusted salinity of 32 and regular water changes were made three times a week. The sea urchins were fed with *Laminaria sp.* three times a week. Spawning of males and females was induced by shaking and larval cultures were maintained at a concentration of ~12,500 larvae/L at 15°C with continuous aeration. For most of the larval experiments 3 and 4 dpf old larvae were used without feeding.

2.2 In silico analysis

2.2.1 Gene mining and structural analysis

The genome of *Strongylocentrotus purpuratus* is fully sequenced and accessible for research purposes on the EchinoBase database (www.echinobase.org, *Strongylocentrotus purpuratus* 5.0 GCF (NCBI)). The DNA and amino acid sequences for phylogenetic analysis were collected from EchinoBase, the Ensembl (<http://www.ensembl.org/>), Reefgenomics (<http://reefgenomics.org>) databases and aligned and compared with the sequenced sequences from the sea urchin larvae via the online tool MAFFT (**M**ultiple **A**lignment using **F**ast **F**ourier **T**ransform) (www.ebi.ac.uk/Tools/msa/mafft/). The sequences were scanned for motives and functional groups with (myhits.sib.swiss/cgi-bin/motif_scan), (https://mendel.imp.ac.at/gpi/gpi_server.html) and (gpcr.biocomp.unibo.it/predgpi/pred.htm). The transmembrane protein structure of Otop2l was predicted with the online tool TOPCONS. The transmembrane protein structure prediction of the amino acid structure of the expressed peptide AQP9 was depicted with 'MemBrain' (<http://www.csbio.sjtu.edu.cn/bioinf/MemBrain/>).

2.2.2 Phylogenetic analysis

For creating the phylogenetic tree of otopetrins, 87 otopetrin homologues of different animal phyla based on deduced amino-acid sequences were used. Blasted sequences with E-values higher than e^{-5} were excluded for following analysis. Selected sequences were aligned via MUSCLE program and further trimmed by Gblocks Server (http://molevol.cmima.csic.es/castresana/Gblocks_server.html). The phylogenetic analysis was generated by MegaX (Stecher et al., 2020) with the best fit model LG+G+F and 500 bootstrap replicates. For the phylogenetic tree Cara7 (XP_003726289.2) and Cara2 (XP_782997.3) sequences were blasted to NCBI (<https://blast.ncbi.nlm.nih.gov/Blast.cgi>) and Reefgenomics databases, and homologous sequences with E-values higher than $9e^{-41}$ ($9e^{-75}$ for iCA and $9e^{-41}$ for eCA) were excluded for the following analysis. Selected sequences were aligned via the MUSCLE program and further trimmed by Gblocks Server (http://molevol.cmima.csic.es/castresana/Gblocks_server.html), and the 140 aa trimmed sequences were used for the phylogenetic analysis. The Maximum Likelihood tree was generated by MegaX (Stecher et al., 2020) with the best fit model LG+G+I and 500 bootstrap replicates.

2.2.3 Single cell transcriptome database analysis

Single-cell RNA sequencing was performed as previously described (Chang et al., 2021) using the 10x Genomics commercial platform. Dimensional reduction was achieved using uniform manifold approximation and projection (UMAP) and projections are plotted as dot plots representing each dot as one cell. Unsupervised clustering of cells resulted in several clusters out of which clusters positive for pan-PMC marker genes *Alx1*, *SpP19L* and *SM50* were identified as PMCs. Scaled and normalized counts per cell of 'gene of interest' are shown in blue. cluster identified with special marker genes to the corresponding cell type of the larvae. The single cell transcriptome database was provided by Jonas Brandenburg (Dr. David Garfield Lab, Berlin). The database analysis was performed with R studio and a written script, changed in aspect to the gene of interest.

2.3 Molecular Techniques

2.3.1 Molecular cloning

The primers for cloning and *in situ* probe synthesis were designed with Primerblast (www.ncbi.nlm.nih.gov/tools/primer-blast/) and re-blasted with (blast.ncbi.nlm.nih.gov/Blast.cgi). The transcript sequences of the sea urchin larvae genes *SPU_004766* (*LOC579173*, *Otop2I*), *SPU_012518* (*LOC579101*, *Cara7*) and *SPU_008685* (*LOC577690*, *Cara2*) were amplified via PCR using the listed primers (Tab. 2.1), including an additional A-tag for TA-cloning. The amplified sequences were cloned into pGEM-T easy cloning vector (Promega) and cultured in NEB 5 α competent *E. coli* cells. *SPU_004511* (*LOC584831*, *spAQP9*) was amplified by Azenta (Genewiz), using the listed primers (Tab. 2.1), cloned into pU57 cloning vector and also cultured in NEB 5 α competent *E. coli* cells. Plasmid extraction using the Monarch Plasmid Miniprep Kit (New England Biolabs) and sequencing (GENEWIZ) was followed by the synthesis of the RNA probes for *in situ* hybridization using M₁₃-F and M₁₃-R primers and the DIG RNA labeling Mix (Roche, Basel, Switzerland) according to manufacturer's protocol.

Tab. 2.1 List of primers used for molecular cloning, *in situ* hybridisation probe synthesis and qPCR.

| Primer Name | Primer Sequence (5'-3') | Application |
|------------------|-------------------------|-------------------------|
| 008658_F | GATACACTGGACACGGAGGC | qPCR |
| 008658_R | TTGACGAGAGCCTTGGTACG | |
| 012518_F | GAACGGTAACGGATGGGGAG | |
| 012518_R | GGGTCCGTTTCATGCCAAAAG | |
| Otop2L_F | GTTGGCAGACGGATCACAGC | |
| Otop2I_R | TAGAAGCACCTGCATGACGG | |
| spAQP9-qF | TGCAAAGACTCCCCTTTAGC | |
| spAQP9-qR | GACATCTGGGTGACTCCATC | |
| EF1a_F | CCGACCTTGAAAGGGATCG | |
| EF1a_R | ACAGTCGGCCTGTGAGGTTT | |
| M13-F | CGCCAGGGTTTTCCAGTCACGA | In situ probe synthesis |
| M13-R | TCACACAGGAAACAGCTATGAC | |
| 008658_F | GATACACTGGACACGGAGGC | |

| | | |
|------------------|-----------------------|---|
| 008658_R | CCACGACCCTCGAAAGACTC | cloning for <i>in situ</i> hybridisation |
| 012518_F | GAACGGTAACGGATGGGGAG | |
| 012518_R | ATAACACCGCAACCGACAGA | |
| Otop2L_F | TTGCGCAAACAACGTCTCAG | |
| Otop2L_R | GATAACGCCACACATCGTGC | |
| spAQP9-F1 | ACCAAGCACACGTGACTCTA | |
| spAQP9-R1 | CGGTTGTTTAACGCTCTCGTG | |
| spAQP9-F2 | GGGTCGCCAGCTCTATACTC | |
| spAQP9-R2 | TCCGACCTAAACTCGACGTTA | |

2.3.2 Whole mount *in situ* hybridization

Larvae were fixed with 4% PFA/FSW and for storage dehydrated with MeOH and stored at -20°C. Larvae were re-hydrated in an ascending series of MeOH and DEPC-PBST, and fully washed with DEPC-PBST in the final step. Pre-hybridization was performed for at least 1 h at 60°C. Digoxigenin-labeled probes (500 – 1,000 ng/mL) were pre-warmed at 70°C and hybridization was performed at 55°C/65°C overnight. Samples were washed with hybridization buffer, wash buffer (50% Formamide, 5x SSC, 0.1% Tween-20) and 2x SSC at 65°C followed by another washing step with 2x SSC at 37°C and by MABT (500 mM Maleic acid, 750 mM NaCl, NaOH, pH 7.5, 0.1% Tween-20) at RT. Samples were washed with MABT for 2 h and transferred to a blocking solution (1x MAB, 2% Block reagent (Roche), 10% sheep serum (Jackson IR), 0.1% Tween-20) for 2 h. Further, samples were incubated overnight with 1:2,000 sheep anti-Digoxigenin-AP Fab fragments (Roche) antibody at 4°C followed by intensive washing with MABT at the next day. The color reaction was performed with BM Purple AP (Roche) according to manufacturer's instructions until color reaction was visible in the location of interest. For evaluation, the treated larvae were screened and from representative larvae pictures were taken with a white background (white paper on top of the sample). Pictures were taken by a Zeiss Observer A1 inverted microscope using the Zeiss Zen 3.3 (blue edition) software. For negative control the larvae treated with the sense probe were analyzed the same.

2.3.3 RT-qPCR

RNA from control and re-calcifying larvae at 0D, 1D, 2D, 3D, 4D, 5D and 6D from three experimental replicates was isolated by using the Direct-zol RNA MicroPrep kit (Zymo Research). RNA samples were reverse transcribed by Super Script IV cDNA synthesis kit (Invitrogen, Waltham, USA) for quantitative RT-PCR. To measure the expression levels of the target genes the 7500 Fast Real-Time PCR System (Applied Biosystems) was used and expression levels of target genes were normalized to the housekeeping gene EIF1 that has been demonstrated to be stable along ontogeny and during skeleton re-calcification (3, 11).

2.3.4 Immunocytochemistry

3 or 4 days old larvae were fixed with 4% PFA/FWS for 10 min, washed with PBS and blocked with PBS containing 5% bovine serum albumin (BSA) for at least 1 h at RT. Afterwards the larvae were incubated overnight at 4°C with the affinity purified polyclonal antibody (dilution 1:250) raised against the sea urchin Otop21 protein (**CLDAMHRKPPEDFKQTR**) or Cara7-specific synthetic peptide (**NH2-CGQNAVGNQHPQWSN-CONH2**) (Pineda, Berlin, Germany) or the antibody (dilution 1:500) raised against the sea urchin AQP9 synthetic peptide (**H-CHHPHKISSRKAKGES-NH2**) (Eurogentec, Belgium). After intensive washing with PBS, larvae were incubated with the secondary antibody, a fluorophore-conjugated Alexafluor 488 anti-rabbit IgG (Invitrogen) at a dilution of 1:300, for 1 h at RT in the dark. After washing with PBS larvae were mounted on glass slides, embedded in Moviol/DABCO containing DAPI or in PBS solution containing DAPI and addition of some Q-tip-strings as spacers between slide and cover slip. Next, pictures were taken on a confocal microscope equipped with an Airyscan function (LSM800/P2, Zeiss) and analyzed with Zen 3.3 blue edition.

2.3.5 Western blot analysis

1000 larvae were collected, removal of as much FSW as possible, instantly frozen using liquid nitrogen and stored at -80°C. For SDS-Page samples were weighted and proteins were extracted by direct mixing with 1:1 (w/vol) 2x Lämmli loading buffer. Samples were incubated at 95°C for 5 min and proteins were fractionated by SDS PAGE on a 10% polyacrylamide gel and blotted to a PVDF membrane (Bio-Rad), using a tank blotting system (Bio-Rad). Blots were blocked for at least 1 h at RT with PBS-Tween buffer containing 5% bovine serum albumin (BSA).

Afterwards the blots were incubated in a 1:10,000 (Cara7) and 1:7,500 dilution (Otop2l, AQP9) of the primary antibody at 4°C overnight. When protein quantity was of interest, additionally washing step with PBS-T buffer followed and the blots were incubated for 15 min at RT with GAPDH antibody in a 1:1,000 dilution. Further for all blots, after intensive washing with PBS-T buffer the blots were incubated for 1 h at RT with the secondary antibody a peroxidase-conjugated goat anti-rabbit IgG (Dianova, Hamburg, Germany) at a 1:40,000 (Cara7) and 1:20,000 (AQP9) dilution (IgG used for Otop2l derived from Santa Cruz Biotechnology, Santa Cruz, CA, and was used in dilution 1:14,000). After washing with PBS-T buffer the protein signals were detected using the ECL Select Western Blotting Detection Reagents (GE Healthcare, Munich, Germany) and pictures were taken on a Gel Doc 2000 system equipped with a CCD camera (Bio-Rad) and evaluated with ImageLab.

For the peptide compensation assay the primary antibody was pre-incubated with the immunization peptide at a concentration 0.1 mg/mL (Otop2l) and 0.04 mg/mL (Cara7) over night at 4°C. Finally, western blot analysis was used to validate our *Cara7* knock-down. Approximately 300 larvae of Cara7 or scramble MO injected larvae were collected and used for WB analysis as described above. The Cara7 protein abundance was normalized to total protein concentrations determined by subsequent Coomassie staining of the membrane. The blot was washed three times with H₂O and stained for ~ 1 h with 0.1% Coomassie in 40% MeOH and 7% acetic acid. Afterwards the membrane was de-stained with 50% MeOH and 7% acetic acid for ~ 1 h, washed with water, air dried and pictures were taken.

2.3.6 Morpholino injection

Micro-injection was performed using the protocol provided by Warner and McClay (Warner & McClay, 2014). Briefly, a gene-specific morpholino-substituted antisense oligonucleotides (MO) 5'-GTTGTTGCCGAAATTATACGCTTAG-3' complementary to the 5' UTR sequence ahead of the sea urchin *otop2l* (LOC579173) start codon, MO_1 (5'-AAAATATATGCATTCATGTTGATCA-3') complementary to the start codon region and a second MO_2 (5'-CGACCTTCAGATATATTCTCACAAA-3') complementary to the 5' untranslated region of the sea urchin *Cara7* gene, as well as one MO (5'-TTTAACGCTCTCGTGAAGGATA-3') complementary to shortly before the start codon region of the sea urchin *AQP9* gene were obtained from Gene Tools (Oregon). In addition, a scramble MO 5'-

CCTCTTACCTCAGTTACAATTTATA-3' that has no biological target in the sea urchin was used to obtain the control group. The MOs were dissolved in injection Buffer (20 mM Hepes, 120 mM KCl, 24% Glycerol, pH 8.0) and were injected into the freshly fertilized egg (one-cell stage) using a micro-injection system (Picospritzer III, Parker) mounted on an inverse microscope (Zeiss Observer D1) equipped with a cooling stage, to ensure a continuous temperature of 15°C. The freshly hatched larvae were transferred to 6-well plates, samples were collected at 2 dpf, 3 dpf and 4 dpf and stored in 4% PFA at 4°C. For validation pictures were taken with the inverse microscope mounted with a Zeiss camera using Zeiss Zen blue 3.3 software to also measure the spicule length.

2.4 In vivo experimental Techniques

2.4.1 Re-calcification assay

The re-calcification assay allows a specific examination of pharmacological effects on the calcification process independent from collateral effects on developmental processes. 3 dpf old usual raised larvae were exposed to 0.03 M MES buffered FSW adjusted to pH 6.0 for 12 to 15 h to fully dissolve their calcitic skeleton. Thereafter, larvae were transferred back into FSW (pH 8.0) to permit the re-calcification of their skeletons. This transfer day is defined as day 0 (OD), while the following days are defined as 1D, 2D, 3D, 4D, 5D and 6D this work.

2.4.2 Determination of calcification and re-calcification rate under pharmacological inhibition/different pH conditions (ocean acidification experiment)

For determination of the usual calcification rate of the larvae, the pharmacological substance was added to the FSW ~16 h post fertilization. One exception, Phloretin was added 48 h after fertilization, because Phloretin would interfere with the early development of the embryo by creating an exogastrulae. This could possibly affect the calcification, which would manipulate the effect of Phloretin on AQP9. When determining the re-calcification rate, the inhibitory substance was added right after dissolving the skeleton.

In general, ~200 larvae were raised in 6-well-plates filled with 10 mL FSW containing the substances in different concentrations (0.1% DMSO, 1 µM, 10 µM, 50 µM and 100 µM). Three

independent biological replicates (n=3) were performed. From the start of the experiment (0D), 20-50 larvae were sampled every day along the period of three to four days (1D, 2D, 3D,4D). Larvae were fixed with 4% PFA/FSW (pH 8.2), the overall morphology was determined and the growth rate of the skeleton was determined by measuring the daily increase in body rod + post-oral rod length, as well as only the length of the post-oral rod. Pictures were taken by a Zeiss Observer A1 inverted microscope and images were analyzed using the Zeiss Zen 3.3 (blue edition) software.

Focusing on the H⁺ channel Otop2l in the ocean acidification experiment, different pH treatments with three biological replicates per pH treatment were of the seawater was used. Larval cultures were continuously aerated with CO₂-enriched air providing constant pCO₂ levels of 400 μatm (pH 8.1), 1250 μatm (pH 7.7) and 4000 μatm (pH 7.5). Seawater physicochemical parameters including salinity, pH and temperature were monitored on a daily basis. Larval samples were collected daily and fixed in 4% PFA, to monitor morphometry and skeleton growth of larvae along the experimental period of five days.

As pharmacological substance interfering with CAs Acetazolamide (AZM; Sigma-Aldrich, Germany) and 6 kDa dextran-bound Acetazolamide (Dex-AZM; Ramidus, Sweden) were used, which are specific inhibitors for carbonic anhydrases (CAs) (Bertucci et al., 2013). While AZM has been demonstrated to be membrane permeable (Newman, 1994; Saarikoski & Kaila, 1992) the Dex-AZM cannot pass biological membranes (Brownlee et al., 2015) and thereby only targets extracellular CAs.

As inhibitory pharmacological substance for AQP9 Phloretin was used. Phloretin is a AQP9 specific inhibitor (Li et al., 2020; Rojek et al., 2008).

2.4.3 Intracellular pH (pH_i) measurements

Before starting with live cell imaging measurements, the larvae were treated for the bag isolation. Therefore, the larvae were collected in 1.5 mL tube, spined down and washed three times with 1 mL Ca²⁺ and Mg²⁺ free seawater. Then followed by two times washing with 1 mL Dissociation Medium (DIM; 1 M Glycine, 100 μM EDTA, pH 8.0), afterwards transferred back into 1 mL FSW. This treatment results in removal of the ectodermal cells and the extracellular matrix. By this the PMCs are viable throughout the experiment.

In general, intracellular pH (pH_i) measurements were performed using the pH-sensitive dye BCECF-AM. After incubation with 50 μM BCECF-AM for 30-45 minutes, the dye permeates into the cells and is trapped by cleavage of the AM ester group, which results in a charged form of BCECF. Now it can detect pH changes inside the cell in a range of $\text{pH } 7.0 \pm 1.0$. The larvae were immobilized on 1% Protamine sulfate coated coverslips that were attached to the bottom of a perfusion chamber. The fluorescence was monitored on an inverted microscope (Zeiss, Observer A1) equipped with an appropriate light source and the imaging software (Visitron).

To translate fluorescent ratios into pH_i values, a calibration curve was created, using a 10 μM nigericin and 150 mM potassium containing solution adjusted to different pH levels ranging from pH 5.5 to 8.5. With the calibration curve, it was possible to estimate the relation between detected fluorescence ratio of BCECF and the corresponding pH_i .

2.4.3.1 Characterization of H^+ fluxes in PMCs

Proton permeability experiments were conducted by using artificial seawater (ASW). ASW containing 5 mM Na^+ and 0 mM HCO_3^- (NMDG⁺) in combination with a pH 5.8 treatment was used to acidify PMCs followed by a restoration of pH_i in Na^+ and HCO_3^- independent PMCs was initiated by the perfusion of ASW adjusted to pH 8.0 in the presence of 5 mM Na^+ and 0 mM HCO_3^- . Finally, ASW containing 450 mM Na^+ and 2 mM HCO_3^- was used to initiate pH_i recovery in Na^+ and HCO_3^- dependent PMCs. After identification of PMCs that regulate pH_i in a Na^+ and HCO_3^- independent manner, a second low pH challenge in combination with three different Zn^{2+} concentrations (0, 1, and 10 mM) was performed. The recovery slope after the low pH challenge was used to address the sensitivity to proton fluxes to different Zn^{2+} concentrations.

Scramble and Otop2l morpholino injected larvae were measured in an alternate mode and from each larva 4-5 cells were simultaneously recorded. Intracellular acidification and pH_i recovery experiments were performed under 0 mM HCO_3^- and 5 mM Na^+ conditions. Only PMCs that did not respond to an exposure to ASW after the 5 mM Na^+ and 0 mM HCO_3^- were regarded as $\text{Na}^+/\text{HCO}_3^-$ independent PMCs and were used for further analyses.

2.4.3.2 Determination of Carbonic Anhydrase Activity

From each larva (3-4 dpf), six to eight PMCs in the rod tips were recorded and treated as one replicate ($n = 1$). A minimum of six larvae were measured for every inhibitor concentration in

an alternating mode. Using BCECF-AM the pH_i was monitored during the measurement. Along the entire duration of the experiment larvae were exposed to FSW pH 8.0 either containing 0.1% DMSO as control or the respective AZM concentration (1 μM , 10 μM , 100 μM and 1 mM). The CO_2 pulse using CO_2 out-of-equilibrium OOE solutions (for details see (Hu et al., 2020)) was performed for 5 min before switching back to FSW containing the respective AZM concentration. All solutions were delivered to the perfusion chamber at a flow rate of 2 mL/min and at 15 °C by a Perfusor with 50 mL Perfusor syringes (B.Braun, Melsungen, Germany). The recovery rate after removal of the OOE solution in the presence of AZM was used to characterize the catalytic activity of intracellular CAs.

2.4.3.3 Determination of pH_i regulatory capacities

The ammonium pre-pulse method was used to quantify pH_i regulatory capacities of PMCs. BCECF-AM incubated PMCs were monitored during the measurement. The PMCs were exposed to FSW containing 20 mM $\text{NH}_3/\text{NH}_4^+$ followed by a washout using FSW containing either DMSO or 100 μM dextran-bound AZM (for inhibition of the extracellular CA). These solutions were applied to the larvae at a flowrate of 6-8 mL/min through a water jacket cooling system set to 15°C. The recovery rate from the ammonium pre-pulse induced acidosis was used to characterize the effects of extracellular CA inhibition and *Cara7* knock-down on pH_i regulatory capacities.

2.4.3.4 pH_i measurements and transfection of HEK-293 cells

HEK293 cells were cultured at 37°C / 5% CO_2 in DMEM supplemented with 10% FCS and Penicillin/ Streptomycin. Cells with 70% confluency were transiently transfected with 0.5 μg *Otop2l* and 0.1 μg mCherry constructs per well (24-well plate) using Lipofectamine 2000 (Invitrogen, Carlsbad, CA) according to the manufacturer's instructions. After 18-24 hours, HEK-293 cells co-transfected with *Otop2l* and mCherry constructs as well as HEK cells only transfected with mCherry sham control vector were dissociated with trypsin/EDTA, seeded on sterile 30 mm coverslips. After 10-15 hours cells were loaded with the intracellular pH indicator dye BCECF-AM as described above. Cells co-transfected with mCherry were identified using a 580ex/633em filter cube and used for pH_i measurements. pH_i in *Otop2l* and sham-transfected cells was measured in response to Tyrodes solutions (145 mM NaCl, 5 mM KCl; 1 mM MgCl_2 , 2 mM CaCl_2 20 mM dextrose

10 mM HEPES) adjusted to pH 7.4 or pH 5.0 buffered with 10 mM MES or with 10 mM acetic acid. On each slide 3-4 mCherry positive cells were measured and traces were averaged leading to one replicate.

2.4.4 Oocyte preparation, coding RNA synthesis and cRNA injection

Xenopus oocyte lobes were obtained from tricaine anesthetized *Xenopus laevis* frogs and incubated in OR2 solution containing (mM): 82.5 NaCl, 2.0 KCl, 1.0 MgCl₂, 5.0 HEPES (pH 7.4) substituted with 2 mg/mL collagenase type II (Sigma-Aldrich/Merck, Germany) for 1 h to remove residual connective tissue. Isolated oocytes were stored at 16.9 °C in ND96 solution containing (mM): 96.0 NaCl, 2.0 KCl, 1.8 CaCl₂, 1.0 MgCl₂, 5.0 HEPES (pH 7.4) supplemented with Na-pyruvate (275 mg/L), theophylline (90 mg/L), and gentamicin (50 mg/L). Otop2l channels and suAQP9 were subcloned into the dual-purpose vector pFAW which can be used for HEK293 as well as expression in *Xenopus* oocytes. cDNA was linearized with NheI or MluI, respectively and cRNA was synthesized *in vitro* using the SP6 or T7 AmpliCap Max High Yield Message Maker Kit (Cellscript, USA) and stored in stock solutions at -80 °C. The quality of cRNA was tested using gel electrophoresis and cRNA was quantified with the NanoDrop 2000 UV-Vis spectrophotometer (Thermo Fisher Scientific, USA). Oocytes were injected with ~50 nL of cRNA for Otop2l and incubated for 7-8 days at 16.9 °C.

Injection of *Xenopus* oocytes with cRNA of suAQP9 36 nL (0.5 µg µL⁻¹) were used and measured at day 4 after injection. (Day of injection = Day 1)

2.4.5 Oocyte swelling experiment

For the measurement of water conductance of control or suAQP9 expressing oocytes were transferred to 2 mL oocyte solution ND96 that contained 0 mM NaCl. This hypotonic solution leads to an uptake of water that depends on the permeability of the oocyte membrane. Water permeabilities were determined for control and suAQP9 expressing oocytes, 4 days after suAQP9 cRNA injection. In addition, the effect of Phloretin, a specific mammalian AQP9 inhibitor was tested by adding different concentrations (final concentration: 10 µM, 50 µM, 100 µM, 200 µM and 500 µM) to the hypotonic ND96 medium. Swelling of the oocytes was recorded by taking images every 30 seconds on a microscope equipped with a camera. The diameter of the oocytes was measured using Zeiss Zen blue 3.3 software and converted to volume assuming a spherical

shape. The oocyte volume was normalized to their own starting volume, so only the increase in volume was used for our analyses.

2.4.6 Oocyte CO₂ excretion experiment

The second method examined the CO₂ transport capability of suAQP9 by measuring the excretion rate of CO₂ in high CO₂ pre-loaded sham and suAQP9 oocytes modified from a previously described protocol for coral Rh proteins expressed in *Xenopus* oocytes (Thies et al., 2022). Briefly, groups of three oocytes were incubated for 15 min in hypercapnic OR2 (in mmol L⁻¹ 82.5 NaCl, 2.5 KCl, 1 MgCl₂, 1 CaCl₂, 1 Na₂HPO₄, 5 HEPES, 5% CO₂, pH 7.5 set by titration with NaHCO₃). After the incubation in hypercapnic OR2, the group of oocytes was rapidly transferred into a 100 mL beaker of normocapnic OR2 (in mmol L⁻¹ 82.5 NaCl, 2.5 KCl, 1 MgCl₂, 1 CaCl₂, 1 Na₂HPO₄, 5 HEPES, pH 7.5) to wash off excess CO₂/HCO₃⁻ and then transferred into a tube containing 95 μL of fresh normocapnic OR2 to create a large oocyte to media pCO₂ gradient. A 45 μL sample of media was immediately taken with a gas-tight Hamilton syringe (t= 0 min), followed by a second 45 μL sample after 1 minute (t = 1 min). The CO₂ concentration of the media samples at 0 and 1 minute was measured in triplicate (15 μL per measurement) using a custom-built total CO₂ analyzer employing a Licor 850 for CO₂ detection. For a detailed explanation of the custom-built CO₂ analyzer, standardization and data analysis see (D. J. Lee et al., 2018). The change in total carbon of the media was used as an indicator of CO₂ excretion as native *Xenopus* oocytes have been previously shown to exhibit no measurable HCO₃⁻ permeability so any measured change in total carbon can be safely attributed to CO₂ excretion (Sasaki et al., 1992). Samples were compared to a NaHCO₃ standard curve ranging from 0-1600 μmol L⁻¹ and produced an R² of 0.99. The CO₂ excretion rates were calculated according to the following equation:

$$CO_2 \text{ excretion rate} = \frac{(CO_{2_1} - CO_{2_0}) \times V}{3 \text{ oocytes} \times t}$$

Where CO_{2_1} is the CO₂ concentration after 1 minute, CO_{2_0} is the CO₂ concentration at 0 minutes, V is the flux volume in liters, and t is the flux time in minutes. The integrity of the oocytes in all tubes was assessed under a microscope at the end of the sampling period and if any damage to the membranes or lysis of oocytes had occurred those oocytes were excluded from the analysis.

2.4.7 Water flux measurements in PMCs

Measurement of cell volume-changes during exposure to different osmotic conditions were used to determine membrane water permeabilities of PMCs. These measurements were performed using the fluorescence dye Calcein-AM that accumulates in the cytosol and that responds to concentration increases by quenching of the fluorescence signal Kitchen et al. (Kitchen et al., 2020). After removal of the ectoderm by the bag isolation method and incubation with 5 μ M Calcein-AM for about 90 minutes, larvae were immobilized on 1% Protamine sulfate coated coverslips that were attached to the bottom of a perfusion chamber. The fluorescence intensity was monitored on an inverted microscope (Zeiss, Axiovert 135) equipped with an appropriate light source and the imaging software (VisiView, Visitron Systems GmbH). From each larva (3-4 dpf), few PMCs along the spicule were recorded and treated as one replicate ($n = 1$). At least six replicates were measured under control conditions only containing 0.1% DMSO or in the presence of Phloretin at a final concentration of 100 and 200 μ M. To measure cellular water flux, the surrounding medium (FSW) was changed from filtered seawater (FSW) (1000 mosmol/L) to a hyperosmotic FSW where D-Mannitol was added to obtain 1750 mosmol/L). After 10 min in this hyperosmotic solution PMCs were exposed back to control FSW. The inhibitor measurements were executed as paired measurements, with a first experiment control and hypertonic solutions containing only the vehicle DMSO followed by a second experiment where the inhibitor Phloretin was added from the start of the experiment. Fluorescence changes of Calcein-AM during the hyperosmotic treatment were plotted against time and analyzed by the following non-linear function:

$$Y=(Y_0 - \text{Plateau}) \cdot \exp(-K \cdot X) + \text{Plateau}.$$

The Plateau is the Y value at infinite times, which indicates the relative total water efflux from the PMCs. K represents the rate constant, which reflects the speed of water efflux across the PMC plasma membrane under control conditions or in the presence of Phloretin.

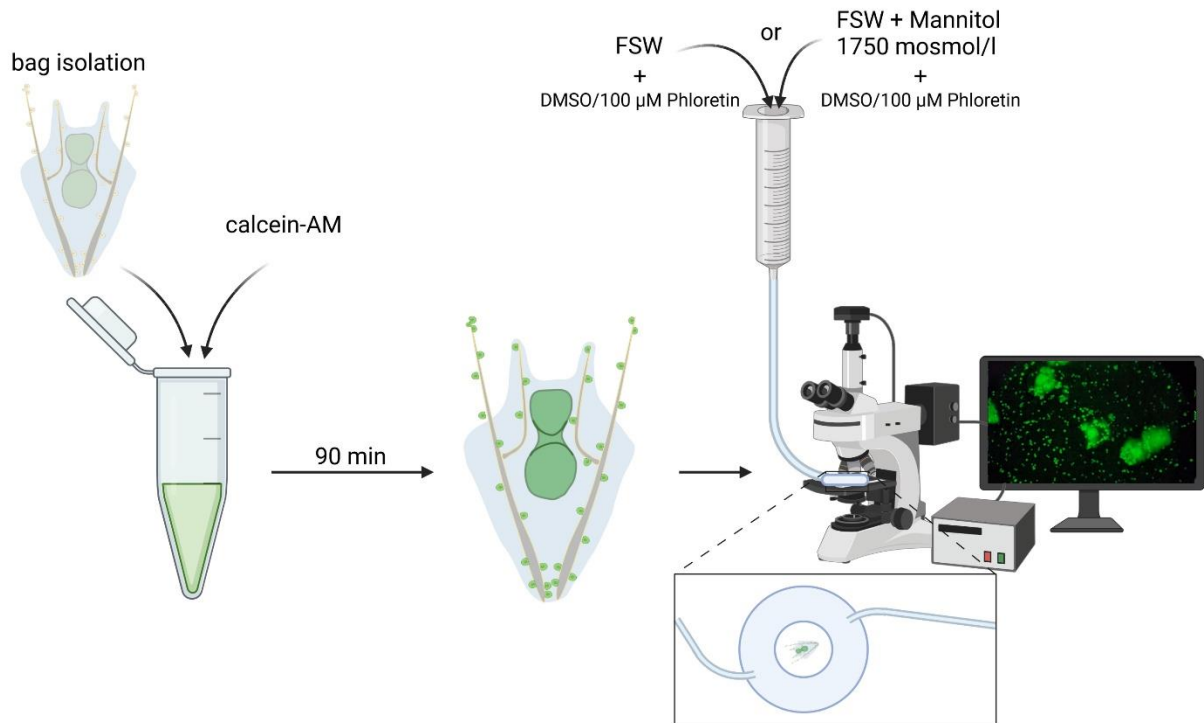


Fig. 2.1: Schematic illustration of the execution of Calcein-measurements using the sea urchin larva. Image created with BioRender.com, with permission.

2.5 Electrophysiology

2.5.1 H^+ selective micro-electrode preparation

Borosilicate glass capillaries were pulled on a DMZ-Universal puller (DMZ Universal Puller, Zeitz) into micropipettes with tip diameters of 1–2 μm . These were then baked at 200 $^{\circ}\text{C}$ for 4 h and vapor-silanized with dimethyl chlorosilane (Sigma-Aldrich) and front-loaded with a 200 μm column of liquid ion exchanger mixture (H^+ ionophore III; Sigma-Aldrich) diluted in 2-nitrophenylether at a concentration of 10.5 mg mL^{-1} . Additionally, micropipettes were again front-loaded with a 100 μm column of the ionophore mixture containing a polyvinylchloride/tetrahydrofuran (330 mg mL^{-1}) solution with a ratio of 1:3 to seal the opening of the electrode tip. The micropipette was backfilled with an electrolyte solution (300 mM KCl, 50 mM NaPO_4 , pH 7.0) to create an ion selective micro-electrode. The micro-electrode was connected to a FD223a dual channel differential electrometer (WPI) and the potential was

measured against an Ag/AgCl electrode connected by a 3 M KCl agar bridge to the perfusion solution. Calibration was performed by placing the electrodes into different pH solutions (ASW solutions with pH 6.0, 7.0, 8.0, and 9.0) and plotting the measured voltage against the respective pH. All electrodes used had a Nernstian slope > 52 mV for 1 pH unit.

2.5.2 Two-electrode voltage-clamp (TEVC) recordings

Prior investigation, oocytes were pre-incubated in recording solution with $100 \mu\text{M}$ 4,4'-Diisothiocyano-2,2'-stilbenedisulfonic acid (DIDS) for 10 minutes to suppress endogenous Ca^{2+} -activated Cl^- channel currents at acidic pH (36, 37).

All TEVC recordings were performed at room temperature ($20\text{-}22^\circ\text{C}$) as previously described (38) with a HEKA multielectrode clamp amplifier iTEV90 (HEKA electronics, Germany) or a TURBO TEC 10CX amplifier (npi electronic instruments, Germany), sampled at 10 kHz and filtered with 3 kHz (-3 dB). Microelectrodes for measurements were fabricated from borosilicate glass capillaries GB200F-8P (Science Products, Germany) and pulled with a DMZ-Universal-Electrode-Puller (Zeitz, Germany), back-filled with 2 M KCl, and had a resistance of 0.5 - 1.2 M Ω . Recording solution contained (mM): 120 KCl, 1.8 CaCl_2 , 2.0 MgCl_2 and 10 HEPES (pH 7.4), 10 TRIS (pH 8.0 and 8.5) or 10 MES (pH 5.0), respectively. ZnCl_2 was directly diluted in the recording solution pH 8.5 to 2 mM. For current measurements the membrane potential was held at -80 mV and voltage ramps were applied every second from -80 mV to $+80$ mV with a sweep interval of 2 seconds. Data was acquired with PatchMaster (HEKA electronics, Germany), analyzed with FitMaster (HEKA electronics, Germany) and Igor Pro 8 (WaveMetrics, USA).

2.5.3 Membrane potential measurements

The membrane potential of PMCs was measured using intracellular electrodes. For the measurements, the ectoderm of the larvae was removed via the bag isolation method. Larvae were immobilized on 1% Protamine sulfate coated coverslips and attached to a microscopy chamber filled with ASW. The recording electrode was pulled from borosilicate glass (GB150F-8P) on a horizontal puller (DMZ Universal Puller, Zeitz), back-filled with 3 M KCL solution and connected via an Ag/AgCl electrode to a dual electrometer with high input resistance (FD223a; WPI). The recording electrode was controlled by a motorized micromanipulator (PatchStar;

Scientifica). Impalements of PMCs were performed under visual control on an inverted microscope at a 100x magnification.

2.5.4 Micro-electrode measurements at the PMC surface

H⁺ selective micro-electrodes were used for the *in vivo* measurement of extracellular CA. To measure extracellular CA activity, we performed a stopped-flow assay using out-of-equilibrium (OOE) solutions (2.5% CO₂/pH 8.0) following a modified protocol for the *in vitro* measurement of carbonic anhydrase activity (50). This OOE state is generated in the moment of mixing of a high CO₂ (5% CO₂ pH 6.2) and a TRIS buffered low CO₂ solution (0.04% CO₂ pH 8.0) (66). When the flow (mixing) is stopped, the solution will acidify due to the relaxation towards the formation of HCO₃⁻ and H⁺. This rate of change in [H⁺] representing the CO₂ hydration speed is detected by our pH sensitive micro-electrodes. After bag isolation, 2 dpf larvae were immobilized on 1% Protamine sulfate coated cover slides and glued to a perfusion chamber using silicon grease. The chamber was mounted on an inverted microscope (Zeiss VisiTronSystem Observer D1) and perfused at a rate of 5 mL min⁻¹ using an OOE solution that was generated by mixing ASW containing 2 mM TRIS adjusted to pH 8.0 and ASW equilibrated with 5.0% CO₂. The solutions were maintained at 15°C by a water jacked cooling system. The pH micro-electrode was placed at the surface of a PMC using a motorized micromanipulator (Patch Star, Scientifica) under visual control at a 40 X 10 magnification. When stable recordings of PMC surface pH were obtained the flow was stopped, leading to a relaxation of the OOE solution within the perfusion chamber towards the formation of HCO₃⁻ and H⁺. The reaction followed a non-linear saturation curve and the speed of this reaction is depending on CA activity. We fitted the [H⁺] change as a function of time by the equation: $[H^+](t) = A + B(1 - e^{-K_{\Delta[H^+]}}t)$ where t is time, A is the [H⁺] value after full equilibration, B is the [H⁺] range and $K_{\Delta[H^+]}$ is the rate constant of the [H⁺] relaxation. We obtained A , B , and $K_{\Delta[H^+]}$ using the curve fitting analysis of Sigma Plot 13.0. [H⁺] recordings in combination with the stopped-flow method were performed in the extracellular matrix ca. 50 μM away from the PMC cell (background) or with the electrode touching the PMC surface. To inhibit CAs, AZM was added at a concentration of 200 μM to the TRIS-buffered ASW solution leading to a final concentration of 100 μM in the perfusion chamber. Since iCA activity has no effect on the detection of eCA activity by this method (that is restricted to detect eCA activity at the cell surface) we used AZM to pharmacologically

demonstrate CA activity at the outer surface of PMCs. In addition, extracellular CA activity measurements were carried out in scramble and *Cara7* morpholino injected larvae.

2.5.5 CO₂ conductivity measurements in Oocytes

The CO₂ conductivity was measured using a H⁺-selective micro-electrode touching the surface of the oocyte. The oocyte was perfused with a 5% CO₂ and 33 mM HCO₃⁻-solution. The presumable transport of CO₂ across the oocyte membrane will shift the equilibrium in direction of additional CO₂ formation. This conversion of H⁺ and HCO₃⁻ to CO₂ and H₂O, consequently the decrease in H⁺ will be measured by the H⁺-selective micro-electrode and translated into an increase in pH.

2.6 Statistics

Our data was tested for variance homogeneity (Levene-test) and was analyzed for statistical significances using GraphPad Prism 6 and 8. Intracellular CA measurements with the CO₂ pulse method, ammonia pre-pulse measurement, IHC signal validation, AQP9 CO₂ conductivity measurements, morpholino injection validation and Calcein-AM measurement were analyzed using the student's t-test (two-sided) with p-value * < 0.05, ** < 0.01, *** < 0.001 and **** < 0.0001. Re-calcification experiments, extracellular CA activity measurement, morphometric analyses of Otop2l, Cara7 and AQP9 knock-down, qPCR, AQP9 water conductivity measurements and calcification rate determination were analyzed for significance using one-way ANOVA, followed by Post-Hoc tests. Differences in proton fluxes between sham-transfected and Otop2l expressing HEK-293 cells were analyzed using Student's t-test. Statistical analyses were conducted using Sigma Stat 13 (Systat Software).

3 Publications and Manuscript

I An otopetrin family proton channel promotes cellular acid efflux critical for biomineralization in a marine calcifier

PNAS
www.pnas.org

Main Manuscript for

An Otopetrin family proton channel promotes cellular acid efflux critical for biomineralization in a marine calcifier

William W. Chang^{1#}, Ann-Sophie Matt^{1#}, Marcus Schewe¹, Marianne Musinszki¹, Sandra Grüssel¹, Jonas Brandenburg², David Garfield², Markus Bleich¹, Thomas Baukrowitz¹, Marian Y. Hu^{1*}

¹Institute of Physiology, Christian-Albrechts-University of Kiel, Hermann-Rodewald-Str. 5 24118 Kiel, Germany

²IRI Life Sciences, Humboldt-Universität zu Berlin, Philippstraße 13, 10117 Berlin, Germany

*Corresponding Author:

Dr. Marian Hu

Institute of Physiology, Christian-Albrechts University of Kiel

Hermann Rodewald Straße 5 24118 Kiel, Germany

e-mail: m.hu@physiologie.uni-kiel.de

phone: +49(0)4318802048

These authors contributed equally to the present work

Keywords: proton channel, calcification, sea urchin larva, intracellular pH, ocean acidification

Abstract

Otopetrins comprise a novel family of proton selective channels that are critically important for the mineralization of otoliths and statoconia in vertebrates, but whose underlying cellular mechanisms remain largely unknown.

Here we demonstrate that otopetrins are critically involved in the calcification process by providing an exit route for protons liberated by the formation of CaCO_3 . Using the sea urchin larva, we examined the Otopetrin orthologue, *otop2l*, which is exclusively expressed in the calcifying primary mesenchymal cells (PMCs) that generate the calcitic larval skeleton. *otop2l* expression is stimulated during skeletogenesis and knock-down of *otop2l* impairs spicule formation. Intracellular pH measurements demonstrated Zn^{2+} sensitive H^+ fluxes in PMCs that regulate intracellular pH in a $\text{Na}^+/\text{HCO}_3^-$ independent manner while Otop2l knock-down reduced membrane proton permeability. Further, Otop2l displays unique features including strong activation by high extracellular pH (> 8.0) and check-valve like outwardly rectifying H^+ flux properties making it to a cellular proton extrusion machine adapted to oceanic living condition. Our results provide first evidence that otopetrin family proton channels are a central component of the cellular pH regulatory machinery in biomineralizing cells. Their ubiquitous occurrence in calcifying systems across the animal kingdom, suggest a conserved physiological function by mediating pH at the site of mineralization. This important role of otopetrin family proton channels has strong implications for our view on the cellular mechanisms of biomineralization and their response to changes in oceanic pH.

Significance statement

Otopetrins comprise a novel family of proton channels that are required for the development of calcified structures including otoliths and statoconia in vertebrates. To date, it remains unknown how otopetrins contribute to the calcification process. Using the sea urchin larva we could demonstrate that the otopetrin orthologue *otop2l* encodes a proton channel that is essential for the formation of the CaCO_3 skeleton. *otop2l* is exclusively expressed by the calcifying primary mesenchyme cells where it promotes the exit of protons liberated by the mineralization process. Given the deep phylogenetic origin of otopetrins in animals, our work identified a key mechanism in the mineralization process with relevance for many calcifying species and their responses to changes in environmental pH.

Introduction

Otopetrins are a recently discovered family of proton channels (1, 2) that play a key role in the acid-sensing taste receptors (3, 4) and were demonstrated to be critically involved in statoconia and otolith formation of the mammalian vestibular organ and the fish inner ear (5, 6). Mutations and knock-down of *otop1* resulted in agenesis of statoconia (5) and otoliths (6), while the physiological function of this proton channel in the CaCO_3 mineralization process remains obscure. Otopetrins are an evolutionary conserved family of proton channels found in animals ranging from basal metazoans to vertebrates and humans (1). In vertebrates, three otopetrin family members, Otop1-Otop3 were identified that have a dimeric architecture with each subunit consisting of 12 transmembrane domains. Electrophysiological characterization of these proteins in heterologous expression systems demonstrated highly selective zinc-sensitive proton conductance (1).

During the formation of CaCO_3 , protons are liberated that need to be removed from the calcification front to protect cellular pH homeostasis and to promote further mineral precipitation (7-9). In this way biomineralization and pH homeostasis are intrinsically linked processes that require efficient proton transport strategies. In the sea urchin larva, which develops an elaborate calcitic skeleton, amorphous CaCO_3 (ACC) is initially formed within intracellular compartments of primary mesenchyme cells (PMCs) that is then exocytosed to the growing skeleton (10, 11). During this process 1.6 moles of protons are liberated per mole of CaCO_3 precipitated leading to a substantial cellular acid-load during the rapid early formation of the larval skeleton (8). To prevent an intracellular acidosis, PMCs must have outward directed proton fluxes that are comparable to those found in acid-secreting cells including osteoclasts, renal tubular cells or gastric parietal cells (9). Previous studies addressing pH regulatory mechanisms in PMCs demonstrated that the Slc4 family transporter Sp-Slc4a10 is critically involved in the cellular accumulation of dissolved inorganic carbon (i.e. HCO_3^-) (12). In PMCs bicarbonate has a dual function by serving as a calcification substrate and acting as a proton buffer in the cytosol (12). During active calcification intracellular pH and HCO_3^- levels are increased accompanied by an up-regulation of Sp-Slc4a10 on the protein and mRNA level (13). Interestingly, PMCs reduce Na^+/H^+ exchange capacities during this phase of active mineralization suggesting an alternative route for the exit of proton across the plasma membrane in place. Although the involvement of vesicular proton accumulation by a

V-type H⁺ ATPase has been suggested by pharmacological approaches, the direct export of protons from the cytosol across the plasma membrane remained obscure (13). A genome-wide analysis of the skeletogenic gene regulatory network demonstrated specific expression of the *otop2L* gene in PMCs of the sea urchin embryo (14). *Otop2I* is the single member of the otopetrin family in the sea urchin located downstream of ALX1 and Ets1 in the PMC gene regulatory network (14). Given their deep phylogenetic origin and their ubiquitous association with calcifying systems, the physiological characterization of otopetrins in mineralizing cells can provide fundamental knowledge about the mechanisms of biomineralization.

In this work we address the cellular expression and localization of Otop2I in PMCs by a suite of molecular and biochemical techniques. Using Otop2I morphants we test the contribution of this channel to the calcification process. The physiological function of Otop2I in PMCs was investigated using intracellular pH recordings to characterize cellular proton fluxes in combination with proton channel inhibitors and knock-down of *otop2I*. Finally, heterologous expression and re-calcification experiments are used to demonstrate that *otop2I* encodes a proton channel that supports the mineralization processes depending on trans-membrane proton gradients.

Results & Discussion

Identification and localization of *Otop2I* in calcifying cells of the sea urchin larva

Orthologues of otopetrin genes were found in marine calcifiers including corals, bryozoans, molluscs, and arthropods (Figure S1). Invertebrate otopetrins form a clade separate from the three otopetrin paralogs found in vertebrates. The sea urchin Otop2I consists of twelve transmembrane domains with highest similarity to the otopetrins of cnidarians and poriferans (Figure S1+S2). In accordance to previous studies (14, 15) *in situ* hybridization demonstrates exclusive expression of this gene in the calcifying primary mesenchyme cells (PMCs) of the sea urchin embryo (Figure 1A). In the late gastrula stage *otop2I* expression is predominantly found in PMCs of the dorsal chain and the ventrolateral cluster (VLC) in which skeletogenesis is initiated. In later development, the highest expression of *otop2I* is located in PMCs of the scheidel region and tips of the body rods where the skeleton is elongated. The exclusive expression of *otop2I* by PMCs is further underlined by single cell transcriptome analyses that indicate *otop2I* to be a Pan-PMC marker that has highest expression in the PMCs of the arm tips and scheidel region in the

pluteus larva (Figure 1B+S3). During early larval development the highest expression of this gene was detected during the period of skeletogenesis when the greatest growth rates of the skeleton were measured (Figure 1C). Morpholino knock-down of *Otop2l* resulted in a substantial reduction in skeleton growth in a dose-dependent manner with no visible collateral effects on the development of ectodermal or endodermal tissues (Figure 1D). This reduction of calcification in the sea urchin embryo underlines the critical role of otopetrins in the mineralization process as observed for the formation of statoconia and otolith in mouse and zebrafish, respectively (5, 6). In the zebrafish, knock-down of *otop1* resulted in otolith agenesis without morphological changes in the sensory epithelium or other structures in the inner ear (6). This agenesis of otoliths was accompanied by a reduction in the secretion of the Starmaker protein which is a structural component of the otolith protein matrix. Furthermore, mutations in *Otop1* have been shown to result in agenesis of statoconia in *tilted* and *mergulhador* mutant mice (5). Using an antibody raised against the vertebrate Otop1, positive immunoreactivity was detected at apical membranes as well as sub-apical regions of the sensory epithelium in the utricle of mouse (5). Localization of the Otop2l protein using a sea urchin specific antibody corroborates the location of *otop2l* mRNA expression in the oral tips and scheidtel region of the spicules (Figure 1E). Similar to the mouse utricle, also in the sea urchin larva Otop2l is localized in the plasma membrane and vesicular structures of the cell body and syncytial extensions of PMCs (Figure 1F). Western blot analyses confirm positive immunoreactivity with a protein in the predicted size range of 65 kDa (Figure 1G). Using this antibody we validated our Otop2l knock-down by demonstrating decreased protein abundance in Otop2l morphants compared to scramble MO injected larvae (Figure 1H). These results demonstrated that sea urchin *otop2l*, like its vertebrate homologs, is an essential component of the cellular mineralization machinery. The deep phylogenetic origin of otopetrins and its frequent association with calcifying systems suggests an evolutionary conserved function in the biomineralization process with the underlying mechanisms being largely unknown.

Physiological role of Otop2l in calcifying cells

Intracellular pH measurements in PMCs in combination with changes in extracellular pH identified two populations of PMCs. One type of PMC transiently acidified in the presence of 5 mM [Na⁺] and 0 mM [HCO₃⁻] and was unable to recover from the low pH treatment until the cells were

exposed back to control Na^+ (450 mM) and HCO_3^- (2.5 mM) conditions (Figure 2A+B). The other type of PMC regulated pH_i in a $[\text{Na}^+]$ and $[\text{HCO}_3^-]$ independent manner with a recovery rate of 0.12 ± 0.02 pH units min^{-1} after the low pH treatment. Within one larva approximately 30% of PMCs regulated pH_i in a $[\text{Na}^+]$ and $[\text{HCO}_3^-]$ independent manner while the remaining 70% required extracellular $[\text{Na}^+]$ and $[\text{HCO}_3^-]$ to recover from the low pH treatment (Fig. 2C). This observation of two functionally distinct populations of PMCs underlines findings of an earlier study that tested the sensitivity of pH_i regulation in PMCs to the specific Na^+/H^+ exchange inhibitor Ethyl-Isopropyl Amiloride (EIPA) (13). This study identified 80% of PMCs to be EIPA sensitive while the remaining 20% were able to regulate pH_i in the presence of the inhibitor. Furthermore, different functional states of PMCs were proposed based on the correlation between Ca^{2+} incorporation rates determined by calcein pulse-chase experiments and the spatial expression level of calcification genes in PMC (16). Based on this information there is strong evidence for the presence of different functional states among PMCs, likely associated with their calcification activity and different pH_i regulatory mechanisms.

To test the contribution of *Otop2l* to the proton permeability in PMCs we performed a series of experiments using Zn^{2+} as a broad-band inhibitor for proton channels as well a specific knock-down of *otop2l* in combination with cellular proton flux measurements. The $\text{Na}^+/\text{HCO}_3^-$ independent proton flux across the plasma membrane of PMCs is sensitive to Zn^{2+} in a dose dependent manner (Figure 2D+E). In the absence of Zn^{2+} , proton efflux rates after the low pH treatment were 0.12 ± 0.02 pH units min^{-1} while they were decreased (One-way ANOVA $F(2;19) = 11.67$; $p < 0.001$) in the presence of Zn^{2+} down to 0.10 ± 0.02 and 0.05 ± 0.004 pH units min^{-1} at 1 mM and 10 mM Zn^{2+} , respectively (Figure 2 E). To exclude the possibility that other pH regulatory mechanisms than *Otop2l* are affected by Zn^{2+} , we performed low pH challenge experiments in the presence and absence of Zn^{2+} in $\text{Na}^+/\text{HCO}_3^-$ -dependent PMCs (Figure S4). These control experiments demonstrated no effect of Zn^{2+} on the recovery kinetics after switching the low pH and low $\text{Na}^+/\text{HCO}_3^-$ conditions back to the pH 8.0 ASW solution. Zn^{2+} sensitive proton currents are also a characteristic of the vertebrate *Otop1*. When expressed in HEK293 cells *Otop1* induced proton currents are sensitive to Zn^{2+} with an IC_{50} of 0.2 mM and a full inhibition between 1 mM to 10 mM (1, 2). Knock-down of *otop2l* resulted in a decreased proton flux across the plasma membrane of PMCs that regulate pH_i in a $\text{Na}^+/\text{HCO}_3^-$ independent manner. Scramble MO injected larvae had proton efflux rates of 0.159 ± 0.018 pH units min^{-1} while those of *Otop2l* knock-out larvae were decreased to 0.096 ± 0.015 pH units min^{-1} in (Fig. 2F+G). In addition to this reduction

in proton permeability, a significant ($p = 0.003$) increase in resting pH_i by 0.34 pH units was measured in PMCs of *otop2l* knock-down larvae ($\text{pH}_i = 7.40 \pm 0.07$) compared to PMCs of control larvae ($\text{pH}_i = 7.05 \pm 0.06$). This increase in intracellular pH may be explained by an enhanced accumulation of HCO_3^- that however, fails to compensate skeleton formation due to a blockade of H^+ removal from the cytosol. This idea of a compensatory accumulation of intracellular dissolved inorganic carbon (DIC) is supported by an upregulation of the $\text{Na}^+/\text{HCO}_3^-$ cotransporter (NBC) Sp-Slc4a10 in *Otop2l* morphants compared to control larvae (Fig. S5). This NBC has been demonstrated to be a critical player in the acquisition of HCO_3^- from the environment to promote intracellular calcification in PMCs (12). Our single cell transcriptome data indicate that *Otop2l* and Sp-Slc4a10 are co-expressed in the same PMC populations (Fig. S6). Accordingly, the incomplete recovery back to a pH_i of approximately 7.0 instead of $\text{pH}_i = 7.40$ after the low pH challenge potentially results from a titration of intracellular HCO_3^- buffers. Our characterization of transmembrane proton fluxes in PMCs provides evidence that *Otop2l* encodes a proton channel that contributes to the cellular proton permeability in calcifying cells of the sea urchin larva.

***Otop2l* encodes a proton channel with biological relevance for the calcification process under changing environmental pH**

Like the vertebrate Otopetrins, *Otop2l* has twelve transmembrane domains separated into an N and C domain. A large extracellular loop is predicted between As243-As415 (Figure 3A). Heterologous expression of *otop2l* in *Xenopus* oocytes and HEK-293 cells in combination with intracellular pH measurements and electrophysiological recordings confirms that the sea urchin *Otop2l* encodes a proton channel analogous to the vertebrate otopetrins. Like the vertebrate Otopetrin homologues, the sea urchin *Otop2l* is also highly selective for protons with a weak sensitivity to voltage. In contrast, to the vertebrate *Otop1* and *Otop3* (1, 2) the sea urchin *Otop2l* has reduced proton conductance under acidic conditions $< \text{pH } 7.0$ but shows strong activation in the range of $\text{pH } 8.0\text{-}8.5$ (Figure 3B+C). When expressed in *Xenopus* Oocytes, *Otop2l* generated large currents in response to increasing pH_{ex} from $\text{pH } 7.4$ to $\text{pH } 8.5$ with the activation potential E_{H^+} shifting by 41 mV (Figure 3D). However, currents saturated at $\text{pH} < 7.0$ and E_{rev} shifted little under acidic conditions. Many marine invertebrates have leaky ectodermal epithelia (18) directly exposing calcifying cells to seawater pH conditions shaping the functional evolution of acid-base regulatory mechanisms in these cells. Together with our functional characterization of *Otop2l* this

underlines a long-term selection on this channel to optimally function under oceanic pH conditions in the range of pH 8.0-8.2 that were stable over the past 10 Myr (19).

Otop2l expressing HEK-293 cells are characterized by an increased in- and efflux of protons during changes in extracellular pH compared to sham-transfected cells (Figure 3E+F). Comparison of the proton in- and efflux kinetics between the vertebrate *Otop1* and the sea urchin *Otop2l* using a similar protocol (1) indicate a moderately elevated influx kinetic during external exposure to pH 5 in *otop2l* expressing cells. However, while HEK-293 cells expressing the vertebrate *Otop1* only partly restore pH_i within 8 minutes (1) cells expressing the sea urchin *Otop2l* largely restore pH_i within one minute. The almost complete restoration of the intracellular $[H^+]$ to $10^{-7.2}$ M (pH 7.2) at a bath (environmental) $[H^+]$ of $10^{-7.4}$ M (pH of 7.4) after the low pH pulse suggests that *Otop2l* enables the almost complete equilibration of transmembrane proton gradients under these pH conditions. The rapid equilibration of intra- and extra-cellular pH in *Otop2l* expressing cells after the low pH pulse together with our Oocyte experiments suggests that the function of *Otop2l* appears to be acid extrusion from cells in a similar way as described for most proton channels (20, 21). Microelectrode measurements demonstrated a native PMCs membrane potential of -20.6 ± 2.7 mV (Figure 4A). This moderately negative membrane potential in combination with natural proton gradients across the plasma membrane of PMCs (i.e. $pH_i = 6.8$; $pH_e = 8.2$) (18) will promote an efflux of protons by *Otop2l*. Given the Nernst potential for protons of -60 mV, the native PMC membrane potential would support the exit of protons at external pH values higher than 7.5 at constant pH_i . Thus, *Otop2l* reveals its biological significance by providing an exit route for protons generated by the calcification process.

To investigate the *in vivo* effects of transmembrane proton gradients on the calcification process, re-mineralization experiments were performed, where the skeleton is dissolved and re-mineralized within the period of 3 days (Figure 4B). During re-mineralization of the skeleton *otop2l* expression is increased (Figure 4C) accompanied by a positive immunoreactivity of the *Otop2l* antibody along the entire re-calcifying spicule (Figure 4D). This observation indicates a recruitment of PMCs to rebuild the skeleton. These re-calcification experiments were further used to address the role of transmembrane proton gradients on the ability to calcify the larval skeleton. These experiments demonstrated that the regeneration of the skeleton decreases linearly with increases in seawater $[H^+]$ (Figure 4E+F), supporting the concept of H^+ efflux driven by H^+ gradients across the plasma membrane. Similar observations were made in the coccolithophore *Emiliania*

huxleyi where the increase in environmental proton concentration has been identified as the major driver for reduced calcification rates under seawater carbonate chemistry perturbations (22). Interestingly, electrophysiological measurements suggested that also in the coccolithophore *Coccolithus pelagicus* a Hv1-like proton channel is employed to remove protons from the cytosol to promote calcification (21). While a Hvcn1 homologue is also found in the sea urchin genome, its physiological function remains unknown. Sea urchin larvae developing under acidified conditions simulating near-future ocean acidification (OA) conditions have substantial reductions in the expression level of *Otop2l* along the developmental period of five days (Figure 4G). This down-regulation of *Otop2l* can be interpreted as a reduction in membrane proton permeability to protect against inward directed proton gradients. Thus, a reduction in cellular proton permeability may require alternative H⁺ transport mechanisms involving Na⁺/H⁺-exchangers or V-Type H⁺-ATPases that are energetically more expensive. Such a shift to energetically expensive proton transport mechanisms may partly explain the higher allocation of energy to ion-regulatory pathways in sea urchin larvae raised under OA conditions (23). This information indicates that changes in seawater carbonate chemistry as predicted for the coming century in the context of “ocean acidification” (24) can directly affect calcifying systems that employ proton channels (e.g. Otopetrins or Hv1) (summarized in figure 4H). Given the relatively leaky ectodermal epithelia of many marine invertebrate larvae (18) and cnidarians (25) changes in seawater pH may directly translate into altered proton gradients at the membranes of calcifying cells. Thus, calcifying systems employing proton channels to remove protons from the calcification front are susceptible to changes in seawater pH if not compensated by a reduction in membrane potential, cytosolic pH or an activation of alternative proton export systems.

Conclusion

Our data show that the sea urchin *otop2l* gene encodes a proton channel that is critically involved in the mineralization process of a marine calcifier. Analogous to the situation in vertebrate systems (5, 6), knock-down of *Otop2l* leads to an impairment of calcification in the sea urchin larva. The intracellular formation of CaCO₃ liberates protons that need to be removed from the calcification front to protect intracellular pH homeostasis and to promote mineralization. Given the negative membrane potential of -20.6 mV in PMCs (Figure 4A), *Otop2l* provides an exit route for protons liberated by the intracellular calcification process under past and present oceanic pH conditions (Figure 4H). Our functional characterization of *Otop2l* in combination with environmental pH perturbation experiments indicated that *Otop2l* facilitates proton efflux in a

physiologically relevant pH range. In contrast to the mammalian Otopetrins the sea urchin *Otop2l* has a relatively narrow pH optimum that may result from a long-term adaptation of this protein to stable environmental pH conditions over long geological timescales. Thus, reductions in seawater pH may impair *Otop2l* function, requiring a reorganization of the cellular pH regulatory machinery to enable calcification under these conditions. This information sheds light on the physiological role of *Otop2l* in the calcification process of the sea urchin larva with strong implications for the contribution of otopetrins in other calcifying systems. Given the ubiquitous occurrence of otopetrins in metazoans, the results of the present work can be used to study the potentially conserved role of this family of proton channels in other calcifying species. This comparative approach will help to identify unifying mechanisms underlying sensitivity of marine calcifiers to changes in oceanic pH.

Material and Methods

Experimental animals, larval cultures and re-calcification assay

Collection and culture of adult sea urchins (*Stongylocentrotus purpuratus*) as well as preparation of larval cultures was performed as previously described (26, 27). The re-calcification assay was performed as previously described (13) following a protocol by Pennington & Hadfield (28). Briefly, larvae were exposed to MES buffered seawater adjusted to pH 6 to dissolve their skeletons and after 12-15 h larvae were transferred back to natural seawater (pH 8.1) to regenerate their calcitic endoskeleton. Skeleton growth rates were calculated from increments in the body rod length determined every 48 hours along a period of three days. Ocean acidification experiments were carried out as previously described (12) including all seawater carbonate chemistry data in the supplemental part of that study.

Phylogenetic analysis, RT-qPCR and whole mount *in situ* hybridization

The amino acid sequences for phylogenetic analyses were collected from the Ensembl (www.ensembl.org), Ensembl Metazoa (metazoan.ensembl.org) and EchinoBase (www.echinobase.org) and Reefgenomics (reefgenomics.org) databases. Blasted sequences with E-values higher than e^{-5} were excluded for following analysis. Selected sequences were aligned via MUSCLE program and further trimmed by Gblocks Server

(http://molevol.cmima.csic.es/castresana/Gblocks_server.html). The phylogenetic analysis was generated by MegaX (29) with the best fit model LG+G+F and 500 bootstrap replicates.

Real-time-qPCR and molecular cloning were performed as previously described (12, 30). Expression levels were normalized to the housekeeping gene EF1a (SPU:000595) and amplification primers used for qPCR analysis are listed in the electronic supplementary material (Table S1). Whole mount *in situ* hybridization was performed as previously described using probes generated by the primers listed in table S1 (27).

Single cell transcriptome analyses

Cells of sea urchin embryos were dissociated at appropriate stage using previously published methods (31). Briefly, embryos were collected through a nitex mesh (20 μm for blastula stage, 80 μm for gastrula and pluteus stage) and incubated in Hyalin Extraction medium (0.3M Glycine, 0.3M NaCl, 0.01M KCl, 0.01 M MgSO₄, 0.01M Tris (pH 8.0) and 0.002 M EGTA, pH adjusted to 8.2 with NaOH) on ice for 5 minutes. Cells were gently dissociated by pipetting until reaching > 95% single cell suspension. Dissociated single cells were washed twice in CFSW (454mM NaCl, 9mM KCl, 48mM MgSO₄, 6mM NaHCO₃, pH adjusted to 8.2 with NaOH) and checked for viability (> 95%) by Propidium Iodine staining and fixed in 90% ice-cold methanol and stored at -20°C for up to one day. Fixed cells were rehydrated in CFSW+BSA 0.1% in presence of RNase inhibitor to prevent RNA degradation (Supersasin, ThermoFisher). Rehydrated cells were processed according to 10x Genomics Single cell 3' v3 user guide. Sequencing of libraries was performed on an Illumina HiSeq system resulting in an average of 23.015 raw reads per cell barcode. Raw reads were demultiplexed, aligned to *S.purpuratus* genome 5.0 (retrieved from Echinobase) and counted using the CellRanger pipeline from 10xGenomics (version 3.0.2). Barcodes with less than 1000 reads, less than 500 expressed genes or more than 25% mitochondrial reads were removed to only keep high quality cells. Per time point examined, between 2781 and 4966 cells were retained for analysis, with a median of 2940 unique mRNA and a median of 1208 genes captured per cell. Basic uniform manifold approximation and projection (UMAP) dimensional reduction and clustering was performed using the Seurat v3.2 workflow (32, 33).

Morpholino injection

Micro injections were performed as previously described (12) according to the protocol provided in Warner & McClay (34). The gene specific morpholino-substituted antisense oligonucleotides (MO) 5'- GTTGTTGCCGAAATTATACGCTTAG -3' complementary to the 5' UTR sequence ahead of the sea urchin *otop2l* (LOC579173) start codon as well as a scramble MO that has no biological target in the sea urchin were obtained from Gene Tools (Oregon, USA). The MO was dissolved in injection buffer (35) and was injected into the fertilized egg (1 cell stage).

Immunofluorescence (IF) staining and western-blot (WB) analysis using a custom made antibody designed against the sea urchin Otop2l protein

IF and WB analysis was performed as previously described (26, 27). The polyclonal primary antibody was generated against a synthetic peptide corresponding to c-terminal region (CLDAMHRKPPEDFKQTR) of the sea urchin Otop2l protein. The affinity chromatography purified antibody was diluted 1:250 and samples were incubated over night at 4°C. After washing, samples were incubated in the secondary antibody for 1 hour, and pictures were taken on a confocal microscope (Axiovert 200M, Zeiss, Germany).

WB analysis was performed as previously described (12) using homogenates from whole larvae that were extracted by gentle pipetting in 1:10 wt/vol of Lämmli loading buffer. Proteins were fractionated by SDS PAGE, and transferred to PVDF membranes (Bio-Rad), using a tank blotting system (Bio-Rad). After blocking of non-specific binding sites by 5% (wt/vol) bovine serum albumin, blots were incubated at 4°C overnight in a 1:7500 dilution of the Otop2l antibody. After washing the blots were incubated for 1 h with horseradish peroxidase-conjugated goat anti-rabbit IgG antibody (Santa Cruz Biotechnology, Santa Cruz, CA) diluted 1:14,000 in TBS-T. Protein signals were visualized with the ECL Western Blotting Detection Reagents (GE Healthcare, Munich, Germany). For the peptide compensation assays used in whole mount IF and WB analysis, the primary antibody was pre-absorbed with the immunization peptide at a concentration of 0.1 mg/ml for 12 hours at 4°C.

Intracellular pH (pH_i) measurements and characterization of H⁺ fluxes in PMCs

pH_i determinations and calibrations using the pH sensitive dye BCECF-AM were performed as previously described (12, 18). Proton permeability experiments were conducted by using artificial seawater (ASW) solutions listed in table S2. ASW containing 5 mM Na⁺ and 0 mM HCO₃⁻ (NMDG⁺) in combination with a pH 5.8 treatment was used to acidify PMCs followed by a restoration of pH_i in Na⁺ and HCO₃⁻ independent PMCs was initiated by the perfusion of ASW adjusted to pH 8.0 in the presence of 5 mM Na⁺ and 0 mM HCO₃⁻. Finally, ASW containing 450 mM Na⁺ and 2 mM HCO₃⁻ was used to initiate pH_i recovery in Na⁺ and HCO₃⁻ dependent PMCs. After identification of PMCs that regulate pH_i in a Na⁺ and HCO₃⁻ independent manner, a second low pH challenge in combination with three different Zn²⁺ concentrations (0, 1, and 10 mM) was performed. The recovery slope after the low pH challenge was used to address the sensitivity to proton fluxes to different Zn²⁺ concentrations.

Scramble and Otop2l morpholino injected larvae were measured in an alternate mode and from each larva 4-5 cells were simultaneously recorded. Intracellular acidification and pH_i recovery experiments were performed under 0 mM HCO₃⁻ and 5 mM Na⁺ conditions. Only PMCs that did not respond to an exposure to ASW after the 5 mM Na⁺ and 0 mM HCO₃⁻ were regarded as Na⁺/HCO₃⁻ independent PMCs and were used for further analyses.

Electrophysiology

Oocyte preparation, cRNA synthesis and cRNA injection: *Xenopus* oocyte lobes were obtained from tricaine anesthetized *Xenopus laevis* frogs and incubated in OR2 solution containing (mM): 82.5 NaCl, 2.0 KCl, 1.0 MgCl₂, 5.0 HEPES (pH 7.4) substituted with 2 mg/ml collagenase type II (Sigma-Aldrich/Merck, Germany) for 1 h to remove residual connective tissue. Isolated oocytes were stored at 16.9 °C in ND96 solution containing (mM): 96.0 NaCl, 2.0 KCl, 1.8 CaCl₂, 1.0 MgCl₂, 5.0 HEPES (pH 7.4) supplemented with Na-pyruvate (275 mg/l), theophylline (90 mg/l), and gentamicin (50 mg/l). Otop2l channels were subcloned into the dual-purpose vector pFAW which can be used for HEK293 as well as expression in *Xenopus* oocytes. cDNA was linearized with NheI or MluI, respectively and cRNA was synthesized *in vitro* using the SP6 or T7 AmpliCap Max High Yield Message Maker Kit (Cellscript, USA) and stored in stock solutions at -80 °C. The quality of cRNA was tested using gel electrophoresis and cRNA was quantified with the NanoDrop 2000 UV-Vis spectrophotometer (Thermo Fisher Scientific, USA). Oocytes were injected with ~50 nl of cRNA for Otop2l and incubated for 7-8 days at 16.9 °C. Prior investigation, oocytes were pre-incubated

in recording solution with 100 μM 4,4'-Diisothiocyano-2,2'-stilbenedisulfonic acid (DIDS) for 10 min. to suppress endogenous Ca^{2+} -activated Cl^- channel currents at acidic pHs (36, 37).

Two-electrode voltage-clamp (TEVC) recordings: All TEVC recordings were performed at room temperature (20-22 $^{\circ}\text{C}$) as previously described (38) with a HEKA multielectrode clamp amplifier iTEV90 (HEKA electronics, Germany) or a TURBO TEC 10CX amplifier (npi electronic instruments, Germany), sampled at 10 kHz and filtered with 3 kHz (-3 dB). Microelectrodes for measurements were fabricated from borosilicate glass capillaries GB200F-8P (Science Products, Germany) and pulled with a DMZ-Universal-Electrode-Puller (Zeitz, Germany), back-filled with 2 M KCl, and had a resistance of 0.5 - 1.2 M Ω . Recording solution contained (mM): 120 KCl, 1.8 CaCl_2 , 2.0 MgCl_2 and 10 HEPES (pH 7.4), 10 TRIS (pH 8.0 and 8.5) or 10 MES (pH 5.0), respectively. ZnCl_2 was directly diluted in the recording solution pH 8.5 to 2 mM. For current measurements the membrane potential was held at -80 mV and voltage ramps were applied every second from -80 mV to +80 mV with a sweep interval of 2 seconds. Data was acquired with PatchMaster (HEKA electronics, Germany), analyzed with FitMaster (HEKA electronics, Germany) and Igor Pro 8 (WaveMetrics, USA).

Membrane potential measurements

The membrane potential of PMCs was measured using intracellular electrodes. For the measurements, the ectoderm of the larvae was removed as described earlier using the bag-isolation method. Larvae were glued onto 1% protamine sulfate coated coverslips and attached to a microscopy chamber filled with ASW. The recording electrode was pulled from borosilicate glass (GB150F-8P) on a horizontal puller (DMZ Universal Puller, Zeitz), back-filled with 3M KCl solution and connected via an Ag/AgCl electrode to a dual electrometer with high input resistance (FD223a; WPI). The recording electrode was controlled by a motorized micromanipulator (PatchStar; Scientifica). Impalements of PMCs were performed under visual control on an inverted microscope at a 100x magnification.

Transfection of HEK-293 cells

HEK293 cells were cultured at 37 $^{\circ}\text{C}$ / 5% CO_2 in DMEM supplemented with 10% FCS and Penicillin/Streptomycin. Cells with 70% confluency were transiently transfected with 0.5 μg *Otop2l* and 0.1 μg mCherry constructs per well (24-well plate) using Lipofectamine 2000 (Invitrogen, Carlsbad, CA) according to the manufacturer's instructions. After 18-24 hours, HEK-293 cells co-transfected with *Otop2l* and mCherry constructs as well as HEK cells only transfected with mCherry sham

control vector were dissociated with trypsin/EDTA, seeded on sterile 30 mm coverslips. After 10-15 hours cells were loaded with the intracellular pH indicator dye BCECF-AM as described above. Cells co-transfected with mCherry were identified using a 580ex/633em filter cube and used for pH_i measurements. pH_i in Otop2l and sham-transfected cells was measured in response to Tyrodes solutions (145 mM NaCl, 5 mM KCl; 1 mM MgCl₂, 2 mM CaCl₂, 20 mM dextrose 10 mM HEPES) adjusted to pH 7.4 or pH 5.0 buffered with 10 mM MES or with 10 mM acetic acid. On each slide 3-4 mCherry positive cells were measured and traces were averaged leading to one replicate. To convert fluorescence ratios into pH_i, a nigericin and high potassium containing solution adjusted to different pH levels was used as previously described (18).

Statistical analyses

Data were tested for normality and homogeneity and significance levels were analyzed using Student's t-tests or one-way ANOVA. Western blot analyses for Otop2l abundance of Scramble and Otop2l morpholino injected larvae was analyzed by Student's t-test. Differences in proton permeability of PMCs treated with different Zn²⁺ concentrations or between scramble and Otop2l morpholino injected larvae was analyzed by one-way ANOVA followed by Holm-Sidak post-hoc test and Student's t-test, respectively. Differences in proton fluxes between sham-transfected and Otop2l expressing HEK-293 cells were analyzed using Student's t-test. Statistical analyses were conducted using Sigma Stat 13 (Systat Software).

Acknowledgements: M.Y.H. was funded by the Emmy Noether Program (403529967) of the German Research Foundation (DFG). M.S. and T.B. were supported by the DFG as part of the Research Unit FOR2518, Dynlon. The authors would like to thank C. Etensohn and M. Stumpp for the fruitful discussions on this work. The authors further thank, F. Thoben J. Hildebrand and R. Lingg for maintenance of the sea urchin culture systems.

References

1. Tu Y-H, *et al.* (2018) An evolutionarily conserved gene family encodes proton-selective ion channels. *Science* 359:1047-1050.
2. Saotome K, *et al.* (2019) Structures of the otopetrin proton channels Otop1 and Otop3.
3. Zhang J, *et al.* (2019) Sour sensing from the tongue to the brain. *Cell* 179(2):392-402.
4. Teng B, *et al.* (2019) Cellular and neuronal responses to sour stimuli require the proton channel Otop1. *Curr Biol* 29(21):3647-3656.

5. Hurle B, *et al.* (2003) Non-syndromic vestibular disorder with otoconial agenesis in *tilted/mergulhador* mice caused by mutations in *otopetrin1*. *Hum Mol Genet* 12(7):777-789.
6. Hughes I, *et al.* (2004) Otopetrin 1 is required for otolith formation in the zebrafish *Danio rerio*. *Dev Biol* 276(2):391-402.
7. Blair HC, *et al.* (2018) Support of bone mineral deposition by regulation of pH. *Am J Physiol Cell Physiol* 315(4):C587-C597.
8. Sikes CS, Okazaki K, & Fink RD (1981) Respiratory CO₂ and the supply of inorganic carbon for calcification of sea urchin embryos. *Comp Biochem Physiol A* 70:285-291.
9. Liu L, Schlesinger PH, Slack NM, Friedmann PA, & Blair HC (2011) High capacity Na⁺/H⁺exchange activity in mineralizing osteoblasts. *J Cell Physiol* 226(6):1702-1712.
10. Beniash E, Aizenberg J, Addadi L, & Weiner S (1997) Amorphous calcium carbonate transforms into calcite during sea urchin larval spicule growth. *Proc Roy Soc Lond B* 264:461-465.
11. Vidavsky N, *et al.* (2014) Initial stages of calcium uptake and mineral deposition in sea urchin embryos. *Proc Nat Acad Sci USA* 111:39-44.
12. Hu MY, *et al.* (2018) A Slc4 family bicarbonate transporter is critical for intracellular pH regulation and biomineralization in sea urchin embryos. *elife* 7:e36600.
13. Hu MY, Petersen I, Chang W, Blurton C, & Stumpp M (2020) Cellular bicarbonate accumulation and vesicular proton transport promote skeleton regeneration in the sea urchin larva. *Proc Roy Soc Lond B* 287:20201506.
14. Rafiq K, Shashikant T, McManus CJ, & Etensohn CA (2014) Genome-wide analysis of the skeletogenic gene regulatory network of sea urchins. *Development* 141(4):950-961.
15. Sun Z & Etensohn CA (2014) Signal-dependent regulation of the sea urchin skeletogenic gene regulatory network. *Gene Expr Patterns* 16(2):93-103.
16. Guss KA & Etensohn CA (1997) Skeletal morphogenesis in the sea urchin embryo: regulation of primary mesenchyme gene expression and skeletal rod growth by ectoderm-derived cues. *Development* 124:1899-1908.
17. Tsirigos KD, Peters C, Shu N, Käll L, & Elofsson A (2015) The TOPCONS web server for consensus prediction of membrane protein topology and signal peptides. *Nucleic Acids Research* 43(W1):W401-W407.
18. Stumpp M, *et al.* (2012) Acidified seawater impacts sea urchin larvae pH regulatory systems relevant for calcification. *Proc Nat Acad Sci USA* 109(44):18192-18197.
19. Zeebe RE (2012) History of seawater carbonate chemistry, atmospheric CO₂ and ocean acidification. *Annu Rev Earth Planet Sci* 40:141-165.
20. Decoursey TE (2003) Voltage-gated proton channels and other proton transfer pathways. *Physiol Rev* 83:475-579.
21. Taylor AR, Chrachri A, Wheeler GS, Goddard H, & Brownlee C (2011) A voltage-gated H⁺ channel underlying pH homeostasis in calcifying coccolithophores. *Plos Biology* 9(6):e1001085.
22. Bach LT, Riebesell U, Gutowska MA, Federwisch L, & Schulz KG (2015) A unifying concept of coccolithophore sensitivity to changing carbonate chemistry embedded in an ecological framework. *Progress in Oceanography* 135:125-138.
23. Pan T-CF, Applebaum SL, & Manahan DT (2015) Experimental ocean acidification alters the allocation of metabolic energy. *Proc Nat Acad Sci USA* 112(15):4696-4701.
24. IPCC (2014) *IPCC 2014: Climate Change 2014: Synthesis report. Contribution of Workinggroups I, II; III to the Fifth Assessment Report of the Intergovernmental Panel on Climate Change* (IPCC, Geneva, Switzerland).

25. Tambutté E, *et al.* (2012) Calcein labeling and electrophysiology: insights on coral tissue permeability and calcification. *Proc Roy Soc Lond B* 279(1726):19-27.
26. Stumpp M, *et al.* (2013) Digestion in sea urchin larvae impaired under ocean acidification. *Nature Climate Change* 3:1044.
27. Stumpp M, *et al.* (2015) Evolution of extreme stomach pH in bilateria inferred from gastric alkalization mechanisms in basal deuterostomes. *Sci Rep* 5:1-9.
28. Pennington JT & Strathmann RR (1990) Consequences of the calcite skeletons of planktonic echinoderm larvae for orientation, swimming, and shape. *Biol Bull* 179:121-133.
29. Stecher G, Tamura K, & Kumar S (2020) Molecular evolutionary genetics analysis (MEGA) for macOS. *Mol Biol Evol* 37(4):1237-1239.
30. Lee H-G, *et al.* (2019) Tipping points of gastric pH regulation and energetics in the sea urchin larva exposed to CO₂-induced seawater acidification. *Comp Biochem Physiol A* 22(234):87-97.
31. McClay DR (2004) Methods for embryo dissociation and analysis of cell adhesion. *Methods in Cell Biology* 74:311-329.
32. Butler A, Hoffman P, Smibert P, Papalexi E, & Satija R (2018) Integrating single-cell transcriptomic data across different conditions, technologies, and species. *Nature Biotechnology* 36:411-420.
33. Stuart T, *et al.* (2019) Comprehensive integration of single cell data. *Cell* 177:1888-1902.
34. Warner J & McClay DR (2014) Perturbation of the Hedgehog pathway in sea urchin embryos. *Developmental biology of the sea urchin and other marine invertebrates*, eds Carroll DJ & Stricker SA (Humana Press, New York), pp 211-223.
35. Yaguchi J (2019) Microinjection methods for sea urchin eggs and blastomeres. *Methods in Cell Biology*, eds Foltz KR & Hamdoun A (Elsevier), Vol 150, pp 173-188.
36. Faria D, *et al.* (2014) The calcium-activated chloride channel Anoctamin 1 contributes to the regulation of renal function. *Kidney Int* 85:1369-1381.
37. Schroeder BC, Cheng T, & Jan YN (2008) Expression cloning of TMEM16A as a calcium-activated chloride channel subunit. *Cell* 134:1019-1029.
38. Streit AK, *et al.* (2011) A specific two-pore domain potassium channel blocker defines the structure of the TASK-1 open pore. *J Biol Chem* 286(16):13977-13984.

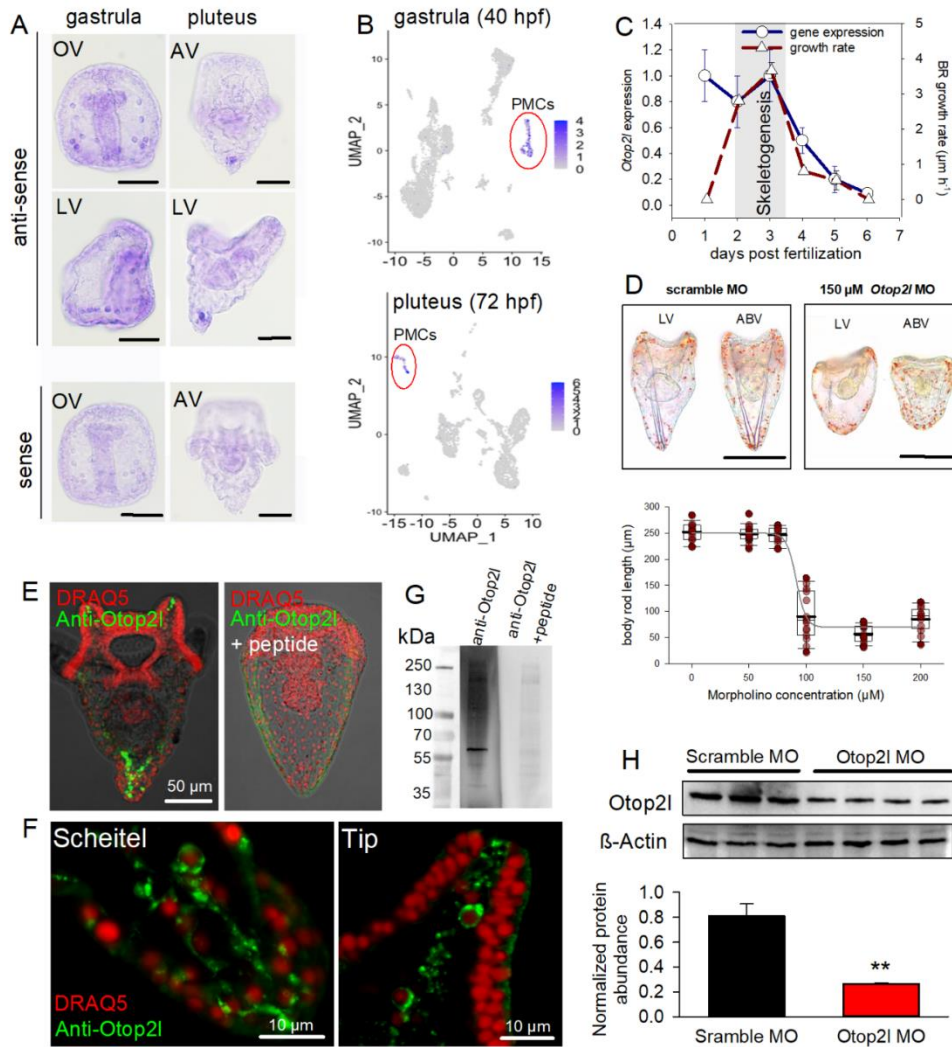


Figure 1 *Otop21* expression in the calcifying primary mesenchyme cells (PMCs) and its contribution to the formation of the CaCO_3 skeleton. (A) *In situ* hybridization using sense and antisense probes demonstrating the expression of *otop21* in PMCs (scale bar 50 μm). (B) Single cell transcriptome analyses for the *Otop21* gene in two developmental stages of the sea urchin larva. Each cell is plotted as a single dot after dimensional reduction using UMAP. Cells cluster by similarity of transcriptome (i.e. cell type). Normalized and scaled counts of *otop21* are shown in blue. Note that expression of *Otop21* is restricted to one cluster of cells (PMCs) in each stage (for additional explanations see Figure S3). (C) Quantitative real time PCR was used to assess expression levels of *Otop21* normalized to the internal control *EF1a* along the first six days of development in unfed larvae. Growth rates of the larval skeleton were determined along for the same developmental period. (D) Morpholino (MO) knock-down of *otop21* was used to assess the role of this gene for skeletogenesis. A scramble morpholino was used as negative control. A dose response curve using different MO concentrations was generated to identify a minimum concentration that is sufficient to inhibit skeletogenesis. Abbreviations: oral view (OV), anal view (AV), lateral view (LV), abanal view (ABV). Values are presented as mean \pm SEM ($n = 3$). Morpholino injections were repeated 3-4 times and measurements were pooled and presented as boxplot

including 5th/95th percentile and mean values. (E) Localization of the Otop2l protein in PMCs of a 4 days-post-fertilization (dpf) pluteus larva using a sea urchin specific antibody and peptide competition assay by pre-absorption of the antibody with the immunization peptide. Nuclei are stained by DraQ5 in red. (F) High magnification image of positive immunoreactivity in PMCs in the schein and the apex region of a body rod (tip) demonstrating the subcellular localization of Otop2l. (G) Western blot analysis of the Otop2l antibody using whole larvae homogenates and pre-absorption of the antibody with 10 mg ml⁻¹ of the immunization peptide. (H) Otop2l protein abundance in 4 dpf larvae injected with 150 μM of scramble and *Otop2l* morpholino. Otop2l protein abundance was normalized to β-actin. Values are presented as mean ± SEM (n = 3-4), **p<0.001.

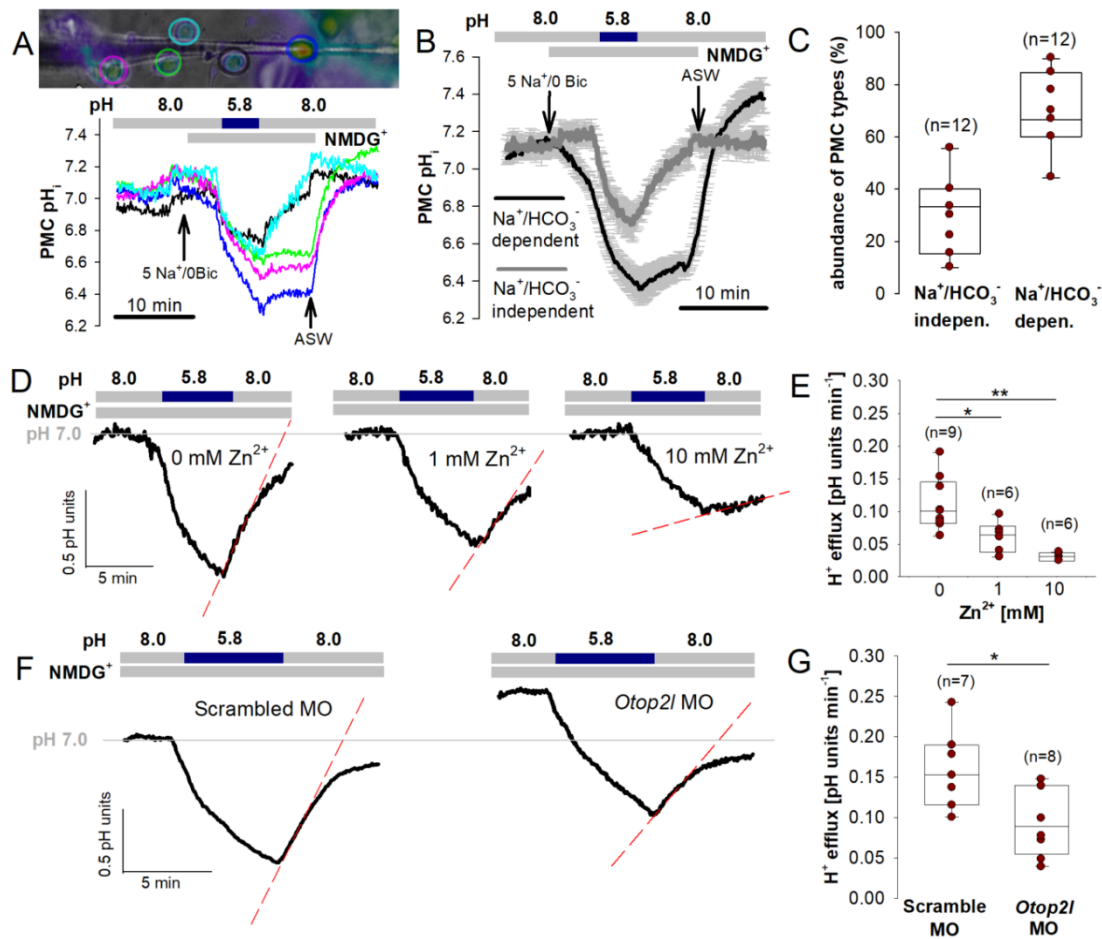


Figure 2 Contribution of *Otop2L* to the proton permeability in calcifying primary mesenchyme cells. (A) Bright field and fluorescence (486/440) overlay of PMCs along a spicule loaded with the ratiometric pH sensitive dye BCECF-AM. Changes in intracellular pH (pH_i) of PMCs to variations in extracellular pH were measured in artificial seawater (ASW) with 5 mM Na^+ and 0 mM HCO_3^- (NMDG $^+$). (B) Using external pH changes in combination with removal of Na^+ and HCO_3^- two populations of PMCs were identified (data are mean \pm SEM; $n = 8$). (C) Relative abundance of the two functional states of PMCs in pluteus larvae. (D) Changes in cellular proton fluxes induced by changes in external pH during exposure to different concentrations of Zn^{2+} . Traces represent average values from 6-10 larvae. (E) Effect of Zn^{2+} on the proton efflux from PMCs during recovery from the acid-load. (F) Changes in pH_i during changes in external pH in larvae injected with 100 μ M of scramble or *Otop2L* morpholino (MO). Traces represent average values from 8 larvae. (G) Changes in cellular proton fluxes induced by changes in external pH in scramble MO or *Otop2L* MO injected larvae. All Zn^{2+} and knock-down experiments were performed in the presence of 5 mM Na^+ and 0 mM HCO_3^- . Additional parameters from pH_i measurements are listed in table S3.

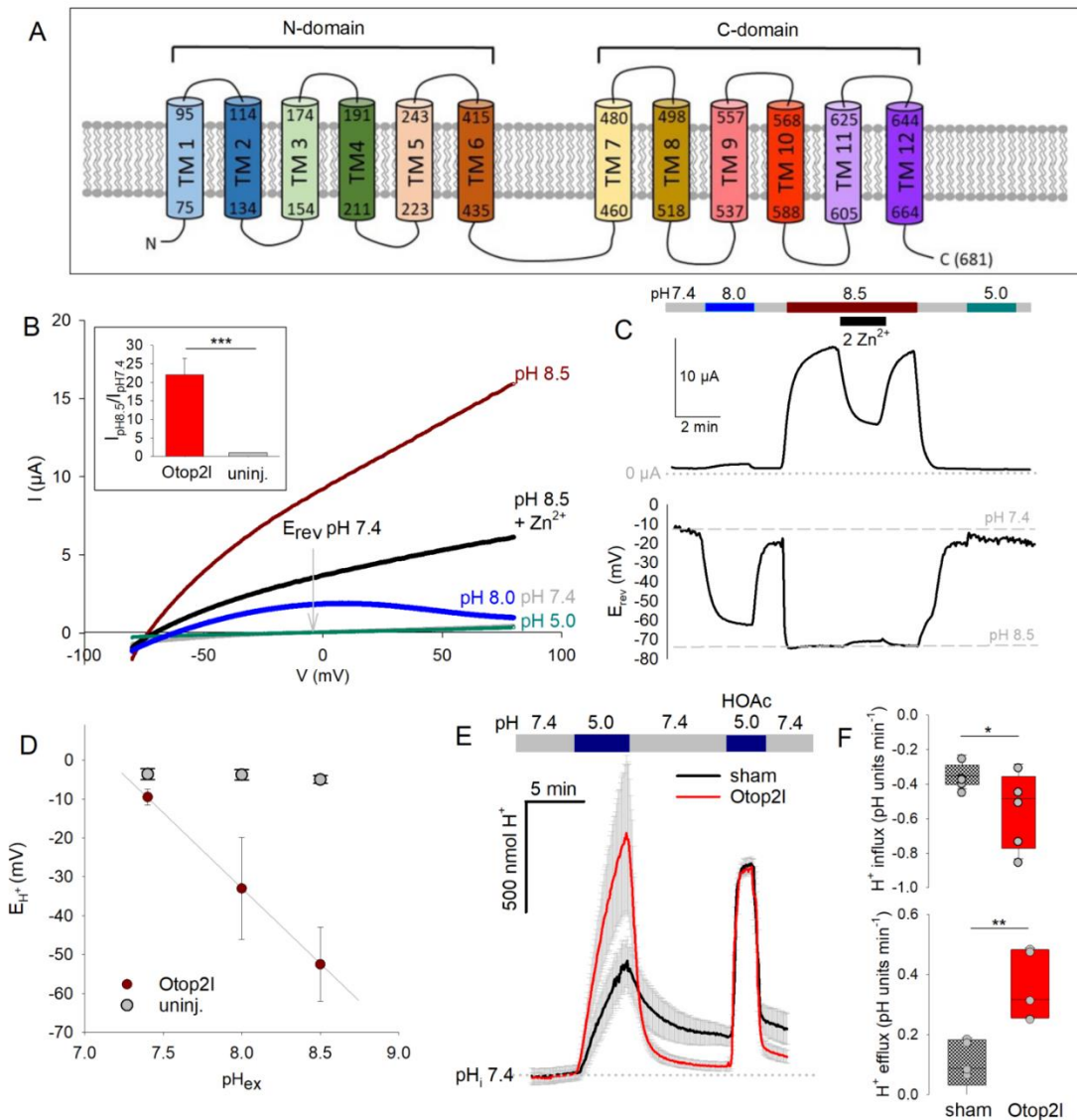


Figure 3 Otop21 encodes a proton channel that is required for biomineralization in the sea urchin larva. (A) Trans-membrane helices of the Otop21 amino acid sequence were predicted by the online tool TOPCONS (17). (B) Representative currents evoked by two-electrode voltage-clamp measurements of sea urchin Otop21 expressing *Xenopus* oocytes in the voltage range from -80 mV to +80 mV (holding membrane potential, $V_m = -80$ mV). Current-Voltage (I/V) relationships in neutral pH_e 7.4 (gray trace, $E_{rev} \sim -12$ mV), alkaline pH_e 8.0 (blue traces) or 8.5 (orange trace, $E_{rev} \sim -71$ mV), acidic pH_e 5.0 (green trace) and during Zn^{2+} application (black trace) are shown. Inset shows the fold activation ($I_{pH_e 8.5}/I_{pH_e 7.4}$) of outward proton current flux of oocytes expressing Otop21 (red bar) and uninjected oocytes (gray bar) at +50 mV ($n = 6$). (C) Evoked Otop21 currents measured in (B) plotted at +50 mV (upper panel) and the corresponding time course of the E_{rev} (lower panel). (D) Category plot of the E_{rev} as a function of pH_e in *Xenopus* oocytes expressing Otop21 (gray circles; $n = 6$) and uninjected oocytes (gray squares; $n = 2$). (E) Changes in intracellular pH of HEK-293 cells expressing Otop21 ($n = 5$) and sham-transfected cells ($n = 6$) in response to

changes in extracellular pH. Acidification with HOAc (acetic acid) that shuttles protons across membranes, served as an indicator for maximum proton permeability in both, *Otop2l* and sham transfected cells. (F) Proton influx and efflux rates in *Otop2l* and sham transfected cells were calculated from the linear part of the slopes during acidification and recovery (n = 5-6, Data were analyzed by two-tailed t-test with *p < 0.05; **p < 0.01; ***p < 0.001). Additional acid-base parameters for HEK-293 measurements are listed in table S3.

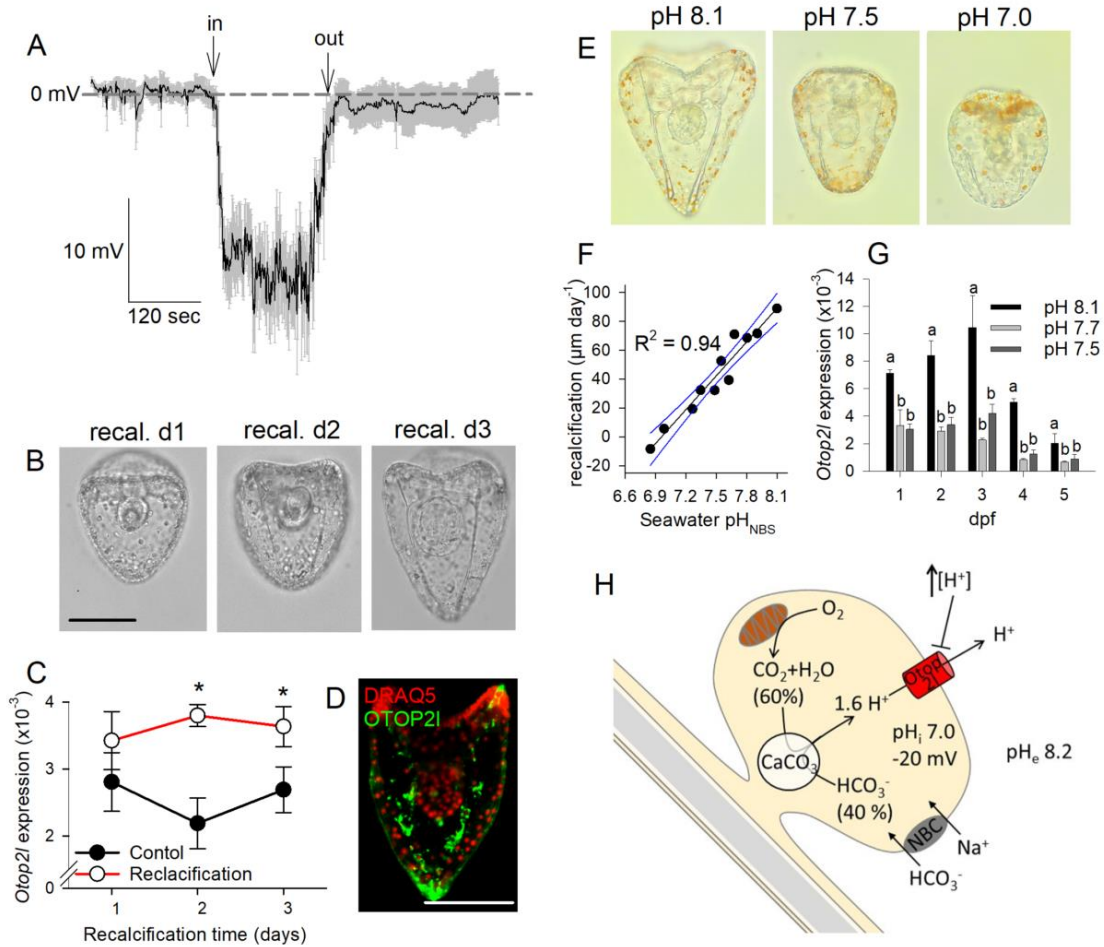


Figure 4 Effects of changes in transmembrane proton gradients on the calcification process (A) Measurement of the PMC membrane potential using intracellular microelectrodes. Values are presented as mean \pm SEM (n = 8). **(B)** Skeletons of 3 dpf larvae were dissolved by exposure to MES buffered seawater adjusted to pH 6.0 for 12 hours. Larvae were transferred back to natural seawater (pH 8.1) to regenerate their skeletons. **(C)** Along the regeneration period of three days, *otop2l* expression was determined by qPCR and normalized to the reference gene *EF1a*. Larvae that were not subjected to the low pH treatment were used as control group. Values are presented as mean \pm SEM (n=5-6) and asterisks denote significant ($p < 0.05$; one-way ANOVA, Holm-Sidak post-hoc) differences to the control group. **(D)** Immunolocalization of Otop2l in a recalcifying (d3) larva (bar = 100 μm). **(E-F)** After dissolution of the larval skeleton by low pH treatment, skeleton regeneration rates were determined under a range of pH adjusted with HCl in HEPES buffered seawater. **(G)** Normalized expression level of *otop2l* in larvae raised under different levels of CO₂-induced seawater acidification (different letters denote significant differences between treatments). **(H)** Schematic working model for the function of Otop2l in calcifying PMCs of the sea urchin larva. 1.6 Protons liberated by the intracellular precipitation of one CaCO₃ molecule can exit the cell through Otop2l along a proton gradient.

Supplementary Information for

An Otopetrin family proton channel promotes cellular acid efflux critical for biomineralization in a marine calcifier

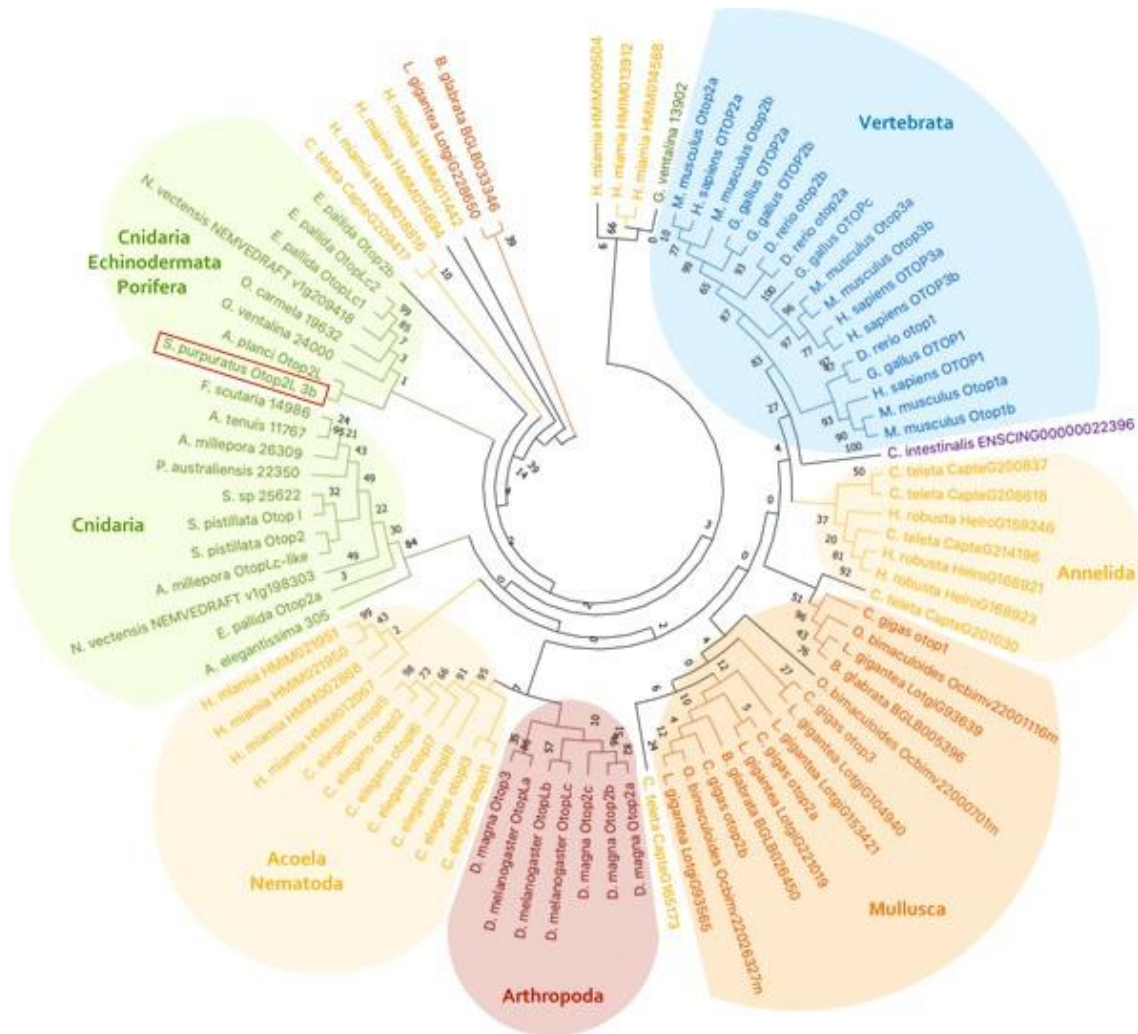


Fig. S1 Phylogenetic tree of Otopetrins from different animal phyla base on deduced amino-acid sequences. Maximum-likelihood phylogenetic tree created from the multi-sequence alignment of 87 Otopetrin homologues. Bootstrap values of the branches were marked on the nodes. The vertebrate sequences form a distinct monophyletic group, separated from those of the invertebrate clades. Within the invertebrate groups different Otopetrin isoforms are distributed across the Arthropoda, Annelida, Mollusca and Acoela phyla. The sea urchin Otop2l protein clusters with those obtained from other echinoderms, stony corals and sponges. Some acoela, anneliada and mollusca Otop sequences appear to have undergone additional gene-duplication events, creating species-specific paralogs.

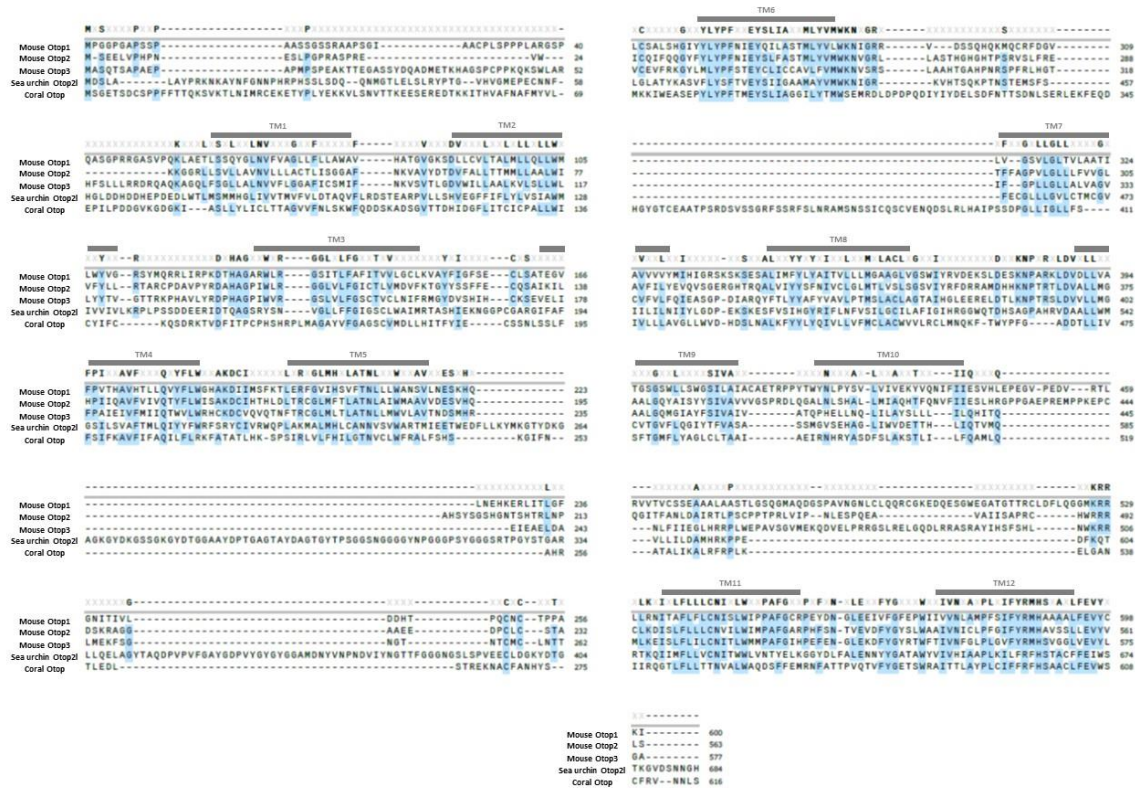


Figure S2 Protein sequence comparison between otopetrins. Amino acid sequence alignment of mouse Otop 1-3 and sea urchin Otop2l and coral Otop crated using the NCBI multiple alignment tool. Blue shading shows identical residues. The transmembrane domains were predicted by TOPCONS (1) base on the free energy of membrane insertion for short peptides (the ΔG -scale). For all the 12 transmembrane domains of Otop2L, the ΔG of center parts were lower than 3 kcal/mol. The sea urchin Otop2L has an identity and E value of 26.42% / 24.38% and $8e^{-14}$ / $7e^{-22}$ to its homologs with known protein structure including the chicken Otop3 and zebrafish Otop1, respectively. The alignment result also shows the share of conserved transmembrane domains.

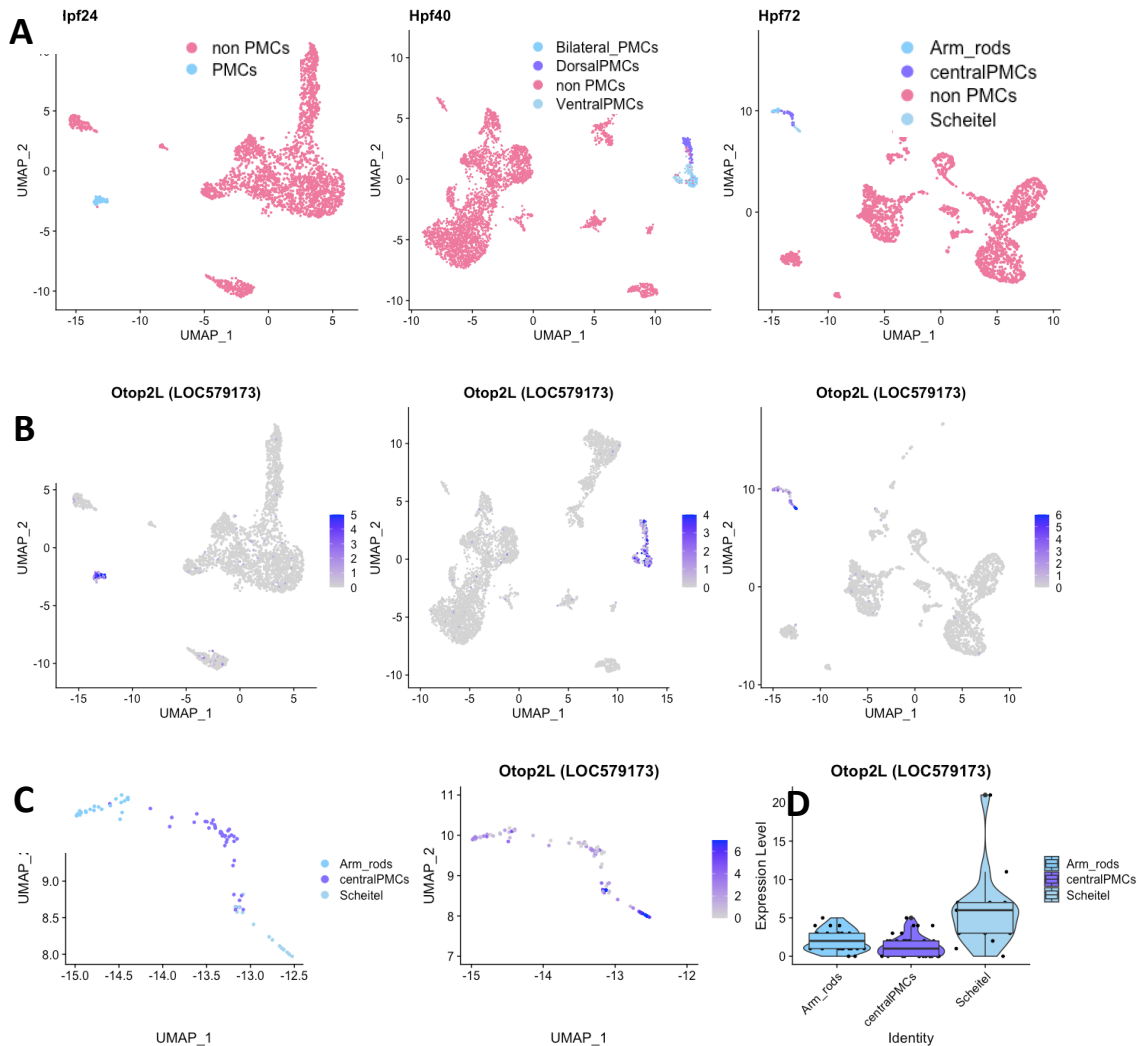


Fig. S3 Single-cell transcriptome analyses of *Otop2l*. Single-cell RNA sequencing was performed on dissociated sea urchin embryos at indicated stages using the 10x Genomics commercial platform. Dimensional reduction was achieved using uniform manifold approximation and projection (UMAP) and projections are plotted as dot plots (each dot represents a cell). Unsupervised clustering of cells resulted in several clusters out of which clusters positive for pan-PMC marker genes *Alx1*, *SpP19L* and *SM50* were identified as PMCs. (A) For each developmental stage, PMCs are shown in shades of blue, sub-clusters of PMCs were identified based on expression of genes that have previously been reported to be specific to subpopulations of PMCs (i.e. *FGF*, *FGFR*, *P16*, *SM30A*, *GATAc*, *BMP2/4*, (2, 3)). (B) Scaled and normalized counts per cell of *Otop2L* are shown in blue in the same UMAP projection as above. (C) *Otop2l* expression in PMC subpopulations at pluteus stage. Zoom into Hpf72 plots from above, to better visualize expression in subclusters of PMCs. Note highest expression of *Otop2l* in PMCs belonging to Scheitel rods. (D)

Box plot overlaid on violin plot of single cell RNA expression of Otop21 in PMC subpopulations at Hpf72. Each dot represents normalized and scaled counts of Otop21 in a single PMC.

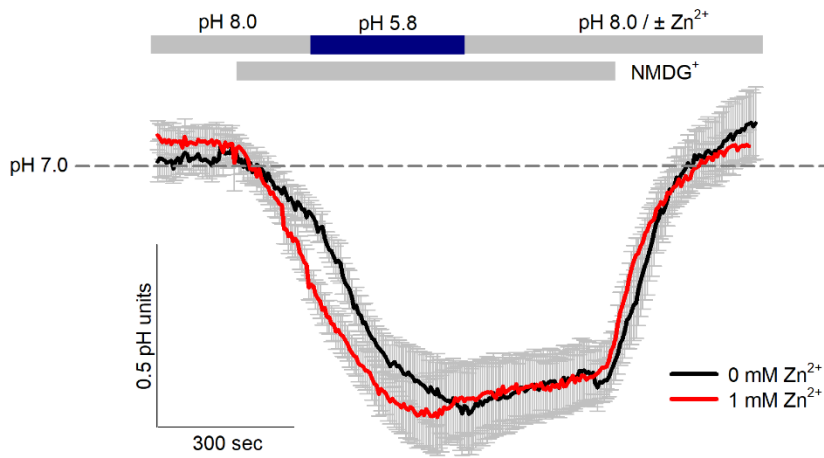


Fig. S4 Effect of Zn²⁺ on pH regulatory mechanisms in Na⁺/HCO₃⁻-dependent PMCs. To test the specificity of the Zn²⁺ treatment on the function of the Otop21 proton channels in PMCs we tested the effect of 1 mM Zn²⁺ on other pH regulatory mechanisms in Na⁺/HCO₃⁻-dependent PMCs. Na⁺/HCO₃⁻-dependent PMCs acidify during removal of external Na⁺ and HCO₃⁻. Lowering of external pH under these conditions rapidly leads to an intracellular acidification. Even when the external pH is restored back to pH 8.0 these PMCs are not able to recover. Only when Na⁺ and HCO₃⁻ levels in the perfusion solution are back to natural seawater conditions (450 mM [Na⁺] and 2.3 mM [HCO₃⁻]) pHi is rapidly restored. This recovery from the low pH and low Na⁺/HCO₃⁻ challenge is not affected by Zn²⁺ (Student's t-test p = 0.84). Values are presented as mean ± SEM.

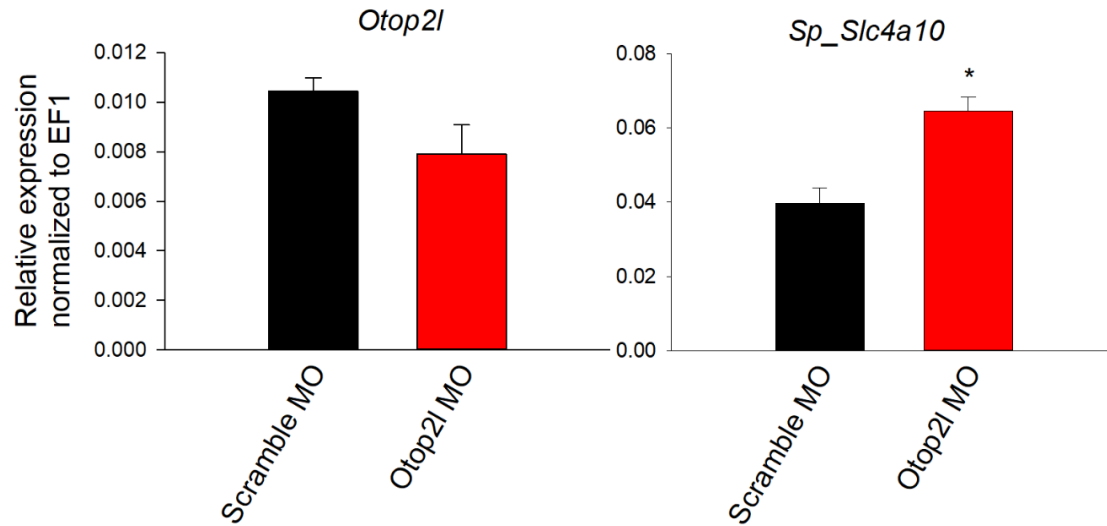


Fig. S5 Expression of *Otop2l* and *Sp_Slc4a10* in control and *Otop2l* knock-down larvae. Expression levels of the proton channel *Otop2l* and the $\text{Na}^+/\text{HCO}_3^-$ cotransporter *Sp-Slc4a10* were measured in Scramble MO and *Otop2l* MO injected larvae. Expression levels were normalized to the housekeeping gene EF1 and are expressed as mean \pm SEM (n=3). Asterisks denote significant ($p < 0.05$, Student's t-test) differences.

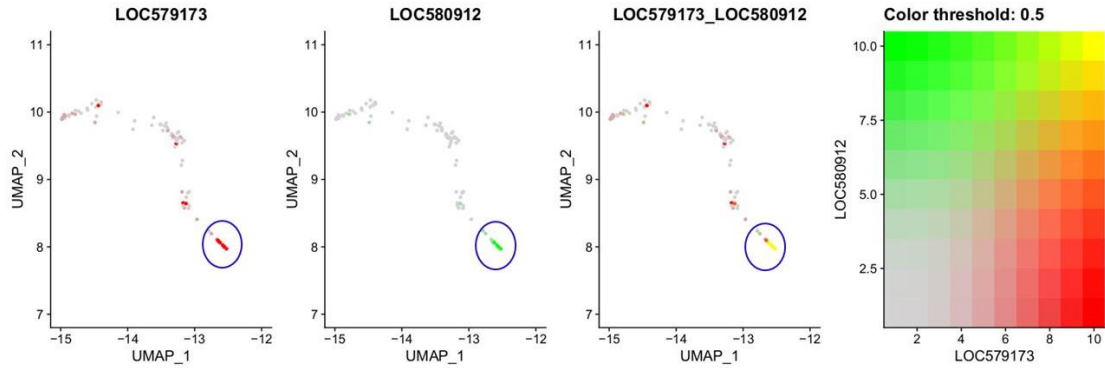


Fig. S6 Co-expression of the $\text{Na}^+/\text{HCO}_3^-$ cotransporter *Slc4a10* and *Otop2l* in subpopulations of PMCs. Single cell transcriptome analyses at 72 h post-fertilization indicate predominant expression of *Otop2l* (LOC579173) in a subpopulation of PMCs in the scheitel region (blue circle) of the larval skeleton. A similar expression pattern is found for the bicarbonate transporter *SpSlc4a10* (LOC580912) that is responsible for the import of HCO_3^- into PMCs (4). These two proteins are largely co-expressed in PMCs of the scheitel region.

Table S1 Primers used for real-time quantitative PCR and *in situ* hybridization

| qPCR primers | Gene | Primer sequences | Amplicon size | Acc. number |
|----------------------|--------|------------------------|---------------|----------------------------|
| | Otop2l | F-GTTGGCAGACGGATCACAGC | 200 bp | SPU_004766 |
| | | R-TAGAAGCACCTGCATGACGG | | |
| | EF1a | F-CCGACCTTGGAAGGGATCG | 194 bp | SPU_000595 |
| | | R-ACAGTCGGCCTGTGAGGTTC | | |
| <i>In situ</i> probe | Otop2l | F-TTGCGCAAACAACGTCTCAG | 727 bp | SPU_004766 |
| | | R-GATAACGCCACACATCGTGC | | |

Table S2. Artificial seawater solutions

| Ions/Buffers | ASW | 5mM Na ⁺ /0 HCO ₃ ⁻ pH 5.8 | 5mM Na ⁺ /0 HCO ₃ ⁻ pH 8.0 |
|-------------------------------|------|--|--|
| Na ⁺ | 420 | 5 | 5 |
| Cl ⁻ | 470 | 480 | 480 |
| K ⁺ | 10 | 10 | 10 |
| Mg ²⁺ | 53 | 53 | 53 |
| Ca ²⁺ | 15 | 15 | 15 |
| SO ₄ ²⁻ | 28 | 28 | 28 |
| HCO ₃ ⁻ | 2.35 | 0 | 0 |
| NMDG ⁺ | 0 | 440 | 440 |
| MES | 0 | 30 | 0 |
| pH | 8.1 | 5.8 | 8.0 |
| Osmolality | 980 | 1031 | 1030 |

Artificial seawater (ASW) solutions (concentrations given in mM)

Table S3. Intracellular pH parameters in HEK-293 cells and PMCs from the low pH pulse experiments

| | | Resting pH _i | Maximum acidification pH 5.0/5.5 | Maximum acidification pH 5.5 HOAc | Residual acidification | Acidification rate (pH units min ⁻¹) | Acidification rate (H ⁺ min ⁻¹) | Recovery rate (pH units min ⁻¹) | Recovery rate (H ⁺ min ⁻¹) |
|---------|-------------|-------------------------|----------------------------------|-----------------------------------|------------------------|--|--|---|---|
| HEK-293 | Sham | 7.30 ± 0.29 | 6.28 ± 0.10 | 5.99 ± 0.02 | 0.72 ± 0.02 | -0.35 ± 0.04 | 107 ± 41 | 0.10 ± 0.04 | -94 ± 32 |
| | Otop2l | 7.41 ± 0.34 | 6.14 ± 0.06 | 6.01 ± 0.02 | 0.32 ± 0.16* | -0.55 ± 0.16* | 168 ± 16 | 0.34 ± 0.05* | -312 ± 16* |
| PMC | Otop2l MO | 7.45 ± 0.07* | 6.55 ± 0.18 | N.D. | 0.51 ± 0.17 | -0.10 ± 0.02 | 66 ± 49 | 0.09 ± 0.02* | -57 ± 37* |
| | Scramble MO | 7.05 ± 0.07 | 6.09 ± 0.11 | N.D. | 0.21 ± 0.12 | -0.09 ± 0.02 | 109 ± 36 | 0.16 ± 0.02 | -201 ± 45 |

References

1. Tsirigos KD, Peters C, Shu N, Käll L, & Elofsson A (2015) The TOPCONS web server for consensus prediction of membrane protein topology and signal peptides. *Nucleic Acids Research* 43(W1):W401-W407.
2. Costa C, Karakostis K, Zito F, & Matranga V (2012) Phylogenetic analysis and expression patterns of *p16* and *p19* in *Paracentrotus lividus* embryos. *Development Genes and Evolution* 222:245-251.
3. Röttinger E, *et al.* (2008) FGF signals guide migration of mesenchymal cells, control skeletal morphogenesis and regulate gastrulation during sea urchin development. *Development* 135:353-365.
4. Hu MY, *et al.* (2018) A Slc4 family bicarbonate transporter is critical for intracellular pH regulation and biomineralization in sea urchin embryos. *elife* 7:e36600.

II Extracellular carbonic anhydrase activity promotes a carbon concentration mechanism in metazoan calcifying cells

PNAS
www.pnas.org

Main Manuscript for

Extracellular carbonic anhydrase activity promotes a carbon concentration mechanism in metazoan calcifying cells

Ann-Sophie Matt¹, William W. Chang¹, Marian Y. Hu^{1*}

¹Institute of Physiology, Christian-Albrechts-University of Kiel, Hermann-Rodewald-Str. 5 24118 Kiel, Germany

*Corresponding Author:

Dr. Marian Y. Hu

Institute of Physiology, Christian-Albrechts University of Kiel

Hermann-Rodewald Straße 5 24118 Kiel, Germany

e-mail: m.hu@physiologie.uni-kiel.de

phone: +49(0)4318802048

Author contributions: A-S.M., W.W.C. and M.Y.H. designed research and conducted experiments. All co-authors analyzed data and wrote the manuscript

Competing Interest Statement: The authors declare no competing interests

Classification: Biological Sciences

Keywords: biomineralization, intracellular pH, metabolic CO₂, carbon fixation, global carbon cycle, ocean acidification

Abstract

Many calcifying organisms utilize metabolic CO_2 to generate CaCO_3 minerals to harden their shells and skeletons. Carbonic anhydrases are evolutionary ancient enzymes that were proposed to play a key role in the calcification process with the underlying mechanisms being little understood.

Here we used the calcifying primary mesenchyme cells of the sea urchin larva to study the role of cytosolic (iCAs) and extracellular carbonic anhydrases (eCAs) in the cellular carbon concentration mechanism (CCM). Molecular analyses identified iCAs and eCAs in PMCs and highlight the prominent expression of a GPI-anchored membrane-bound CA (Cara7). Intracellular pH recordings in combination with CO_2 pulse experiments demonstrated iCA activity in PMCs. iCA activity measurements together with pharmacological approaches revealed an opposing contribution of iCAs and eCAs on the CCM. H^+ -selective electrodes were used to demonstrate eCA catalyzed CO_2 hydration rates at the cell surface. Knock-down of Cara7 reduced extracellular CO_2 hydration rates accompanied by impaired formation of specific skeletal segments. Finally, reduced pH_i regulatory capacities during inhibition and knock-down of Cara7 underline a role of this eCA in cellular HCO_3^- uptake.

This work revealed the function of carbonic anhydrases in the cellular CCM of a marine calcifying animal. Extracellular hydration of metabolic CO_2 by Cara7 coupled to HCO_3^- uptake mechanisms mitigates the loss of carbon and reduces the cellular proton load during the mineralization process. The findings of this work provide insights into the cellular mechanisms of an ancient biological process that is capable of utilizing CO_2 to generate a versatile construction material.

Significance Statement

Biological calcifying systems are capable of generating a versatile construction material from metabolic CO_2 . Here the transformation of CO_2 to HCO_3^- is of critical importance with very limited information about the underlying mechanisms. Carbonic anhydrases (CAs) are evolutionary ancient enzymes that catalyze the reversible hydration of CO_2 and were often associated with calcifying tissues. Using the calcifying cells of the sea urchin larva as model system, the present work uncovered a cellular carbon concentration mechanism that depends on the presence of an extracellular CA (Cara7). Molecular, cell physiological and histological evidence support this conclusion and highlight the elegance of biomineralizing systems in using carbon resources in the most sustainable manner.

Introduction

Biom mineralization is an evolutionary ancient process that is used by organisms from the five kingdoms to harden their tissues for protection and mechanical support (1). In the marine environment, the majority of organisms generate CaCO_3 minerals, including calcite and aragonite to construct their skeletons and shells. The process of calcification has profound impacts on the geology of our planet and is an integral part of the global carbon cycle by generating large amounts of CaCO_3 bound in coral reefs, chalk mountains and deep-sea sediments (2). To generate CaCO_3 , marine organisms must acquire Ca^{2+} and dissolved inorganic carbon (DIC) (i.e. CO_2 , HCO_3^- , CO_3^{2-}) that are concentrated at the site of mineral formation to promote precipitation (3–9). While calcium is usually absorbed from the environment, DIC can derive from the seawater as HCO_3^- or from the hydration of metabolic CO_2 . Marine calcifiers including corals (8), sea urchins (10) and foraminifera (11) were demonstrated to utilize substantial amounts of metabolic CO_2 to produce their shells and skeletons. In the calcifying coral *Stylophora pistillata* ^{14}C radioisotopic labeling methods demonstrated that 70-75% of the DIC, used for calcification derives from metabolic CO_2 (8, 11). Likewise 63% of DIC incorporated into the skeleton of the sea urchin larva originates from respiratory CO_2 while the remaining 37% are absorbed from the seawater (10). These studies indicated that metabolic CO_2 is the primary carbon source for the calcification process in several key marine calcifiers.

Carbonic anhydrases (CAs) are metallo-enzymes that catalyze the reversible hydration of CO_2 to form H_2CO_3 (carbonic acid) that then dissociates into HCO_3^- (bicarbonate) or CO_3^{2-} (carbonate) (12–14). The direction of this chemical equilibrium is dictated by the pH, with alkaline conditions favoring the formation of HCO_3^- and CO_3^{2-} while acidic conditions shift the equilibrium towards CO_2 . CAs occur ubiquitous in all organisms to mediate pH and CO_2 homeostasis on the cellular and organismic level (12). CAs are evolutionary ancient enzymes that comprise five different families, including α -CA, β -CA, γ -CA, δ -CA, ζ -CA and are found in the five kingdoms of life. α -CAs are the most common carbonic anhydrase family found in animals, plants and prokaryotes (12, 15) and can occur as cytosolic form, membrane bound and secreted isozymes (16, 17). Membrane bound CAs are characterized by the presence of a GPI-anchor that attaches the enzyme to the plasma-membrane (12). These extracellular and secreted forms were observed to be specifically associated with mineralizing tissues in corals (7, 18), sponges (16), mollusks (19) and sea urchins (20). Furthermore, pharmacological experiments using compounds (i.e. acetazolamide) that inhibit carbonic anhydrases, demonstrated reductions in calcification rates in sponges (21), mollusks (19, 22), corals (23, 24), coccolithophores (25) and sea urchins (6, 26–28). While these studies point towards a central role of CAs in the calcification process, their exact mechanism of promoting cellular carbon concentration remains largely hypothetical.

In the sea urchin larva, the primary mesenchyme cells (PMCs) are responsible for the generation of the larval endoskeleton. PMCs form syncytial cables that enclose the calcitic spicules (29–31). The initial phase of CaCO_3 formation happens intracellularly by the precipitation of amorphous calcium carbonate (ACC) within vesicular compartments (32). The current model denotes that Ca^{2+} is endocytosed from the seawater-like fluids of the primary body cavity (33) into vesicles, in a process that resembles micropinocytosis (34). Following a substantial concentration of calcification substrates (i.e. Ca^{2+} and CO_3^{2-}), probably by the removal of water and salts from the calcification vesicle (35), ACC is formed and exocytosed to build the calcitic endoskeleton (34, 36). While the route of Ca^{2+} uptake has been well described, the mechanisms of DIC transport remain less well understood. A previous study demonstrated that the PMC specific $\text{Na}^+/\text{HCO}_3^-$ co-transporter (NBC), Sp-Slc4a10, is critically involved in the calcification process by absorbing HCO_3^- from the primary body cavity (5). Knock-down of Sp-Slc4a10 resulted in a substantial reduction in skeleton growth, associated with decreased capacities of HCO_3^- transport into the cytosol (5). While this transporter presents a route for the uptake of DIC from the environment, mechanistic knowledge for the conversion of metabolic CO_2 by carbonic anhydrases to promote cellular carbon concentration is currently lacking.

Using the calcifying PMCs of the sea urchin larva as a model, this work aimed at revealing the physiological role of carbonic anhydrases in the cellular carbon concentration mechanism (CCM). We used a suite of molecular tools including *in situ* hybridization, expression analyses, single cell transcriptomics, gene knock-down and immunocytochemistry to identify and localize calcification relevant carbonic anhydrases in the sea urchin larva. We developed microfluorimetric and ion-selective micro-electrode protocols for the *in vivo* measurement of intra- and extracellular carbonic anhydrase activity. These *in vivo* techniques in combination with pharmacological inhibition of CAs and knock-down of *Cara7* activity revealed the differential contribution of intra- and extracellular CAs in the calcification process. The findings of this work led to a deep mechanistic understanding and a new working model for the role of carbonic anhydrases in the CCM of a marine calcifier.

Results and Discussion

Identification of intra- and extracellular carbonic anhydrases in calcifying cells

Gene mining for carbonic anhydrases (CAs) in the genomic data bases of the purple sea urchin *Strongylocentrotus purpuratus* confirmed the presence of three major carbonic anhydrase isoforms expressed in the calcifying primary mesenchyme cells (PMCs) (37, 38) including *Cara7* (LOC579101), *Cara2* (LOC577690) and *Cara14-like* (LOC591885) (table S1). Our *in situ* hybridization result and single cell transcriptomic analyses demonstrated that *Cara14-like* and *Cara2* are also expressed in other

tissues and cell types of ecto-, meso- and endodermal origin (figure 1A, table S1, figure S1). In accordance to earlier studies (37, 38) we confirm that *Cara7* is exclusively and highly expressed in PMCs of actively calcifying regions including the initial cluster of skeleton formation in the gastrula stage as well as PMCs of the scheidel and post-oral rods in the pluteus larva (figure 1B, S1, S2). *Cara7* is a downstream effector of key regulatory genes in the skeletogenic cell lineage including VEGF (39). Along the first 72 hours of development *Cara2* has highest expression levels shortly before the initial formation of the skeleton (figure 1 C) while *Cara7* has its expression peak during the period of skeleton formation (figure 1 D). This indicates that *Cara7* is likely associated with the initiation of skeletogenesis.

In silico sequence analyses suggest that *Cara2* is an intracellular carbonic anhydrase in PMCs while *Cara7* displays features of an extracellular carbonic anhydrase including a N-terminal signal sequence and a C-terminal GPI anchor (figure S3, table S1) and thereby corroborates earlier studies that identified this PMC specific CA to be an extracellular isozyme (28, 38, 40). *Cara7* also possesses the typical α -carbonic anhydrase signature sequence including a glycine-rich region and several histidines that represent the active centre (H217) and zinc ion binding sites (i.e. H244, H246 and H269) (20). Our phylogenetic analysis of carbonic anhydrases highlights the deep separation of intra- and extra-cellular alpha-CAs in metazoans (figure 1E). The sea urchin *Cara7* belongs to the clade of secreted or membrane bound extracellular CAs (eCAs) while *Cara2* clusters with cytosolic CAs (iCAs) from other animals ranging from cnidarians over molluscs to arthropods and vertebrates.

Intra- and extra-cellular carbonic anhydrases have an opposing contribution to the calcification process

In a next step, we used a pharmacological approach to address the contribution of intra- and extra-cellular CA activity to the calcification process. Normally developing larvae were exposed to different concentrations of the CA inhibitor acetazolamide (AZM) and AZM coupled to a 6 kDa dextran molecule (Dex-AZM) during the time of skeleton formation (16 hpf-64 hpf). Since AZM is a small uncharged molecule that can pass biological membranes within several seconds (41, 42), this compound targets both, intra- and extra-cellular CAs. To disentangle the role of intra- vs. extra-cellular CAs in the calcification process we used Dex-AZM that only targets extracellular CAs. The results of these experiments demonstrated no effect of AZM on skeleton formation up to a concentration of 100 μ M (Figure 2A+B; figure S4). However, using Dex-AZM we found a substantial reduction in spicule length from $247.9 \pm 0.8 \mu$ m in DMSO treated larvae down to $101.5 \pm 25.6 \mu$ m at a concentration of 100 μ M. The reduction in skeleton length in the Dex-AZM-treated larvae is largely attributed to a shorter post-oral rod that was often absent in the 100 μ M Dex-AZM treated larvae (Figure 2A+B; figure S4C).

To assure no collateral effects of the inhibitors on developmental processes in the gastrula and blastula stage we used a previously described re-calcification assay where pluteus larvae re-calcify their skeletons within two to three days (3). Re-calcification rates were slightly reduced in the presence of the CA inhibitor acetazolamide (AZM) at a concentration of 1 μM (figure 2C), but these inhibitory effects were attenuated at higher doses (10 μM and 100 μM). However, in accordance to our inhibitor experiments performed on normally developing larvae, Dex-AZM substantially reduced re-calcification rates in a dose-dependent manner from 1 to 100 μM (figure 2D), indicating that mainly eCA activity is required for the mineralization process. We explain the differential inhibitory effect of the membrane permeable AZM and membrane impermeable Dex-AZM by the following hypothesis. Low concentrations of cell permeable AZM primarily inhibit eCAs, with little amounts of the inhibitor actually reaching the cytosol. However, higher concentrations of AZM also effectively inhibit iCAs, and thereby counteract the inhibition of eCAs. These pharmacological experiments suggest an opposing role of iCAs and eCAs in the calcifying PMCs of the sea urchin larva.

The importance of eCA activity in the calcification process is further underlined by a stimulation of *Cara7* expression during re-calcification of the larval skeleton (figure 2E). Increased expression levels of *Cara7* during skeleton re-mineralization are due to a recruitment of non-mineralizing PMC along the re-calcifying spicules (figure 2F). Such an activation of PMCs from the resting to the calcification state has been previously demonstrated by increased mRNA and protein levels of other calcification-relevant ion transporters and channels in PMCs during skeleton re-calcification (3, 43). In contrast, the major iCA in PMCs, *Cara2*, did not show a pronounced expression in re-mineralizing PMCs as observed for *Cara7*, underpinning a differential contribution of intra- vs. extra-cellular CAs to the calcification process.

The hypothesis for an opposing contribution of intra- vs. extra-cellular CAs in the calcification process is further corroborated by our intra-cellular CA activity measurements. Intracellular pH recordings in combination with the CO_2 -pulse method were used to measure the intra-cellular, CA catalyzed, hydration and de-hydration speed of CO_2 (figure 3). The pH_i recovery rate after washout of the out-of-equilibrium (OOE) solution (2.5% CO_2 , pH 8.0) was decreased by AZM in a dose-dependent manner (IC_{50} 7.5 μM), reflecting the intracellular CA activity (figure 3A+B). Similar IC_{50} values using AZM were obtained for iCA activity measurements in muscle fibres (IC_{50} 10 μM) (42) and corneal endothelial cells (IC_{50} 7 μM) (44). Against our initial hypothesis that iCA activity is stimulated in re-calcifying larvae to support the increased calcification rates, we found the opposite result. The recovery rate after the CO_2 pulse was substantially decreased in re-calcifying PMCs compared to those of control larvae (figure 3C+D). Also, the share of the AZM sensitive fraction of the CO_2 de-hydration reaction was dramatically reduced reflecting a reduction in iCA activity (figure 3D). Despite this seemingly counterintuitive

observation, such a reduction in iCA activity during high mineralization rates may serve an important biological function. The extensive intracellular hydration of metabolic CO_2 to promote CaCO_3 formation generates large amounts of protons (i.e. 2 moles of H^+ per mole of CaCO_3 precipitated) that may cause a substantial proton load to the calcifying cells. Thus, it can be suggested that reductions in cytosolic CA activity may help to decrease the cellular proton load during the mineralization process. Another benefit of reducing iCA activity lies in the fact that intracellular calcifiers draw on a cytosolic HCO_3^- pool (3, 45). Here the intracellular pH of ~ 7.0 together with cytosolic CA activity may shift the equilibrium towards the formation of CO_2 and thereby causes a loss of the otherwise membrane impermeable HCO_3^- ion. Similar concepts for the opposing function of intra- and extra-cellular CAs to promote CCM were developed for photosynthetic marine algae (46–48). Depending on the species, diatoms can predominantly utilize carbon that derives from CO_2 (“ CO_2 -user”) or from HCO_3^- (“ HCO_3^- -user”). In “ HCO_3^- -users” the CO_2 leaking out of the cell is converted by eCA to HCO_3^- and subsequently taken up by HCO_3^- transporters. In contrast “ CO_2 -users” prevent extracellular conversion of CO_2 to HCO_3^- and disequilibrium in the boundary layer persists. Thus, a high $p\text{CO}_2$ in the boundary layer also increases the intracellular CO_2 partial pressure and thereby supports photosynthesis (47). Interestingly, these different modes of carbon concentration in marine algae are associated with the opposing presence of iCAs and eCAs. While “ CO_2 -users” are characterized by high iCA levels, “ HCO_3^- -users” usually have low iCA activities. In some “ HCO_3^- -users” like *Synechococcus*, iCA activity is even absent for minimizing CO_2 leakage (48). Further evidence for considering the calcifying PMCs of the sea urchin larva a “ HCO_3^- -user”-type of CCM is seen in an upregulation of the $\text{Na}^+/\text{HCO}_3^-$ cotransporter (*Sp-Slc4a10*) and *Cara7* under low HCO_3^- conditions, while the iCA *Cara2* is substantially down-regulated under reductions in environmental HCO_3^- (figure S7). Based on the findings of the present work and the existing concepts for the CCM in photosynthetic organisms, we propose that also in the calcifying cells of the sea urchin larva iCAs and eCAs act in an opposing manner with iCA activity being reduced during active mineralization to promote the cellular CCM.

The extracellular carbonic anhydrase *Cara7* promotes a carbon concentration mechanism in calcifying cells

In a next step, we used a multi-pronged approach to study the localization of the *Cara7* protein and the effect of *Cara7* genetic perturbation on skeletal development and function of the cellular CCM. Therefore, we developed a *Cara7* specific antibody that demonstrated detection of a ~ 50 kDa protein (figure 4A) that is in the predicted size range (49 kDa) for this protein. Pre-absorption of the antibody with the immunization peptide largely reduced the signal demonstrating the specificity of the antibody to its *Cara7* specific immunization peptide. To perturb the expression of *Cara7* we used two different

morpholinos targeting the 5'-untranslated region and another one designed close to the start codon of the *Cara7* gene. Western blot analyses validated the *Cara7* knock-down by demonstrating a 43% reduction in *Cara7* protein abundance in *Cara7* morphants compared to scramble MO injected larvae (figure 4B).

Knock-down of *Cara7* led to a decreased development of the post-oral rods in the pluteus larva (figure 4C). This relatively mild effect was confirmed by a second morpholino targeting the 5'-untranslated region of the *Cara7* gene (Figure S5) and suggests that *Cara7* is primarily involved in the formation of the post-oral and anterolateral rods. This finding is corroborated by immuno-histochemical analysis demonstrating that positive immuno-reactivity of the *Cara7* antibody is only found in the actively calcifying regions of the post-oral and anterolateral rods (figure 4D+E). Positive immuno-reactivity was detected in membranes of PMC cell bodies, within vesicular structures, along the syncytial cables and probably also the spicule itself. The latter is supported by proteomic analyses that demonstrated high concentration of *Cara7* occluded in the larval skeleton (49). This observation suggests that besides the outer membrane facing the extracellular matrix, *Cara7* must be additionally localized in the inner plasma membrane facing the spicule cavity. *Cara7* potentially has another physiological function in the inner membrane or could be a result of endocytosis and vesicular trafficking from the outer to the inner membrane following the route of Ca^{2+} uptake described in PMCs (34). Here it remains an important future task to understand if *Cara7* has other physiological functions in the inner membrane facing the spicule and within vesicles. The immunolocalization of *Cara7* together with our single cell transcriptomic analyses (figure S8) demonstrated a co-localization of *Cara7* with the $\text{Na}^+/\text{HCO}_3^-$ co-transporter (*SpSlc4a10*) (5) and the proton channel *otop2l* (43) in the same population of PMCs. Together, our results indicate that the *Cara7* protein is localized in PMCs and spicule compartment at the edges of the post-oral and anterolateral rods and its activity is essential for the elongation of these rods.

To address the function of *Cara7* we specifically developed an *in vivo* method using pH micro-electrodes to measure eCA activity at the surface of PMCs. The concept for this method is based on an earlier study that used CO_2 out-of-equilibrium (OOE) solutions in combination with a stop-flow protocol to measure CA activity during lysis of red-blood cells (50). We successfully modified this protocol to measure the CO_2 hydration kinetics during the relaxation of the OOE solution at the surface of PMCs (figure 5A+B). Using this method, we determined the CO_2 hydration rate at the surface of PMCs that was reduced in the presence of AZM (figure 5C-E) and in *Cara7* knock-down larvae (figure 5F-H). In addition, no differences in the hydration rate constant ($k\Delta[\text{H}^+]$) were measured between *Cara7* morphants exposed to 100 μM AZM or 100 μM DMSO (figure S10). These results demonstrated

that Cara7 is responsible for eCA activity at the outer cell surface of PMCs associated with reductions in the formation of specific skeleton segments where this enzyme is highly expressed.

Based on these observations we propose that Cara7 mediated eCA activity in PMCs may serve as cellular CCM by generating HCO_3^- from metabolic CO_2 at the cell surface that is re-absorbed by HCO_3^- transport mechanisms. In previous studies the $\text{Na}^+/\text{HCO}_3^-$ co-transporter (NBC; *Sp-Slc4a10*) has been demonstrated to control the transport of HCO_3^- into PMCs (3, 5). This essential role of HCO_3^- transport in the calcification process is underlined by our low HCO_3^- experiments that dramatically reduced skeleton growth by 75% in the absence of HCO_3^- (figure S11). Such reductions in environmental HCO_3^- not only reduce a part of the carbon source used for calcification but also impair the function of HCO_3^- transporters (51).

To test the concept for the involvement of Cara7 in cellular carbon concentration we performed pH_i recordings in combination with the ammonia pre-pulse method to determine pH_i regulatory capacities of PMCs. Previous studies demonstrated that primary and secondary active pH_i regulatory capacities in PMCs largely reflect HCO_3^- uptake (5, 52) and to a lesser extent H^+ export (3). Active pH_i regulatory capacities of PMC were decreased by ~50% during pharmacological inhibition of eCAs (figure 6A+B) or by *Cara7* knock-down (figure 6C+D). In these studies pH_i regulatory capacities decreased by 65% to 70% during pharmacological inhibition of HCO_3^- transporters or by knock-down of the $\text{Na}^+/\text{HCO}_3^-$ co-transporter (*SpSlc4a10*) (5, 33). The present work further demonstrated that in the absence of external HCO_3^- , addition of Dex-AZM further decreased pH_i regulatory capacities (figure 6E+F), indicating that metabolic CO_2 must be an additional source for cellular HCO_3^- uptake. These results provide strong evidence that Cara7 contributes to the cellular CCM by generating HCO_3^- in the cellular boundary layer from metabolic CO_2 , which is then re-absorbed by HCO_3^- transporters (summarized in figure 6G). Similar mechanisms for the concentration of carbon have been described in photosynthetic systems of micro algae (47, 53, 54). These photosynthetic systems mitigate the loss of carbon from the cell by recycling CO_2 in the boundary layer using an extracellular carbonic anhydrase and HCO_3^- transport systems (47). This interaction of CO_2 hydration by eCA and HCO_3^- transporters would be most efficient when these proteins are localized in close vicinity acting as a metabolon. Such a HCO_3^- transport metabolon has been described in red blood cells and cancer cells where HCO_3^- transporters physically bind to iCAs and eCAs to promote gas transport and intracellular acid-base homeostasis, respectively (55, 56). In the sea urchin larva this extracellular conversion of CO_2 has several advantages with respect to carbon concentration and intracellular acid-base balance. On one hand, this mechanism allows to re-capture metabolic CO_2 that diffused out of the cell and feeds this otherwise “lost” carbon back into the cellular carbon pool. On the other hand, extracellular hydration of CO_2 and subsequent uptake of the generated HCO_3^- ion leaves one mole of protons per mole of hydrated CO_2 in the extracellular space

and thereby substantially reduces the net intracellular proton load during calcification. A further benefit of this CCM lies in the fact that the extracellular pH (pH_e 8.1) is more alkaline than the intracellular conditions (pH_i 7.0) and thereby substantially favors the formation of HCO_3^- in concert with eCA activity. In this way eCA activity in calcifying cells plays an important role in optimizing the CCM by mitigating the loss of carbon and by reducing the intracellular acid load during calcification.

Conclusion

Calcifying organisms evolved sophisticated mechanisms to generate Ca^{2+} minerals for the construction of protective and stabilizing shells and skeletons. Many of these calcifying systems were demonstrated to use metabolic CO_2 as a major carbon source (8, 10, 11), with carbonic anhydrases playing a central role in this process. The present work revealed the role of eCAs underlying a cellular carbon concentration mechanism and acid-base balance in calcifying cells of a marine animal. Given the deep evolutionary origin of eCAs and their strong association with calcifying systems (7, 16, 18–20) the results of the present work have strong implications for understanding the role of CAs in other calcifying organisms.

Moreover, this work also contributes to a more differentiated view on how changes in oceanic carbonate chemistry affect calcifying systems in past and future oceans. On one hand, reductions in seawater pH also reduce the pH of the primary body cavity (33) and thereby making extracellular hydration of CO_2 by *Cara7* less effective. Gene expression analyses from the present work (figure S7) and earlier studies (57) demonstrated a stimulation of the PMC-specific *Cara7* and HCO_3^- transporter (*Sp-Slc4a10*) under hypercapnic conditions. These observations suggest a compensatory mechanism in place, that however is associated with increased energetic demands that were reported for sea urchin larvae raised under elevated $p\text{CO}_2$ conditions (52, 58). On the other hand, calcifying systems that largely utilize CO_2 as a carbon source may benefit from increases in environmental $p\text{CO}_2$ similar to the situation in photosynthetic organisms. However, the reduction in carbonate saturation states along with increases in seawater $[\text{H}^+]$ may outweigh the positive effects of ocean acidification on the calcification process. In fact, changes in proton gradients across the plasma membrane of calcifying cells were demonstrated to be the dominating factor leading to reductions in calcification rates of several marine animals and microalgae (43, 59, 60). In this way, a better mechanistic understanding underlying calcification in marine organisms may help to formulate unifying principles that explain and predict sensitivities of marine calcifiers to past and future oceanic conditions (61).

Finally, the present study unraveled the mechanisms by which carbonic anhydrases promote cellular carbon concentration for the generation of a versatile construction material from CO_2 . At the rising

anthropogenic CO₂ emissions to fuel our life on this planet, this work highlights the elegance of biological systems in utilizing carbon resources in the most sustainable manner.

Material and Methods

Larval Cultures

Adult purple sea urchins (*Strongylocentrotus purpuratus*) were collected from the coast of California (Ja Jolla, USA), and shipped to the Helmholtz Centre for Ocean Research Kiel (GEOMAR). The animals were maintained in a re-circulating natural seawater system at 12°C, a salinity of 32 and regular water changes were made three times a week. Animals were fed with *Laminaria sp.* three times a week. Spawning of males and females was induced by shaking and larval cultures were maintained at a concentration of 25,000 larvae/L at 15°C with continuous aeration as previously described (62).

Whole mount in situ hybridization

Whole mount *in situ* hybridization was essentially performed according to the protocol described by Walton (63) with some minor modifications. Briefly, larvae were fixed with 4% PFA/FSW and dehydrated with MeOH and stored at -20°C. Larvae were re-hydrated in an ascending series of MeOH and DEPC-PBST, and fully washed with DEPC-PBST in the final step. Pre-hybridization was performed for at least 1 h at 60°C. Primers for generating and cloning of the probes are listed in table S4. Digoxigenin-labeled probes (500 – 1,000 ng/mL) were pre-warmed at 70°C and hybridization was performed at 55°C overnight. Samples were washed with hybridization buffer, wash buffer (50% Formamide, 5x SSC, 0.1% Tween-20) and 2x SSC at 55°C followed by another washing step with 2x SSC at 37°C and by MABT (500 mM Maleic acid, 750 mM NaCl, NaOH, pH 7.5, 0.1% Tween-20) at RT. Samples were washed with MABT for 2 h and transferred to a blocking solution (1x MAB, 2% Block reagent (Roche), 10% sheep serum (Jackson IR), 0.1% Tween-20) for 2 h. Samples were incubated overnight with 1:2,000 sheep anti-Digoxigenin-AP Fab fragments (Roche) antibody at 4°C followed by intensive washing with MABT at the next day. The color reaction was performed with BM Purple AP (Roche) according to manufacturer's instructions for about 3 – 28 h.

Re-calcification assay and determination of calcification rates under pharmacological inhibition of CAs

The re-calcification assay was performed as previously described (3) and allows a specific examination of pharmacological effects on the calcification process independent from collateral effects on developmental processes. Briefly, larvae (3 dpf) were exposed to 0.03 M MES buffered FSW adjusted to pH 6.0 for 12 to 15 h to fully dissolve their calcitic spicules. To re-calcify their skeletons, larvae were transferred back into filtered seawater (FSW) (pH 8.0). This transfer day is defined as day 0 (0D), while the following days are defined as 1D, 2D and 3D throughout this manuscript. This re-calcification assay was used to test the effects of intra- and extra-cellular carbonic anhydrase inhibition on the calcification process. Acetazolamide (AZM; Sigma-Aldrich, Germany) and 6 kDa dextran-bound Acetazolamide (Dex-AZM; Ramidus, Sweden) were used, which are specific inhibitors for carbonic anhydrases (CAs) (18). While AZM has been demonstrated to be membrane permeable (41, 42) the Dex-AZM cannot pass biological membranes (45) and thereby only targets extracellular CAs. After dissolution of the skeleton by the low pH treatment larvae were transferred to 6-well-plates filled with 10 mL FSW containing only 0.1% DMSO, 1 μ M, 10 μ M and 100 μ M of AZM or dextran-bound AZM, respectively. Each well contained 200 larvae and three experimental replicates were performed for each inhibitor concentration with 24 wells in total (two inhibitors, four concentrations and three replicates). From the start of the experiment (0D), 20-50 larvae were sampled every day along the period of three days (1D, 2D, 3D). Larvae were fixed with 4% PFA/FSW (pH 8.2) and the growth rate of the skeleton was determined by measuring the daily increase in body rod + post-oral rod length. Pictures were taken by a Zeiss Observer A1 inverted microscope and images were analyzed using the Zeiss Zen 3.3 (blue edition) software. A second set of experiments exposed normally developing larvae from 16 hpf up to 64 hpf to AZM and Dex-AZM using the same concentrations as mentioned above. Three independent replicates (n=3) were performed and from each replicate 20-70 larvae were used for biometric analyses. Biometric analyses of the skeleton were made by measuring the length of the total spicule (body rod+ post-oral rod) as well as only the length of the post-oral rod.

Phylogenetic analysis and molecular cloning

The amino acid sequences for phylogenetic analysis were collected from EchinoBase (www.echinobase.org) (64), the Ensembl (<http://www.ensembl.org/>), Reefgenomics (<http://reefgenomics.org>) databases and aligned and compared with the sequenced sequences from the sea urchin larvae via the online tool MAFFT (**M**ultiple **A**lignment using **F**ast **F**ourier **T**ransform) (www.ebi.ac.uk/Tools/msa/mafft/). The sequences were scanned for motives and functional groups with (myhits.sib.swiss/cgi-bin/motif_scan), (https://mendel.imp.ac.at/gpi/gpi_server.html) and

(gpcr.biocomp.unibo.it/predgpi/pred.htm). For the phylogenetic tree Cara7 (XP_003726289.2) and Cara2 (XP_782997.3) sequences were blasted to NCBI (<https://blast.ncbi.nlm.nih.gov/Blast.cgi>) and Reefgenomics databases, and homologous sequences with E-values higher than $9e^{-41}$ ($9e^{-75}$ for iCA and $9e^{-41}$ for eCA) were excluded for the following analysis. Selected sequences were aligned via the MUSCLE program and further trimmed by Gblocks Server (http://molevol.cmima.csic.es/castresana/Gblocks_server.html), and the 140 a.a. trimmed sequences were used for the phylogenetic analysis. The Maximum Likelihood tree was generated by MegaX (65) with the best fit model LG+G+I and 500 bootstrap replicates.

The primers for cloning and *in situ* probe synthesis (table S4) were designed with Primerblast (www.ncbi.nlm.nih.gov/tools/primer-blast/) and re-blasted with (blast.ncbi.nlm.nih.gov/Blast.cgi). The transcript sequences of the sea urchin larvae genes *SPU_012518* (*LOC579101*), *SPU_008685* (*LOC577690*) were amplified via PCR. The amplified sequences were cloned into pGEM-T easy cloning vector (Promega) and cultured in NEB 5 α competent *E. coli* cells. Plasmid extraction, sequencing (GENEWIZ) was followed by the synthesis of the RNA probes for *in situ* hybridization using M₁₃-F and M₁₃-R primers and the DIG RNA labeling Mix (Roche).

RT-qPCR and Single cell transcriptomic analyses

RT-qPCR was performed as previously described (5). Briefly, RNA from control and re-calcifying larvae at 0D, 1D, 2D and 3D from three experimental replicates was isolated by using the Direct-zol RNA MicroPrep kit (Zymo Research). RNA samples were reverse transcribed by Super Script IV cDNA synthesis kit (Invitrogen, Waltham, USA) for quantitative RT-PCR. To measure the expression levels of the target genes the 7500 Fast Real-Time PCR System (Applied Biosystems) was used and expression levels of target genes were normalized to the housekeeping gene EIF1a that has been demonstrated to be stable along ontogeny and during skeleton re-calcification (3, 43). qPCR primers used in this study are listed in table 1. Single cell transcriptomic analyses were carried out as previously described (43).

Morpholino injection

Micro-injection was performed as previously described (5). Two gene-specific morpholino-substituted antisense oligonucleotides (MO) (5'-AAAATATATGCATTCATGTTGATCA-3') complementary to the start codon region of the sea urchin *Cara7* gene and a second MO (5'-CGACCTCAGATATATTCTCACAAA-3') complementary to the 5' untranslated region were obtained from Gene Tools (Oregon). In addition, a scramble MO 5'-CCTTTACCTCAGTTACAATTTATA-3' that has no biological target in the sea urchin was

used to obtain the control groups. The MOs were dissolved in injection Buffer (20 mM Hepes, 120 mM KCl, 24% Glycerol, pH 8.0) and were injected into the freshly fertilized egg (one-cell stage) using a micro-injection system (Picospritzer III, Parker) mounted on an inverse microscope (Zeiss Observer D1) equipped with a cooling stage.

In vivo determination of intracellular CA activity and pH_i regulatory capacities in PMCs

Measurements of intracellular pH (pH_i) of PMCs using the pH-sensitive dye BCECF-AM was essentially performed as previously described (5, 33, 43). Briefly, after removal of the ectoderm by the bag isolation method and incubation with 50 μ M BCECF-AM for 30-45 minutes, larvae were immobilized on 1% Protamine sulfate coated coverslips that were attached to the bottom of a perfusion chamber. The fluorescence was monitored on an inverted microscope (Zeiss, Observer A1) equipped with an appropriate light source and the imaging software (Visitron). From each larva (3-4 dpf), six to eight PMCs in the rod tips were recorded and treated as one replicate ($n = 1$). A minimum of six larvae were measured for every inhibitor concentration in an alternating mode. To translate ratios to actual pH_i values we performed a Nigericin calibration as previously described (33). Along the entire duration of the experiment larvae were exposed to FSW pH 8.0 either containing 0.1% DMSO as control or the respective Acetazolamide (AZM) concentration (1 μ M, 10 μ M, 100 μ M and 1 mM). The CO₂ pulse using CO₂ out-of-equilibrium OOE solutions (for details see (3)) was performed for 5 min before switching back to FSW containing the respective AZM concentration. All solutions were delivered to the perfusion chamber at a flow rate of 2 mL/min and at 15 °C by a Perfusor with 50 mL Perfusor syringes (B.Braun, Melsungen, Germany). The recovery rate after removal of the OOE solution in the presence of AZM was used to characterize the catalytic activity of intracellular CAs.

The ammonium pre-pulse method was used to quantify pH_i regulatory capacities of PMCs and performed as previously described (5). Briefly, during pH_i recordings using BCECF-AM PMCs were exposed to FSW containing 20 mM NH₃/NH₄⁺ followed by a washout using FSW containing either DMSO or 100 μ M dextran-bound AZM (for inhibition of the extracellular CA). These solutions were applied to the larvae at a flowrate of 6-8 mL/min through a water jacket cooling system set to 15°C. The recovery rate from the ammonia pre-pulse induced acidosis was used to characterize the effects of extracellular CA inhibition and Cara7 knock-down on pH_i regulatory capacities.

Cell surface CA activity determinations using proton selective micro-electrodes

H⁺ selective micro-electrodes were used for the *in vivo* measurement of extracellular CA activity in PMCs. The construction of H⁺ selective micro-electrodes has been previously described (5, 33, 62). Briefly, borosilicate glass capillaries were pulled on a DMZ-Universal puller (Zeiss Instruments) into micropipettes with tip diameters of 1–2 μm. These were vapor-silanized with dimethyl chlorosilane (Sigma-Aldrich) and front-loaded with a 200 μm column of liquid ion exchanger mixture (H⁺ ionophore III; Sigma-Aldrich). The micropipette was backfilled with an electrolyte solution (300 mM KCl, 50 mM NaPO₄, pH 7.0) to create an ion selective micro-electrode. The micro-electrode was connected to a FD223a dual channel differential electrometer (WPI) and the potential was measured against an Ag/AgCl electrode connected by a 3 M KCl agar bridge to the perfusion solution. Calibration was performed by placing the electrodes into different pH solutions and plotting the measured voltage against the respective pH. All electrodes used had a Nernstian slope > 52 mV for 1 pH unit.

To measure extracellular CA activity, we performed a stopped-flow assay using out-of-equilibrium (OOE) solutions (2.5% CO₂/pH 8.0) following a modified protocol for the *in vitro* measurement of carbonic anhydrase activity (50). This OOE state is generated in the moment of mixing of a high CO₂ (5% CO₂ pH 6.2) and a Tris buffered low CO₂ solution (0.04% CO₂ pH 8.0) (66). When the flow (mixing) is stopped, the solution will acidify due to the relaxation towards the formation of HCO₃⁻ and H⁺. This rate of change in [H⁺] representing the CO₂ hydration speed is detected by our pH sensitive micro-electrodes. After bag isolation (see above for methodology), 2 dpf larvae were immobilized on 1% Protamine sulfate coated cover slides and glued to a perfusion chamber using silicon grease. The chamber was mounted on an inverted microscope (Zeiss VisiTronSystem Observer D1) and perfused at a rate of 5 mL min⁻¹ using an OOE solution that was generated by mixing artificial seawater (for ASW composition see (43)) containing 2 mM Tris adjusted to pH 8.0 and ASW equilibrated with 5.0% CO₂. The solutions were maintained at 15°C by a water jacked cooling system. The pH micro-electrode was placed at the surface of a PMC using a motorized micromanipulator (Patch Star, Scientifica) under visual control at a 40 X 10 magnification. When stable recordings of PMC surface pH were obtained the flow was stopped, leading to a relaxation of the OOE solution within the perfusion chamber towards the formation of HCO₃⁻ and H⁺. The reaction followed a non-linear saturation curve and the speed of this reaction is depending on CA activity. We fitted the [H⁺] change as a function of time by the equation: $[H^+](t) = A + B(1 - e^{-K_{\Delta[H^+]t}})$ where t is time, A is the [H⁺] value after full equilibration, B is the [H⁺] range and $K_{\Delta[H^+]}$ is the rate constant of the [H⁺] relaxation. We obtained A , B , and $K_{\Delta[H^+]}$ using the curve fitting analysis of Sigma Plot 13.0. [H⁺] recordings in combination with the stopped-flow method were performed in the extracellular matrix ca. 50 μm away from the PMC cell (background) or with the electrode touching the PMC surface. To inhibit CAs, AZM was added at a concentration of

200 μM to the Tris-buffered ASW solution leading to a final concentration of 100 μM in the perfusion chamber. Since iCA activity has no effect on the detection of eCA activity by this method (that is restricted to detect eCA activity at the cell surface) we used AZM to pharmacologically demonstrate CA activity at the outer surface of PMCs. In addition, extracellular CA activity measurements were carried out in scramble and *Cara7* morpholino injected larvae.

Immunofluorescence (IF) staining and western blot (WB) analysis of the sea urchin Cara7 protein

IF and WB analysis was performed as previously described (5). Briefly, for IF larvae were fixed with 4% PFA/FWS for 10 min, washed with PBS and blocked with PBS containing 5% bovine serum albumin (BSA) for at least 1 h at RT. Afterwards the larvae were incubated overnight at 4°C with the affinity purified polyclonal antibody (dilution 1:250) raised against the sea urchin *Cara7*-specific synthetic peptide (**NH2-CGQNAVGNQHPQWSN-CONH2**) (Pineda, Berlin, Germany). After intensive washing with PBS larvae were incubated with the secondary antibody, a fluorophore-conjugated Alexafluor 488 anti-rabbit IgG (Invitrogen) at a dilution of 1:300, for 1 h at RT in the dark. After washing with PBS larvae were mounted on glass slides and pictures were taken on a confocal microscope equipped with an Airyscan function (LSM800/P2, Zeiss) and analyzed with Zen 3.3 blue edition.

For WB, at least 200-300 larvae were collected, and extracted by direct mixing with 1:10 (w/vol) 1x Lämmli loading buffer. Samples were incubated at 95°C for 5 min and proteins were fractionated by SDS PAGE on a 10% polyacrylamide gel and blotted to a PVDF membrane (Bio-Rad), using a tank blotting system (Bio-Rad). Blots were blocked for at least 1 h at RT with PBS-Tween buffer containing 5% bovine serum albumin (BSA). Afterwards the blots were incubated in a 1:10,000 dilution of the primary antibody at 4°C overnight. After intensive washing with PBS-T buffer the blots were incubated for 1 h at RT with the secondary antibody a peroxidase-conjugated goat anti-rabbit IgG (Dianova, Hamburg, Germany) at a 1:40,000 dilution. After washing with PBS-T buffer the protein signals were detected with the ECL Select Western Blotting Detection Reagents (GE Healthcare, Munich, Germany) and photographed with a Gel Doc 2000 system equipped with a CCD camera (Bio-Rad) and evaluated with ImageLab. For the peptide compensation assay the primary antibody was pre-incubated with the immunization peptide at a concentration 0.04 mg/mL over night at 4°C. Finally, western blot analysis was used to validate our *Cara7* knock-down. Approximately 300 larvae of *Cara7* or scramble MO injected larvae were collected and used for WB analysis as described above. The *Cara7* protein abundance was normalized to total protein concentrations determined by subsequent Coomassie staining of the membrane. The blot was washed three times with H₂O and stained for ~ 1 h with 0.1%

Coomassie in 40% MeOH and 7% acetic acid. Afterwards the membrane was de-stained with 50% MeOH and 7% acetic acid for ~ 1 h, washed with water, air dried and pictures were taken.

Statistical analyses

Our data was tested for variance homogeneity (Levene-test) and were analyzed for significance using GraphPad Prism6. Intracellular CA measurements with the CO₂ pulse method, morpholino injection validation and ammonia pre-pulse measurement were analyzed using the student's t-test (two-sided) with p-value < 0.05 and < 0.001. Re-calcification experiments, extracellular CA activity measurement, morphometric analyses of Cara7 knock-down and qPCR results were analyzed for significance using one-way ANOVA, followed by Post-Hoc tests.

Acknowledgements

M.Y.H. was funded by the Emmy Noether Program (403529967) of the German Research Foundation (DFG). We would like to thank M. Stumpp for the fruitful discussions on this work and D. Garfield and J. Brandenburg for provision of the single cell transcriptome database. We further thank F. Thoben and R. Lingg for the maintenance of the sea urchin culture systems and two anonymous reviewers for their constructive comments on this work.

References

1. K. M. Towe, Overview of Biomineralization. *Paleobiology* 16, 521–526 (1990).
2. P. Van Cappellen, Biomineralization and Global Biogeochemical Cycles. *Rev. Mineral. Geochemistry* 54, 357–381 (2003).
3. M. Y. Hu, I. Petersen, W. W. Chang, C. Blurton, M. Stumpp, Cellular bicarbonate accumulation and vesicular proton transport promote calcification in the sea urchin larva: Mechanism of skeleton calcification. *Proc. R. Soc. B Biol. Sci.* 287 (2020).
4. G. L. Decker, W. J. Lennarz, Skeletogenesis in the sea urchin embryo. *Development* 103, 231–247 (1988).
5. M. Y. Hu, *et al.*, A SLC4 family bicarbonate transporter is critical for intracellular pH regulation and biomineralization in sea urchin embryos. *Elife* 7, 1–17 (2018).
6. G. Benson, C. & Chow, Carbonic anhydrase activity in developing sea urchin embryos. *Exp. Cell Res.* 124 (1979).
7. A. Moya, *et al.*, Carbonic anhydrase in the scleractinian coral *Stylophora pistillata*: Characterization, localization, and role in biomineralization. *J. Biol. Chem.* 283, 25475–25484 (2008).

8. P. Furla, I. Galgani, I. Durand, D. Allemand, Sources and mechanisms of inorganic carbon transport for coral calcification and photosynthesis. *J. Exp. Biol.* 203, 3445–3457 (2000).
9. S. Bentov, C. Brownlee, J. Erez, The role of seawater endocytosis in the biomineralization process in calcareous foraminifera. *Proc. Natl. Acad. Sci. U. S. A.* 106, 21500–21504 (2009).
10. C. S. Sikes, K. Okazaki, R. D. Fink, Respiratory CO₂ and the supply of inorganic carbon for calcification of sea urchin embryos. *Comp. Biochem. Physiol. -- Part A Physiol.* 70, 285–291 (1981).
11. J. Erez, Vital Effect on stable-isotope composition seen in Foraminifera and coral skeletons. *Nature* 273, 199–202 (1978).
12. C. T. Supuran, Carbonic anhydrases: An overview. *Carbon. Anhydrases Biochem. Pharmacol. an Evergr. Pharm. Target*, 3–16 (2008).
13. S. Lindskog, Structure and mechanism of Carbonic Anhydrase. *Pharmacol. Ther.* 74, 1–20 (1997).
14. M. A. Rahman, T. Oomori, The role of carbonic anhydrase enzyme in the biocalcification process of coral and its resilience to global climate change. *Ocean. IEEE Sydney, Ocean. 2010*, 1–5 (2010).
15. B. C. Tripp, K. Smith, J. G. Ferry, Carbonic Anhydrase: New Insights for an Ancient Enzyme. *J. Biol. Chem.* 276, 48615–48618 (2001).
16. D. J. Jackson, L. Macis, J. Reitner, B. M. Degnan, Sponge Paleogenomics Reveals an Ancient Role for Carbonic Anhydrase in Skeletogenesis. *Science*. 1054, 1893–1895 (2007).
17. W. S. Sly, P. Y. Hu, Human carbonic anhydrases and carbonic anhydrase deficiencies. *Annu. Rev. Biochem.* 64, 375–401 (1995).
18. A. Bertucci, *et al.*, Carbonic anhydrases in anthozoan corals - A review. *Bioorganic Med. Chem.* 21, 1437–1450 (2013).
19. N. Le Roy, D. J. Jackson, B. Marie, P. Ramos-Silva, F. Marin, Carbonic anhydrase and metazoan biocalcification: A focus on molluscs. *Key Eng. Mater.* 672, 151–157 (2015).
20. K. Karakostis, C. Costa, F. Zito, F. Brümmer, V. Matranga, Characterization of an Alpha Type Carbonic Anhydrase from *Paracentrotus lividus* Sea Urchin Embryos. *Mar. Biotechnol.* 18, 384–395 (2016).
21. W. C. Jones, P. W. Ledger, The effect of diamox and various concentrations of calcium on spicule secretion in the calcareous sponge *Sycon ciliatum*. *Comp. Biochem. Physiol. -- Part A Physiol.* 84, 149–158 (1986).
22. M. R. Sharker, *et al.*, Molecular Characterization of Carbonic Anhydrase II (CA II) and Its Potential Involvement in Regulating Shell Formation in the Pacific Abalone, *Haliotis discus hannai*. *Front. Mol. Biosci.* 8, 1–11 (2021).
23. J. M. Lucas, L. W. Knapp, A physiological evaluation of carbon sources for calcification in the octocoral *Leptogorgia virgulata* (Lamarck). *J. Exp. Biol.* 200, 2653–2662 (1997).
24. L. F. de Barros Marangoni, *et al.*, Effects of CO₂-driven acidification of seawater on the calcification process in the calcareous hydrozoan *Millepora alcicornis* (Linnaeus, 1758). *Coral Reefs* 36, 1133–1141 (2017).
25. H. Zhang, *et al.*, An isotope label method for empirical detection of carbonic anhydrase in the calcification pathway of the coccolithophore *Emiliania huxleyi*. *Geochim. Cosmochim. Acta* 292, 78–93 (2020).

26. A. C. Love, M. E. Andrews, R. A. Raff, Gene expression patterns in a novel animal appendage: The sea urchin pluteus arm. *Evol. Dev.* 9, 51–68 (2007).
27. K. Mitsunaga, *et al.*, Carbonic anhydrase activity in developing sea urchin embryos with special reference to calcification of spicules. *Cell Differ.* 18, 257–262 (1986).
28. Z. Sun, C. A. Etensohn, Signal-dependent regulation of the sea urchin skeletogenic gene regulatory network. *Gene Expr. Patterns* 16, 93–103 (2014).
29. K. Okazaki, Skeleton Formation of Sea Urchin Larvae. *Embryologia (Nagoya)*. 7, 21–38 (1960).
30. K. Okazaki, Spicule formation by isolated micromeres of the sea urchin embryo. *Integr. Comp. Biol.* 15, 567–581 (1975).
31. F. H. Wilt, Biomineralization of the spicules of sea urchin embryos. *Zoolog. Sci.* 19, 253–261 (2002).
32. E. Beniash, L. Addadi, S. Weiner, Cellular control over spicule formation in sea urchin embryos: A structural approach. *J. Struct. Biol.* 125, 50–62 (1999).
33. M. Stumpp, *et al.*, Acidified seawater impacts sea urchin larvae pH regulatory systems relevant for calcification. *Proc. Natl. Acad. Sci. U. S. A.* 109, 18192–18197 (2012).
34. N. Vidavsky, *et al.*, Calcium transport into the cells of the sea urchin larva in relation to spicule formation. *Proc. Natl. Acad. Sci. U. S. A.* 113, 12637–12642 (2016).
35. K. Kahil, *et al.*, Cellular pathways of calcium transport and concentration toward mineral formation in sea urchin larvae. *Proc. Natl. Acad. Sci. U. S. A.* 117, 30957–30965 (2020).
36. M. R. Winter Id, M. Morgulis, T. Gildor, A. R. Cohen Id, S. Ben-Tabou De-Leonid, Calcium-vesicles perform active diffusion in the sea urchin embryo during larval biomineralization. *PLoS Comput. Biol.* (2021) <https://doi.org/10.1371/journal.pcbi.1008780>.
37. K. Rafiq, *et al.*, Genome-wide analysis of the skeletogenic gene regulatory network of sea urchins (Development, (2014), 141, (950-961), 10.1242/dev.105585). *Dev.* 141, 2542 (2014).
38. B. T. Livingston, *et al.*, A genome-wide analysis of biomineralization-related proteins in the sea urchin *Strongylocentrotus purpuratus*. *Dev. Biol.* 300, 335–348 (2006).
39. M. Morgulis, *et al.*, Possible cooption of a VEGF-driven tubulogenesis program for biomineralization in echinoderms. *Proc. Natl. Acad. Sci. U. S. A.* 116, 12353–12362 (2019).
40. B. Eisenhaber, P. Bork, F. Eisenhaber, Prediction of potential GPI-modification sites in proprotein sequences. *J. Mol. Biol.* 292, 741–758 (1999).
41. E. A. Newman, A Physiological Measure of Carbonic Anhydrase in Müller Cells. *Glia* 11, 291–299 (1994).
42. J. Saarikoski, K. Kaila, Simultaneous measurement of intracellular and extracellular carbonic anhydrase activity in intact muscle fibres. *Pflügers Arch. Eur. J. Physiol.* 421, 357–363 (1992).
43. W. W. Chang, *et al.*, An otopetrin family proton channel promotes cellular acid efflux critical for biomineralization in a marine calcifier. *Proc. Natl. Acad. Sci. U. S. A.* 118, e2101378118 (2021).
44. J. A. Bonanno, S. P. Srinivas, M. Brown, Effect of acetazolamide on intracellular pH and bicarbonate transport in bovine corneal endothelium. *Exp. Eye Res.* 60, 425–434 (1995).
45. C. Brownlee, G. L. Wheeler, A. R. Taylor, Coccolithophore biomineralization: New questions, new answers. *Semin. Cell Dev. Biol.* 46, 11–16 (2015).

46. S. Thoms, M. Pahlow, D. A. Wolf-Gladrow, Model of the carbon concentrating mechanism in chloroplasts of eukaryotic algae. *J. Theor. Biol.* 208, 295–313 (2001).
47. S. Trimborn, *et al.*, Inorganic carbon acquisition in potentially toxic and non-toxic diatoms: The effect of pH-induced changes in seawater carbonate chemistry. *Physiol. Plant.* 133, 92–105 (2008).
48. G. D. Price, M. R. Badger, Expression of Human Carbonic Anhydrase in the Cyanobacterium *Synechococcus* PCC7942 Creates a High CO₂-Requiring Phenotype. *Plant Physiol.* 91, 505–513 (1989).
49. K. Mann, F. H. Wilt, A. J. Poustka, Proteomic analysis of sea urchin (*Strongylocentrotus purpuratus*) spicule matrix. *Proteome Sci.* 8, 1–12 (2010).
50. P. Zhao, R. R. Geyer, W. F. Boron, A novel stopped-flow assay for quantitating carbonic-anhydrase activity and assessing red-blood-cell hemolysis. *Front. Physiol.* 8, 1–15 (2017).
51. M. F. Romero, A. P. Chen, M. D. Parker, W. F. Boron, The SLC4 family of bicarbonate (HCO₃⁻) transporters. *Mol. Aspects Med.* 34, 159–182 (2013).
52. M. Stumpp, J. Wren, F. Melzner, M. C. Thorndyke, S. T. Dupont, CO₂ induced seawater acidification impacts sea urchin larval development I: Elevated metabolic rates decrease scope for growth and induce developmental delay. *Comp. Biochem. Physiol. Part A Mol. Integr. Physiol.* 160, 331–340 (2011).
53. N. A. Nimer, Q. Guan, M. J. Merrett, Extra- and intra-cellular carbonic anhydrase in relation to culture age in a high-calcifying strain of *Emiliana huxleyi* Lohmann. *New Phytol.* 126, 601–607 (1994).
54. N. A. Nimer, C. Brownlee, M. J. Merrett, Extracellular carbonic anhydrase facilitates carbon dioxide extracellular carbonic availability for photosynthesis in the marine dinoflagellate *prorocentrum micans*. *Plant Physiol.* 120, 105–111 (1999).
55. D. Sterling, R. A. F. Reithmeier, J. R. Casey, A transport metabolon: Functional interaction of carbonic anhydrase II and chloride/bicarbonate exchangers. *J. Biol. Chem.* 276, 47886–47894 (2001).
56. H. M. Becker, Carbonic anhydrase IX and acid transport in cancer. *Br. J. Cancer* 122, 157–167 (2020).
57. A. E. Todgham, G. E. Hofmann, Transcriptomic response of sea urchin larvae *Strongylocentrotus purpuratus* to CO₂-driven seawater acidification. *J. Exp. Biol.* 212, 2579–2594 (2009).
58. T. C. F. Pan, S. L. Applebaum, D. T. Manahan, Experimental ocean acidification alters the allocation of metabolic energy. *Proc. Natl. Acad. Sci. U. S. A.* 112, 4696–4701 (2015).
59. A. R. Taylor, A. Chrachri, G. Wheeler, H. Goddard, C. Brownlee, A voltage-gated H⁺ channel underlying pH homeostasis in calcifying Coccolithophores. *PLoS Biol.* 9, 1–14 (2011).
60. L. T. Bach, U. Riebesell, K. G. Schulz, Distinguishing between the effects of ocean acidification and ocean carbonation in the coccolithophore *Emiliana huxleyi*. *Limnol. Oceanogr.* 56, 2040–2050 (2011).
61. A. H. Knoll, Biomineralization and Evolutionary History. *Rev. Mineral. Geochemistry* 54, 329–356 (2003).
62. I. Petersen, W. W. J. Chang, M. Y. Hu, Na⁺/H⁺exchangers differentially contribute to midgut fluid sodium and proton concentration in the sea urchin larva. *J. Exp. Biol.* 224 (2021).
63. K. D. Walton, J. C. Croce, T. D. Glenn, S. Y. Wu, D. R. McClay, Genomics and expression profiles of the Hedgehog and Notch signaling pathways in sea urchin development. *Dev. Biol.* 300, 153–164 (2006).

64. B. I. Arshinoff, *et al.*, Echinobase: leveraging an extant model organism database to build a knowledgebase supporting research on the genomics and biology of echinoderms. *Nucleic Acids Res.* 50, D970–D979 (2022).
65. G. Stecher, K. Tamura, S. Kumar, Molecular evolutionary genetics analysis (MEGA) for macOS. *Mol. Biol. Evol.* 37, 1237–1239 (2020).
66. K. Suffrian, K. G. Schulz, M. A. Gutowska, U. Riebesell, M. Bleich, Cellular pH measurements in *Emiliana huxleyi* reveal pronounced membrane proton permeability. *New Phytol.* 190, 595–608 (2011).

Figures and Legends

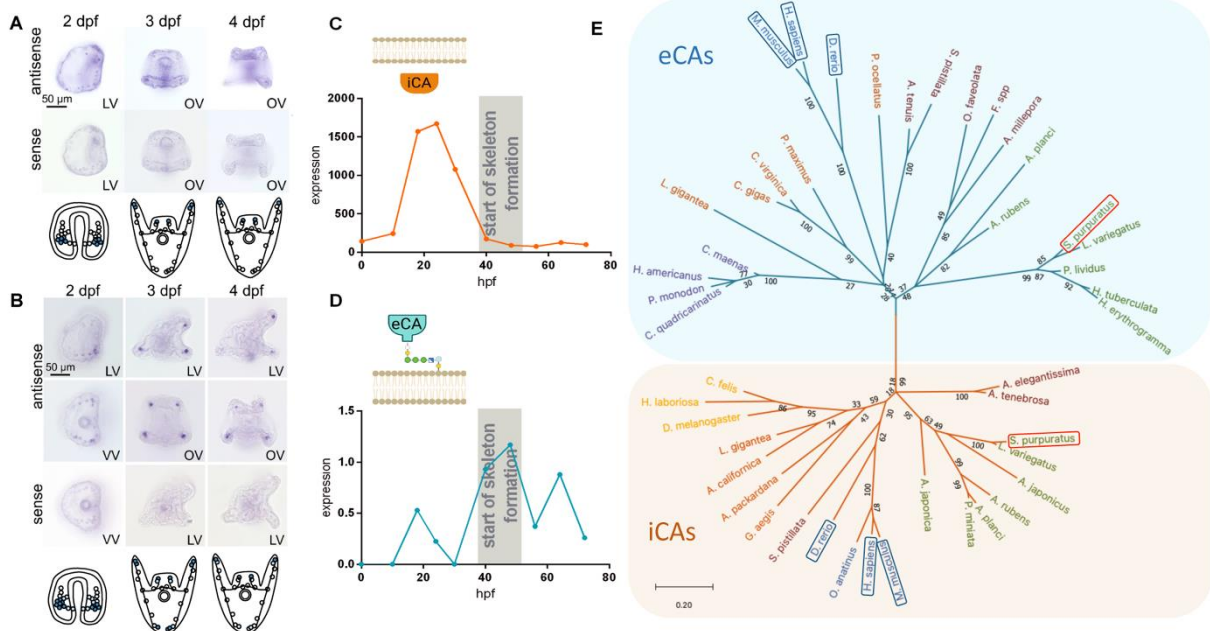


Figure 1. Phylogenetic analysis and expression patterns of iCAs and eCAs in the sea urchin larva. Whole mount *in situ* hybridization using anti-sense and sense probes against *Cara2* (A) and *Cara 7* (B) at 2, 3 and 4 days post fertilization (dpf). Schematic illustration of the *Cara2* and *Cara7* expression pattern in the primary mesenchyme cells (PMCs) of the gastrula and pluteus larva (lower panels). Abbreviations: lateral view: LV; oral view: OV ventral view: VV. Expression of intracellular CA *Cara2* (C) and extracellular CA *Cara7* (D) along the first 72 hours post fertilization (hpf) (data obtained from Echinobase.org(64)). (E) Phylogenetic tree of extracellular (blue lines) and intracellular (orange lines) alpha-CAs in metazoans. A complete list of species, genes and accession numbers are provided in table S2. Red boxes indicate the two CAs (*Cara2* and *Cara7*) from *S. purpuratus* investigated in this work and blue boxes highlight other experimentally confirmed eCAs and iCAs. The bootstrap values were labelled at branch nodes and the branch lengths information (scale bar) that is proportional to the amino acid divergence is shown.

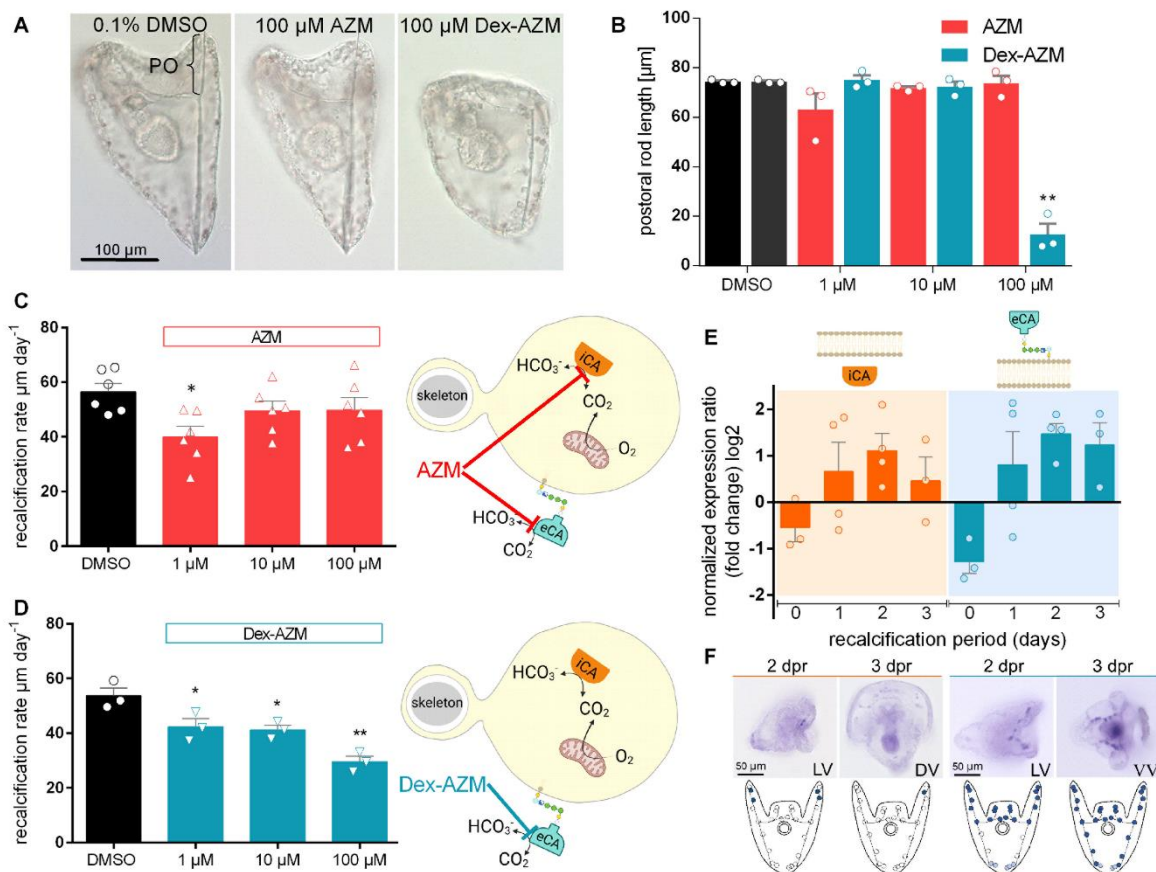


Figure 2. Extracellular carbonic anhydrase activity is required for the calcification of the larval skeleton. (A) Representative images of larvae raised from 16 hpf to 64 hpf under the treatment of 0.1% DMSO, AZM and Dex-AZM respectively. Bracket indicates the post-oral rod (PO). (B) Biometric analyses of the post-oral rod and other skeletal segments (Figure S4) after treatment with different concentrations of AZM and Dex-AZM. Asterisks indicate significant differences compared to controls with $**p < 0.001$ ($n = 3$, One-Way ANOVA + Post-Hoc Test (Holm-Sidak)). Values are presented as mean \pm SEM. (C) Determination of re-calcification rates by measuring the growth rate of the dissolved skeleton under pharmacological inhibition of CA activity by four concentrations (0 μ M, 1 μ M, 10 μ M, 100 μ M; red triangle) of Acetazolamide (AZM). For the controls (0 μ M) only the vehicle DMSO was added. Values are presented as mean \pm SEM; $n = 6$, $*p < 0.05$ (One-Way ANOVA + Post-Hoc Test). Right panel: schematic model illustrating the site of AZM inhibition. (D) Re-calcification rates during pharmacological inhibition of extracellular CAs by dextran-bound Acetazolamide (Dex-AZM) at four concentrations (0 μ M, 1 μ M, 10 μ M, 100 μ M; blue triangle). Values are presented as mean \pm SEM; $n = 3$, $*p < 0.05$; $**p < 0.001$ (One-Way ANOVA + Post-Hoc Test (Holm-Sidak)); right panel: schematic model illustrating the site of Dex-AZM inhibition. (E) Expression levels of *Cara2* (iCA) and *Cara7* (eCA) under re-calcifying conditions along the period of three days. Expression levels were normalized to the internal control *EIF1a*. mean \pm SEM; $n = 3 - 4$. (F) Whole mount in situ hybridization of *Cara2* (left) and *Cara7* (right) at two and three days of re-calcification. Schematic illustration of *Cara2* (left) and *Cara7* (right) expression in PMCs under re-calcifying conditions.

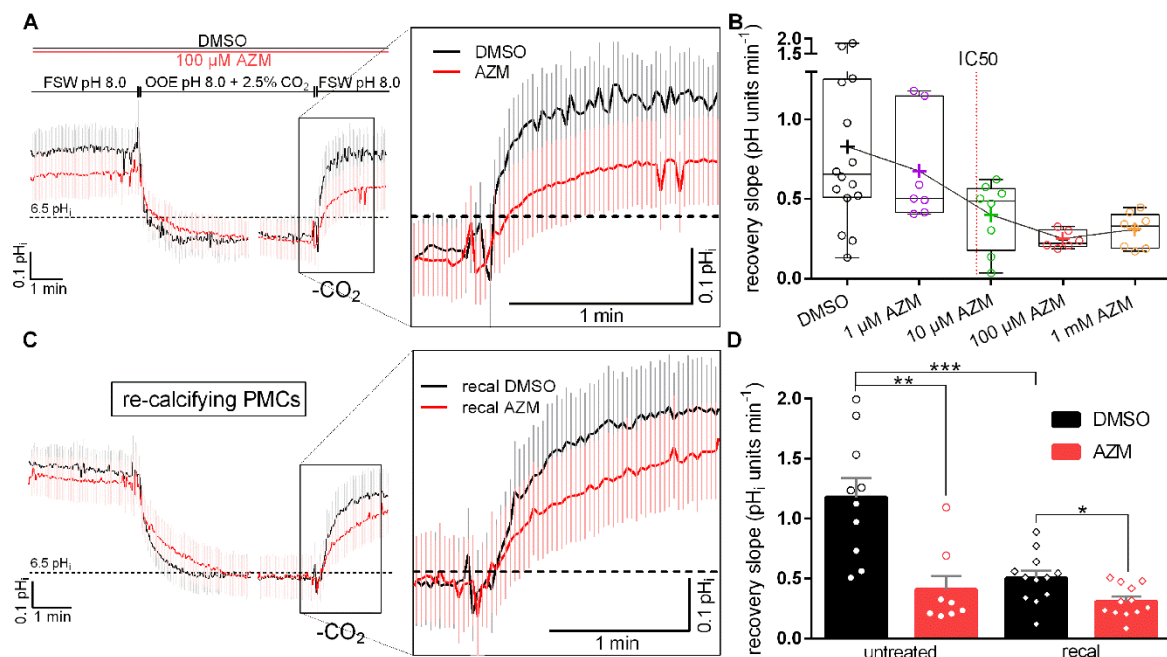


Figure 3. Intracellular pH recordings in combination with the CO₂-pulse method demonstrated iCA activity in PMCs that was decreased under re-calcifying conditions. (A) Intracellular pH (pH_i) was measured using the ratiometric pH sensitive dye BCECF-AM. pH_i of PMCs was recorded during exposure to out-of-equilibrium (OOE) solution (2.5% CO₂, pH 8.0) in the presence of 100 μM AZM (red line, n = 8, mean ± SEM) or DMSO (black line, n = 10, mean ± SEM). The rate in pH_i change during addition and removal of the OOE solution reflects the hydration and de-hydration speed of CO₂ within the cell. The enlarged area depicts the area of interest that was used to analyze iCA activity during CO₂ removal. (B) The recovery rate from the 2.5% CO₂ pulse is inhibited by AZM in a dose-dependent manner with an IC₅₀ value of 7.5 μM reflecting the iCA catalyzed fraction of the de-hydration reaction. Boxplots include single measurements (circles), mean values (crosses), 95th percentiles and standard deviation bars. The membrane impermeable dextran coupled AZM (Dex-AZM) had no effect on iCA activity (Figure S5). (C) iCA activity measurements performed with actively re-calcifying larvae. Changes in pH_i during exposure to 2.5% CO₂ OOE solution were measured in the presence of DMSO (black line, n = 12, mean ± SEM) or 100 μM AZM (red line, n = 12, mean ± SEM). The enlarged area depicts the area of interest that was used to analyze iCA activity during CO₂ removal under re-calcifying conditions. (D) Comparison of recovery rates (pH_i units per minute) of untreated (circles) and re-calcifying larvae (diamonds) and the inhibitory effects of 100 μM AZM (red bars) compared to DMSO controls (black bars). Values are presented as mean ± SEM and statistical analyses were performed using Student's t-test with *p<0.05; **p<0.001; ***p<0.0001).

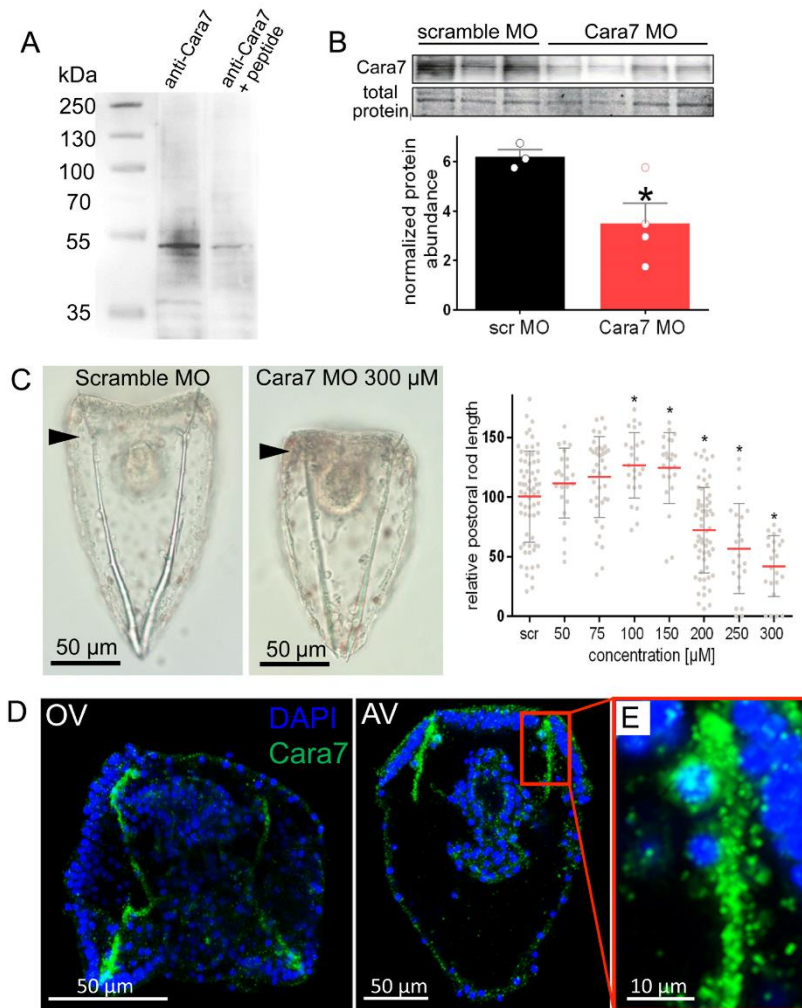


Figure 4. Phenotype of Cara7 knock-down morphants and immunocytological localization of Cara7. (A) Western-blot analysis of the Cara7 antibody using crude extracts of whole pluteus (3 dpf) larvae including a peptide compensation assay by pre-absorption of the primary antibody with the immunization peptide. (B) Western blot analysis of Cara7 protein abundance in 3 dpf larvae injected with scramble or Cara7 MO at a concentration of 200 μ M. The Cara7 protein abundance was normalized to total protein concentrations. Values are presented as mean \pm SEM ($n = 3-4$). Student's t-tests * $p < 0.05$. (C) Representative phenotypes of Cara7 MO (300 μ M) and scramble MO injected larvae at 4 dpf. The length of the post-oral rod (indicated by arrow heads) is predominantly affected in Cara7 morphants. Relative post-oral rod length as a function of different MO concentrations. Morpholino injections were repeated three to five times and individual measurements ($n = 12-44$, grey dots) are presented including mean (red lines) \pm SEM. (D) Positive immunoreactivity of the polyclonal Cara7-specific antibody in pluteus larvae raised for four days under control conditions. Oral view (OV) and anal view (AV) of pluteus larvae stained with the Cara7 antibody (green) and DAPI counter-stain (blue). Negative control showed no autofluorescence (figure S9). (E) High magnification image of the positive immunoreactivity in PMCs of the post-oral rod tips.

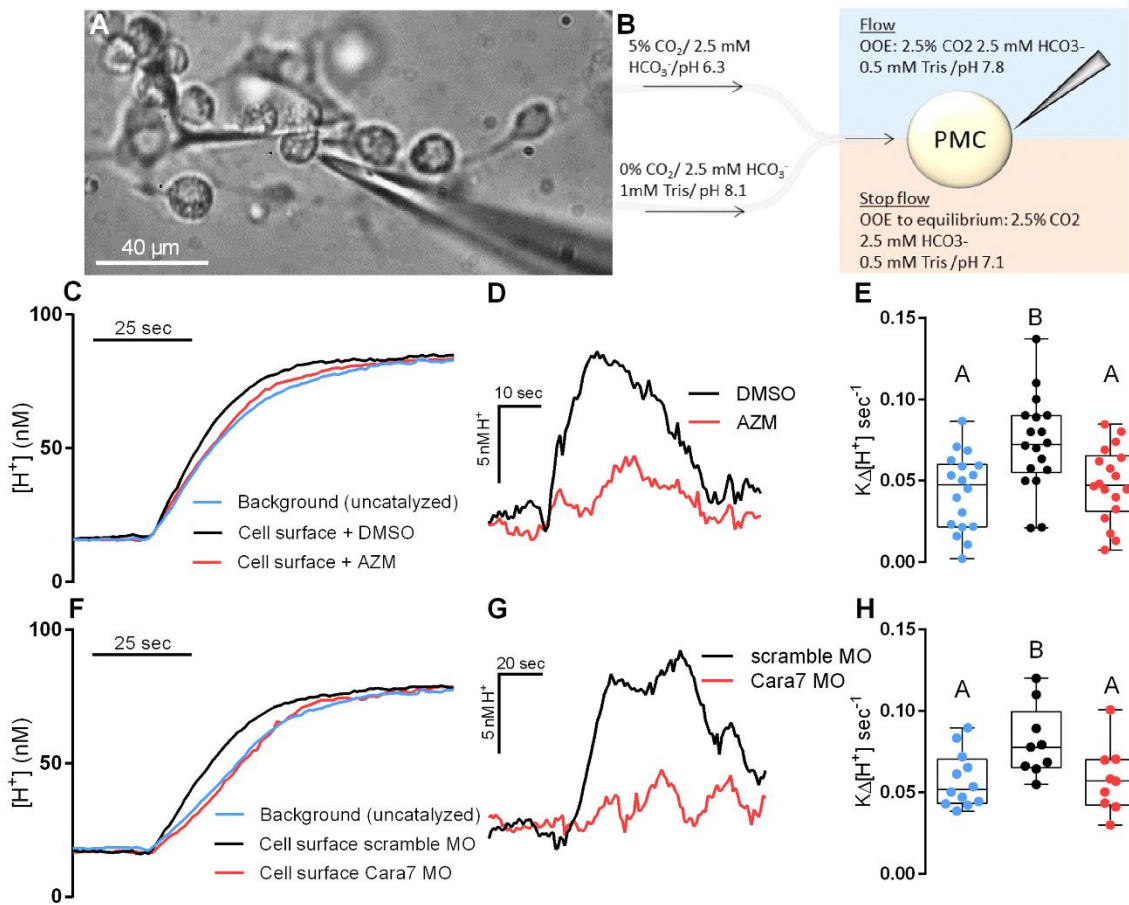


Figure 5. pH selective micro-electrode measurements demonstrated that Cara7 is responsible for extracellular CA activity at the surface of PMCs. (A) Brightfield image of PMCs attached to the larval skeleton at 2 dpf with the micro-electrode positioned at the surface of one PMC. (B) Illustration of the principle used in the stop-flow method for the measurement of eCA activity using H^+ -selective micro-electrodes. Upon stopping the flow of the OOE solution (2.5% CO_2 / pH 7.8) surface pH decreased due to the relaxation of the solution towards the formation of HCO_3^- and H^+ . The speed of CO_2 hydration depends on the catalytic activity of CAs and was used to determine eCA activity. (C) Comparison of OOE relaxation kinetics in the bulk solution (background) and at the cell surface in the presence of 0.1% DMSO or 100 μM of AZM. (D) Presentation of the average ($n = 18$) hydration kinetics at the cell surface in the presence of DMSO or AZM after subtraction of the background CO_2 hydration curve. Here the increase of H^+ at any time point is depicted, compared between control conditions (DMSO, black line) and CA inhibition (AZM, red line). (E) Dependence of the rate constant of the pH change on the presence of extracellular CA activity. We obtained $K\Delta[H^+]$ -values from non-linear least-squares curve fits like those presented in (C, F) demonstrating increased AZM-sensitive CO_2 hydration at the cell surface of PMCs ($n = 18$). (F) Comparison of OOE relaxation kinetics in the bulk solution (background) and at the cell surface of Cara7 morphants and scramble morpholino injected larvae. (G) Presentation of the average ($n = 9-12$) hydration kinetics at the cell surface in scramble morpholino injected or Cara7 knock-down larvae after subtraction of the background CO_2 hydration curve. (H) Comparison of the rate constant of the pH change on the presence of extracellular CA activity in scramble and Cara7 morpholino injected larvae. Letters denote significant differences between treatments (One-Way ANOVA + Post-Hoc Test (Holm-Sidak)).

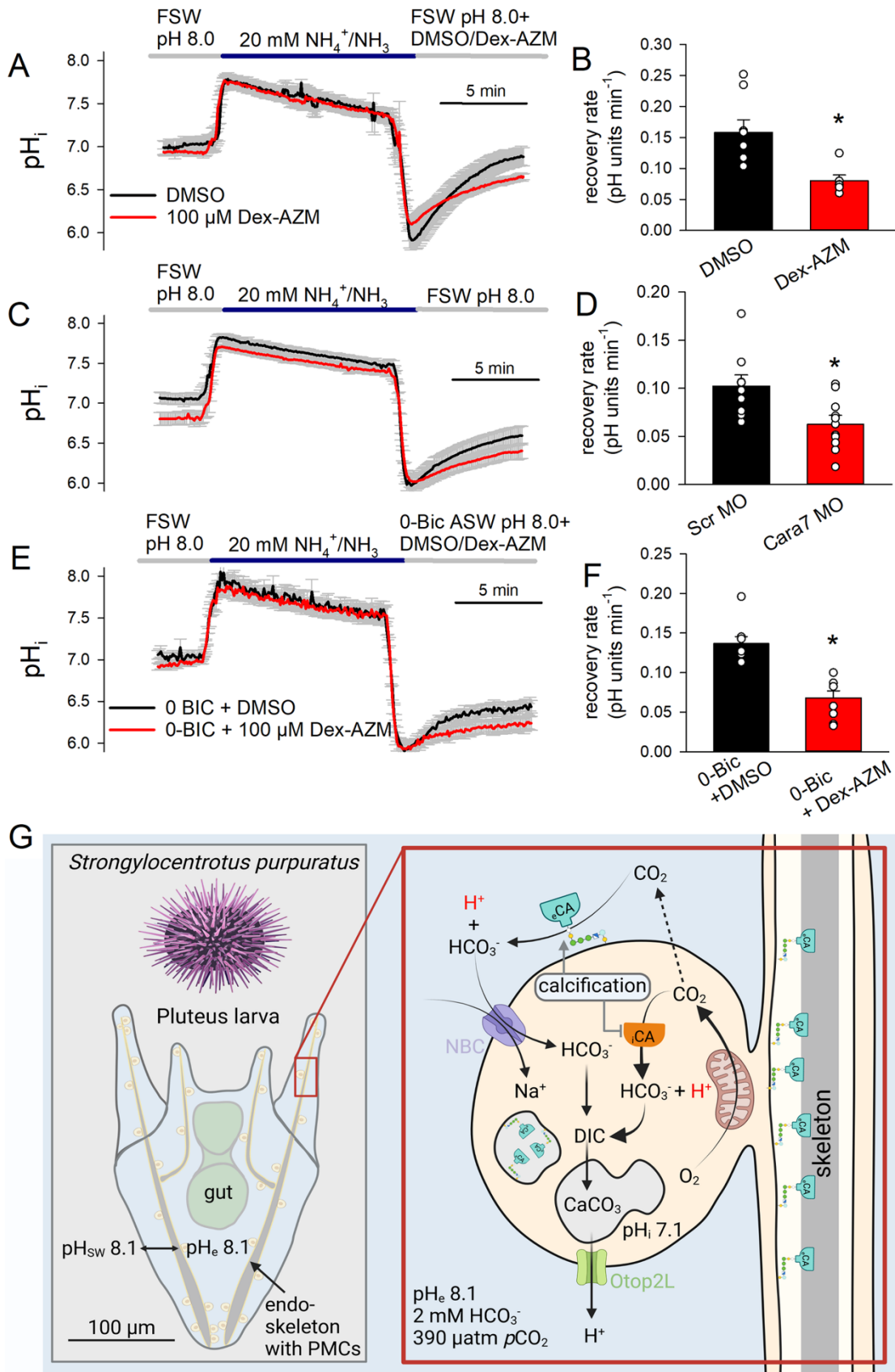


Figure 6. Dependence of pH_i regulatory capacities on eCA activity and proposed CCM for PMCs. (A) pH_i regulatory capacities of PMCs in control larvae investigated by the ammonia pre-pulse method. Average traces of pH_i recordings with 0.1% DMSO (black line, n = 8) or 100 μM dextran-bound AZM (Dex-AZM) (red line, n = 6) in the perfusion solution during the wash-out period. (B) pH_i regulatory

capacities of control (DMSO, black) and Dex-AZM (red) treated PMCs (mean \pm SEM; n = 6-8; Student's t-test *p < 0.05). (C) Average traces of pH_i recordings in PMCs of *Cara7* (red line) or scramble morpholino (black line) injected larvae at 3-4dpf. (D) Comparison of pH_i regulatory capacities in larvae injected with scramble MO (black) or with *Cara7* MO (red) at a concentration of 200 μ M. (mean \pm SEM; n = 10-11; Student's t-test * p < 0.05). (E) Average traces of pH_i recordings with 0.1% DMSO (black line, n = 8) or 100 μ M dextran-bound AZM (Dex-AZM) (red line, n = 8) in the absence of HCO₃⁻ (0-Bic) in the artificial seawater (ASW) solution during the wash-out period. (F) pH_i regulatory capacities of control (DMSO, black) and Dex-AZM (red) treated PMCs (mean \pm SEM; n = 8; Student's t-test *p < 0.05) in the absence of HCO₃⁻ during the washout period. (G) Schematic model summarizing the CCM in PMCs of the sea urchin larva. PMCs form syncytial cables surrounding the calcitic spicule. Cross section of an enlarged PMC cell including validated transporters (Na⁺/HCO₃⁻ co-transporter: NBC and Otopetrin proton channel (Otop2l)) and carbonic anhydrases investigated in the present work. While a certain fraction of the metabolic CO₂ is hydrated by intracellular CAs, the remaining CO₂ diffuses across the plasma-membrane where alkaline (~pH 8.0) extracellular conditions favor the formation of HCO₃⁻ catalyzed by *Cara7*. This HCO₃⁻ is re-imported by the Na⁺/HCO₃⁻ co-transporter Sp-Slc4a10 and feeds back into the cellular carbon pool. Dissolved inorganic carbon (DIC) is imported into the calcification vesicle by so far unknown mechanisms. Intracellular hydration of CO₂ depends on iCA activity that is reduced during active mineralization to promote the CCM and to reduce the cellular proton load. The remaining protons generated by the intracellular formation of CaCO₃ can exit the cell through the proton channel Otop2l (43).

PNAS

www.pnas.org

Supplementary information for

Extracellular carbonic anhydrase activity promotes a carbon concentration mechanism in metazoan calcifying cells

A-S. Matt¹, W. W-J. Chang¹, M. Y. Hu¹

¹Institute of Physiology, Christian-Albrechts-University of Kiel, 24118 Kiel, Germany

Corresponding author

Marian Y. Hu

Email: m.hu@physiologie.uni-kiel.de

Table S1 Complete list of carbonic anhydrases found in the genome and transcriptomes of the purple sea urchin *S. purpuratus*.

| LOC-ID | description | other_ designations | Acc. number (mRNA) (protein) | B.P | A.A. | PMC EST | RNA seq. PMC 1/2 | RNA-seq non-PMC 1/2 | Single cell seq. | GPI anchor | Signal peptide |
|--------------|---------------------------------------|---------------------|--------------------------------|------|------|---------|------------------|---------------------|------------------|------------|----------------|
| LOC579101 | carbonic anhydrase 7-like | cah2, Cara7LA | XM_003726241 XP_003726289.2 | 3116 | 439 | + | +/+ | +/+ | + | + | + |
| LOC577690 | carbonic anhydrase 2 | ca2, Cara7LB | XM_777904 XP_782997.3 | 3330 | 266 | + | +/+ | +/+ | + | - | - |
| LOC590675 | carbonic anhydrase-related protein | ca8, Cara8LA | XM_790272 XP_795365.3 | 1183 | 330 | + | L/- | +/- | - | - | - |
| LOC763149 | carbonic anhydrase 1-like | ca1-like, Cara4LB | XM_011681537 XP_011679839.1 | 1042 | 294 | + | -/- | -/- | n.d. | - | + |
| LOC576041 | carbonic anhydrase 2-like | ca2-like, Cara2LA | XM_030974001 XP_011679839.1 | 990 | 286 | + | -/- | -/- | n.d. | - | + |
| LOC575052 | carbonic anhydrase 14-like | ca14-like, Cara12LA | XM_030974790 XP_030830650.1 | 717 | 160 | + | -/- | -/- | n.d. | - | - |
| LOC115928879 | carbonic anhydrase 12-like | ca12-like, Cara12LB | XM_030996909 XP_030852769.1 | 1506 | 249 | + | L/- | +/- | - | - | - |
| LOC591885 | carbonic anhydrase 14 | ca14, Cara14LA | XM_030973782 XP_030829642.1 | 1857 | 314 | - | +/+ | +/+ | + | + | - |
| LOC100892103 | carbonic anhydrase 1-like | ca1-like, Cara5L | XM_030974504 XP_030830364.1 | 933 | 295 | - | -/- | -/- | n.d. | + | + |
| LOC585798 | carbonic anhydrase 1-like | ca1-like, Cara1LA | XM_030974503 XP_030830363.1 | 816 | 256 | - | -/- | -/- | n.d. | - | - |
| LOC100891441 | putative carbonic anhydrase 3 | ca3, Cara4LA | XM_003725490 XP_003725538.2 | 1563 | 313 | - | -/- | -/- | - | + | + |
| LOC579596 | carbonic anhydrase-related protein 10 | ca10/11, Cah10L | XM_030981147 XP_030837007.1 | 2507 | 259 | - | -/- | -/L | - | - | - |
| LOC583821 | carbonic anhydrase 14-like | ca14-like, Cah14L | XM_030974906 XP_030830766.1 | 1302 | 305 | - | L/- | -/- | - | + | + |
| LOC581001 | beta carbonic anhydrase 1 | 1,bca1, Cahb | XM_030981941 XP_030837801.1 | 2425 | 275 | - | +/+ | +/+ | - | - | - |

Gene mining was performed on Echinobase (www.echinobase.org) and transcriptomic information were obtained for early developmental stages (20-72 hours-post-fertilization) from the following sources: <https://blast.ncbi.nlm.nih.gov/Blast.cgi> (PMC est library), NCBI Sequence Read Archive (SRA accession number SRP033427) (RNA sequencing of PMCs and non-PMCs) as well as single cell transcriptomics (figure S1). For single cell sequencing methodology see (1). Information about the presence (+) or absence (-) in PMCs was analyzed by blastn (NCBI, NIH) against the PMC EST library, and by analysing the read numbers in the PMC RNA-seq database with >100 reads (+) 20-100 reads (L) and <20 reads (-) and by analysis of single cell transcriptomic analyses. In addition, information about the presence of a GPI anchor or signal peptide motive are provided. Base pairs: B.P.; Amino acids: A.A. Two sequencing runs were performed for the RNA-seq. data indicated by 1/2

Table S2 Species names and corresponding accession numbers used for phylogenetic analyses.

| Name | Number |
|--------------------------------------|----------------------|
| <i>Stylophora pistillata</i> | Spis16865 |
| <i>Acropora tenuis</i> | Aten 0.1.m1.14784.m1 |
| <i>Orbicella faveolata</i> | XP 020612573.1 |
| <i>Fungia spp</i> | Ffun1.m4.22490.m1 |
| <i>Acropora millepora</i> | B7T142 |
| <i>Pseudocheilinus ocellatus</i> | GFO10585.1 |
| <i>Paralongidorus maximus</i> | XP033748427.1 |
| <i>Crassostrea virginica</i> | XP 022339696.1 |
| <i>Crassostrea gigas</i> | XP 011435378.2 |
| <i>Lottia gigantea</i> | XP 009053021.1 |
| <i>Crassostrea maens</i> | ABX71209.1 |
| <i>Homarus americanus</i> | XP 042233835.1 |
| <i>Penaeus monodon</i> | XP 037782058.1 |
| <i>Cheax quadricarinatus</i> | AIW68601.1 |
| <i>Homo sapiens</i> | XP 006711324.1 |
| <i>Danio rerio</i> | NP 001315073.1 |
| <i>Mus musculus</i> | NP 001342680.1 |
| <i>Acanthaster planci</i> | XP 022085775.1 |
| <i>Asterias rubens</i> | XP 033628377.1 |
| <i>Strongylocentrotus purpuratus</i> | XP 003726289.2 |
| <i>Lytechinus variegatus</i> | XP 041455962.1 |
| <i>Paracentrotus lividus</i> | CDG49295.1 |
| <i>Heliocidaris tuberculata</i> | ABE27961.1 |
| <i>Heliocidaris erythrogramma</i> | ABE27962.1 |
| <i>Stylophora pistillata</i> | Spis12076 |
| <i>Anthopleura elegantissima</i> | AAD32675.1 |
| <i>Actinia tenebrosa</i> | P 031563864.1 |
| <i>Lottia gigantea</i> | XP 009052992.1 |
| <i>Aplysia californica</i> | XP 012941697.1 |
| <i>Archivesica packardana</i> | QFP92279.1 |
| <i>Gigantopelta aegis</i> | XP 041377168.1 |
| <i>Chlamydomphila felis</i> | XP 026474423.1 |
| <i>Habropoda laboriosa</i> | XP 017790715.1 |
| <i>Drosophila melanogaster</i> | NP 523561.1 |
| <i>Homo sapiens</i> | 4PXXA |
| <i>Danio rerio</i> | NP 954685.2 |
| <i>Mus musculus</i> | NP 001344263.1 |
| <i>Ornithorhynchus anatinus</i> | XP 028919104.1 |
| <i>Acanthaster planci</i> | XP 022094576.1 |
| <i>Asterias rubens</i> | XP 033625982.1 |
| <i>Strongylocentrotus purpuratus</i> | XP 782997.3 |
| <i>Lytechinus variegatus</i> | XP 041453651.1 |
| <i>Acanthurus japonicus</i> | PIK49738.1 |
| <i>Patiria miniata</i> | XP039069820.1 |
| <i>Aphelasterias japonica</i> | XP 033107726.1 |

Table S3 Summary of parameters obtained from intracellular pH recordings during CO₂ pulse experiments.

| | Untreated larvae | | Re-calcifying larvae | |
|------------------------------------|---------------------|---------------------|----------------------|---------------------|
| | DMSO | 100 μ M AZM | DMSO | 100 μ M AZM |
| pH _i start | 6.7335 \pm 0.074 | 6.6237 \pm 0.077 | 6.9130 \pm 0.070 | 6.8706 \pm 0.081 |
| slope +CO ₂ | -0.9109 \pm 0.118 | -0.4482 \pm 0.092 | -0.7618 \pm 0.104 | -0.4472 \pm 0.056 |
| delta + CO ₂ | 0.3049 \pm 0.036 | 0.1892 \pm 0.036 | 0.4279 \pm 0.030 | 0.3718 \pm 0.021 |
| slope during CO ₂ pulse | 0.0043 \pm 0.007 | -0.0102 \pm 0.004 | -0.0039 \pm 0.006 | -0.0141 \pm 0.007 |
| slope -CO ₂ | 1.1779 \pm 0.153 | 0.4070 \pm 0.107 | 0.5042 \pm 0.057 | 0.3103 \pm 0.036 |
| delta -CO ₂ | -0.3014 \pm 0.032 | -0.1759 \pm 0.029 | -0.3178 \pm 0.040 | -0.2382 \pm 0.021 |
| pH _i final | 6.7300 \pm 0.081 | 6.6104 \pm 0.081 | 6.8030 \pm 0.091 | 6.7370 \pm 0.089 |

Addition (+ CO₂) and removal (-CO₂) of CO₂ solution. Slopes are given as pH units min⁻¹

Table S4 List of primers used for molecular cloning and RT-qPCR.

| Primer Name | Primer Sequence | Amplicon size | Application |
|-----------------|------------------------|---------------|-------------|
| 008658_F | GATACACTGGACACGGAGGC | 172 bp | qPCR |
| 008658_R | TTGACGAGAGCCTTGGTACG | | |
| 012518_F | GAACGGTAACGGATGGGGAG | 148 bp | qPCR |
| 012518_R | GGGTCCGTTCATGCCAAAAG | | |
| EF1a_F | CCGACCTTGAAAGGGATCG | 194 bp | qPCR |
| EF1a_R | ACAGTCGGCCTGTGAGGTTT | | |
| 008658_F | GATACACTGGACACGGAGGC | 715 bp | In Situ |
| 008658_R | CCACGACCCTCGAAAGACTC | | |
| 012518_F | GAACGGTAACGGATGGGGAG | 711 bp | In Situ |
| 012518_R | ATAACACCGCAACCGACAGA | | |
| M13-F | CGCCAGGGTTTTCCAGTCACGA | | Cloning |
| M13-R | TCACACAGGAAACAGCTATGAC | | |

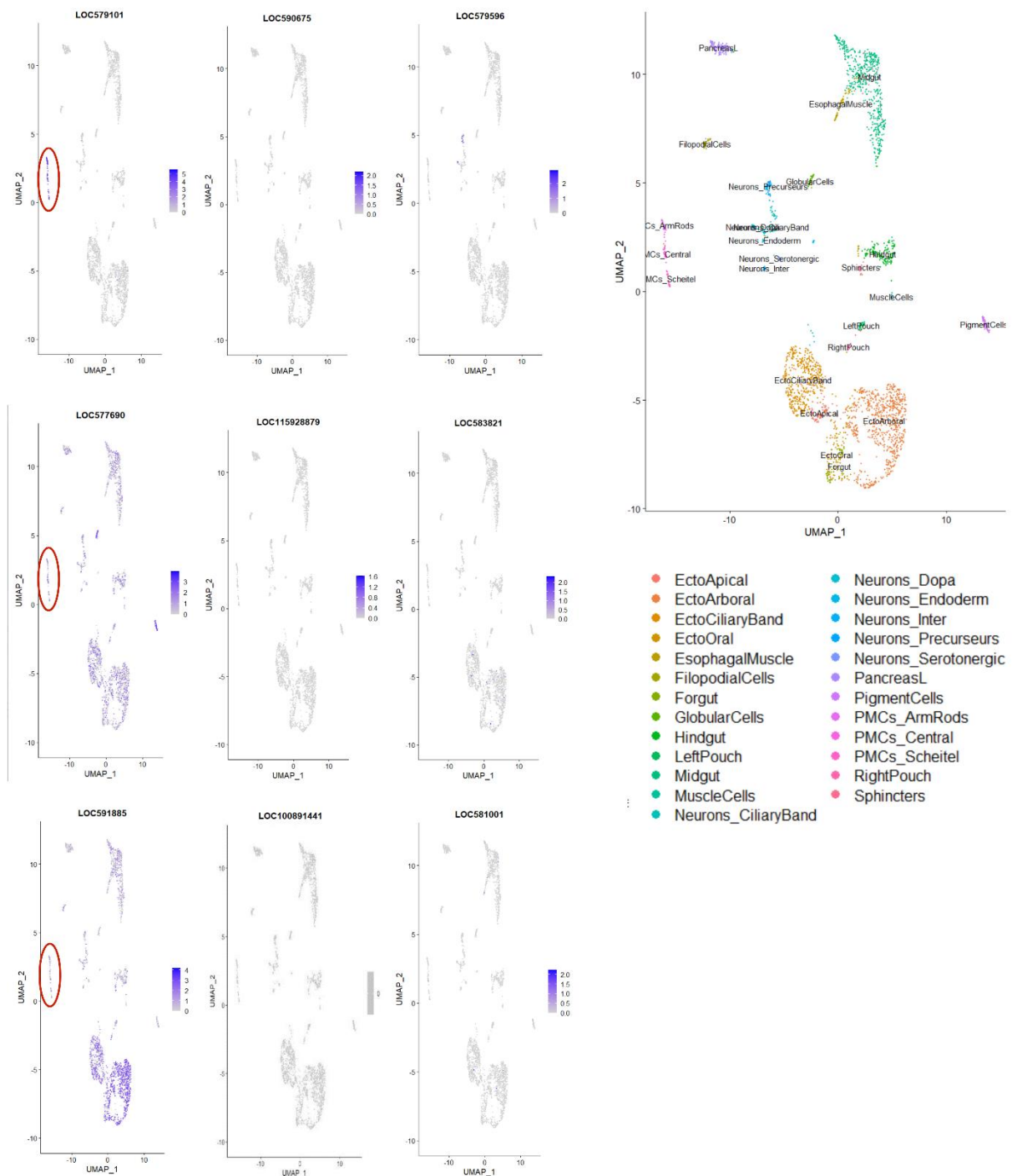


Figure S1. Single-cell transcriptomic analyses of all 14 carbonic anhydrases found in the sea urchin genome. Single cell transcriptomic analyses in the pluteus larva (72 hours-post-fertilization) detected expression of three carbonic anhydrases (CAs) in PMCs. From these CAs LOC579101 (*Cara7*) and LOC577690 (*Cara2*) showed highest expression in PMCs with peak expression levels at the onset of skeleton formation (Figure 1 main manuscript). LOC591885 (*Cara14*) was predominantly expressed in ectodermal cells.

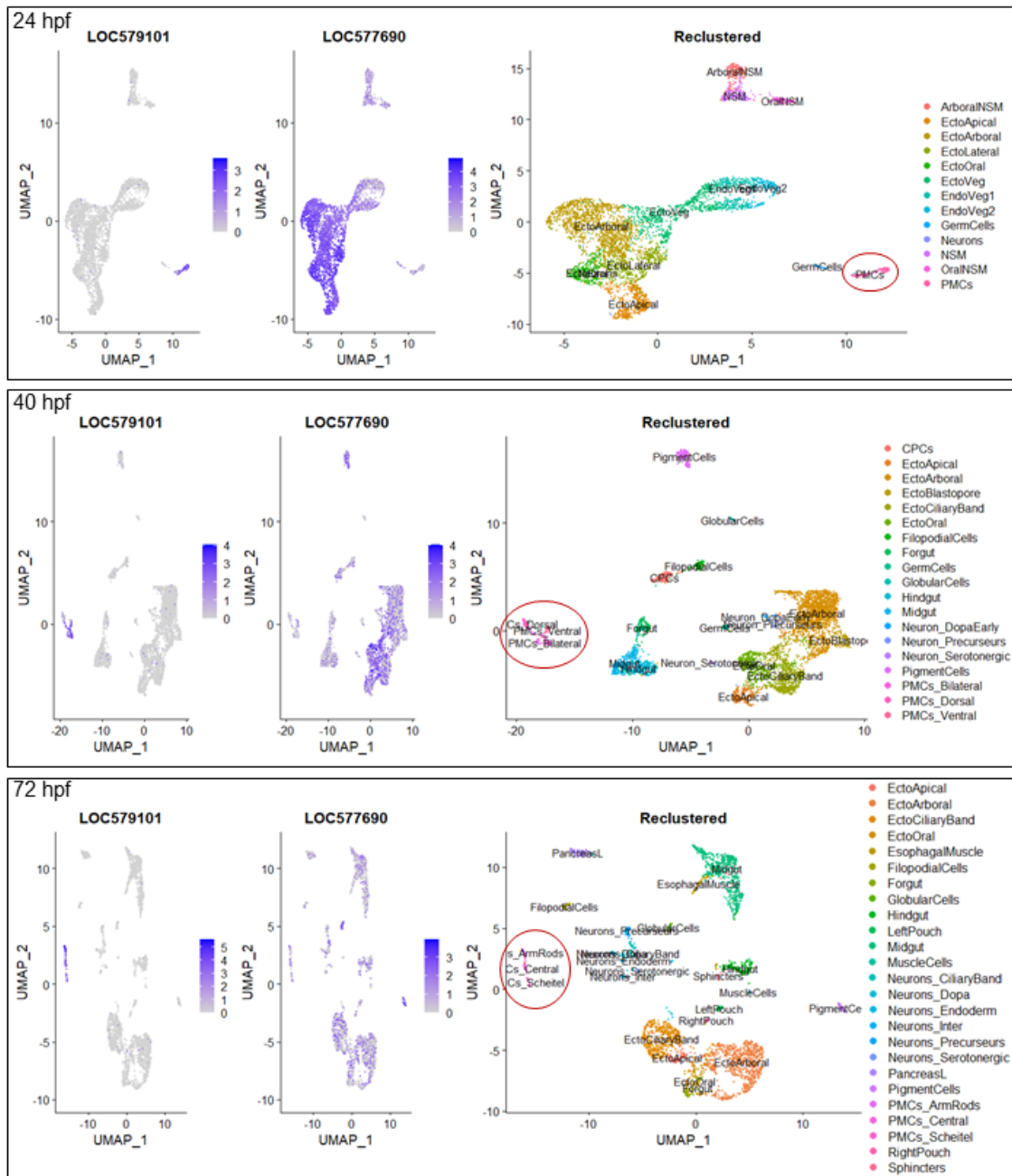


Figure S2. Single-cell transcriptomic analyses of two carbonic anhydrases with peak expressions in the phase of skeletogenesis. Single-cell RNA sequencing was performed as previously described (1) using the 10x Genomics commercial platform. Dimensional reduction was achieved using uniform manifold approximation and projection (UMAP) and projections are plotted as dot plots representing each dot as one cell. Unsupervised clustering of cells resulted in several clusters out of which clusters positive for pan-PMC marker genes *Alx1*, *SpP19L* and *SM50* were identified as PMCs (red circle). Scaled and normalized counts per cell of 'gene of interest' are shown in blue. cluster identified with special marker genes to the corresponding cell type of the larvae. LOC579101 = SPU_012518 (*Cara7*), LOC577690 = SPU_008658 (*Cara2*). Single cell transcriptomes were obtained for three different developmental time points, including 24 hpf, 40 hpf and 72 hpf. PMC subpopulations are indicated by red circle.

```

SPU_012518 MNAYILLSLATLTLTLLYQECLGANWHYHQHGPLGPNW-PTIPGSHCGGRKQSPINIESRS
SPU_008658 M-----CEWGYTGHG--GPAHWHESEFP--QAGGKRQSPIDI----

SPU_012518 VIQADLGEFVFEGQLQTTYGTQVGAGGNQPGQGGGQGGGSGFNWGGAGAGGGGGGGVGG
SPU_008658 -----

SPU_012518 VGGGGGWNWNSWWNGNGWGGSNNGGQNAVGNQHPQWSNPFGNLQMGPKPTVNPYQPFGMN
SPU_008658 -----N

SPU_012518 GPERMFTDNNQAYAPRALH-GYNSAPTTKVEVSNDGHTLKVSTEGM-YVLKGGGLPFD
SPU_008658 TTDARFDT-----ALVDRPLKISYD--PSRTKALVNNGHTFRVDIDACDYNLSGGPLEDN

SPU_012518 AKPAQLHFWGTTPERGSEHTIDGRPFSAEHLHLYHYN-AKYRTIAEAVKQPDGLAVLGFF
SPU_008658 YQLVQFHAHWGKEDKEGAEHTINGKQYAAEHLVHWNTGQFKAVSDAIKCDKGIAVLGSF

SPU_012518 IQDSGSYENPAFDPLLDITENVKFKDKTKVEYYAHLPLRDMLPTDLSCFYRYNGSLTVPKC
SPU_008658 IKVGKPH--VGFEKLVPCLLKALNKNCTAPVEGGFDPSCLLPENKKDYWTYEGSLTTPPC

SPU_012518 WESVTWSVCGCVIHLSHNQLDMFRELY---QGFFMEPNGQLEMLHIEDNFRPVQPLFDRQ
SPU_008658 YESVSFILFKDAIEVSEEQLQVLRNLQDHCDGESFEGRGK-----VVNNYRPLCDLNGR-

SPU_012518 VIRSGFPSRAGMGYSANNSANLISVNLFLLLSATMAFVCRSL
SPU_008658 VVRATFEN-----

```

Figure S3. Amino acid sequence multiple alignments for SPU_012518 (Cara7) and SPU_008658 (Cara2). Multiple alignments with MAFFT (Multiple Alignment using Fast Fourier Transform) of Cara7 (455 aa) and Cara2 (266 aa). The following motifs are highlighted: signal peptide (light blue), glycine rich region (light grey), active site (red), zinc binding sites (green), α -CA signature (pink), phospholipase (dark grey), omega site for GPI anchor (yellow), trans-membrane domain (purple) and cytoplasmic domain (blue).

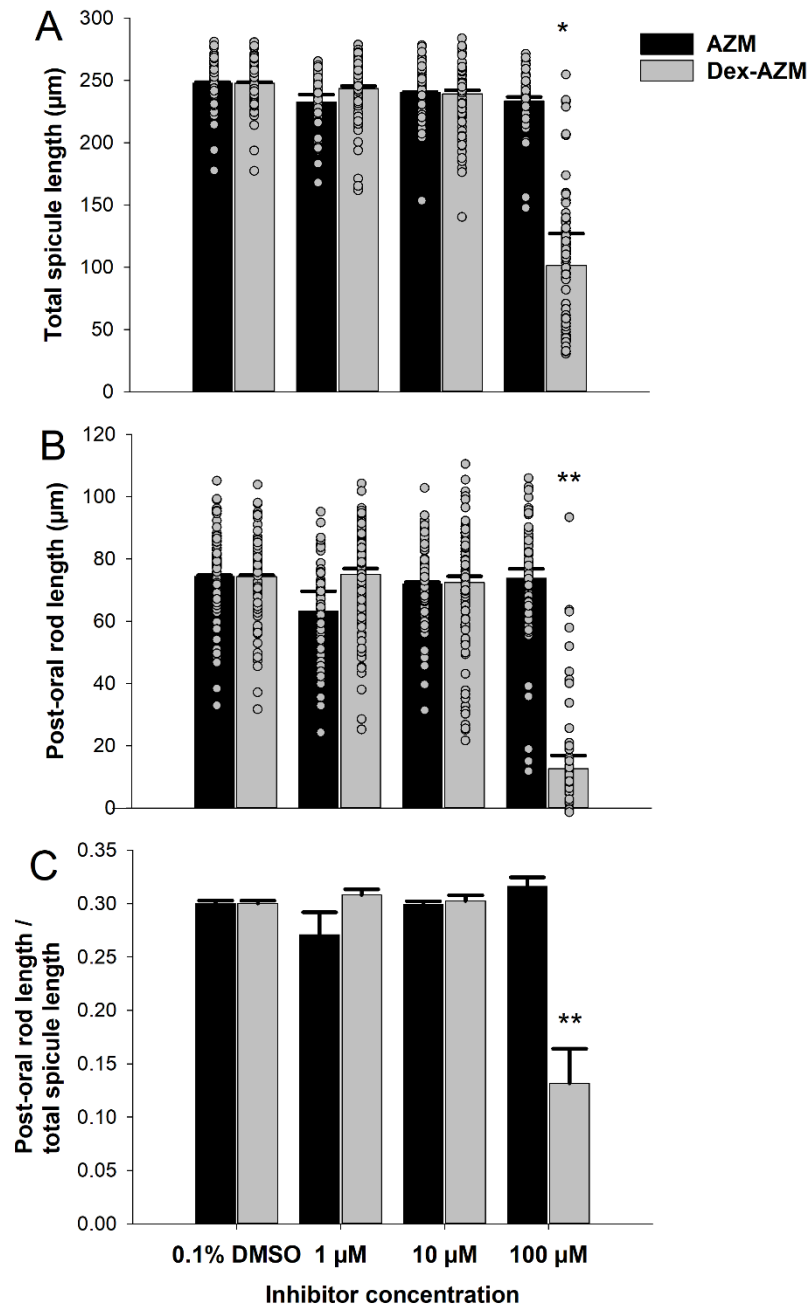


Figure S4. Differential effect of acetazolamide (AZM) and dextran coupled AZM on the formation of the skeleton in the developing sea urchin larva. Normally developing larvae were exposed to different concentrations (0 μM, 1 μM, 10 μM, 100 μM) of AZM and Dex AZM from 16 hpf to 64 hpf. Morphometric analyses of the larval skeleton after 64 h of development included determination of the total spicule length (body rod+ post-oral rod) (A) and the post-oral rod length (B). All experiments were performed in triplicates (n=3) with 20-70 larvae being measured from each experimental replicate (grey dots). (C) The ratio of the post-oral rod length and the total spicule length is used to demonstrate the change in the proportions of the different spicule segments. Values are presented as mean±SEM (n=3) Asterisks indicate significant differences with * < 0.05 and ** < 0.001 between Inhibitor treatments and the control group (One-Way-ANOVA followed by Holm-Sidak post-hoc test)

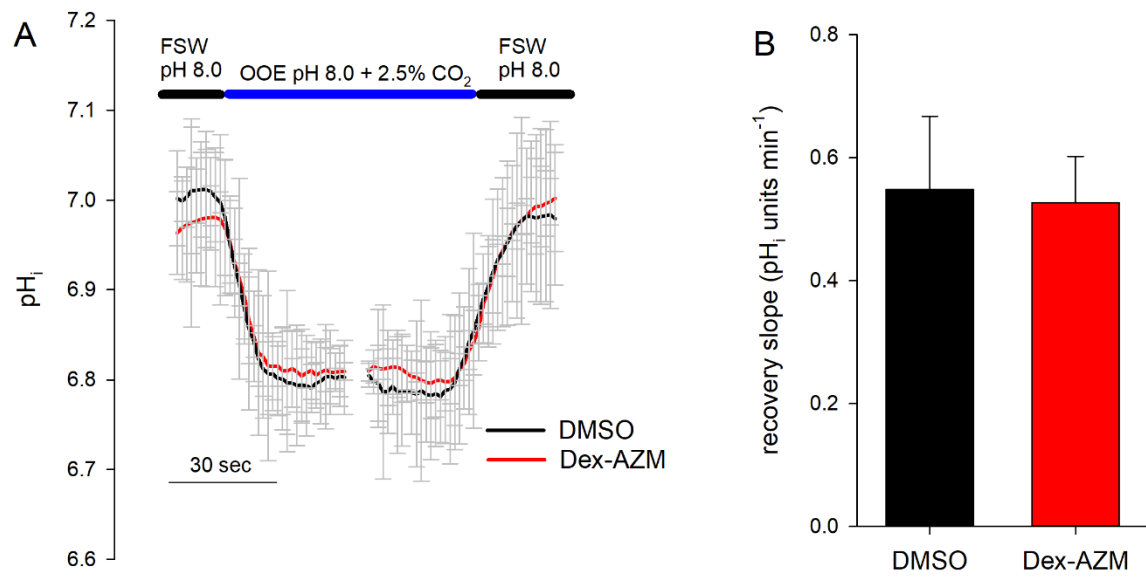


Figure S5 Effect of dextran coupled acetazolamide (Dex-AZM) on the intracellular carbonic anhydrase activity. (A) Traces of CO_2 pulse recordings performed in the presence of 0.1% DMSO or 100 μM Dex-AZM. (B) the recovery slope after the CO_2 -pulse was used to analyse the effects of Dex-AZM on the intracellular carbonic anhydrase activity. Experiments were performed in triplicates ($n=3$) with 4-7 cells measured for each larva (replicate). Student's t-test could not detect significant differences between the two treatments. Values are presented as mean \pm SEM ($n=3$).

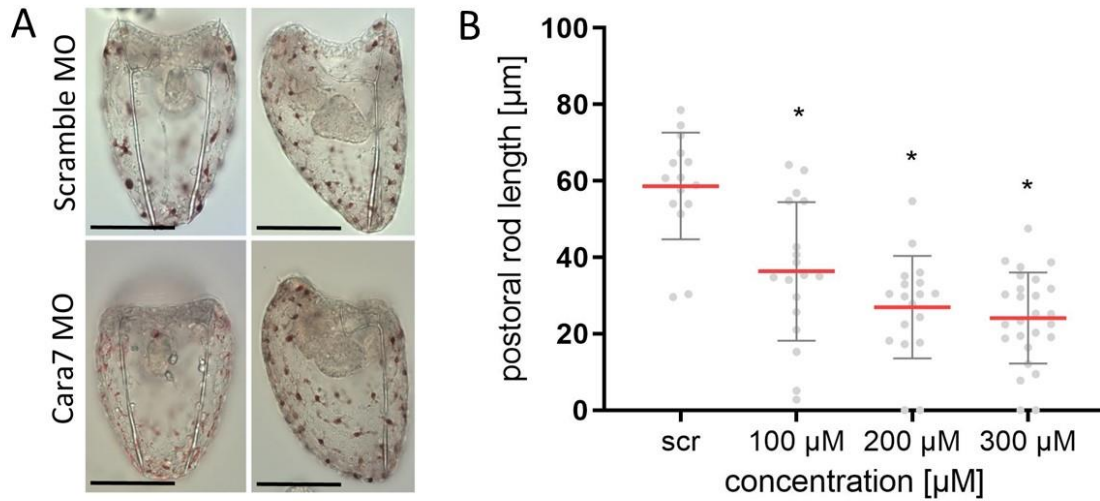


Figure S6 Reductions in post-oral rod length of sea urchin larvae confirmed by a second Cara7 MO. Fertilized eggs were injected with a scramble morpholino (MO) or different concentrations (100 μM, 200 μM or 300 μM) of a second MO designed against the 5' untranslated region of the Cara7 gene. (A) Representative phenotypes of scramble and 300 μM Cara7 MO injected larvae at 3 days post fertilization. (bar: 100 μm). (B) Measurements of the post-oral rod length in larvae injected with scramble MO or different concentrations of the Cara7 MO. MO Injection experiments were performed twice and 20-26 larvae were used for biometric analyses. Values are presented as mean ± SEM. With each dot representing the measurements from a single individual. Asterisks indicate significant differences compared to scramble MO injected larvae with $p < 0.05$ (One-way-ANOVA; Holm-Sidak post-hoc test).

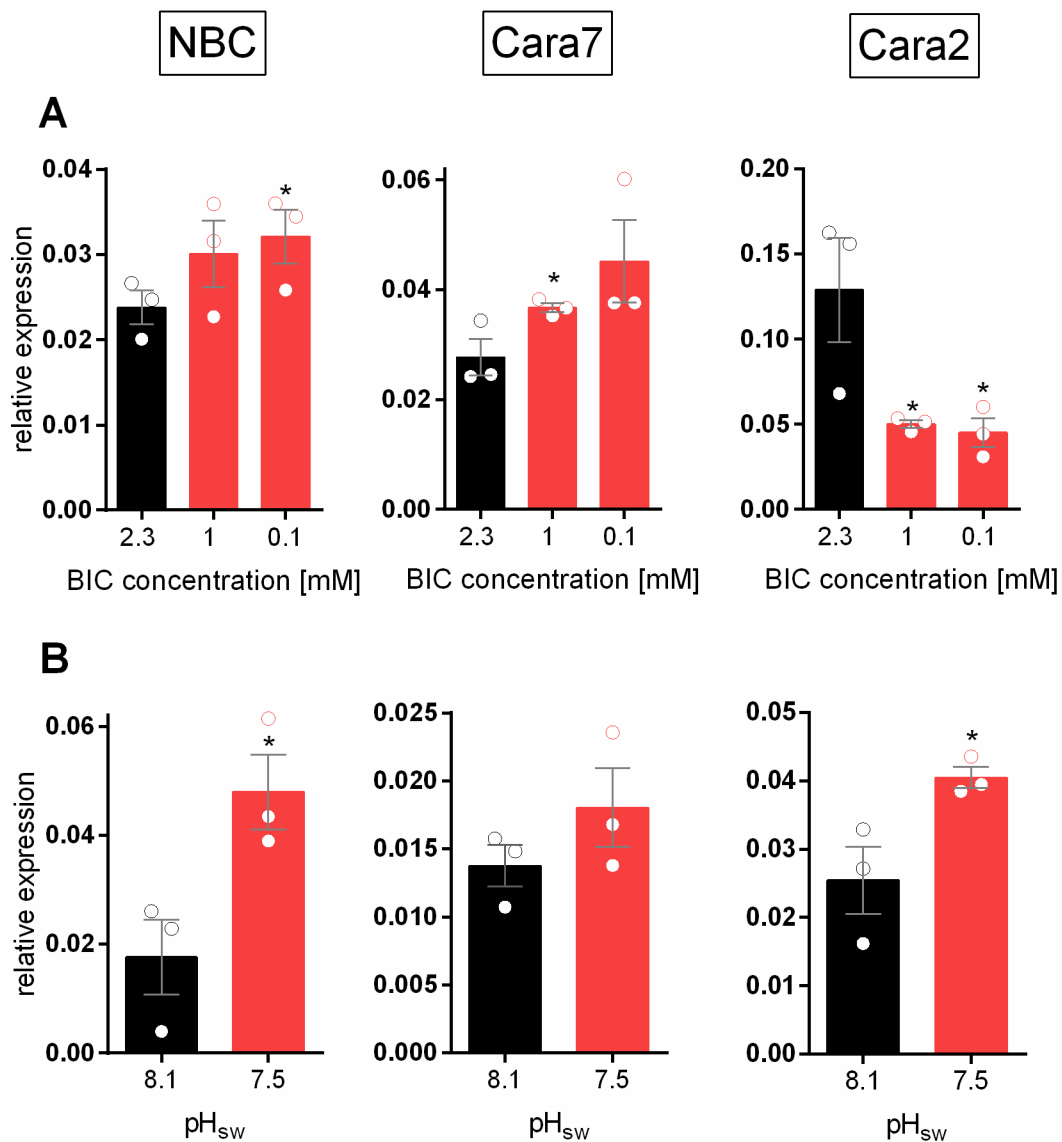


Figure S7. Expression pattern of the $\text{Na}^+/\text{HCO}_3^-$ co-transporter (Sp-Slc4a10) and the two carbonic anhydrase genes, Cara2 and Cara7, under different bicarbonate (BIC) and CO_2 concentrations. (A) Expression levels of NBC, Cara2 and Cara7 in 3 dpf larvae exposed to different HCO_3^- concentrations for 24 hours. Values are presented as mean \pm SEM; (n= 3). (B) Expression levels of NBC, Cara2 and Cara7 at 2 dpf under different CO_2 levels. The samples from the CO_2 manipulation experiment derived from a previously published work (2), _{sw} = seawater. All values are presented as mean \pm SEM (n= 3). Expression of target genes was normalized to the internal control EF1a.

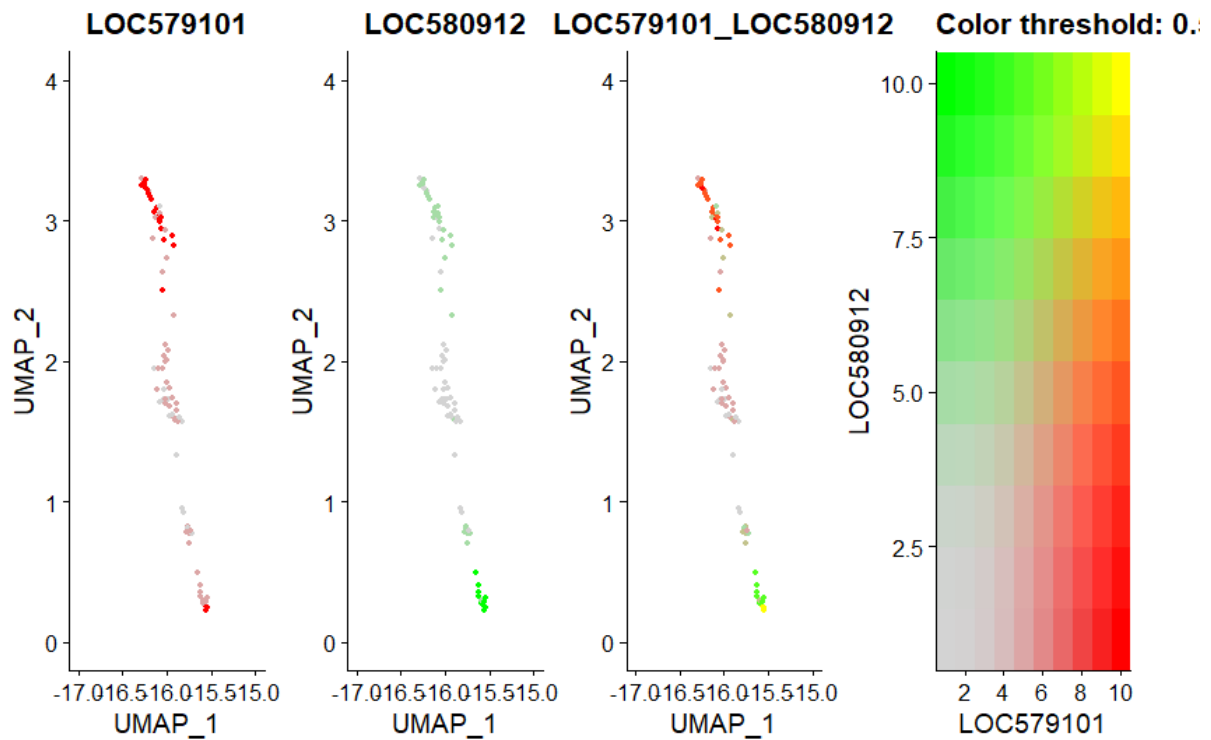


Figure S8. Co-expression of the $\text{Na}^+/\text{HCO}_3^-$ cotransporter *Slc4a10* and *Cara7* in subpopulations of PMCs. Single cell transcriptomic analyses at 72 h post-fertilization indicate predominant expression of *Cara7* (LOC579101) in a subpopulation of PMCs of the scheitel region and post-oral rod tips (red circle) of the larval skeleton. A similar expression pattern is found for the bicarbonate transporter *SpSlc4a10* (LOC580912) that is responsible for the import of HCO_3^- into PMCs(2). These two proteins are largely co-expressed in PMCs of the scheitel region and in the tips of the post-oral rods.

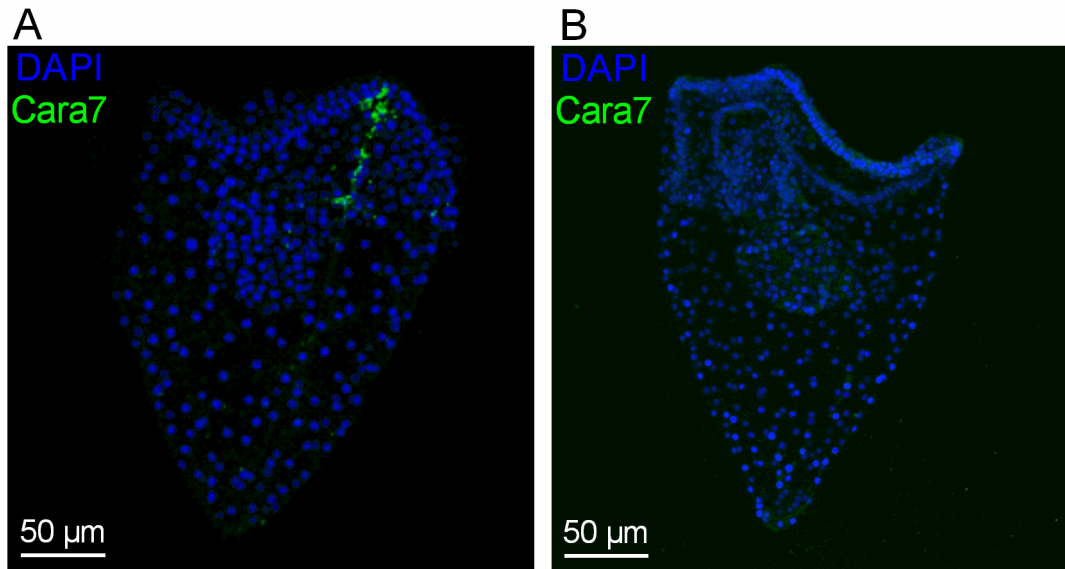


Figure S9. Negative controls for immune-labeling experiments. (A) Positive immuno-reactivity of the polyclonal Cara7-specific antibody in pluteus larvae raised for four days under control conditions. Pluteus larva were stained with the Cara7 antibody (green) and DAPI counter-stain (blue). (B) Negative control by omitting the primary antibody demonstrated no auto-fluorescence or unspecific binding of the secondary antibody.

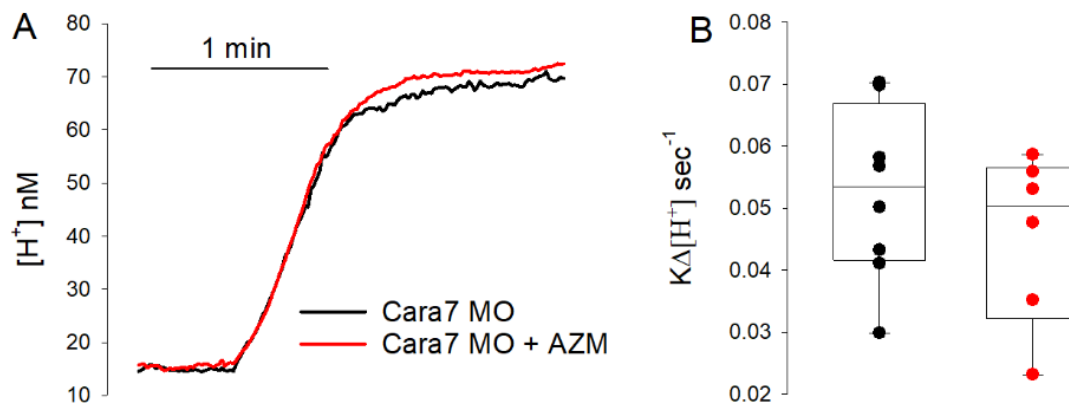


Figure S10. Extracellular carbonic anhydrase activity measurements using pH selective micro-electrodes. (A) Real time $[H^+]$ recordings of OOE relaxation kinetics at the cell surface of Cara7 knock-down larvae (PMCs) in the presence of 0.1% DMSO or 100 μM of acetazolamide (AZM). (B) Rate constants ($K\Delta[H^+]$) of the pH change in Cara7 knock-down larvae on the presence in the presence of 0.1% DMSO or 100 μM of AZM. We obtained $K\Delta[H^+]$ –values from non-linear least-squares curve fits like those presented in (A) demonstrating no significant difference in CO_2 hydration rates in the presence or absence of 100 μM AZM at the cell surface of Cara7-morphants ($n = 6$).

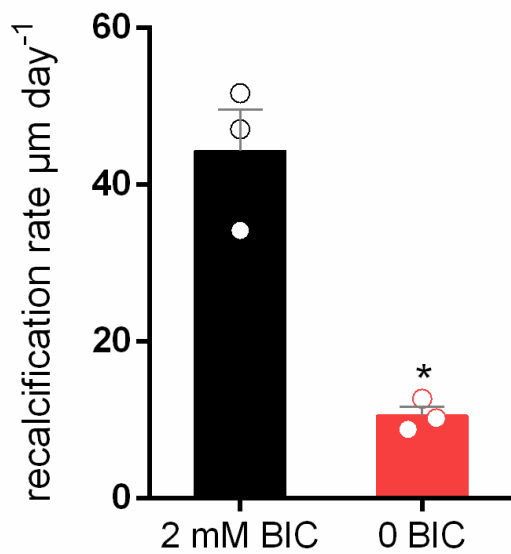


Figure S11. Dependence of calcification rates on the presence of environmental $[\text{HCO}_3^-]$. Recalcification rates in the presence (2.0 mM) or absence (0 mM) of seawater HCO_3^- . Decalcified larvae were transferred to artificial seawater (ASW) with the respective HCO_3^- (BIC) concentrations in closed vessels to prevent equilibration of the low HCO_3^- solution with environmental CO_2 . Skeleton recalcification rates are expressed as $\mu\text{m day}^{-1}$ and values are presented as mean \pm SEM (Student's t-test * $p < 0.05$)

SI References

1. W. W. Chang, *et al.*, An otopetrin family proton channel promotes cellular acid efflux critical for biomineralization in a marine calcifier. *Proc. Natl. Acad. Sci. U. S. A.* 118, e2101378118 (2021).
2. M. Y. Hu, *et al.*, A SLC4 family bicarbonate transporter is critical for intracellular pH regulation and biomineralization in sea urchin embryos. *Elife* 7, 1–17 (2018).
3. M. Stumpp, *et al.*, Acidified seawater impacts sea urchin larvae pH regulatory systems relevant for calcification. *Proc. Natl. Acad. Sci. U. S. A.* 109, 18192–18197 (2012).

III Dual role of an aquaglyceroporin mediating water and CO₂ conductance identified in the calcifying cells of the sea urchin embryo

Dual role of an aquaglyceroporin mediating water and CO₂ conductance identified in calcifying cells of the sea urchin embryo

Ann-Sophie Matt¹, Alex Quijada-Rodriguez², Marcus Schewe¹, Dirk Weihrauch³, Marian Y. Hu¹

¹Institute of Physiology, Christian-Albrechts-University, Kiel, Germany

²Department of Biology, Wilfrid Laurier University, Waterloo, Canada

³Department of Biological Sciences, University of Manitoba, Winnipeg, Canada

Abstract

Biom mineralization is ubiquitously used by most marine organisms. This efficient and elaborated mechanism is intensively studied, but the mode of action on the cellular level is poorly understood. Here, we report that an aquaglyceroporin (spAQP9) in the sea urchin larva is involved in the cellular calcification process. spAQP9 is exclusively found in the calcifying primary mesenchyme cells and its peak expression at the onset of skeleton formation and stimulation during re-mineralization, suggesting a key role in skeletogenesis initiation and spicule elongation. Expression of *spAQP9* in a heterologous expression system, the *Xenopus* oocyte, revealed H₂O channel activity as well as CO₂ conductance. Immunohistological staining disclosed the sub-cellular localization of spAQP9 in vesicular structures, coincide with the Ca²⁺- rich vesicles, in which ACC precipitation for the calcification process occurs. Furthermore, antibody staining combined with the re-calcification assay revealed two different PCM types regarding spAQP9 sub-cellular allocation, corresponding to an active PMC and a resting PMC. Pharmacological inhibition with Phloretin led to impaired spicule formation and cellular water flux measurements in living larvae, using the Calcein quenching method, showed altered H₂O conductivity in osmotic stress balance. The results of this work revealed another pivotal participator of the sophisticated cellular calcification mechanisms in marine species.

Introduction

Biom mineralization is a widespread evolutionary ancient process, used by organisms from all branches of the tree of life, ranging from bacteria, archaea to eukarya (1). The most abundant minerals generated by marine organisms consist of calcium carbonate that are used to stabilize their skeletons and shells serving their structure and protection (2, 3) (4). Calcification in marine organisms is an intricate process that requires the accumulation of calcium and carbonate ions within confined intra- and extracellular compartments. This physiological process is prevalent among marine invertebrates such as corals, mollusks, echinoderms and calcareous algae (5–8) and requires the interplay of different enzymes, transporters and matrix proteins to generate and maintain specific conditions promoting the mineralization process (9, 10).

The sea urchin larva has a calcitic endoskeleton and is a well-established model system to study the cellular processes underlying mineralization (1, 11, 12). In the sea urchin larva the first step of mineral formation occurs within the calcifying primary mesenchyme cells (PMCs) that form a syncytial cable surrounding the larval skeleton (12, 13). Amorphous calcium carbonate (ACC) is produced and stabilized in intracellular vesicles that are exocytosed to the mineralization front where high Mg^{2+} calcite is formed (14). This intracellular formation of $CaCO_3$ requires transport of Ca^{2+} , carbon species, other major ions like Na^+ and Cl^- ions, water as well as acid-base equivalents to control specific pH conditions (15–17) within the calcifying PMCs. While Ca^{2+} ions are suggested to be predominantly absorbed by endocytosis from seawater like fluids, dissolved inorganic carbon can derive from environmental (i.e. HCO_3^-) as well as endogenous metabolic (i.e. CO_2) sources (15, 18, 19). While recent research has revealed key aspects of the cellular carbon concentration mechanism and pH regulation, these transport processes remain unknown for the calcification vesicle. Cryo-STEM EDS analyses of vesicles in PMCS suggested, that in Ca^{2+} rich vesicles, where hydrated ACC is formed, water is progressively removed to form anhydrous ACC that is then deposited towards the calcitic skeleton (5, 20). Accordingly, it is likely that PMCs and potentially also the calcification vesicles have water transport systems to support concentration of calcification substrates and ACC formation (21).

Channels and transporters, located in the cell membrane allow the selective passage of molecules, ions and water across the lipid bilayer. Aquaporins are special integral membrane proteins, which facilitate the transport of water along an osmotic gradient, across cell membranes (22). Since their first discovery by Peter Agre in 1988 (23) aquaporins were associated with a large diversity of biological functions ranging from osmotic regulation over acid-base balance to gas transport in cells and epithelia (24). Aquaporins (AQP) have a conserved structure, consisting of six transmembrane α -helices and two half-transmembrane helices, linked by extra- and intracellular loops and cytoplasmic C- and N-termini

(25). This structure creates a hydrophobic pore where the unique arrangement of amino acid motifs (like NPA signature motif and ar/R) determine the selectivity of the channel (26, 27). Four of these monomers assemble to form a homo-tetramer in the plasma membrane (24) and thus the functional aquaporin can transport four water molecules simultaneously. AQPs were demonstrated to conduct water with exclusion of other solutes as well as gases like CO₂ and NH₃ (25). Within the AQPs, aquaglyceroporins, represent a subfamily of AQPs that differ in their pore composition and pore size leading to different selectivity properties. Hence, aquaglyceroporins not only transport water, but also facilitate the movement of other small uncharged solutes like glycerol, ammonia, CO₂, urea and H₂O₂ (27–31). The aquaglyceroporins (AQP 3, 7, 9, 10) in humans are involved in many processes, including skin hydration, cell proliferation, water permeability (AQP3) (24, 32) and urine concentration (AQP7) (32, 33) in the kidney, gluconeogenesis and glycolysis in the liver, osteoclast differentiation (AQP9) (31, 32, 34) as well as in water and nutrient absorption in the intestine (AQP10) (30). Although their primary function has been largely associated with water transport, their function as gas channels facilitating the passage of CO₂ across the plasma membrane has received considerable attention (35). For example, CO₂ transport via AQPs, has been demonstrated in different organisms, like the tobacco plant (36), red blood cells (35) and marine diatoms (37). These findings highlight the great diversity of physiological processes in which AQPs are involved that go beyond their mere function as water channels (24).

In this work we identified an aquaglyceroporin (spAQP9) in the sea urchin larva that is exclusively found in the calcifying primary mesenchyme cells. We studied its tissue specific expression, sub-cellular localization and provide functional evidence for water and CO₂ conductance using heterologous expression systems. Pharmacological approaches and cellular water flux measurements together with localization and expression studies underline a role of spAQP9 in the mineralization process.

Material and Methods

Larval Cultures

The collection and the care of the adult purple sea urchins (*Strongylocentrotus purpuratus*), as well as preparation of larval cultures were performed as previously described (38).

In silico and structural analysis

Expression of spAQP9 along the first 72 h of development of the sea urchin larva *Strongylocentrotus purpuratus* was taken from the platform Echinobase.org.

The transmembrane protein structure prediction of the amino acid structure of the expressed peptide spAQP9 was depicted with 'MemBrain' <http://www.csbio.sjtu.edu.cn/bioinf/MemBrain/>.

Whole mount in situ hybridization

Whole mount *in situ* hybridization was essentially performed according to the protocol described by Walton (39) with some minor modifications. Briefly, larvae were fixed with 4% PFA/FSW and dehydrated with MeOH and stored at -20°C. Larvae were re-hydrated in an ascending series of MeOH and DEPC-PBST, and fully washed with DEPC-PBST in the final step. Pre-hybridization was performed for at least 1 h at 60°C. Primers for generating and cloning of the probes are listed here: spAQP9-F: AGGCTTCACATCGGTAAGTGG; spAQP9-R: AAATGGTCACCAGATGGAGTCA. Digoxigenin-labeled probes (500 – 1,000 ng/mL) were pre-warmed at 70°C and hybridization was performed at 65°C overnight. Samples were washed with hybridization buffer, wash buffer (50% Formamide, 5x SSC, 0.1% Tween-20) and 2x SSC at 65°C followed by another washing step with 2x SSC at 37°C and by MABT (500 mM Maleic acid, 750 mM NaCl, NaOH, pH 7.5, 0.1% Tween-20) at RT. Samples were washed with MABT for 2 h and transferred to a blocking solution (1x MAB, 2% Block reagent (Roche), 10% sheep serum (Jackson IR), 0.1% Tween-20) for 2 h. Samples were incubated overnight with 1:2,000 sheep anti-Digoxigenin-AP Fab fragments (Roche) antibody at 4°C followed by intensive washing with MABT at least 6 times for 20 min on a shaker at the next day. The color reaction was performed with BM Purple AP (Roche) according to manufacturer's instructions for about 7 – 24 h at 37°C and RT.

Determination of calcification rates under pharmacological inhibition of spAQP9

Eggs were fertilized with sperm and cultured under control conditions in FSW for 48 h at 15°C. After completion of gastrulation, the larvae were transferred into 6 well-plates containing 250 larvae in 10 mL FSW and different concentrations of phloretin (1 µM, 10 µM, 50 µM, 100 µM) were added while 0.1% DMSO served as vehicle control. Samples were taken at 1, 2, 3 and 4 dpf and fixed with 4% PFA/FSW (pH 8.2). Three biological replicates (n=3) of each treatment were performed. The overall morphology was determined including determination of spicule dimensions where the total length of the spicule was measured as well as the post-oral rods and the body rod alone. Images were taken on a Zeiss Observer A1 inverted microscope and images were analyzed using the Zeiss Zen 3.3 (blue edition) software.

Re-calcification assay

To stimulate calcification processes in the sea urchin larva we used a re-calcification assay that was performed as previously described (16). This assay allows a development independent analysis of genetic effects triggered by the calcification process. Briefly, larvae (3 dpf) were exposed to 0.03 M MES buffered FSW adjusted to pH 6.0 for 12 to 15 h to fully dissolve their calcitic spicules. To re-calcify their skeletons, larvae were transferred back into filtered seawater (FSW) (pH 8.0). This transfer day is defined as day 0 (0D), while the following days are defined as 1D, 2D, 3D, 4D, 5D and 6D throughout this manuscript. Samples for molecular analyses were taken at the respective timepoints and further treated according to the methods described below.

Molecular cloning

The primers for cloning and *in situ* probe synthesis were designed with Primerblast (www.ncbi.nlm.nih.gov/tools/primer-blast/) and re-blasted with (blast.ncbi.nlm.nih.gov/Blast.cgi). The transcript sequence of the sea urchin gene *SPU_004511 (LOC584831)* was amplified by Azenta (Genewiz), using the following primers, spAQP9-F1: ACCAAGCACACGTGACTCTA; spAQP9-F2: CGGTTGTTAACGCTCTCGTG; spAQP9-R1: GGGTCGCCAGCTCTATACTC; spAQP9-R2: TCCGACCTAAACTCGACGTTA, into pUC57 cloning vector. The cloned vector was cultured in NEB 5 α competent *E. coli* cells. Plasmid extraction using the Monarch Plasmid Miniprep Kit (New England Biolabs) and sequencing (GENEWIZ) was followed by the synthesis of the RNA probes for *in situ* hybridization using M₁₃-F and M₁₃-R primers (38) and the DIG RNA labeling Mix (Roche) according to the manufacturer's protocols.

RT-qPCR and Single cell transcriptomic analyses

RT-qPCR was performed as previously described (40). Briefly, RNA from control and re-calcifying larvae at 0D, 1D, 2D, 3D, 4D, 5D and 6D from three experimental replicates was isolated by using the Direct-zol RNA MicroPrep kit (Zymo Research). RNA samples were reverse transcribed by Super Script IV cDNA synthesis kit (Invitrogen, Waltham, USA) for quantitative RT-PCR. To measure the expression levels of the target genes the 7500 Fast Real-Time PCR System (Applied Biosystems) was used and expression levels of target genes were normalized to the housekeeping gene ELF1 that has been demonstrated to be stable along ontogeny and during skeleton re-calcification (16, 41). The following qPCR primers were used in this study: spAQP9-qF: TGCAAAGACTCCCCTTTAGC; spAQP9-qR: GACATCTGGGTGACTCCATC; ELF1-F: CCGACCTTGGAAAGGGATCG; ELF1-R: ACAGTCGGCCTGTGAGGTTTC. Single cell transcriptomic analyses were carried out as previously described (38, 41). Shortly, single-cell transcriptomic analyses of AQP9 in the sea urchin larva. Single-cell RNA sequencing was performed using the 10x Genomics commercial platform. Dimensional reduction was achieved using uniform

manifold approximation and projection (UMAP) and projections are plotted as dot plots representing each dot as one cell. Unsupervised clustering of cells resulted in several clusters out of which clusters positive for pan-PMC marker genes *Alx1*, *SpP19L* and *SM50* were identified as PMCs. Scaled and normalized counts per cell of 'gene of interest' are shown in different intensity of blue scales. Clusters were identified with special marker genes to the corresponding cell type of the larvae. LOC584831 = *SPU_AQP9* (*spAQP9*).

Morpholino injection

Micro-injection was performed as previously described (40). Briefly, a gene-specific morpholino-substituted antisense oligonucleotides (MO) 5'-TTTAACGCTCTCGTGGGAAGGATA-3' complementary to shortly before the start codon region of the sea urchin *AQP9* gene were obtained from Gene Tools (Oregon). In addition, a scramble MO 5'-CCTCTTACCTCAGTTACAATTTATA-3' that has no biological target in the sea urchin was used to obtain the control group. The MOs were dissolved in injection Buffer (20 mM Hepes, 120 mM KCl, 24% Glycerol, pH 8.0) and were injected into the freshly fertilized egg (one-cell stage) using a micro-injection system (Picospritzer III, Parker) mounted on an inverse microscope (Zeiss Observer D1) equipped with a cooling stage.

Water flux / Volume change of PMCs with Calcein-Measurements

Measurement of cell volume-changes during exposure to different osmotic conditions were used to determine membrane water permeabilities of PMCs. These measurements were performed using the fluorescence dye Calcein-AM that accumulates in the cytosol and that responds to concentration increases by quenching of the fluorescence signal Kitchen et al. (42). After removal of the ectoderm by the bag isolation method and incubation with 5 μ M Calcein-AM for about 90 minutes, larvae were immobilized on 1% Protamine sulfate coated coverslips that were attached to the bottom of a perfusion chamber. The fluorescence intensity was monitored on an inverted microscope (Zeiss, Axiovert 135) equipped with an appropriate light source and the imaging software (VisiView, Visitron Systems GmbH). From each larva (3-4 dpf), few PMCs along the spicule were recorded and treated as one replicate ($n = 1$). At least six replicates were measured under control conditions only containing 0.1% DMSO or in the presence of Phloretin at a final concentration of 100 and 200 μ M. To measure cellular water flux, the surrounding medium (FSW) was changed from filtered seawater (FSW) (1000 mosmol/L) to a hyperosmotic FSW where D-Mannitol was added to obtain 1750 mosmol/L). After 10 min in this hyperosmotic solution PMCs were exposed back to control FSW. The inhibitor measurements were executed as paired measurements, with a first experiment control and hypertonic solutions containing only the vehicle DMSO followed by a second experiment where the inhibitor

Phloretin was added from the start of the experiment. Fluorescence changes of Calcein-AM during the hyperosmotic treatment were plotted against time and analyzed by the following non-linear function: $Y=(Y_0 - \text{Plateau}) \cdot \exp(-K \cdot X) + \text{Plateau}$.

The Plateau is the Y value at infinite times, which indicates the relative total water efflux from the PMCs. K represents the rate constant, which reflects the speed of water efflux across the PMC plasma membrane under control conditions or in the presence of Phloretin.

Immunofluorescence (IF) staining and western blot (WB) analysis of the sea urchin spAQP9 protein

IF and WB analysis were performed as previously described. Briefly, for IF larvae were fixed with 4% PFA/FWS for 10 min, washed with PBS and blocked with PBS containing 5% bovine serum albumin (BSA) for at least 1 h at RT. Afterwards the larvae were incubated overnight at 4°C with the affinity purified polyclonal antibody (dilution 1:500) raised against the sea urchin spAQP9 synthetic peptide (**H-CHHPHKISSRKAKGES-NH2**) (Eurogentec, Belgium). After intensive washing with PBS, larvae were incubated with the secondary antibody, a fluorophore-conjugated Alexafluor 488 anti-rabbit IgG (Invitrogen) at a dilution of 1:300, for 1 h at RT in the dark. After washing with PBS, larvae were mounted on glass slides and were embedded in Moviol/DABCO containing DAPI. Pictures were taken on a confocal microscope equipped with an Airyscan function (LSM800/P2, Zeiss) and analyzed with Zen 3.3 blue edition.

For WB, 1000 larvae were collected and frozen at -80°C without any remaining seawater. For SDS-Page samples were weighed and proteins were extracted by direct mixing with 1:1 (w/vol) 2x Lämmli loading buffer. Samples were incubated at 95°C for 5 min and proteins were fractionated by SDS PAGE on a 10% polyacrylamide gel and blotted to a PVDF membrane (Bio-Rad), using a tank blotting system (Bio-Rad). Blots were blocked for at least 1 h at RT with PBS-Tween buffer containing 5% bovine serum albumin (BSA). Afterwards the blots were incubated in a 1:7,500 dilution of the primary antibody at 4°C overnight. Following washing with PBS-T buffer the blots were incubated for 15 min at RT with GAPDH antibody in a 1:1,000 dilution. After intensive washing with PBS-T buffer the blots were incubated for 1 h at RT with the secondary antibody a peroxidase-conjugated goat anti-rabbit IgG (Dianova, Hamburg, Germany) at a 1:20,000 dilution. After washing with PBS-T buffer the protein signals were detected using the ECL Select Western Blotting Detection Reagents (GE Healthcare, Munich, Germany) and pictures were taken on a Gel Doc 2000 system equipped with a CCD camera (Bio-Rad) and evaluated with ImageLab.

Western blot analysis was additionally used to validate our spAQP9 knock-down. Approximately 300 larvae of spAQP9 or scramble MO injected larvae were collected and used for WB analysis as described above. The spAQP9 protein abundance was normalized to GAPDH protein concentrations.

Oocyte preparation, coding RNA synthesis and cRNA injection

Heterologous expression of the sea urchin spAQP9 in *Xenopus* oocytes was performed as previously described (41). *Xenopus* oocyte lobes were obtained from tricaine anesthetized *Xenopus laevis* frogs and incubated in OR2 solution containing (mM): 82.5 NaCl, 2.0 KCl, 1.0 MgCl₂, 5.0 HEPES (pH 7.4) substituted with 2 mg/mL collagenase type II (Sigma-Aldrich/Merck, Germany) for 1 h to remove residual connective tissue. Isolated oocytes were stored at 16.9 °C in ND96 solution containing (mM): 96.0 NaCl, 2.0 KCl, 1.8 CaCl₂, 1.0 MgCl₂, 5.0 HEPES (pH 7.4) supplemented with Na-pyruvate (275 mg/L), theophylline (90 mg/L), and gentamicin (50 mg/L). SpAQP9 was subcloned into the dual-purpose vector pFAW. cDNA was linearized with NheI or MluI, respectively and cRNA was synthesized *in vitro* using the SP6 or T7 AmpliCap Max High Yield Message Maker Kit (Cellscript, USA) and stored in stock solutions at -80 °C. The quality of cRNA was tested using gel electrophoresis and cRNA was quantified with the NanoDrop 2000 UV-Vis spectrophotometer (Thermo Fisher Scientific, USA). Oocytes were injected with 36 nL cRNA suAQP9 (0.5 µg µL⁻¹) and incubated at 16 °C for four days until water and CO₂ conductance experiments were performed. Sham injected oocytes served as control group. For the measurement of CO₂ conductance by suAQP9 two methodologically independent methods were used that are described below.

Oocyte swelling experiment

For the measurement of water conductance of control or spAQP9 expressing oocytes were transferred to 2 mL oocyte solution ND96 that contained 0 mM NaCl. This hypotonic solution leads to an uptake of water that depends on the permeability of the oocyte membrane. Water permeabilities were determined for control and spAQP9 expressing oocytes. In addition, the effect of Phloretin a specific mammalian AQP9 inhibitor was tested by adding different concentrations (final concentration: 10 µM, 50 µM, 100 µM, 200 µM and 500 µM) to the hypotonic ND96 medium. Swelling of the oocytes was recorded by taking images every 30 seconds on a microscope equipped with a camera. The diameter of the oocytes was measured using Zeiss Zen blue 3.3 software and converted to volume assuming a spherical shape. The oocyte volume was normalized to their own starting volume, so only the increase in volume was used for our analyses.

CO₂ conductivity measurements using micro-electrodes in oocytes

The first approach to determine CO₂ conductivity of spAQP9 in oocytes is based on the change in surface pH when the cell is exposed to a high CO₂/HCO₃⁻ solution as described earlier (43, 44). H⁺-selective micro-electrodes were fabricated as previously described (15) and positioned at the surface of an oocyte that was held in place within a perfusion chamber. First, the oocyte was perfused with a

regular ND96 solution (pH 7.4) and surface pH was measured by our H⁺-selective microelectrode. Then the oocyte was exposed to a ND96 solution (pH 7.4) that contained 5% CO₂ and 33 mM HCO₃⁻. This solution leads to alkalization of the oocyte surface due to the influx of CO₂ into the oocyte, that acts as a CO₂ sink. Accordingly, the carbonate system is shifting towards the CO₂ side, reducing HCO₃⁻ and H⁺ leading to an increase in oocyte surface pH that depends on the conductivity of CO₂ by the plasma membrane. This increase in oocyte surface pH was used as a measure to determine CO₂ conductivity in control and suAQP9 injected oocytes.

Oocyte CO₂ excretion experiment

The second method examined the CO₂ transport capability of spAQP9 by measuring the excretion rate of CO₂ in high CO₂ pre-loaded sham and spAQP9 oocytes modified from a previously described protocol for coral Rh proteins expressed in *Xenopus* oocytes (45). Briefly, groups of three oocytes were incubated for 15 min in hypercapnic OR2 (in mmol L⁻¹ 82.5 NaCl, 2.5 KCl, 1 MgCl₂, 1 CaCl₂, 1 Na₂HPO₄, 5 HEPES, 5% CO₂, pH 7.5 set by titration with NaHCO₃). After the incubation in hypercapnic OR2, the group of oocytes was rapidly transferred into a 100 mL beaker of normocapnic OR2 (in mmol L⁻¹ 82.5 NaCl, 2.5 KCl, 1 MgCl₂, 1 CaCl₂, 1 Na₂HPO₄, 5 HEPES, pH 7.5) to wash off excess CO₂/HCO₃⁻ and then transferred into a tube containing 95 μL of fresh normocapnic OR2 to create a large oocyte to media pCO₂ gradient. A 45 μL sample of media was immediately taken with a gas-tight Hamilton syringe (t = 0 min), followed by a second 45 μL sample after 1 minute (t = 1 min). The CO₂ concentration of the media samples at 0 and 1 minute was measured in triplicate (15 μL per measurement) using a custom-built total CO₂ analyzer employing a Licor 850 for CO₂ detection. For a detailed explanation of the custom-built CO₂ analyzer, standardization and data analysis see (46). The change in total carbon of the media was used as an indicator of CO₂ excretion as native *Xenopus* oocytes have been previously shown to exhibit no measurable HCO₃⁻ permeability so any measured change in total carbon can be safely attributed to CO₂ excretion (47). Samples were compared to a NaHCO₃ standard curve ranging from 0-1600 μmol L⁻¹ and produced an R² of 0.99. The CO₂ excretion rates were calculated according to the following equation:

$$CO_2 \text{ excretion rate} = \frac{(CO_{2_1} - CO_{2_0}) \times V}{3 \text{ oocytes} \times t}$$

Where CO_{2_1} is the CO₂ concentration after 1 minute, CO_{2_0} is the CO₂ concentration at 0 minutes, V is the flux volume in liters, and t is the flux time in minutes. The integrity of the oocytes in all tubes was assessed under a microscope at the end of the sampling period and if any damage to the membranes or lysis of oocytes had occurred those oocytes were excluded from the analysis.

Statistical analyses

Our data was tested for variance homogeneity (Levene-test) and was analyzed for statistical significances using GraphPad Prism8. IHC signal validation, spAQP9 CO₂ conductivity measurements, morpholino injection validation and Calcein-AM measurement were analyzed using the student's t-test (two-sided) with p-value * < 0.05, ** < 0.01, *** < 0.001 and **** < 0.0001. qPCR, spAQP9 water conductivity measurements, calcification rate determination and morphometric analyses of spAQP9 knock-down results were analyzed for significance using one-way ANOVA, followed by Post-Hoc tests.

Results

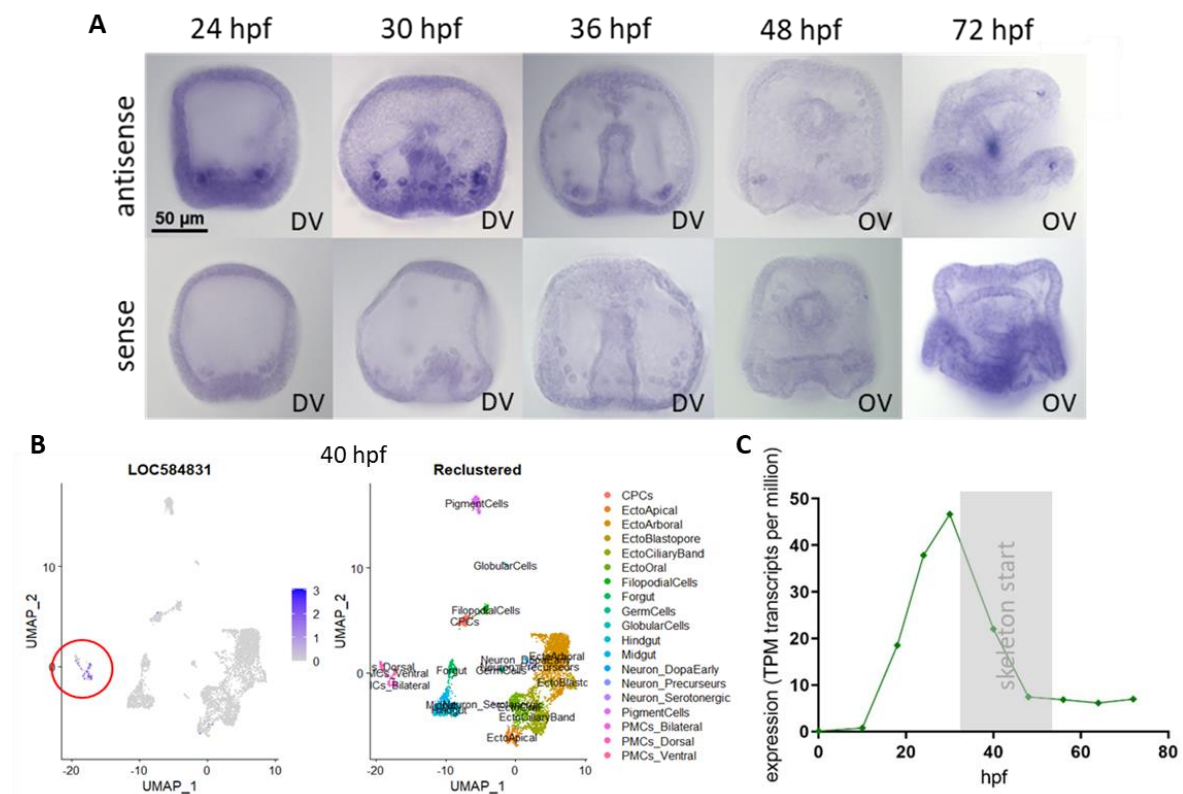


Fig. 1. Expression pattern of spAQP9 in the sea urchin larva. (A) Whole-mount *in situ* hybridization using antisense and sense probes against spAQP9 at 24, 30, 36, 48 and 72 hpf. Abbreviations: OV, oral view; DV, dorsal view. (B) . Single cell transcriptomes were obtained for one developmental time point, 40 hpf at the onset of skeletogenesis. PMC cell populations are indicated by red circle. (C) Ontogeny expression pattern of spAQP9 along the first 72 hpf [data obtained from Echinobase.org] TPM = transcripts per million.

Identification and localization of water channels spAQP in calcifying cells. Gene mining in the genomic databases of the purple sea urchin *Strongylocentrotus purpuratus* for aquaporins (AQP) confirmed the

presence of only one AQP that is exclusively expressed in the calcifying PMCs, *spAQP9* (LOC584831). Whole mount *in situ* hybridization results (Fig. 1 A) and single-cell transcriptomic analyses (Fig. 1 B) verified the expression primarily in PMCs throughout the developmental stages of the sea urchin larva, including the initial cluster of skeleton formation in the gastrula stage as well as PMCs of the postoral and antero-lateral rods in the pluteus larva. The expression pattern of *spAQP9* shows a peak at 30 hpf that steeply decreases until a plateau at 48 hpf is reached (Echinobase.org) (Fig. 1 C). The expression peak at 30 hpf coincides with the initiation of skeleton formation.

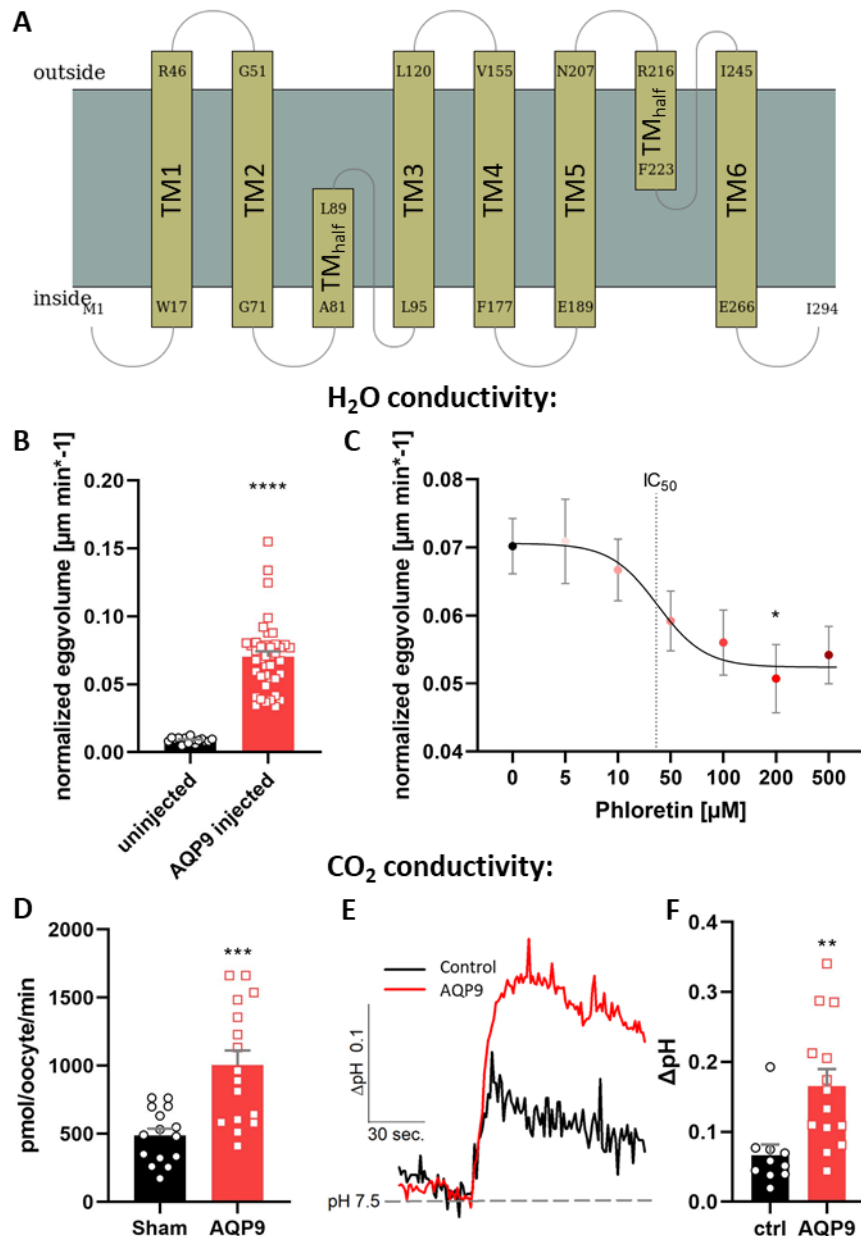


Fig. 2. Characterization of sea urchin larval *spAQP9* in *Xenopus* oocytes. (A) Transmembrane peptide topology of *spAQP9* predicted and created with *MemBrain 3.1*. (B) Swelling experiments with *Xenopus* oocytes expressing the *spAQP9* demonstrated water channel activity of *spAQP9*. This was performed by measuring the oocyte volume increase in $\mu\text{m}^3 \cdot \text{min}^{-1}$ during exposure to a hypotonic solution. Every single measurement of the oocyte volume was normalized to their own starting volume as 100%.

Water injected oocytes, (black circles), as well as spAQP9 injected oocytes (red squares) were measured. Values are presented as mean \pm SEM; n = 15-41, Student's t-test: ****p < 0.0001. (C) Water permeability measurements performed in the presence of seven different Phloretin concentrations (0, 5, 10, 50, 100, 200, 500 μ M). As control (0 μ M) only the vehicle DMSO was added. Phloretin inhibits oocyte swelling in a dose-dependent manner with an IC₅₀ value of 38 μ M. Values are presented as mean \pm SEM. n = 12-41, *p < 0.05 (one-way ANOVA + post-hoc test [Holm-Sidak]). (D, E+F) CO₂ conductivity measurements of sham and spAQP9 injected *Xenopus* oocytes using two different methods. (D) CO₂ conductance was measured by the rate of CO₂ release in control and spAQP9 expressing Oocytes after equal CO₂ preloading. The bar plot depicts CO₂ conductivity as Oocyte CO₂ release rate (pmol per oocyte per minute) of control oocytes (sham, black circles, n = 15) and spAQP9 injected oocytes (red squares, n = 16). Values are expressed as mean \pm SEM; Student's t-test: ***p < 0.001. (E) H⁺-selective microelectrode measurements at the oocyte surface in combination with high CO₂ solutions were used to measure CO₂ permeabilities in control and spAQP9 expressing oocytes. H⁺ change (converted in pH) at the oocyte surface over time when perfused with 5% CO₂/33 mM HCO₃⁻ solution, which reflects the CO₂ transport into the oocyte. Black line = control, red line = AQP9 injected oocytes. (F) This bar plot depicts the average Δ pH after perfusion with 5% CO₂/33 mM HCO₃⁻ solution of control oocytes (black circles) and spAQP9 injected oocytes (red squares). Values are presented as mean \pm SEM; n = 10-14; Student's t-test: **p < 0.01.

Water and CO₂ conductance by spAQP9. The sea urchin spAQP9 shows the same topology as other AQPs (Fig. 2 A), consisting of six transmembrane domains, two half transmembrane domains and cytoplasmic C- and N-termini. Heterologous expression of spAQP9 in *Xenopus* oocytes was used to characterize the conductance properties of this channel for water and CO₂. Exposure of spAQP9 injected oocytes to a hypotonic solution (ND96 + 0 mM NaCl) induced a volume increase by water influx, of $0.071 \pm 0.005 \mu\text{m}^3 \text{ minute}^{-1}$. In contrast, the volume increase of sham injected oocytes subjected to the hypotonic solution was only $0.009 \pm 0.0005 \mu\text{m}^3 \text{ minute}^{-1}$ (Fig. 2 B). In the presence of Phloretin, an inhibitor for AQP9, a dose-dependent decrease in oocyte swelling upon exposure to the hypoosmotic solution with an IC₅₀ of 38 μ M was observed (Fig. 2 C). Control oocytes were treated equally and showed no effect of Phloretin.

Two different methods using *Xenopus* oocytes were performed to test if spAQP9 also facilitates the conductance of CO₂. The first experimental approach used the CO₂ efflux method where CO₂ release was measured in control and spAQP9 injected Oocytes after equal CO₂ pre-loading. spAQP9 injected oocytes had a significant higher conductivity for CO₂ of $1004.3 \pm 109.5 \text{ pmol min}^{-1}$ compared to sham injected oocytes (control) that had an excretion rate of $487.2 \pm 50.9 \text{ pmol min}^{-1}$ (Fig. 2 D). The second experimental approach to access CO₂ permeability of spAQP9 used changes in oocyte surface pH during exposure to a high pCO₂ (5% CO₂/33 mM HCO₃⁻) solution. pH recordings using H⁺-selective micro-electrodes, demonstrated a decrease in surface [H⁺] (increase in pH) at the surface of oocytes when perfused with the high pCO₂ (5% CO₂/33 mM HCO₃⁻) solution. In control oocytes Δ pH values were 0.07 ± 0.02 while those expressing spAQP9 had Δ pH values of 0.17 ± 0.02 (Fig. 2 E+F). Both

experiments demonstrated significantly increased CO₂ permeabilities in oocytes that expressed spAQP9.

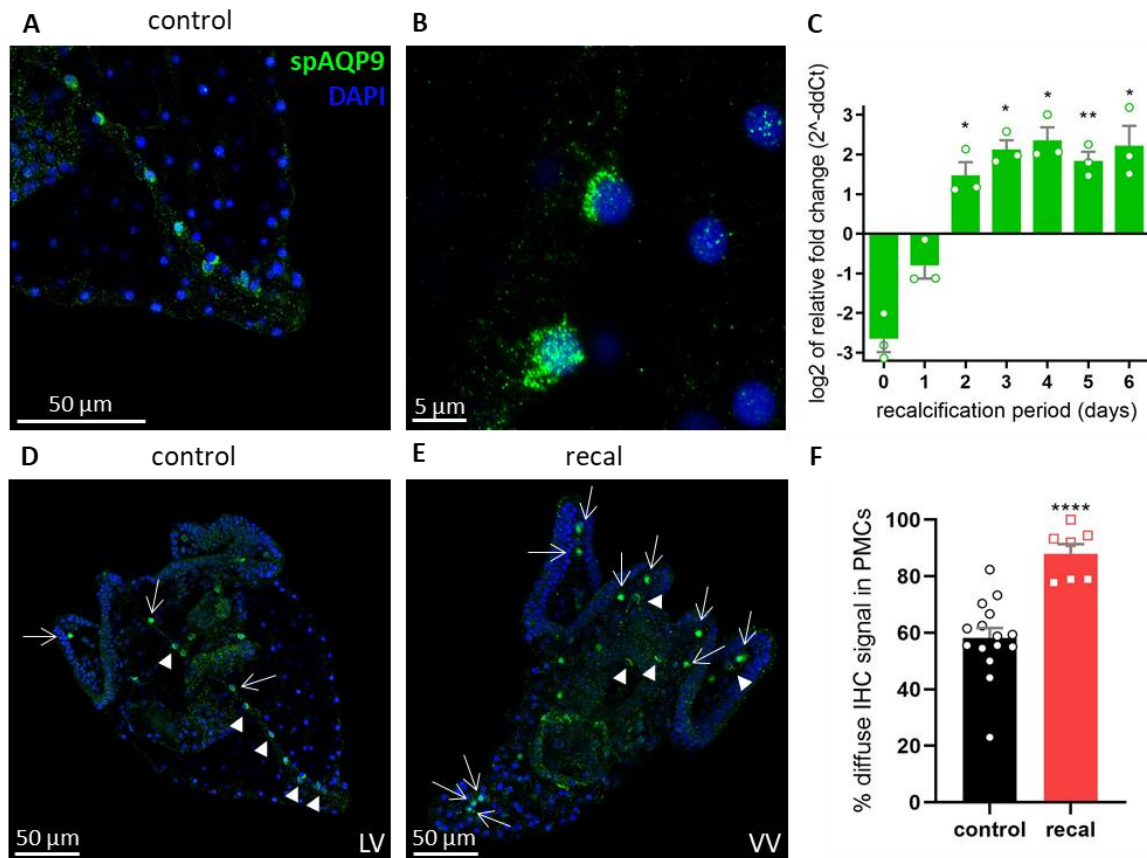


Fig. 3. Immunohistological localization of spAQP9 in the sea urchin larva. (A) Positive immunoreactivity of the polyclonal spAQP9-specific antibody in pluteus larvae raised for 4 days under control conditions. (B) High-magnification image (63x) of the positive immunoreactivity in PMCs of the body rod in the scheitel area. (C) Expression levels of spAQP9 under recalcification conditions along the period of 6 days. Expression levels were normalized to the internal control *EF1a*. Values are presented as mean \pm SEM; n = 3, one-way ANOVA [Post-Hoc test]: *p < 0.05; **p < 0.001. (D) Positive immunoreactivity spAQP9 antibody in pluteus larvae raised for 4 days under control conditions. White arrows point on diffuse IHC signal in PMCs, white arrowheads point on crescent shaped IHC signal. (E) Positive immunoreactivity of spAQP9 antibody in re-calcifying pluteus larvae 4 dpd (days post decalcification). Lateral view (LV), ventral view (VV) of pluteus larvae stained with the spAQP9 antibody (green) and DAPI counter stain (blue). Arrows point on diffuse IHC signal in PMCs, arrowheads point on crescent shaped IHC signal. (F) Bar plot depicting the percentage of diffuse spAQP9 signals in PMCs under control conditions (black bar) or re-calcification conditions (red bar). Values are presented as mean \pm SEM; n = 7, 15; Student's t-test: ****p < 0.0001.

Subcellular localization of spAQP9 in control and re-calcifying larvae. Immunohistological analyses with our spAQP9 antibody demonstrated positive immunoreactivity in PMCs but not in other tissues (Fig. 3 A). Positive spAQP9 immunoreactivity was detected in most PMCs along the entire spicule. Higher magnification revealed that spAQP9 is located in subcellular structures resembling intracellular

vesicles with a diameter ranging between 140 - 220 nm (Figure 3 B). Interestingly, two distinct patterns of spAQP9 positive vesicles were observed in PMCs. One population of PMCs had a crescent shape organization of spAQP9 positive vesicles around the nucleus, facing the side of the spicule. The other population had a diffuse signal of spAQP9 positive vesicles evenly distributed within the whole cell (Fig. 3 B).

Gene expression analyses of re-calcifying larvae demonstrated a drastic decrease of *spAQP9* expression by -2.65 ± 0.27 fold at day 0, when larvae were transferred from the low pH treatment back to control pH conditions compared to control larvae of the same age that stayed at control pH conditions. At day 1 of re-mineralization, *spAQP9* expression levels returned back close to control levels of -0.8 ± 0.27 fold. In the following three days where highest rates of skeleton re-mineralization occur *spAQP9* expression levels significantly increase to peak levels of 2.36 ± 0.26 fold. A significant increase of *spAQP9* expression was still seen at day 6 where skeleton remineralization rates decreased back to control levels (Fig. 3 C). During the phase of intense skeleton re-mineralization (i.e. 3-4 days of re-mineralization) immunohistochemical analyses demonstrated an increase in the number of PMCs that have the diffuse IHC signal (Fig. 3 E+F). While only 58.2 ± 3.4 % of all spAQP9 positive PMCs have the diffuse signal in control larvae, $87.9 \pm 3.2\%$ were detected in re calcifying larvae (Fig. 3 D).

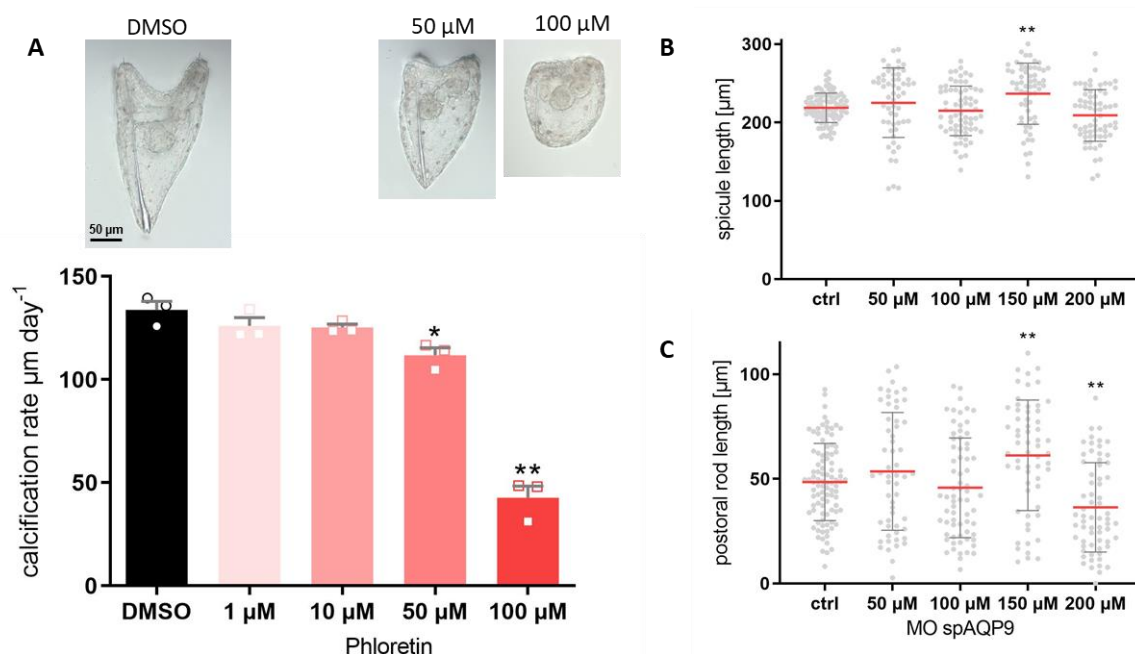


Fig. 4. Morphology changes of the larvae under spAQP9 knock-down and inhibition by Phloretin. (A) Determination of calcification rates in normally developing larvae under pharmacological inhibition of AQP9 by five different concentrations (0, 1, 10, 50, 100 μM) of Phloretin added after 2 dpf shortly after gastrulation to avoid collateral effects on other developmental processes. 0.1% DMSO (0 μM Phloretin) served as the vehicle. Values are presented as mean \pm SEM; n = 3, *p < 0.05; **p < 0.001 (one-way

ANOVA + post-hoc test [Holm-Sidak]). Representative pictures of larvae developing their skeletons under different Phloretin concentration (upper panel). (B) Whole spicule length of larvae 4 dpf was determined for larvae injected with different concentrations of AQP9 morpholino (50, 100, 150, 200 μM) while 200 μM scramble MO (ctrl) injected larvae served as control. Morpholino injections were repeated three times and individual measurements ($n = 41-68$, grey dots) are presented including mean (red lines) \pm SEM, $**p < 0.001$ (one-way ANOVA + post-hoc test [Holm-Sidak]). (C) Determination of the postoral rod length of larvae 4 dpf in ctrl MO and spAQP9 MO injected larvae.

Phloretin effect on skeleton formation. Using a pharmacological approach, we investigated the contribution of spAQP9 to the calcification process. Larvae were raised under control conditions until 2 dpf until completion of gastrulation. Thereafter, larvae were exposed to different concentrations of Phloretin, and the calcification rate in $\mu\text{m day}^{-1}$ was determined. Phloretin reduced calcification rates in a dose-dependent manner from $133.8 \pm 4.1 \mu\text{m day}^{-1}$ in larvae only exposed to the vehicle (0.1% DMSO) down to $111.9 \pm 3.6 \mu\text{m day}^{-1}$ and $42.6 \pm 5.7 \mu\text{m day}^{-1}$ at a concentration of 50 μM and 100 μM , respectively (Fig. 4 A). No collateral effects of phloretin were observed on the development of the tripartite digestive tract. spAQP9 morpholino (MO) injected larvae revealed no significant reduction in spicule length (Fig. 4 B). Considering just the postoral rod length, with injection of 200 μM spAQP9 MO the rod length was reduced to $36.4 \pm 2.6 \mu\text{m}$ compared to $46.1 \pm 1.9 \mu\text{m}$ injected with the control morpholino (Fig. 4 C). Due to no clear impact of spAQP9 knock-down on the skeleton development, a second morpholino will be used for further validation.

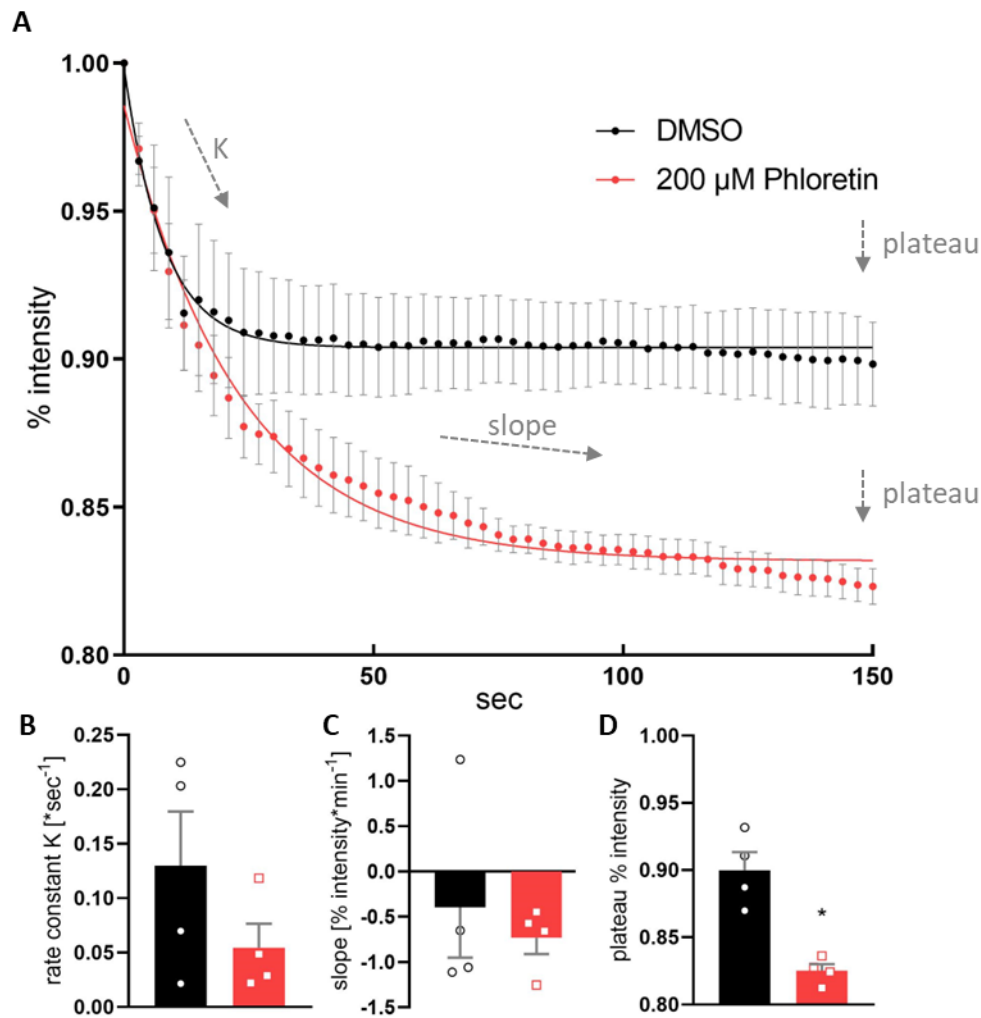


Fig. 5. Cellular water permeability measurements using the Calcein-AM quenching-method in PMCs of the sea urchin larva. (A) The water efflux from PMCs was measured by the quenching of cytosolic Calcein fluorescence intensity over time during exposure to a hypertonic solution. Cellular water efflux kinetics were determined under control (0.1% DMSO) conditions and in the presence of 200 μM Phloretin. Values are expressed as mean \pm SEM; $n = 4$. (B) The rate constant K in sec^{-1} reflecting the speed of water efflux was determined by a nonlinear fit, one phase decay. In addition, the slope of % fluorescent intensity min^{-1} reflecting further water efflux from PMCs (C) as well as the final plateau indicating the relative total water efflux from PMCs (D) were determined. Student's t-test: * $p < 0.05$.

To test whether the water channel activity of spAQP9 is also measurable under physiological conditions in the organism, we performed live-cell imaging measurements of the larvae using Calcein-AM. The fluorescent intensity of Calcein decreases by water efflux and shrinkage of the cell, due to quenching of the dye. By adding the hypertonic solution, the fluorescence intensity decreases over time and a plateau of $0.9 \pm 0.01\%$ is reached (Fig. 5 A, black line). In the presence of the inhibitor Phloretin, the rate constant K is decreased from $0.13 \pm 0.04 \text{ sec}^{-1}$ under control conditions to $0.05 \pm 0.02 \text{ sec}^{-1}$ (Fig. 5 B), suggesting an almost significant decreased water efflux. This decrease in fluorescence intensity over time is expressed as slope in % intensity min^{-1} and extended from -0.4 ± 0.48 under control conditions

to -0.83 ± 0.15 by inhibition with Phloretin with no significant differences (Fig. 5 C). However, inhibition by Phloretin leads to a significantly lower plateau at the end of the hypertonic treatment with $0.83 \pm 0.004\%$ compared to control conditions $0.9 \pm 0.02\%$ (Fig. 5 D).

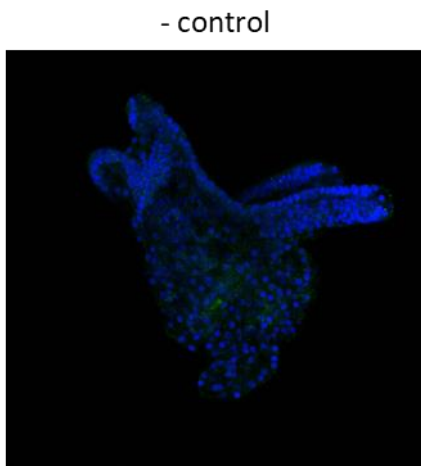


Fig.1 S1. Negative control for immunocytological localization of spAQP9. Negative control by omitting the primary antibody in a pluteus larvae raised for 4 days under control conditions. Acquisition settings were maintained the same as in the positive staining. DAPI was used as counter staining (blue).

Discussion

In the present work we demonstrated the presence of an aquaglyceroporin, spAQP9, that is exclusively expressed in the calcifying primary mesenchyme cells (PMCs) of the sea urchin larva. This was proven by *in silico* analysis, single-cell RNA sequencing, *in situ* whole mount hybridisation and western blot analysis. Expression levels along the early embryonic development of the sea urchin larva showed a peak at 30 hpf, shortly after initiation of skeleton formation. This indicates, that spAQP9 is presumably involved in the initiation of skeletogenesis as well as elongation of the spicule. *In silico* analysis of the present work demonstrated, that spAQP9 is an aquaglyceroporin with the typical structure consisting of six transmembrane helices and two short ones, as well as the characteristic NPA motif, similar to the mammalian homologous.

Further functional characterization of spAQP9 were conducted using heterologous expression in *Xenopus* oocytes. Swelling experiments induced by a hypotonic solution revealed a significantly increased water permeability in spAQP9 expression oocytes. Addition of the AQP9 inhibitor Phloretin led to a decrease in oocyte water uptake rate in a dose-dependent manner with an IC_{50} of $38 \mu\text{M}$. Phloretin is a compound that has been demonstrated to inhibit specific AQP isoforms, including AQP3

and AQP9. Earlier studies could clearly demonstrate that the mammalian AQP9 and AQP3 promote, water permeability when expressed in heterologous expression systems, such as *Xenopus* oocytes (48), as well as proteoliposomes (49), and that water conductance was strongly inhibited by treatment with 100 μ M Phloretin. In addition, inhibitory effect of 100 μ M Phloretin on water reabsorption was also confirmed *in vivo* in the intact rat epididymis using a perfusion approach (50). These results provide a strong line of evidence, that the sea urchin spAQP9 protein encodes an aquaglyceroporin similar to its mammalian homologues, that promotes water conductance in PMCs.

Since spAQP9 shares all features with mammalian aquaglyceroporins, it is likely that it may also allow passage of other uncharged small molecules (28, 30, 51). The ability of aquaporins to transport CO₂ was already revealed by earlier research ranging from human erythrocytes, plants and diatoms (35–37, 52). With mass spectrometric measurements using ¹⁸O-labelled CO₂/HCO₃⁻ and perfusion with high CO₂ solution, *Xenopus* oocytes expressing human AQP1 showed a 2-fold increase in *p*CO₂. In the mouse model, Colton null (AQP1^{-/-}) red blood cells showed a reduction of their *p*CO₂ by 60% (35). Using membrane inlet mass spectrometry (MIMS) with ¹⁸O-labelled DIC, Matsui et al. could determine membrane permeability for CO₂ that was increased in diatoms overexpressing *PtAQP2* (37). Other research showed increased membrane permeability of oocytes expressing *NtAQP1* of tobacco to CO₂ by up to 45% by tracking pH_i with microelectrodes and perfusion with a 5% CO₂/95% O₂ solution (36). Moreover, using oocytes expressing rat *rAQP9*, increased permeability to CO₂ has been measured by tracking surface pH with microelectrodes and perfusion with high CO₂/HCO₃⁻ solutions (52). In the present study we performed two different experimental approaches to measure CO₂ conductance by spAQP9. Both methods, including CO₂ release of preloaded oocytes, as well as pH changes during perfusion with a high CO₂/HCO₃⁻ solution at the oocyte surface revealed substantial increases (doubled) in CO₂ conductivity across the oocyte membrane, when expressing spAQP9. It has been suggested, that the transport mechanism for CO₂ is achieved via a tetrameric pore that forms in between the four AQP9 monomers (53). Here our functional characterizations confirm, besides its function as a H₂O channel spAQP9 also promotes the passage of CO₂ across biological membranes.

Immunohistological analysis, conducted in the present work, demonstrated positive immunoreactivity by our custom made spAQP9 antibody mainly in the PMCs, corroborating our previous results from single-cell RNA sequencing and *in situ* hybridization analyses. However, in contrast to our *in situ* hybridization results, where spAQP9 was predominantly detected in highly calcifying PMCs of the scheidel and spicule tips, the IHC signal was visible in almost all PMCs. Interestingly, two different types of IHC signals were observed in PMCs along the spicule rod. One signal was a crescent shape around the nucleus, facing the spicule while the other spAQP9 immunoreactivity pattern was a diffuse signal covering the whole cell. Under higher magnification, it seemed like the IHC signal is situated in small vesicular structures in both, the crescent shaped as well as the diffuse PMC type. Immunohistological

staining performed with re-calcifying larvae showed a different IHC signal pattern in the PMCs, when compared to PMCs from control animals. In fact, the two different IHC signal shapes changed in their relative number with significantly more PMCs having the diffuse signal, while the number of PMCs with the crescent shaped signal was reduced. From these observations, together with an increased expression in *spAQP9* during re-mineralization, we conclude the diffuse IHC signal represents the active state of calcifying PMCs, whereas the crescent shaped IHC signal represents the passive “resting” state. Such functional difference among PMCs have been previously described based on morphological as well as functional evidences, that can be directly related to the calcification process (16, 41).

Here it can be hypothesized, vesicular trafficking of *spAQP9* is potentially involved in mediating water permeabilities of the plasma membrane or within subcellular vesicles. The vesicles, detected by our *spAQP9* antibody, had a diameter ranging between 140 – 220 nm. In actively calcifying PMCs these vesicles were evenly distributed across the entire cytoplasm, resembling the sub-cellular localization of Ca^{2+} -rich vesicles, identified by Cryo-SEM observations (20, 21). These Ca^{2+} -rich vesicles had a size ranging between 180 - 280 nm and were demonstrated to have different atomic orders reflecting Ca^{2+} in solution over hydrated to anhydrous ACC. The Ca^{2+} concentration in these vesicles ranged between 1-15 M and it was concluded that water must be substantially expelled from these particles (21, 54). Based on the histological and functional analyses of *spAQP9* of the present work, we propose that *spAQP9* may be involved in the transport of water across the vesicle membrane in Ca^{2+} -rich vesicles. However, further studies, including colocalization of *spAQP9* with Ca^{2+} , as well as functional evidence for H_2O transport in vesicles are needed to provide a more definite conclusion.

Moreover, water extrusion from vesicles is essential for ACC maturation, rather than changing order phases. The first phase of ACC is disordered and still contains one molecule of water per calcium carbonate unit. For maturation into the second phase or the full order of calcite, dehydration has to occur (55). This phenomenon is not only seen in the example of sea urchin PMCs, but also in the maturation and hardening of sponge siliceous spicules (56). Also, the hydrated phase is enriched in the most recently deposited parts of the spicule, like in the postoral and anterolateral rod tips (57), which would coincide with our *in situ* hybridization results, where *spAQP9* expression is located areas of highest calcification rates (e.g. rod tips at 3-4 dpf). Accordingly, it can be hypothesized that our inhibition or knock-down of *spAQP9*, impaired water extrusion from the vesicles or the PMCs and thereby negatively impacted the ACC order maturation and further crystallization in the spicule.

Given the dual role of *spAQP9* as a water and CO_2 channel, *spAQP9* may additionally support the calcification process by promoting CO_2 diffusion across PMC membranes. In the sea urchin larva, metabolic CO_2 released by mitochondrial metabolism, represents the main carbon source (60%) for CaCO_3 formation (18, 19). This intracellular CO_2 is proposed to diffuse out of the cell, where it is converted to HCO_3^- by the extracellular carbonic anhydrase *Cara7* in the PMC boundary layer and

transported back into the cell via the $\text{Na}^+/\text{HCO}_3^-$ cotransporter (NBC) *spSlc4a10* (38). *spAQP9* located in the plasma membrane of the PMCs could facilitate the exit of CO_2 out of the cell across the natural gradient from the cell to the environment and thereby supporting HCO_3^- formation and uptake at the plasma membrane. In addition, *spAQP9* in subcellular vesicles may represent a mechanism of post translational activity regulation by translocation, which is a well-known regulatory mechanism for AQPs in the mammalian kidney (58–60). However, it is also tempting to speculate, that increased CO_2 permeabilities in vesicles may serve an uptake and concentration of metabolic CO_2 in calcification vesicles. The similar size and sub-cellular distribution of *spAQP9* positive vesicles compared to Ca^{2+} -rich vesicles described in PMCs, as well as the ACC forming vesicles undergoing phase transformation, underline the possibility that they are the same vesicle type. Given the presence of membrane bound carbonic anhydrase in PMC vesicles (38), high CO_2 permeabilities may support the rapid conversion from CO_2 to HCO_3^- inside the calcifying vesicles. Protons, that are liberated during the formation of HCO_3^- and CO_3^{2-} during CaCO_3 precipitation, must be removed from the vesicle to further promote HCO_3^- formation and calcification. The vesicular network of the PMCs consists of vesicles with different pH conditions, 33% acidic (pH < 6.5), 15% neutral (pH 6.5-7.5) and 52% alkaline (pH > 7.5) (16). It is proposed, that alkaline vesicles are the calcification vesicles, favouring the HCO_3^- formation, and acidic vesicles could possibly be a site of proton storage or serve other cellular functions like lysosomal protein recycling (16). Thus, it remains an important future task to better understand the mechanisms underlying vesicular alkalization in calcifying cells.

To examine the response of *spAQP9* under active calcification conditions in the organism, we used the re-calcification assay in combination with a range of biochemical and molecular investigations. For example, *spAQP9* expression was upregulated when the larvae start to re-calcify their skeleton, from day 2 after de-calcification. This indicates that *spAQP9* is certainly involved in the calcification process. Another potential role of *spAQP9* in the calcification process comes from the ontogeny-dependent expression pattern, as well as the nature of a growing syncytium that continuously increases its cytoplasm including high filopodial activity. The gene expression profile of *spAQP9* reveals peak expression levels starting from 10 hpf up to 48 hpf, suggesting potential involvement in water channel activity during growth of the syncytial cables and the initiation of filopodia formation. Filopodia formation in PMCs occurs in early development of the embryo. At ~30 hpf, mesenchyme cells undergo ingress into the blastocoel, followed by the invagination of the archenteron, leading to the gastrulation (61–63). The ingress requires motility of the cells, likely achieved through filopodia-mediated migration (17, 64). Additionally, PMCs extend filopodia for intercellular connections, leading to cell fusion of the cells and the establishment of the syncytial cord (17, 65). The observed correlation between *AQP9* expression and the concurrent increased water influx, coupled with filopodia formation in motile cells, has already been demonstrated in other systems (66, 67). For example, overexpression

of *AQP9* in HEK-293 cells resulted in rapid influx of water and subsequent filopodia formation (67). Similarly, *AQP9* expression in fibroblasts induced the generation of numerous filopodia, promoting cellular motility, whereas mock-transfected cells lack filopodia (66). Furthermore, cell volume growth of the PMCs could contribute to syncytial cable elongation during skeleton development that also requires an uptake of water to keep up with the increase in cytoplasmic volume. Moreover, filopodia may serve as point of interaction with other cell types, such as blastocoelar filopodia cells, blastoderm and epithelial cells (16).

Furthermore, pharmacological inhibition of spAQP9 by addition of Phloretin after gastrulation of the larvae showed a massive reduction of the calcification rate. While our heterologous expression experiments clearly demonstrated an inhibition of spAQP9 by Phloretin, we cannot rule out that Phloretin also affects other transport systems located in the PMC membrane. For example, Phloretin has been demonstrated to inhibit voltage gated K^+ channel activity in nerve fibres of *Xenopus* (68) as well as the K^+ conductance and Na^+ channel gating in squid giant axons (69). Other studies demonstrated an inhibitory effect of Phloretin on Cl^- channel, specifically on its open probability, selectivity, permeability and gating mechanisms in the inner membrane of extracted mitochondria of rat cardiomyocytes (70). Finally, Phloretin has also been demonstrated to impair urea excretion in embryos of zebra fish and rainbow trout to affect probably by the inhibition of an urea transporter (71, 72). To exclude the interference of Phloretin with other ion channels in the sea urchin larva, a knock-down of spAQP9 by morpholino injections was performed. Larvae injected with a high concentration up to 200 μ M of the spAQP9 morpholino, showed a reduction in the postoral rod length. However, we could not observe a dose dependent knock-down and also the total length of the spicule (body rod + postoral rod) was not affected by the treatment.

To elucidate the physiological water channel dynamics of spAQP9 within the living organism, we conducted live-cell imaging experiments in the sea urchin larva to measure the water flux across the plasma membrane of PMCs. Exposure to a hypertonic solution led to Calcein quenching in PMCs providing a clear readout for the cellular water efflux. We expected that in the presence of Phloretin the water efflux from PMCs will be decreased due to the inhibitory effects on spAQP9. According to our hypothesis, a decrease in the rate constant K was observed under Phloretin inhibition, indicative of a decelerated water efflux. Intriguingly, under inhibition by Phloretin, the water efflux persisted for an extended time compared to control conditions, as evidenced by a steeper slope towards the significantly lower plateau of fluorescent intensity. This observation implies a potential localization of spAQP9 within the membrane of intracellular vesicles rather than in the plasma membrane of the PMCs, coincide with our findings from the antibody staining, which revealed binding to intracellular vesicular structures. Moreover, it is plausible that Phloretin may exert interference with other ion

channels situated in the PMC membrane, such as K^+ channel, Na^{2+} channel or Cl^- channel that would usually counter the osmotic imbalance. Accordingly, these experiments could not deliver conclusive evidence for the function of spAQP9 in PMCs and deserve further experimental investigations.

Conclusion

To conclude, our investigation has elucidated the exclusive expression of the aquaglyceroporin *spAQP9* in the calcifying PMCs of the sea urchin larvae. The temporal expression pattern, peaking at 30 hpf, aligns with the onset of skeleton formation, suggesting a pivotal role for spAQP9 in skeletogenesis initiation and spicule elongation.

Furthermore, our heterologous expression experiments provide strong evidence for the sea urchin spAQP9 to exhibit a dual role as water and CO_2 channel. Although the exact function of spAQP9 in PMCs remains speculative it may serve PMC motility due to water influx inducing filipodia formation during the early development of the larvae and also volume increase of the syncytial cable during spicule development.

A very exiting finding of the present work was the sub-cellular localization of spAQP9 positive vesicles in PMCs during different calcification states. These findings align with previous studies indicating two distinct states of PMCs during the calcification process (16, 41). The sub-cellular structures share similar diameters with Ca^{2+} -rich vesicles that are involved in the mineralization process (20, 21). Given the very high reported Ca^{2+} concentration in those vesicles ranging from 1 M up to 15 M, together with a dehydration of the disordered form of ACC, it is very tempting to speculate that spAQP9 may also be involved in the vesicular water transport to support calcification substrate concentration (21, 54). Finally, the dual role of spAQP9 in conducting H_2O and CO_2 may additionally serve a carbon concentration mechanism within the cell by promoting CO_2 diffusion into the calcification vesicle. However, although of great importance for the mineralization mechanisms, these concepts are highly speculative and deserve extensive future experimental investigations.

In summary, our comprehensive study underscores the multifaceted role of spAQP9 in sea urchin larval calcification, encompassing water and CO_2 transport, filopodia formation in early development of the larvae and spicule, involvement in vesicular dynamics and potential contribution to ACC maturation. While providing valuable insights into the role of aquaporins in the calcification process, this work also shows great potential for future venues to unravel the cellular mechanism underlying the biomineralization process.

References

1. H. C. W. Skinner, A. H. Jahren, "Biomineralization" in *Treatise on Geochemistry*, (2007), pp. 2–60.
2. J. M. Lucas, L. W. Knapp, A physiological evaluation of carbon sources for calcification in the octocoral *Leptogorgia virgulata* (Lamarck). *J. Exp. Biol.* **200**, 2653–2662 (1997).
3. P. U. P. A. Gilbert, *et al.*, Biomineralization: Integrating mechanism and evolutionary history. *Sci. Adv.* **8** (2022).
4. A. H. Knoll, Biomineralization and Evolutionary History. *Rev. Mineral. Geochemistry* **54**, 329–356 (2003).
5. K. Kahil, S. Weiner, L. Addadi, A. Gal, Ion Pathways in Biomineralization: Perspectives on Uptake, Transport, and Deposition of Calcium, Carbonate, and Phosphate. *J. Am. Chem. Soc.* (2021) <https://doi.org/10.1021/jacs.1c09174>.
6. F. H. Wilt, Biomineralization of the spicules of sea urchin embryos. *Zoolog. Sci.* **19**, 253–261 (2002).
7. E. Beniash, J. Aizenberg, L. Addadi, S. Weiner, Amorphous calcium carbonate transforms into calcite during sea urchin larval spicule growth. *Proc. R. Soc. B Biol. Sci.* **264**, 461–465 (1997).
8. T. Mass, *et al.*, Amorphous calcium carbonate particles form coral skeletons. *Proc. Natl. Acad. Sci. U. S. A.* **114**, E7670–E7678 (2017).
9. H. S. Findlay, *et al.*, Comparing the impact of high CO₂ on calcium carbonate structures in different marine organisms. *Mar. Biol. Res.* **7**, 565–575 (2011).
10. G. Benson, C. & Chow, Carbonic anhydrase activity in developing sea urchin embryos. *Exp. Cell Res.* **124** (1979).
11. C. A. Etness, *Sea Urchins as a Model System for Studying Embryonic Development* (Elsevier Inc., 2017) <https://doi.org/10.1016/b978-0-12-801238-3.99509-6>.
12. S. C. Benson, N. C. Benson, F. Wilt, The organic matrix of the skeletal spicule of sea urchin embryos. *J. Cell Biol.* **102**, 1878–1886 (1986).
13. F. H. Wilt, Matrix and mineral in the sea urchin larval skeleton. *J. Struct. Biol.* **126**, 216–226 (1999).
14. J. Cavanaugh, M. L. Whittaker, D. Joester, Crystallization kinetics of amorphous calcium carbonate in confinement. *Chem. Sci.* **10**, 5039–5043 (2019).
15. M. Stumpp, *et al.*, Acidified seawater impacts sea urchin larvae pH regulatory systems relevant for calcification. *Proc. Natl. Acad. Sci. U. S. A.* **109**, 18192–18197 (2012).
16. M. Y. Hu, I. Petersen, W. W. Chang, C. Blurton, M. Stumpp, Cellular bicarbonate accumulation and vesicular proton transport promote calcification in the sea urchin larva: Mechanism of skeleton calcification. *Proc. R. Soc. B Biol. Sci.* **287** (2020).
17. G. L. Decker, W. J. Lennarz, Skeletogenesis in the sea urchin embryo. *Development* **103**, 231–247 (1988).
18. C. S. Sikes, K. Okazaki, R. D. Fink, Respiratory CO₂ and the supply of inorganic carbon for calcification of sea urchin embryos. *Comp. Biochem. Physiol. -- Part A Physiol.* **70**, 285–291 (1981).

19. P. Furla, I. Galgani, I. Durand, D. Allemand, Sources and mechanisms of inorganic carbon transport for coral calcification and photosynthesis. *J. Exp. Biol.* **203**, 3445–3457 (2000).
20. K. Kahil, *et al.*, Elemental compositions of sea urchin larval cell vesicles evaluated by cryo-STEM-EDS and cryo-SEM-EDS. *Acta Biomater.* **155**, 482–490 (2023).
21. K. Kahil, *et al.*, Cellular pathways of calcium transport and concentration toward mineral formation in sea urchin larvae. *Proc. Natl. Acad. Sci. U. S. A.* **117**, 30957–30965 (2020).
22. J. A. Dix, A. K. Solomon, Role of membrane proteins and lipids in water diffusion across red cell membranes. *BBA - Biomembr.* **773**, 219–230 (1984).
23. B. M. Denker, B. L. Smith, F. P. Kuhajda, P. Agre, Identification, purification, and partial characterization of a novel M(r) 28,000 integral membrane protein from erythrocytes and renal tubules. *J. Biol. Chem.* **263**, 15634–15642 (1988).
24. A. S. Verkman, Aquaporins at a glance. *J. Cell Sci.* **124**, 2107–2112 (2011).
25. A. Verkman, A. S.; Mitra, K., Structure and function of aquaporin water channels. *Am. J. Physiol. - Ren. Physiol.* **278**, F13–F28 (2000).
26. K. Hedfalk, *et al.*, Aquaporin gating. *Curr. Opin. Struct. Biol.* **16**, 447–456 (2006).
27. J. S. Hub, B. L. De Groot, Mechanism of selectivity in aquaporins and aquaglyceroporins. *Proc. Natl. Acad. Sci. U. S. A.* **105**, 1198–1203 (2008).
28. H. Tsukaguchi, S. Weremowicz, C. C. Morton, M. A. Hediger, Functional and molecular characterization of the human neutral solute channel aquaporin-9. *Am. J. Physiol. - Ren. Physiol.* **277**, 685–696 (1999).
29. S. Li, C. Li, W. Wang, *Molecular aspects of aquaporins*, 1st Ed. (Elsevier Inc., 2020).
30. K. Ishibashi, T. Morinaga, M. Kuwahara, S. Sasaki, M. Imai, Cloning and identification of a new member of water channel (AQP10) as an aquaglyceroporin. *Biochim. Biophys. Acta - Gene Struct. Expr.* **1576**, 335–340 (2002).
31. R. Aharon, Z. Bar-Shavit, Involvement of aquaporin 9 in osteoclast differentiation. *J. Biol. Chem.* **281**, 19305–19309 (2006).
32. A. Rojek, J. Praetorius, J. Frøkiaer, S. Nielsen, R. A. Fenton, A current view of the mammalian aquaglyceroporins. *Annu. Rev. Physiol.* **70**, 301–327 (2008).
33. A. S. Verkman, Aquaporins. *Curr. Biol.* **23**, 52–55 (2013).
34. J. M. Carbrey, *et al.*, Aquaglyceroporin AqP9: Solute permeation and metabolic control of expression in liver. *Proc. Natl. Acad. Sci. U. S. A.* **100**, 2945–2950 (2003).
35. V. Endeward, *et al.*, Evidence that aquaporin 1 is a major pathway for CO₂ transport across the human erythrocyte membrane. *FASEB J.* **20**, 1974–1981 (2006).
36. N. Uehlein, C. Lovisollo, F. Siefert, R. Kaldenhoff, The tobacco aquaporin NtAQP1 is a membrane CO₂ pore with physiological functions. *Nature* **425**, 734–737 (2003).
37. H. Matsui, B. M. Hopkinson, K. Nakajima, Y. Matsuda, Plasma membrane-type aquaporins from marine diatoms function as CO₂/NH₃ channels and provide photoprotection. *Plant Physiol.* **178**, 345–357 (2018).
38. A. S. Matt, W. W. Chang, M. Y. Hu, Extracellular carbonic anhydrase activity promotes a carbon concentration mechanism in metazoan calcifying cells. *Proc. Natl. Acad. Sci. U. S. A.* **119**, 1–11 (2022).

39. K. D. Walton, J. C. Croce, T. D. Glenn, S. Y. Wu, D. R. McClay, Genomics and expression profiles of the Hedgehog and Notch signaling pathways in sea urchin development. *Dev. Biol.* **300**, 153–164 (2006).
40. M. Y. Hu, *et al.*, A SLC4 family bicarbonate transporter is critical for intracellular pH regulation and biomineralization in sea urchin embryos. *Elife* **7**, 1–17 (2018).
41. W. W. Chang, *et al.*, An otopetrin family proton channel promotes cellular acid efflux critical for biomineralization in a marine calcifier. *Proc. Natl. Acad. Sci. U. S. A.* **118**, e2101378118 (2021).
42. P. Kitchen, *et al.*, Calcein Fluorescence Quenching to Measure Plasma Membrane Water Flux in Live Mammalian Cells. *STAR Protoc.* **1** (2020).
43. G. J. Cooper, W. F. Boron, Effect of PCMBs on CO₂ permeability of xenopus oocytes expressing aquaporin 1 or its C189S mutant. *Am. J. Physiol. - Cell Physiol.* **275**, 1481–1486 (1998).
44. Y. Wang, J. Cohen, W. F. Boron, K. Schulten, E. Tajkhorshid, Exploring gas permeability of cellular membranes and membrane channels with molecular dynamics. *J. Struct. Biol.* **157**, 534–544 (2007).
45. A. B. Thies, A. R. Quijada-Rodriguez, H. Zhouyao, D. Weihrauch, M. Tresguerres, “A Rhesus channel in the coral symbiosome membrane suggests a novel mechanism to regulate NH₃ and CO₂ delivery to algal symbionts” (2022).
46. D. J. Lee, M. Gutbrod, F. M. Ferreras, P. G. D. Matthews, Changes in hemolymph total CO₂ content during the water-to-air respiratory transition of amphibiotic dragonflies. *J. Exp. Biol.* **221** (2018).
47. S. Sasaki, K. Lshibashi, T. Nagai, F. Marumo, “Regulation mechanisms of intracellular pH of *Xenopus laevis* oocyte” (1992).
48. H. Tsukaguchi, *et al.*, Molecular characterization of a broad selectivity neutral solute channel. *J. Biol. Chem.* **273**, 24737–24743 (1998).
49. A. Müller-Lucks, *et al.*, Preparative scale production and functional reconstitution of a human aquaglyceroporin (AQP3) using a cell free expression system. *N. Biotechnol.* **30**, 545–551 (2013).
50. K. H. Cheung, C. T. Leung, G. P. H. Leung, P. Y. D. Wong, Synergistic effects of cystic fibrosis transmembrane conductance regulator and aquaporin-9 in the rat epididymis. *Biol. Reprod.* **68**, 1505–1510 (2003).
51. K. Ishibashi, *et al.*, Cloning and functional expression of a new water channel abundantly expressed in the testis permeable to water, glycerol, and urea. *J. Biol. Chem.* **272**, 20782–20786 (1997).
52. R. R. Geyer, R. Musa-Aziz, X. Qin, W. F. Boron, Relative CO₂/NH₃ selectivities of mammalian aquaporins 0-9. *Am. J. Physiol. - Cell Physiol.* **304** (2013).
53. J. Yu, A. J. Yool, K. Schulten, E. Tajkhorshid, Mechanism of Gating and Ion Conductivity of a Possible Tetrameric Pore in Aquaporin-1. *Structure* **14**, 1411–1423 (2006).
54. E. Beniash, L. Addadi, S. Weiner, Cellular control over spicule formation in sea urchin embryos: A structural approach. *J. Struct. Biol.* **125**, 50–62 (1999).
55. Y. Politi, *et al.*, Structural characterization of the transient amorphous calcium carbonate precursor phase in sea urchin embryos. *Adv. Funct. Mater.* **16**, 1289–1298 (2006).

56. X. Wang, W. E. G. Müller, Involvement of aquaporin channels in water extrusion from biosilica during maturation of sponge siliceous spicules. *Biol. Bull.* **229**, 24–37 (2015).
57. S. Weiner, L. Addadi, Crystallization pathways in biomineralization. *Annu. Rev. Mater. Res.* **41**, 21–40 (2011).
58. K. Takata, *et al.*, Aquaporin water channels in the kidney. *Acta Histochem. Cytochem.* **38**, 199–207 (2005).
59. P. Kitchen, *et al.*, Beyond water homeostasis: Diverse functional roles of mammalian aquaporins. *Biochim. Biophys. Acta - Gen. Subj.* **1850**, 2410–2421 (2015).
60. K. Ishibashi, S. Sasaki, Aquaporin Water Channels in Mammals. *Clin. Exp. Nephrol.* **1**, 247–253 (1997).
61. D. R. McClay, Evolutionary crossroads in developmental biology: Sea urchins. *Development* **138**, 2639–2648 (2011).
62. S. E. Gilbert, *Developmental Biology 6th edition* (2000) <https://doi.org/10.1016/B978-0-323-46294-5.00028-5>.
63. M. Saina, *et al.*, A cnidarian homologue of an insect gustatory receptor functions in developmental body patterning. *Nat. Commun.* **6** (2015).
64. G. C. Karp, M. Solursh, Dynamic activity of the filopodia of sea urchin embryonic cells and their role in directed migration of the primary mesenchyme in vitro. *Dev. Biol.* **112**, 276–283 (1985).
65. K. Tarsis, T. Gildor, M. Morgulis, S. Ben-Tabou de-Leon, Distinct regulatory states control the elongation of individual skeletal rods in the sea urchin embryo. *Dev. Dyn.* **251**, 1322–1339 (2022).
66. V. M. Loitto, C. Huang, Y. J. Sigal, K. Jacobson, Filopodia are induced by aquaporin-9 expression. *Exp. Cell Res.* **313**, 1295–1306 (2007).
67. M. A. Khajah, Y. A. Luqmani, Involvement of Membrane Blebbing in Immunological Disorders and Cancer. *Med. Princ. Pract.* **25**, 18–27 (2016).
68. D. S. Koh, G. Reid, W. Vogel, Effect of the flavoid phloretin on Ca²⁺-activated K⁺ channels in myelinated nerve fibres of *Xenopus laevis*. *Neurosci. Lett.* **165**, 167–170 (1994).
69. G. R. Strichartz, G. S. Oxford, F. Ramon, Effects of the dipolar form of phloretin on potassium conductance in squid giant axons. *Biophys. J.* **31**, 229–246 (1980).
70. L. Malekova, *et al.*, Inhibitory effect of DIDS, NPPB, and phloretin on intracellular chloride channels. *Pflugers Arch. Eur. J. Physiol.* **455**, 349–357 (2007).
71. M. H. Braun, S. L. Steele, S. F. Perry, The responses of zebrafish (*Danio rerio*) to high external ammonia and urea transporter inhibition: Nitrogen excretion and expression of rhesus glycoproteins and urea transporter proteins. *J. Exp. Biol.* **212**, 3846–3856 (2009).
72. C. M. Pilley, P. A. Wright, The mechanisms of urea transport by early life stages of rainbow trout (*Oncorhynchus mykiss*). *J. Exp. Biol.* **203**, 3199–3207 (2000).

4 unpublished data

PMC differences along the spicule of the larvae

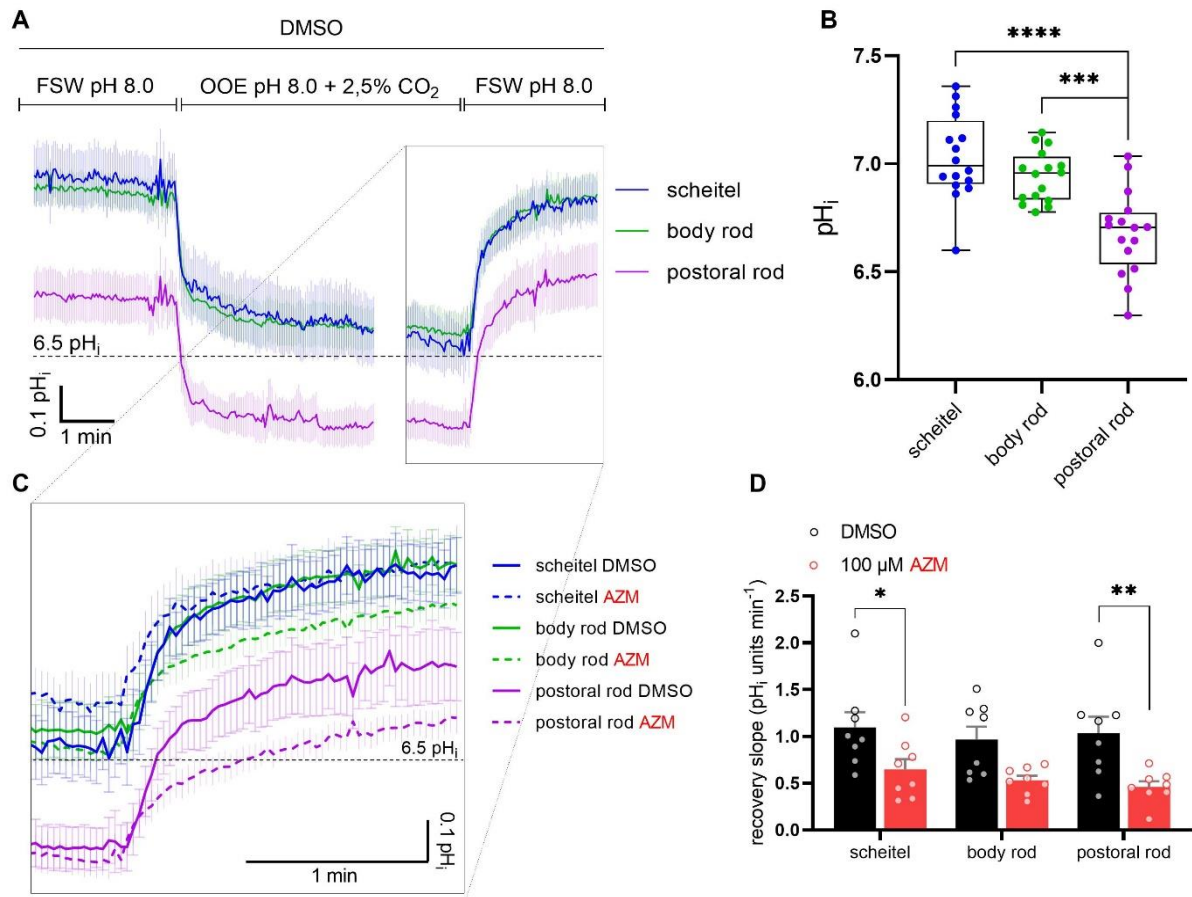


Fig. 4.1. Intracellular pH recordings in combination with the CO₂-pulse method. (A) Intracellular pH (p*H*_i) was measured using the ratiometric pH sensitive dye BCECF-AM. p*H*_i of PMCs was recorded during exposure to out-of-equilibrium (OOE) solution (2.5% CO₂, pH 8.0) under control condition using only the vehicle DMSO. It was distinguished between the location of the PMCs along the spicule, in scheitel (blue line, n = 8, mean ± SEM), body rod (green line, n = 8, mean ± SEM) and postoral rod (purple line, n = 8, mean ± SEM). The rate in p*H*_i change during addition and removal of the OOE solution reflects the hydration and de-hydration speed of CO₂ within the cell. (B) Depicted are the p*H*_i starting values of the PMCs in different locations on the spicule; scheitel (blue circles, n = 16), body rod (green circles, n = 16) and postoral rod (purple circles, n = 16). Boxplots include single measurements (circles), median values and min and max values. Statistical analyses were performed using one-way ANOVA + post hoc test [Holm-Sidak] with ***p>0.001; ****p>0.0001). (C) The enlarged area depicts the area of interest, the recovery rate from the 2.5% CO₂ pulse, that was used to analyze iCA activity. Additionally, the values were added obtained by the measurements in the presence of 100 μM AZM (dashed line, n = 8, mean ± SEM) or DMSO (solid line, n = 8, mean ± SEM). Once more, it was distinguished between the location of the PMCs along the spicule, in scheitel (blue line), body rod (green line) and postoral rod (purple line). (D) Comparison of recovery rates (p*H*_i units per minute) of the different location of the PMCs (scheitel, body rod postoral rod) and the inhibitory effects of 100 μM AZM (red bars) compared to DMSO controls (black bars). Values are presented as mean ± SEM, including all single values and statistical analyses were performed using two-way ANOVA + post hoc test [Sidak] with ***p>0.001; ****p>0.0001).

Intracellular pH measurements in combination with the CO₂-pulse method were used to measure intracellular hydration and dehydration speed of CO₂, catalyzed by CA. Additionally, the differences depending on the location of the PMCs along the spicule, were examined. Therefore, the recorded PMCs on the spicule were divided into scheitel area, body rod and postoral rod (Fig. 4.1 A). Differences in the starting pH_i of the PMCs were recognizable. PMCs located in the scheitel area as well as at the body rod showed a similar pH_i of 7.03 ± 0.05 and 6.94 ± 0.03 , respectively, which coincide within the scope of the proposed pH_i of PMCs (~ 7.1 pH_i). In contrast, the PMCs located at the postoral rod exhibit a significantly lower starting pH_i of 6.68 ± 0.05 (Fig. 4.1 B). By addition of 100 μ M AZM, as showed before, the de-hydration kinetics during withdrawal of the OOE solution was decreased in all three PMC locations (Fig. 4.1 C). In the scheitel area from 1.10 ± 0.15 to 0.65 ± 0.1 pH_i units min⁻¹, at the body rod from 0.97 ± 0.13 to 0.53 ± 0.05 pH_i units min⁻¹ and at the postoral rod from 1.03 ± 0.17 to 0.46 ± 0.06 pH_i units min⁻¹ (Fig. 4.1 D). No significant difference in the AZM inhibition among the three different PMC locations was detected.

5 Discussion

Biom mineralization in marine organisms is a complex process that requires the orchestrated interplay of different factors ranging from cellular homeostasis over vesicular trafficking to protein biochemical pathways. In this thesis I focused on the pH and carbon homeostasis in calcifying cells that represent key factors in the calcification process, with new insight regarding the underlying membrane transport mechanisms. Based on the findings of my work I was able to propose a novel cellular carbon concentration mechanism (CCM) in calcifying primary mesenchyme cells (PMCs) of the sea urchin larva. Furthermore, a new family of proton channels, otopetrins were discovered in PMCs that play a key role in cellular pH regulatory abilities required for the mineralization process. Finally, my functional study of aquaporins in PMCs suggest a significant role of cellular water transport to support skeleton formation in the sea urchin larva. This deep mechanistic understanding regarding calcifying systems allows us to conduct hypothesis-driven research to study the effects of ocean acidification on the mineralization process. Knowledge obtained from these studies will allow us to better understand this evolutionary ancient process and to explain and predict sensitivities of marine calcifying organisms in past and future marine systems.

5.1 Carbon concentration mechanisms

Biom mineralization is the process by which organisms form biominerals, serving protection against predators, locomotion, reproduction or orientation purposes by the detection of gravity, just to name a few (P. Gilbert et al., 2022). For example, the mollusc *Crassostrea gigas* forms a shell for protection against the environment and predators (Min et al., 2023). This shell is composed of 95% CaCO_3 , more precisely of calcite and aragonite (Song et al., 2019). The small otoconia within the vertebrate inner ear and the larger otoliths located in the inner ear of the fish, represent notable example for how biominerals are employed for orientation (Hughes et al., 2004). Both predominantly comprise of CaCO_3 . The sea urchin larva for example uses its calcitic skeleton for tissue support, locomotion and orientation (Wilt, 2002).

For the generation of the most abundant biomineral, CaCO_3 , an organism must acquire Ca^{2+} and CO_3^{2-} ions at sufficient saturation states to promote mineral formation. CO_3^{2-} is acquired from dissolved inorganic carbon (DIC) species like HCO_3^- , CO_3^{2-} and CO_2 that can be obtained from the environment or through endogenous metabolic CO_2 . Ca^{2+} is always obtained from the seawater but it can be stored in cellular compartments like the endoplasmic reticulum (Decker et al., 1987). The sea urchin larva, for

example, uses at least two pathways to obtain their Ca^{2+} ions. One pathway involves a calcium channel in the PMC membrane and the second pathway takes place by endocytosis (Vidavsky et al., 2016). In the latter, that resembles micropinocytosis, seawater containing 10 mM of Ca^{2+} is taken up into vesicles, which form a vesicular network in the PMC (Vidavsky et al., 2016). Ca^{2+} ions are concentrated by up to three orders of magnitude in vesicles, where an amorphous CaCO_3 precursor is formed (Kahil et al., 2020). In the sea urchin larva, like in many other calcifying organisms, at least 25-30% of the DIC that is incorporated into the skeleton derives from the seawater, while the remaining 70-75% are obtained from metabolically generated CO_2 of the organism itself (Al-Horani et al., 2003; Furla et al., 2000; Lucas & Knapp, 1997). The non-photosynthetic soft coral *Leptogorgia virgulata* developed several pathways to obtain DIC for the generation of their calcitic spicules. Using carbon labeled isotopes in combination with different inhibitors targeting key enzymes and transporters, three pathways could be identified. The first pathway describes the CO_2 diffusion across the plasma membrane and further intracellular conversion with water to $\text{HCO}_3^- + \text{H}^+$ by carbonic anhydrase (CA). The second pathway uses extracellular conversion of CO_2 to HCO_3^- and subsequent active transport into the cell through anion transporter or antiporter. The last proposed pathway uses the metabolic CO_2 that feeds into the calcification process. Using glucose as the substrate for glycolysis, followed by the citrate cycle, CO_2 is produced and subsequently converted by CA to form HCO_3^- (Lucas & Knapp, 1997).

However, the amount of DIC, needed for calcification, has to be dramatically higher than its concentration in the surrounding seawater or generated by the metabolism. To solve this problem and to accumulate the calcification substrates, mostly DIC species, marine phytoplankton species have developed efficient carbon concentration mechanisms (CCM) that allows them to concentrate DIC against steep outward directed gradients. In photosynthesis prosecuting organisms, such as the scleractinian coral *Galaxea fascicularis*, this CCM is primarily used for accumulation of CO_2 to fuel the endosymbiotic zooxanthellae as well as concentration of HCO_3^- for the calcification process (Al-Horani et al., 2003). However, the exact mechanisms including the enzymes and transporters involved remained largely speculative for any of these CCMs.

5.1.1 Extracellular carbonic anhydrase activity supports a HCO_3^- uptake mechanism in calcifying cells

In this thesis I was able to identify and characterize a cellular CCM in the PMCs of the sea urchin larva with a key role of the extracellular carbonic anhydrase Cara7. Already in 1959, Goreau proposed that CA plays a central role in the calcification process in corals (Goreau, 1959). Later, CAs were

associated with calcifying tissues and cells of many different organisms including, corals, mollusks and echinoderms (Le Roy et al., 2014; Tambutté et al., 2007; X. Wang, Wang, Jia, Qiu, et al., 2017), while the mechanistic contribution of this enzyme in concentrating DIC remained largely speculative. Therefore, the first chapter of my thesis aimed at understanding the mechanistic basis how CAs help to increase the DIC pool in the calcifying cells of the sea urchin larva. Carbonic anhydrases catalyze the reversible interconversion of $\text{CO}_2 + \text{H}_2\text{O}$ to H_2CO_3 which further dissociates into HCO_3^- and H^+ . Already in earlier studies, pharmacological approaches suggested an important role of CA in the calcification process where the CA inhibitor, acetazolamide (AZM), caused a reduction in the spicule length of the sea urchin pluteus larva (Mitsunaga et al., 1986; Zito et al., 2015). Phylogenetic analysis as well as single cell transcriptome analysis of the sea urchin larva of *S. purpuratus*, revealed two carbonic anhydrases that are exclusively expressed in the PMCs. The first one is an intracellular CA (iCA, *Cara2*) and the second one is an extracellular CA (eCA, *Cara7*) linked with a GPI-anchor to the plasma membrane (Publication II, Fig. 1 A, B, E + Fig. S2). The role of eCA activity in the mineralization process could be demonstrated by a substantial decrease of the postoral rod length and the re-calcification rate in the presence of dextran-bound AZM, that cannot pass biological membranes due to its molecular size. Interestingly, interference with only AZM that targets both, intracellular and extracellular CAs no significant effect on calcification was observed (Publication II, Fig. 2 A - D). Knock-down of *Cara7* with a custom made Morpholino (MO) confirmed decreased postoral rod length (Publication II, Fig. 4 C). H^+ selective microelectrode measurements in combination with a newly designed stop flow protocol allowed me to measure CA activity at the surface of PMCs in vivo (Publication II, Fig. 5 C - H). These measurements together with pharmacological inhibitions and MO knock-down demonstrated that *Cara7* promotes the formation of HCO_3^- and H^+ from CO_2 at the cell surface of PMCs. Colocalization of *Cara7* and the $\text{Na}^+/\text{HCO}_3^-$ cotransporter (NBC) *Sp_Scl4a10* in some populations of PMCs indicate that the HCO_3^- that is generated at the cell surface is further transported into the cell via the NBC transporter (Publication II, Fig. S8; Fig. 5.1 A). In contrary, the results of my first chapter demonstrated that iCA activity is downregulated during the mineralizing process. *Cara2* shows no significant gene expression increase during active re-calcification of the skeleton, while *Cara7* is upregulated (Publication II, Fig. 2 E). In addition, a method to measure intracellular CA activity was developed that demonstrated a substantial decrease in the proportion of AZM-sensitive fraction involved in the CO_2 dehydration reaction within re-calcifying larvae. These results provided functional evidence for a reduction in iCA activity under increased remineralization efforts (Publication II, Fig. 3 D).

These observations provide strong evidence for an unexpected opposing contribution of iCA and eCA in the calcification process in the PMCs. From a physiological point of view, an advantage for converting CO_2 to HCO_3^- extracellularly instead of intracellularly by iCA lies in the fact that hydration of CO_2 outside the cell reduces the cellular H^+ load by leaving the accrued H^+ outside the cell (Fig. 5.1 A). At a closer

look, reductions in iCA activity may also be advantageous to keep the cytosolic HCO_3^- pool, which is important for intracellular calcifiers (Brownlee et al., 2015; Hu et al., 2020). Although at an intracellular pH of 7 the majority of DIC will be present in the form of HCO_3^- , reductions in iCA activity may still help to minimize the loss of DIC by the formation of CO_2 from HCO_3^- . Similar observations for opposing functions of iCAs and eCAs to promote CCM were made in photosynthetic marine algae (Price & Badger, 1989; Thoms et al., 2001; Trimborn et al., 2008). Depending on the species, diatoms were distinguished in two CCM types for carbon acquisition, “ CO_2 -user” and “ HCO_3^- -user”. The CO_2 -user *N. navis-varingica* utilizes its carbon predominantly from CO_2 and exhibits high iCA activity while it prevents eCA activity to decrease CO_2 hydration outside the cell. In contrast, the HCO_3^- -user *S. stellaris* shows high eCA levels to convert the leaking CO_2 to HCO_3^- outside the cell that is then transported back into the cell by HCO_3^- transporter (Trimborn et al., 2008). This mechanism allows the concentration of HCO_3^- inside the cell while CO_2 gradients still support the exit of CO_2 from the cell. Based on our findings and the information obtained from the CCM proposed in microalgae we concluded, that the calcifying PMCs of the sea urchin larva operate like the “ HCO_3^- -user”, due to high eCA activity and reduced iCA activity during the active calcification process to promote the cellular CCM. Additional evidence includes the increased expression of the $\text{Na}^+/\text{HCO}_3^-$ cotransporter and the eCA Cara7 in response to low HCO_3^- levels, while iCA Cara2 expression was decreased under these conditions (Publication II, Fig. S7).

The efficiency of the CCM is not only dependent on carbon uptake, but also on the CO_2 efflux (Rost et al., 2006; Trimborn et al., 2008). As previously stated, a substantial amount of DIC employed for carbon utilization for the mineralization process of key marine calcifiers, such as corals (Bentov et al., 2009), sea urchins (Sikes et al., 1981) and foraminifera (Erez, 1978), consist of the metabolic waste product CO_2 (Furla et al., 2000), which can diffuse out of the cell. We propose that metabolically derived CO_2 diffuses out of the cell, is subsequently transformed at the cellular boundary layer by eCA Cara7 to HCO_3^- and then reabsorbed by HCO_3^- transport mechanisms back into the PMC. This resembles an efficient and resource saving recycling mechanism to acquire DIC for calcification. This CCM model is further substantiated by our observation that even in the absence of external HCO_3^- , addition of the eCA inhibitor Dex-AZM led to reductions in pH_i regulatory capacities, which are largely reflecting reduced HCO_3^- uptake (Publication II, Fig. 6 E + F). Taken together these observations provide compelling evidence for a role of the eCA Cara7 in supporting a HCO_3^- uptake mechanism by the extracellular hydration of metabolic CO_2 (Fig. 5.1 A).

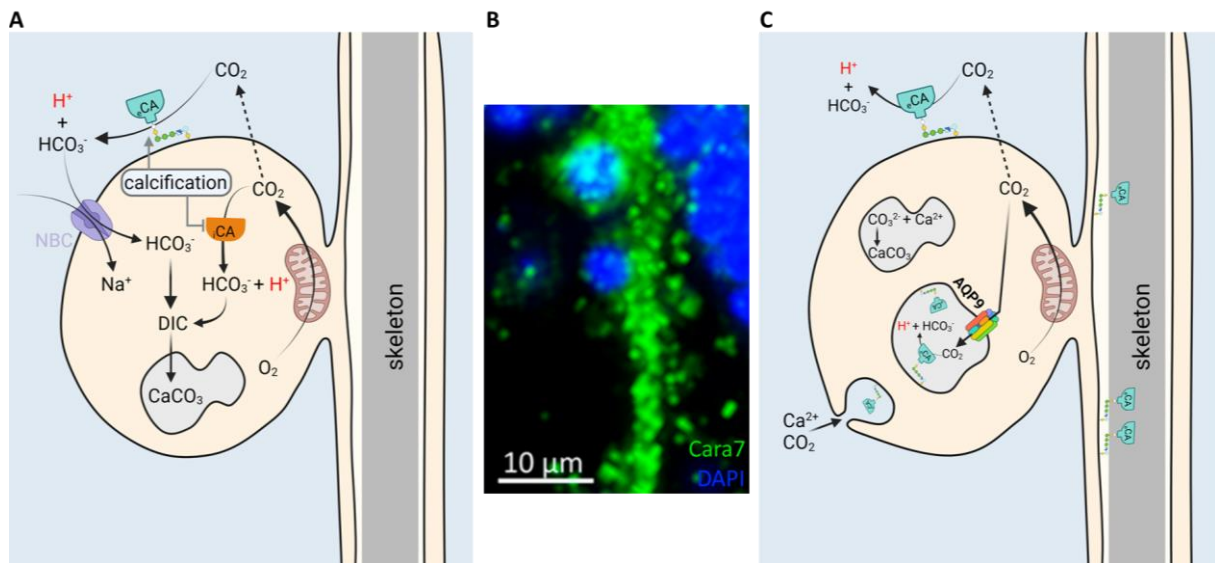


Fig. 5.1: Proposed schematic model summarizing the role of CAs in the CCM in PMCs of the sea urchin larva. (A) Cross-section of an enlarged PMC including Na⁺/HCO₃⁻ cotransporter (NBC), intracellular CA (iCA) and extracellular CA (eCA). (B) High-magnification image of the positive immunoreactivity of the polyclonal Cara7-specific antibody and DAPI in PMCs of the postoral rod tip of a pluteus larvae (4 dpf). (C) Cross-section of an enlarged PMC including eCAs and spAQP9 (**AQP9**) in the vesicular network. Image created with BioRender.com, with permission.

5.1.2. A potential role of extracellular carbonic anhydrase in sub-cellular compartments

Endocytosis of seawater into the calcifying PMC and further into a network of vacuoles and vesicles has been hypothesized to be the major route of Ca²⁺ uptake to the site of calcification (Kahil et al., 2020). These vesicles contain a metastable form of calcium carbonate, amorphous calcium carbonate (ACC), which is the transient precursor for the later crystallized calcite (Addadi et al., 2003; Beniash et al., 1997). The current model denotes that the vesicles containing the ACC are transported to the syncytial cord membrane, exocytosed towards the growing spicule to elongate or thicken the skeletal rod (Vidavsky et al., 2016). This mechanism of intracellular calcification by seawater endocytosis was also proposed for other marine organisms, such as corals and foraminifera (Bentov et al., 2009; Mass et al., 2017). Using calcein-labeling of Ca²⁺-rich vesicles and cryo-STEM-EDS/cryo-SEM-EDS analysis, it was discovered in the sea urchin larva that the intracellular vesicles contain high concentrations of Ca²⁺ ranging from 1 to 15 M. The Ca²⁺ concentration of the seawater is much lower and has to be increased at least three orders of magnitude. Moreover, equimolar concentrations of carbonate ions have to be introduced or produced in the intracellular vesicles, to allow ACC precipitation (Kahil et al., 2021, 2023). Here the membrane bound CA Cara7 could additionally play an important role in carbonate ion generation in the vesicles. Our antibody staining of Cara7 shows

positive signal in membranes of PMC cell bodies and vesicular structures across the PMCs as well as in the syncytial cables along the spicule (Fig. 5.1 B; Publication II, Fig. 4 D + E). In addition, the antibody-signal of Cara7 was also visible in the spicule itself, suggesting an incorporation of the enzyme into the mineral. This observation was underlined by proteomic analyses, which demonstrated high concentration of Cara7 present in the spicule matrix (Mann et al., 2010). Based on these observations, it is tempting to speculate that Cara7, anchored in the PMC plasma membrane facing the extracellular matrix, is introduced into the vesicles by endocytotic uptake of seawater-like fluids and further incorporated into the inner membrane of the syncytial cable facing the spicule, which correlates with the well described route of Ca^{2+} uptake in the PMCs (Kahil et al., 2020, 2023; Vidavsky et al., 2016). Here, it remains to be investigated if Cara7 is indeed localized in the ACC forming vesicles. If this is the case, Cara7 may support the formation of carbonate ions by catalyzing the hydration of CO_2 inside the vesicles (Fig. 5.1 C). However, this attractive model requires proton export mechanisms from the calcification vesicle and from the cytoplasm, that were studied in the second chapter of my thesis and that will be discussed in the latter in this discussion.

5.1.3. A potential function of the aquaglyceroporin spAQP9 in vesicular carbon concentration

Single-cell transcriptomic analyses demonstrated that the mammalian AQP9 homologue spAQP9 was found to be exclusively expressed in the PMCs of the sea urchin larva. I generated a polyclonal antibody against spAQP9 in the sea urchin larvae that confirmed an exclusive presence of this protein in the PMCs. In addition, positive immunoreactivity was restricted to vesicular structures in the PMCs (Manuscript III, Fig. 3 A +B). The vesicles detected by the spAQP9 antibody coincide in size with the Ca^{2+} -rich vesicles identified by cryo-SEM observations (Kahil et al., 2020, 2023). To better understand the function of the sea urchin AQP9 we expressed this channel in a heterologous expression system in combination with assays to measure H_2O and CO_2 conductivity across the plasma membrane. Given that spAQP9 exhibits all the characteristics shared with mammalian aquaglyceroporins, it is presumable that it could facilitate the passage of other uncharged small molecules, such as CO_2 , too (Ishibashi et al., 1997, 2002; Tsukaguchi et al., 1999). Indeed, when spAQP9 was expressed in *Xenopus* oocytes, we were able to demonstrate substantially increased H_2O but also CO_2 permeabilities across the oocyte membrane (Manuscript, Fig. 2 B – F).

CO_2 diffusion promoted by aquaglyceroporins and orthodox aquaporins has been demonstrated in human erythrocytes, plants and diatoms (Endeward et al., 2006; Geyer et al., 2013; Matsui et al., 2018; Uehlein et al., 2003). Human AQP1, rat rAQP9 or tobacco NtAQP1 expressed in heterologous expression systems, such as *Xenopus* oocytes, showed increased membrane permeability to CO_2

(Endeward et al., 2006; Geyer et al., 2013; Uehlein et al., 2003). Furthermore, using membrane inlet mass spectrometry (MIMS) with ^{18}O -labeled DIC increased CO_2 membrane permeability was revealed by overexpressing *PtAQP2* in diatoms (Matsui et al., 2018). The fact that spAQP9 facilitates diffusion of CO_2 across the biological membranes, demonstrated by two independent methods, may have interesting consequences for the vesicular calcification process. Based on our findings it can be hypothesized that spAQP9 promotes CO_2 influx into the vesicle to increase the carbon supply. Subsequently, Cara7 would catalyze the rapid conversion of CO_2 to HCO_3^- and H^+ , followed by binding of Ca^{2+} to further create ACC (Fig. 5.1 C). However, additional experiments, addressing the CO_2 permeability of vesicle membranes, together with localizations of ACC bearing vesicles and spAQP9 vesicles are necessary.

Given a vesicular carbon concentration mechanism as described above, a fundamental requisite would be the removal of H^+ that are liberated by the hydration of CO_2 inside the vesicle. However, such proton transport mechanisms to excluded acids from the calcification vesicles, but also from the cytoplasm of the cell, are relatively little explored and will be addressed in the following part of the discussion.

5.2 Cellular pH regulation (buffer import) & H^+ export

The concentration and availability of the different carbon species to generate the biomineral CaCO_3 are dependent on the surrounding pH. Since the sea urchin larva used 60% of metabolic CO_2 and 40% of environmental HCO_3^- as a carbon source for mineralization the formation of one mole of CaCO_3 liberates 1.6 moles of protons, which strain the cell with a substantial acid load (Sikes et al., 1981). To further promote the calcification process, the calcifying cells require mechanisms to regulate their intracellular pH. This general necessity to remove protons from the site of mineral formation is seen in many marine organisms (Buitenhuis et al., 1999; McConnaughey & Whelan, 1997), as well as in the formation of vertebrate bone mineral (Blair et al., 2018; Liu et al., 2011).

The sea urchin larva exhibits a one to two μm thin ectodermal epithelium that has a high permeability for ions and small molecules, which makes the body cavity fluid very similar to the surrounding seawater (Stumpp et al., 2012). Accordingly, the extracellular pH of the body cavity fluid resembles the seawater pH of 8.1 and changes in environmental pH will directly translate into pH changes in the matrix filled body cavity. The intracellular pH of the calcifying PMC however exhibits a pH_i of 7.1 and must be maintained during the calcification process by the export of protons and/ or by the import of anionic buffers like HCO_3^- (Stumpp et al., 2012). Here the changes in seawater pH may cause a challenge to pH regulatory systems of PMCs due to the direct impact of seawater pH on the extracellular compartment in which PMCs are embedded.

5.2.1 Anionic buffer import of HCO_3^-

The sea urchin larva possesses a HCO_3^- cotransporter system, which is localized in the plasma membrane, as well as in the intracellular vesicular structures of the PCMs (Hu et al., 2018). This $\text{Na}^+/\text{HCO}_3^-$ cotransporter (*SpSlc4a10*, NBC) shares high similarities with the mammalian electroneutral $\text{Na}^+/\text{HCO}_3^-$ cotransporter (NBCn2) with Cl^- self-exchanging activity (Parker et al., 2008), as well as the Na^{2+} -dependent $\text{Cl}^-/\text{HCO}_3^-$ exchanger (NBCE) controlling the pH_i in neurons (C. Z. Wang et al., 2000). The $\text{Na}^+/\text{HCO}_3^-$ cotransporter in the sea urchin larva has been suggested to serve a dual function, on the one hand importing dissolved inorganic carbon (HCO_3^-) for calcification, on the other hand importing a proton buffer into the cytosol (Hu et al., 2020). An earlier study demonstrated that the anion exchange inhibitor DIDS (4,4'-diisothiocyanatostilbene-2,2'-disulfonic acid) leads to an inhibition of HCO_3^- uptake and Ca^{2+} incorporation in the spicule (Yasumasu et al., 1985). The pH recovery after an induced acidosis by the $\text{NH}_3/\text{NH}_4^+$ pre-pulse method can be used to determine the buffer capacity of PMCs, according to calculations described by Graber et al. (Graber et al., 1991). This pH_i compensation reaction in the PMC of the sea urchin larva was highly Na^+ and HCO_3^- dependent (Stump et al., 2012). Moreover, knock-down of *SpSlc4a10* leads to reduced skeleton length and abnormally formed spicules accompanied by a reduced ability to compensate for an intracellular acidosis (Hu et al., 2018). Furthermore, during active calcification, the intracellular pH is increased simultaneously with increases in *SpSlc4a10* mRNA levels, potentially serving an elevation in intracellular $[\text{HCO}_3^-]$ to increase the cytosolic carbon pool (Hu et al., 2020). These observations suggest that this bicarbonate transporter plays a central role not only in HCO_3^- supply for the calcification process, but also in intracellular pH homeostasis. A comparable mechanism was identified in mammalian ventricular myocytes, where a $\text{Na}^+/\text{HCO}_3^-$ symporter contributes to restoring intracellular pH from intracellular acid load, which is likewise inhibited by DIDS (Lagadic-Gossman et al., 1992). Using a $\text{NH}_4^+/\text{NH}_3$ pre-pulse induced acidosis of PMCs, we could further demonstrate an involvement of the eCA *Cara7* in intracellular pH homeostasis. pH_i regulatory capacities of PMCs were decreased by 50% during inhibition of eCAs or knock-down of *Cara7* (Publication II, Fig. 6 A – D). Reduced pH_i recovery by pharmacological inhibition of CA was also seen in mantle epithelial cells of the pacific oyster *C. gigas* (Ramesh et al., 2020). Similar observations were also made in ventricular myocytes where the rate of acid extrusion is dependent on the involvement of a CA. Additional evidence for the involvement of *Cara7* in defending pH_i homeostasis in PMCs is provided by the observation that even in the absence of external HCO_3^- , the pH_i regulatory capacity is further diminished through the addition of membrane impermeable dextran-bound AZM (Dex-AZM) (Publication II, Fig. E + F). This implies, that *Cara7* converts CO_2 to HCO_3^- at the cell surface that can serve as the substrate for the NBC transporter

to subsequently support intracellular buffering capacities. External CA supporting bicarbonate mediated pH_i regulatory mechanisms have already been shown in heterologous expression systems. Co-transfected HEK293 cells with human NBC1 and GPI-anchored CA exhibited increased pH_i recovery rate by 44% compared to cells only expressing NBC1 (Alvarez et al., 2003). A prerequisite for these transporters and enzymes to work in concert to regulate pH_i homeostasis, would be a localization in close proximity. Single-cell transcriptomic analyses, demonstrated a co-expression of *Cara7* and *SpSlc4a10* in the same PMC populations (Publication II, Fig. S8). A transport metabolon consisting of CAs and HCO_3^- transporters have already been identified for example in cancer cells, where extracellular CAIX forms a complex with the bicarbonate transporter as well as with $\text{Cl}^-/\text{HCO}_3^-$ exchanger (AE), to facilitate an efficient pH_i regulation of tumor cells (Becker, 2020). Furthermore, red blood cells exhibit a metabolon consisting of the $\text{Cl}^-/\text{HCO}_3^-$ exchanger (AE1) with a cytosolic CA to mediate an efficient CO_2 transport to the lungs (D. E. Johnson & Casey, 2009). A potential buffering role of a membrane-bound CA by interaction with a bicarbonate transporter of the SLC4 family could also be identified in the human kidney (S. K. Lee et al., 2023). The cooperation of CA and a bicarbonate transporter in kidney cells has already been indicated in an earlier study by addition of the CA inhibitor AZM inducing a decreased bicarbonate transport activity due to the lack of substrate availability at the surface of the kidney cells (Soleimani et al., 1987).

However, the import of bicarbonate buffers only represents one mechanism to defend intracellular pH homeostasis. In many cases the direct export of protons from cells serves as another significant mechanism to compensate for acid-base disturbances, particularly notable in the calcifying PMCs. This phenomenon will be further elucidated in the following section.

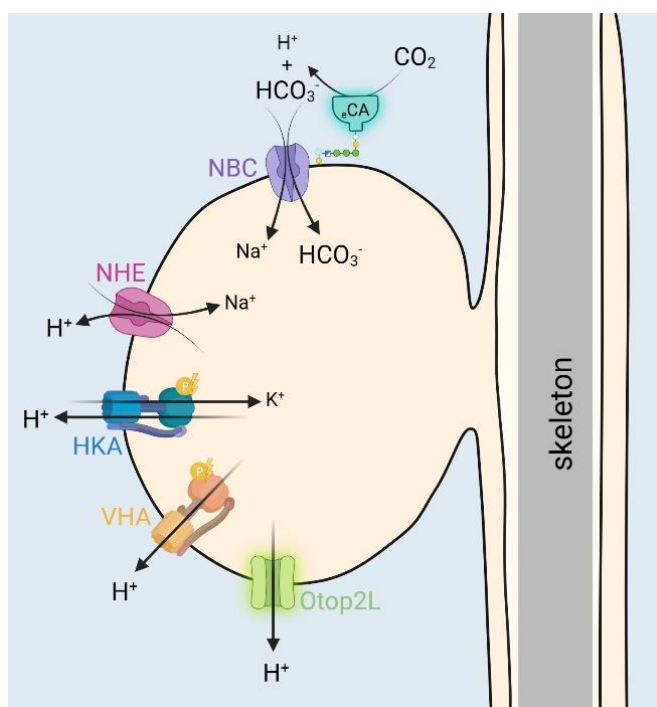


Fig. 5.2: Proposed participants in intracellular pH homeostasis during biomineralization in PMCs of the sea urchin larva. Cross-section of an enlarged PMC including Na⁺/HCO₃⁻ cotransporter (NBC), Na⁺/H⁺-exchanger (NHE), the energy consuming H⁺/K⁺ ATPase (HKA) and V-type H⁺ ATPase (VHA), as well as the newly in this thesis discovered participants extracellular CA (eCA) and proton channel (Otop2L) during the calcification process. Image created with BioRender.com, with permission.

5.2.2 H⁺ export

Another mechanism to deal with the intracellular acid load generated by the calcification process is the export of accumulating protons. The sea urchin larva possesses different transporters located in the PMC membrane that may serve as export of protons from the cell including a Na⁺/H⁺ exchanger (NHE), a V-type H⁺ ATPase (VHA) and a putative H⁺/K⁺ ATPase (HKA) (Fig. 5.2) (Hu et al., 2020). HKA activity could only be demonstrated by pharmacological inhibition with SCH28080, which resulted in an impaired skeletogenesis potentially due to inhibition of ACC precipitation in the vesicles (Schatzberg et al., 2015). However, a HKA could not be identified in the genome of the sea urchin larva so far (Hu et al., 2020). The ATP consuming VHA is also expressed in the PMCs and has been suggested to mediate H⁺ extrusion from the PMCs, due to the observation that addition of the VHA inhibitor bafilomycin decreased calcification rates in a dose-dependent manner (Hu et al., 2020). Another important group of acid-base transporters are the Na⁺/H⁺ exchangers that depend on the inward directed sodium gradient to export protons from the cell. In osteoblasts a Na⁺/H⁺ exchanger has been identified as an exit route for protons for maintenance of the alkaline pH_i to further promote mineralization (Liu et al., 2011). In the sea urchin larva, inhibition of the Na⁺/H⁺ exchanger NHE by EIPA (5-(N-ethyl-N-isopropyl)amiloride), revealed no significant effect on pH_i regulation of PMCs (Hu et al., 2020). However, a significant decrease in Ca²⁺ incorporation into the spicule, primarily in the body rod, has been detected (Hu et al., 2020), which was mainly due to a decrease in Ca²⁺ uptake by inhibition

of micropinocytosis and a subsequent decrease of vesicular trafficking (Ivanov, 2008). Further pH_i measurements revealed two PMC populations in older pluteus larvae (4 dpf), where 80% were sensitive to EIPA whereas the other 20% were insensitive. Furthermore, during active re-mineralization of the spicule, NHE activity was decreased (Hu et al., 2020). Taken together it has been concluded, that NHEs only have a minor contribution to pH_i regulation supporting the calcification process, but may serve acid-base housekeeping functions in non-mineralizing PMCs (Hu et al., 2020).

Based on the examinations of various proton export systems in PMCs the existence of an alternative route for H^+ exit during the calcification process can be proposed. We identified a proton channel, *Otop2L*, which exhibits high expression during skeletogenesis and exclusive expression in the PMCs (Publication I, Fig. 1 A – C). Otopetrins are a relatively new family of proton channels, playing a key role in acid-sensing of taste receptors (Teng et al., 2019) and are associated with the calcification processes, in statoconia of the vestibular organ (Hurle et al., 2003) and the otolith formation of the fish inner ear (Hughes et al., 2004). Knock-down of *Otop1* in zebra fish and mutation of *Otop1* in mice revealed agenesis of the otoliths or statoconia (Hughes et al., 2004; Hurle et al., 2003). These processes are comparable to the calcification process in the sea urchin larva. Otopetrin orthologs suggest a conserved role in the formation of mineralized structures, due to their detection in tissues associated with calcium secretion and calcium carbonate biomineralization (Hughes et al., 2008), for example in mollusks (Mount et al., 2004) or the blue crab (Wheatly, 1999). In the sea urchin larva, knock-down of *Otop2L* resulted in a substantial reduction of the skeleton growth (Publication I, Fig. 1 D), underlining a critical involvement in the biomineralization process of the sea urchin larva. H^+ conductivity of *Otop2L* was investigated in the PMCs using an external low pH pulse in combination with the broadband H^+ channel inhibitor Zn^{2+} . Zn^{2+} is proven to have an effect on proton currents in vertebrate *Otop1* (Saotome et al., 2019; Tu et al., 2018) and also inhibits H^+ extrusion in the calcifying coccolithophore *C. braarudii* leading to an increased malformation of coccoliths (Kottmeier et al., 2022). In the sea urchin larva only 30% of the PMCs showed Zn^{2+} sensitive pH_i regulation, which was also independent of external $[Na^+]$ and $[HCO_3^-]$ (Publication I, Fig. 2 B – E). Moreover, during later developmental stages of the larva, *Otop2L* expression and its location is observed in the scheidel region and the rod tips, where active calcification occurs as a result of spicule thickening or elongation (Publication I, Fig. 1 A + E). This led to the conclusion that *Otop2L* is the main exit route of H^+ across the PMC membrane during active calcification, meanwhile NHE is primarily active in the other 70-80% of PMCs along the body rod to maintain the skeleton (Hu et al., 2020). Knock-down of *Otop2L* showed comparable reduction in H^+ efflux as seen by the inhibition using Zn^{2+} (Publication I, Fig. 2 F + G). Interestingly, knock-down of *Otop2L* also resulted in a higher resting pH_i in the PMCs. This may be explained by a compensatory upregulation of the NBC transporter and the subsequent accumulation of HCO_3^- ions, which failed to be incorporated into the skeleton due to blockage of H^+ removal (Publication I, Fig. S5). This hypothesis

is supported by co-expression of *SpSlc4a10* and *Otop2l* in the same PMC populations in the scheitel region of the skeleton (Publication I, Fig. S6). Heterologous expression of the sea urchin *Otop2l* in HEK293 cells and *Xenopus* oocytes demonstrated that Otop2L encodes a proton channel that is activated by alkaline conditions of pH > 7.5 indicating an adaptation of this channel to the very stable pH conditions of ~ 8.2 – 8.1 in the marine environment over a long evolutionary timescale. In contrast, vertebrate otopetrins were demonstrated to be active under acidic to neutral conditions, while newer studies also indicate an activation of vertebrate otopetrins under alkaline conditions (Tian et al., 2023).

5.2.3 pHi differences

Additional results of this study revealed various intracellular pH of PMCs depending on their localization at the spicule (see 4 unpublished data). Earlier studies have shown, the location of the PMCs along the spicule determine the activity in the calcification process (Guss & Etensohn, 1997). The PMCs also differ in their composition of matrix proteins and acid-base transport systems. The bicarbonate co-transporter *spSlc4a10* is located both in the scheitel area and the postoral rod tips, while *Otop2l* is mainly found in the scheitel area and *Cara7* primarily in the postoral rod tips (Chang et al., 2021; Hu et al., 2018; Matt et al., 2022). This indicates, depending on the location of the PMCs, they differ in their intracellular pH regulation and CCM, which reflects the different pHi.

5.3 Water transport in PMCs

Biological membranes have a hydrophobic inner layer that prevents an easy passage of water. However, water transport is essential for all cells to maintain proper osmotic equilibria. Aquaporins are integral membrane proteins that facilitate the passage of water molecules as well as other unpolarized solutes across cellular membranes. Several homologues of the mammalian aquaporins (AQPs) were identified in the sea urchin genome. One of them, *spAQP9* was exclusively found in the PMCs with peak expression levels during the period of skeleton formation (Manuscript III, Fig. 1 A +B), visualized with *in situ* hybridization and single cell RNA sequencing analyses. Expression of *spAQP9* in heterologous expression systems like the *Xenopus* oocyte in combination with swelling experiments confirmed water transport function by this membrane protein. Water transport in cellular systems has been demonstrated to be related to cell migration and filopodia movement (Karlsson, 2013; Karlsson et al., 2013; Loitto et al., 2007). Accordingly, it can be hypothesized that in the very early development of the sea urchin larva, *spAQP9* could potentially play a role in the filopodia formation and thereby mediated migration of the mesenchyme cells during gastrulation of the blastula (Fig. 5.3 A – E) (Karp

& Solorsh, 1985). Furthermore, overexpression of *AQP9* induced cellular motility through filopodia formation in HEK-293 cells (Khajah & Luqmani, 2016) as well as in fibroblasts (Loitto et al., 2007). Additionally, it should be noted that the early larval development is an extensive period of PMCs migration and filopodia formation (Fig. 5.3 B + C) (Wolpert & Gustafson, 1961), thereby PMCs fuse together and form the syncytium in which the spicule of the larva is formed (Fig. 5.3 E). Therefore, water influx mediated by spAQP9 is potentially supporting cellular volume growth during syncytium formation. Finally, the PMC syncytium that forms a sheath around the spicule must increase its size during skeletogenesis. Since the absolute number of PMCs remains the same during development this process must be associated with an increase in cytoplasm by the uptake of water.

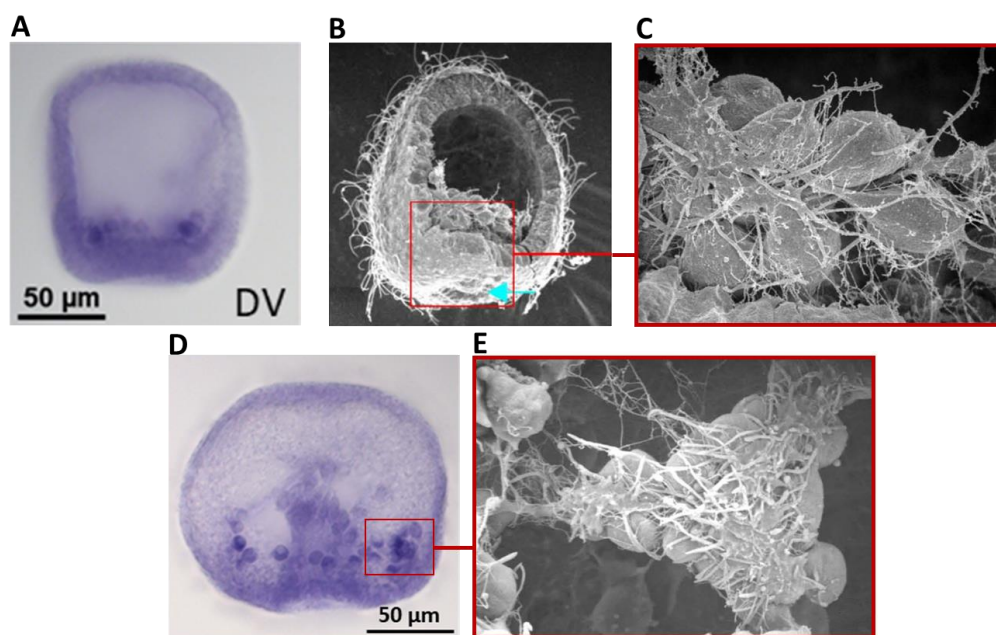


Fig. 5.3: (A) Positive whole-mount *in situ* hybridization signal in the PMCs, using antisense probes against spAQP9 at 24 hpf. DV = dorsal view. (B) SEM picture of an early gastrula with primary invagination of the archenteron (8 small micromeres, blue arrow). (C) Enlargement of boxed area showing filopodia around the initial PMC aggregation center. (adapted from (Morrill & Marcus, 2005)) (D) Positive whole-mount *in situ* hybridization signal in the PMCs, using antisense probes against spAQP9 at 30 hpf. (E) SEM picture resembling the enlarged boxed area showing well developed triradiate syncytium with numerous anchoring filopodia of a mid-gastrula stage embryo. (adapted from (Morrill & Marcus, 2005))

Using a custom-made antibody against spAQP9, we could demonstrate positive immunoreactivity in almost all PMCs of the larva. Higher magnification, indicated that spAQP9 is located rather in vesicular structures than in the plasma membrane of the PMCs (Fig. 5.4 A). Interestingly, we were able to detect two different types of IHC signal, which we further classified in two types of PMC populations. One population showed a crescent shape of suAQP9 positive vesicles close to the skeleton, that we interpreted as the “resting” state and the other population exhibited a diffuse arrangement all across the PMC, that we interpreted as the “active” state of the cell. We came to this hypothesis, due to our

results of the re-calcification experiment. During the re-calcification phase, after dissolution of the skeleton an increased number of PMCs had the diffuse IHC signal compared to non-remineralizing PMCs (Manuscript III, Fig. 3 D - F). Together with an increase in *spAQP9* expression in recalcifying larvae this change in sub-cellular localization of *spAQP9* suggests a participation in the calcification process. This observation corroborates earlier findings demonstrating functional differences among PMCs in highly calcifying regions vs. non calcifying regions of the larval skeleton (Guss & Etensohn, 1997; Ramesh et al., 2020).

Besides the potential role in mediating cell migration and filopodia movement of PMCs it is tempting to speculate that the vesicles, detected by our *spAQP9* antibody (Fig. 5.4 A), correspond to the Ca^{2+} -rich vesicles, containing the ACC for the skeleton. Evidence comes from the comparison to cryo-SEM observations where ACC containing vesicles have a very similar size and distribution pattern in the PMC compared to our *spAQP9* IHC signal (Kahil et al., 2020, 2023). ACC forming, Ca^{2+} -rich vesicles contain high Ca^{2+} concentrations ranging between 1-15 M. However, the seawater, surrounding the larva, only contains about 10 mM Ca^{2+} , implying the existence of a mechanism to drastically increase the Ca^{2+} concentration at the site of mineralization. One possible way of increasing the Ca^{2+} content in the vesicle, would be the extrusion of water and consequently vesicle shrinking (Fig. 5.4 B) (Beniash et al., 1999; Kahil et al., 2020). It remains to be investigated if this process could be accomplished by the water channel *spAQP9*. Another purpose for the water efflux through *spAQP9* out of the calcification vesicle could help to support the exit of water molecules during the formation of anhydrous ACC. During ACC maturation, CaCO_3 is going from a disordered phase to second phase of full ordered calcite that requires dehydration (Politi et al., 2006). The same phenomenon of water resorption from the mineralization space is also seen during the maturation and hardening of sponge siliceous spicules (Wang & Müller, 2015) suggesting a conserved role of water transport in place.

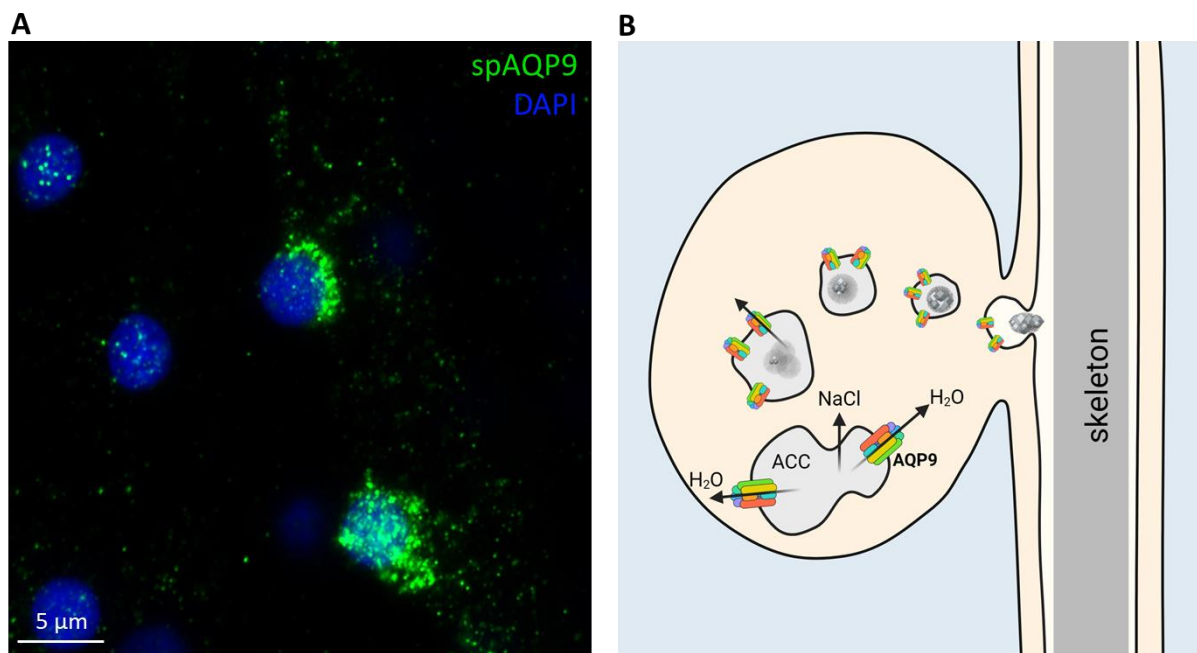


Fig. 5.4: (A) High-magnification image of the positive immunoreactivity of the polyclonal spAQP9-specific antibody and DAPI in PMCs of the body rod in the scheitel area of a pluteus larvae (4 dpf). (B) Cross-section of an enlarged PMC showing the proposed schematic model summarizing the role of water extrusion through spAQP9 (AQP9) in the vesicular network during the calcification process in PMCs of the sea urchin larva. Image created with BioRender.com, with permission.

5.4 Effect of Ocean Acidification

Since the industrial revolution 250 years ago, the release of anthropogenic CO₂ into the atmosphere has continuously increased. Approximately one third is absorbed by the ocean, resulting in a subsequent increase in [H⁺] leading to a decrease of the ocean surface pH, termed as ocean acidification (OA) (Caldeira & Wickett, 2003; Martins Medeiros & Souza, 2023). These changing ocean conditions may have a significant effect on marine calcifying organisms. Therefore, numerous studies have been focusing on the effect of ocean acidification on marine calcifying invertebrates, such as corals, echinoderms, mollusks and crustaceans (Martins Medeiros & Souza, 2023). Metabolism, acid-base homeostasis, calcification and growth were demonstrated to be among the most negatively affected physiological processes by OA (Bach et al., 2015; Caldeira & Wickett, 2005; Cao & Caldeira, 2008; Li et al., 2016; Martins Medeiros & Souza, 2023; Wang, Wang, Jia, Qiu, et al., 2017). Studies addressing the effect of elevated pCO₂ on the sea urchin larva, revealed increased metabolic rates (Stumpp et al., 2012; Stumpp, Wren, et al., 2011) to support pH regulatory systems potentially explaining reduced growth and developmental rates (Publication I, Fig. 4 E + F; (Hu & Stumpp, 2023)). This concept of energy allocations has been well documented in the sea urchin larva and have been

identified as a key factor that determines the resilience of the organism to reduced seawater pH (Pan et al., 2015; Stumpp et al., 2012).

For the sea urchin larva, it can be suggested that changes in the carbonate equilibrium decreasing the availability of CO_3^{2-} may not be problematic for the calcification process, since primarily HCO_3^- and not CO_3^{2-} is absorbed from the seawater. In addition, increased $p\text{CO}_2$ could even be beneficial for the calcification process in the sea urchin larva, considering that over 60% of the carbon source for the CCM is made by CO_2 and further converted to HCO_3^- by the extracellular carbonic anhydrase (CA) (Furla et al., 2000; Matt et al., 2022; Mitsunaga et al., 1986). Surprisingly, CA gene transcription has been demonstrated to be reduced in response to OA conditions in several marine species (Moya et al., 2012; Richier et al., 2011; Stumpp, Dupont, et al., 2011; X. Wang, Wang, Jia, Qiu, et al., 2017; Zoccola et al., 2016). In the coral *A. millepora* and *S. pistillata* a reduction in seawater pH resulted in a downregulation of a membrane-bound CA gene (Moya et al., 2012; Zoccola et al., 2016), as well as a cytosolic CA gene in the coccolithophore *E. huxleyi* and the oyster *C. gigas* (Richier et al., 2011; X. Wang, Wang, Jia, Qiu, et al., 2017). Furthermore, in the sea urchin larva, downregulation of a CA gene *CA15* (corresponding to our *Cara7*) has been demonstrated (Stumpp, Dupont, et al., 2011). Consequently, CA could act as a potential biomarker for the global impact of OA (Zebral et al., 2019).

In corals and coccolithophores it has been suggested, that the increase in $[\text{H}^+]$ of the seawater, negatively affects pH regulatory systems relevant for calcification (Cyronak et al., 2016; Suffrian et al., 2011). For maintaining CaCO_3 precipitation, it is necessary to exclude the H^+ that are liberated during the calcification process. Due to the proton-permeable ectoderm and extracellular matrix of the sea urchin larva, subsequent changes in seawater pH will directly change the proton gradient across the plasma membrane of PMCs (Hu & Stumpp, 2023). Given a key role of the H^+ channel *Otop2l* in promoting export of protons from the cell, OA conditions may negatively affect cellular pH homeostasis and calcification. This is revealed in a reduction in the expression level of *Otop2l* the first days of larval development exposed to elevated $p\text{CO}_2$ levels (Publication I, Fig. 4 G). Impairment of voltage gated H^+ channel activity under OA conditions was also recognized in coccolithophores (Kottmeier et al., 2022; Von Dassow, 2022). However, some tolerance against future OA conditions must be present in the sea urchin larva. Larvae, re-growing their skeleton and raised in seawater with pH 7.7 still show 60% growth of control calcification rate (Publication I, Fig. 4 F). This indicates, that the larva must elude on alternative ways to regulate its pH_i . In a previous study, it was shown that gene transcription of the bicarbonate transporter *SpSlc4a10* is increased, under OA conditions (Hu et al., 2018). This suggests that an increased bicarbonate import could partially compensate the enhanced acidification to further maintain the calcification process. Further alternative H^+ transport mechanisms to regulate pH_i might be the Na^+/H^+ exchanger or the V-type H^+ ATPase, as well as the Na^+/K^+ ATPase (NKA) to provide the

electrochemical gradient for secondary transport, which however, may be energetically disadvantageous (Hu & Stumpp, 2023; Stumpp et al., 2012).

In general, ocean acidification has been clearly demonstrated to force the larva to reallocate its energy to compensatory processes including ion regulation, protein synthesis and NKA activity. This leads to reduced availability of energy by -40% that can be used for development and growth (Hu & Stumpp, 2023; Pan et al., 2015). Additionally, the uptake of energy may be also affected due to reductions in digestion efficiency induced by lower midgut pH (Stumpp et al., 2013). Interestingly calcification in the sea urchin larva was not affected by elevated $p\text{CO}_2$ when corrected for the developmental delay (Hu et al., 2018), however, acidified conditions produced by the addition of acid significantly decreased calcification in the sea urchin larva (Chang et al., 2021). These observations suggest that i) an increase in H^+ may be the major factor that negatively impacts calcifying systems due to impaired H^+ flux from the cell and ii) that increased CO_2 may support the calcification process by providing more DIC to the cellular CCM.

The potential of sea urchins and their larvae to adapt to future OA predictions lies in their ability to allocate energy for essential physiological processes. Tipping point analyses suggested that larvae of the purple (H. G. Lee et al., 2019) as well as green sea urchin (Dorey et al., 2013) cannot maintain physiological functions at a CO_2 induced acidification level $< \text{pH } 7.2$. However, some sea urchin populations already inhabit low pH environments, such as in close proximity to volcanic CO_2 vents, upwelling regions and intertidal pools (Byrne & Hernández, 2020). These populations suggest a potential for local adaptation to the low pH conditions. For example, the adult sea urchin *A. lixula* is able to regulate the acid-base balance of their coelomic fluid, but accompanied by a loss in body size and reduction in spine length (Byrne & Hernández, 2020). Thus, future studies are needed to identify unifying principles underlying sensitivity in marine species and to better understand the adaptation potential of key physiological processes to better predict vulnerability in times of rapid climate change.

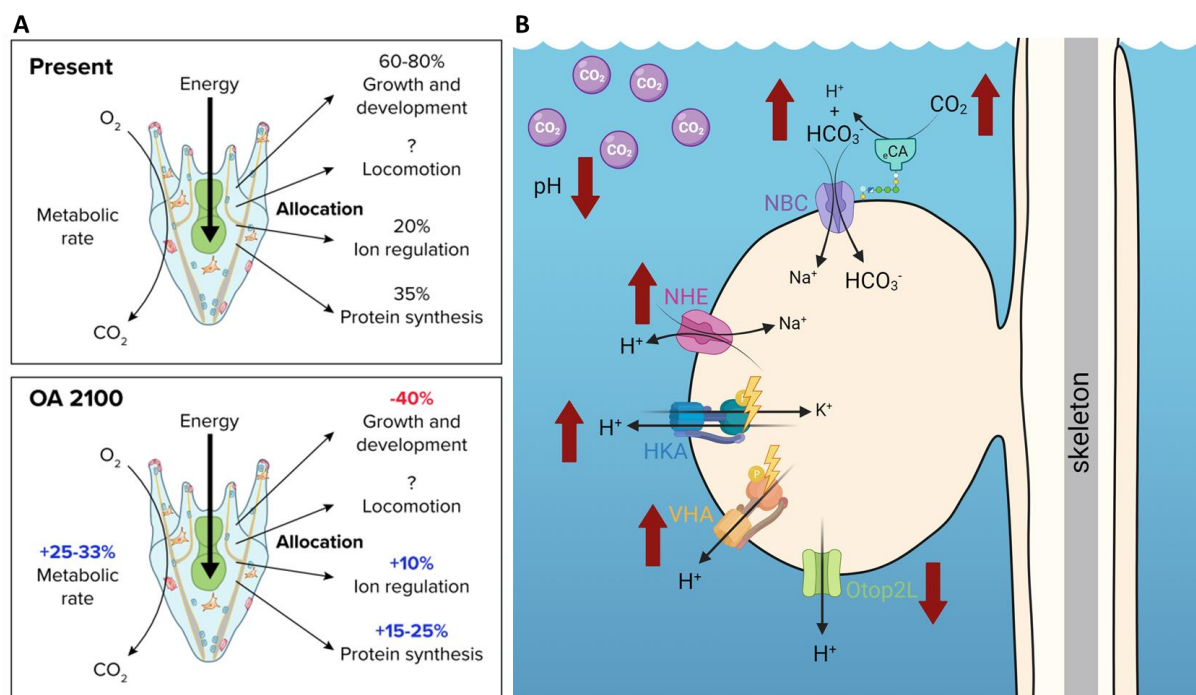


Fig. 5.5: (A) Energy budget distribution of major energy-consuming processes of the larva under present-day and future ocean acidification (OA) 2100 conditions. (adapted from (Hu & Stumpp, 2023)) (B) Schematic model of the proposed changes in the CCM and pH_i homeostasis in the PMCs of the sea urchin larva, contributing to the calcification process under future OA conditions, including the proposed alternative proton exit routes HKA and VHA, which require ATP. Image created with BioRender.com, with permission.

5.4.1 Impact of Global Warming

Not only ocean acidification is a threat to marine organisms, also global warming due to climate change and subsequent temperature increase of the oceans are a potential danger. More than 90% of the global warming heat is absorbed by the ocean, which increases the ocean's temperature steadily (Johnson & Lyman, 2020). Until today the ocean water temperature has already increased by $\sim 1.1^\circ\text{C}$ (UN Educational, Scientific and Cultural Organization) or 360 Zettajoules (ZJ) since 1955 (NOAA/NCEI World Ocean Database, (Levitus et al., 2012)), respectively. This heat stress, on the one hand has shown to downregulate the transcription of CA genes in the coral *A. aspera* (Zebra et al., 2019), but on the other hand increase CA activity in the scleractinian coral *M. Hartii* and the adult mussel *M. edulis* (Fonseca et al., 2017; Matoo et al., 2021). Studies using larvae of the sea urchin *H. tuberculata* and *T. gratilla*, which combined OA conditions with seawater warming in their experimental setups, detected that seawater warming of $+3 - 4^\circ\text{C}$ counteracted the negative effect on the larval growth rate caused by reductions in seawater pH to pH 7.8 - 7.6 (Byrne et al., 2013; Sheppard Brennan et al., 2010). This implies, that some species may be less vulnerable to the synergistic effects of climate change. However, the complexity of climate change phenomena may have repercussions which have

to be included, such as decrease in available oxygen and other vital nutrients, sea level rising and shrinkage of habitats (Intergovernmental Panel on Climate Change IPCC, 2019).

5.5 Evolutionary aspects of Biomineralization mechanisms

Biomineralization is an ancient biological process with fossil records dating back to the Cambrian and Ordovician periods over 540 million years ago (mya) (P. Gilbert et al., 2022). Carbonate skeletons evolved independently at least twenty-eight times pointing towards a repeated evolution of calcified structures with environmental, ecological and physiological homologies that led to this convergence (Knoll, 2003). The process of skeleton formation can be energetically costly, for example corals use 30% of their energy budget to generate their skeletons (Cohen & Holcomb, 2009). The gastropod *Nucella* spp. requires 1-2 J to produce 1 mg of CaCO_3 (Palmer, 1992) and larvae of the Pacific oyster require 1 J per mg CaCO_3 produced (Frieder et al., 2017). This corresponds to approximately 67% of the total energy required by the organism. Despite these substantial energetic efforts, the benefits of possessing a protective layer against predators and therefore ecological fitness, outweighed the energetic costs (P. Gilbert et al., 2022). Since there is no common ancestor with a biomineralized skeleton, this process must have evolved independently but convergently across the phyla. However, even on the molecular level calcifying organisms share a conserved set of genes, which governs carbonate biomineralization, including carbonic anhydrases, tyrosinases and chitin-binding proteins (Clark, 2020). These genes are not only essential for the mineralization process, but are associated with essential biological cell functions and were independently co-opted into the process of calcification. Carbonic anhydrases cover fundamental functions in aiding intracellular regulation of the acid-base homeostasis and to convert CO_2 to HCO_3^- and vice versa. Interestingly CAs play fundamental roles in calcifying systems and were independently co-opted for HCO_3^- production or served as a nucleation activator for biomineralization (Le Roy et al., 2014). This hypothesis is supported by conserved domains involved in activity of the enzyme, compared to lineage-specific repetitive or non-repetitive lox-complexity domains (RLCDs/LCDs), which are a result of gene duplication and insertion (Le Roy et al., 2014). Furthermore, bicarbonate transporters associated with calcifying systems evolved also via gene duplication which can be regarded as a key step in the evolution of biomineralization in basal metazoans (Zoccola et al., 2015). Both, bicarbonate transporters and carbonic anhydrases, are fundamentally involved in today's calcification process of marine organisms, as was demonstrated in the carbon concentration mechanism (CCM) of the sea urchin larva in the present work.

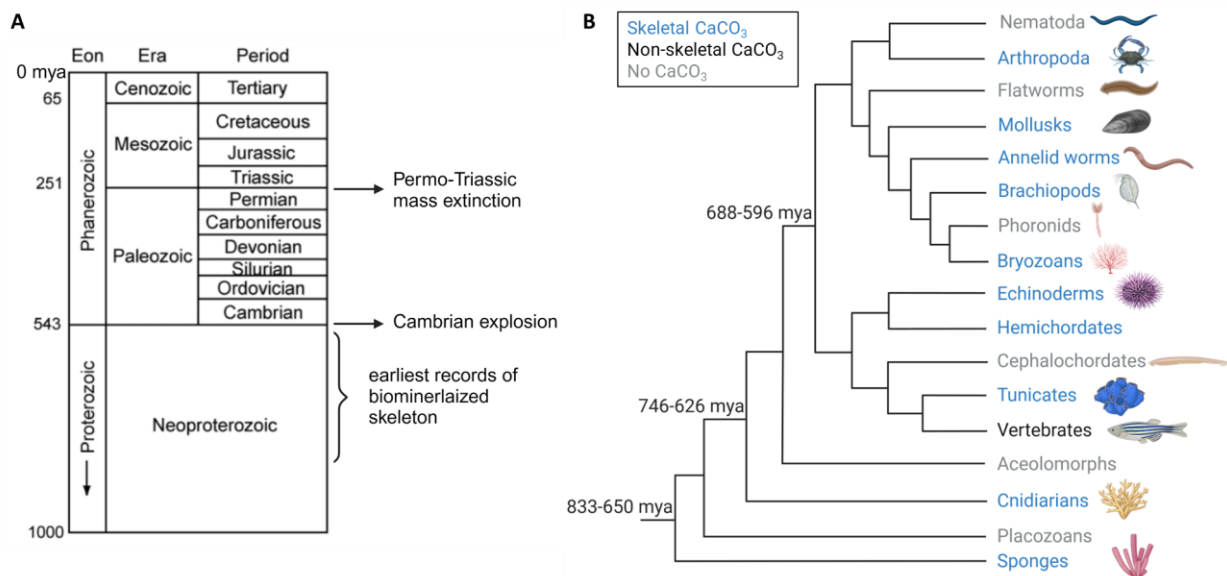


Fig. 5.6: (A) A geologic time scale for the past 1000 million years, showing the principal time divisions used in Earth science and the timing of some major evolutionary events. (adapted from (Knoll, 2003)) (B) Phylogenetic distribution of CaCO_3 biomineralization in animals. Species, also making a CaCO_3 skeleton, such as foraminiferans, coccolithophorids, algae and dinoflagellates are not shown. CaCO_3 skeleton-forming animals are shown in blue font; black font indicates animals that form non-skeletal CaCO_3 biominerals and gray font indicate animals that do not form CaCO_3 at all. All clades started biomineralizing after they diverged from another. (adapted from (P. Gilbert et al., 2022)); Image created with BioRender.com, with permission.

In the Cambrian period over 540 mya ago, environmental changes, such as oversaturation of CaCO_3 , favored skeleton biomineralization in the pre-historic oceans (Knoll, 2003). Incisive events, like volcanic activity, at the end of the Permian period (252 mya) changed environmental conditions drastically. The high emission of volcanic CO_2 and other chemicals led to ocean acidification, global warming and deoxygenation of marine waters (Knoll et al., 2007). This catastrophe resulted in one of the five big mass extinctions in earth history and led to mass extinctions of many marine taxa, including major marine calcifiers like cnidarians and stalked echinoderms (P. Gilbert et al., 2022; Racki, 2019). CO_2 emissions ranging from 1000 – 2000 ppmv and subsequent temperature increases by $\sim 5^\circ\text{C}$ accompanied by reductions in seawater pH by 0.5 pH units strongly resemble the ongoing climate change phenomenon driven by human activities in the 21st century (Wu et al., 2021, 2023). Thus, research on the mineral compositions in extinct and present-day calcifiers, in combination with a mechanistic understanding regarding the calcification process may help to explain and predict the evolution of calcifying systems including their responses to environmental change in past, present and future marine systems.

6 Conclusion

Based on the results of this work the objectives formulated earlier can be addressed.

- I. The role of an otopetrin-like proton channel in the PMCs of the sea urchin larva as a potential proton exit route during the calcification process.

The study shows that the sea urchin *Otop2l* in PMCs conducts protons and is critically involved in the calcification process. Knockdown of *Otop2l* leads to a reduction in skeleton formation in the larvae, and recalcification induces increased expression levels of *Otop2l*. *Otop2l* provides an exit route for the accrued protons by intracellular CaCO_3 formation in the PMCs during mineralization and maintain intracellular pH homeostasis to further enable calcification. Functional characterization and pH perturbation experiments revealed proton efflux activity under past and present ocean pH conditions, indicating adaptation to a long-term stable oceanic pH. Larvae, raised under reduced seawater pH conditions exhibit decreased calcification rate. Accordingly, ocean acidification induced reduction in seawater pH may compromise *Otop2l* function and proton efflux from the cell and therefore impair cellular pH homeostasis during calcification. Considering the widespread presence of otopetrins across metazoans, our findings offer a platform for examining the potentially conserved function of this proton channel family in other calcifying organisms. Such a comparative analysis stands to unveil overarching mechanisms governing the susceptibility of marine calcifiers to ocean acidification.

- II. Understanding the function of carbonic anhydrases in the PMCs of the sea urchin larva and their involvement in the carbon concentration mechanisms for the calcification process.

The study reveals the crucial role of extracellular carbonic anhydrases (eCAs) underlying a cellular carbon concentration mechanism and intracellular pH homeostasis within the calcifying PMCs of the sea urchin larva. Pharmacological inhibition or knock-down of the eCA *Cara7* leads to impaired formation of the postoral rod. Functional characterization and CO_2 perfusion experiments suggest that in a first step metabolic CO_2 , diffusing out of the cell, is transformed to HCO_3^- by eCA to minimize the intracellular acid load. In a second step bicarbonate is transported into the cell to increase the cellular carbon pool and to support further CaCO_3 formation.

This research provides a differentiated understanding of how changes in oceanic carbonate chemistry impact calcifying systems. While hypercapnic conditions stimulate the expression of PMC-specific CA *Cara7* and bicarbonate transporter *Sp-Slc4a10*, the associated energetic demands may pose challenges. Conversely, increased environmental $p\text{CO}_2$ may be beneficial for calcifying systems that rely on CO_2 as a carbon source, yet reduced carbonate saturation states and elevated seawater acidity counteract these benefits, impacting calcification rates. Given the deep evolutionary history of eCAs

and their association with the calcification process, these findings offer insights into their role across diverse calcifying species. This study sheds light on how carbonic anhydrases support cellular carbon concentration mechanism using mainly the metabolic waste product CO₂, showcasing nature's ability to utilize carbon resources in a highly sustainable manner.

III. The role of aquaporins in the PMCs of the sea urchin larva and their potential contribution in the calcification process.

Our investigation unveils the exclusive expression of the aquaglyceroporin *spAQP9* in PMCs of the sea urchin larval. Its peak expression at 30 hpf coincides with skeleton formation initiation, suggesting a pivotal role in skeletogenesis and spicule elongation. Heterologous expression experiments confirm *spAQP9*'s dual function as a water and carbon dioxide channel. While its exact role in PMC motility and vesicular dynamics remains speculative, its sub-cellular localization within vesicles during calcification hints at involvement in the intracellular (vesicular) mineralization process. The dual role of *spAQP9* in water and CO₂ transport suggests potential contributions to intracellular carbon concentration mechanisms. Despite these promising findings, further experimental validation is required. Our study underscores the multifaceted role of *spAQP9* in sea urchin larval calcification, from water and CO₂ transport to potential involvement in vesicular dynamics and ACC maturation. This work paves the way for future investigations into the cellular mechanisms driving biomineralization.

In conclusion, the process of biomineralization in marine organisms is a complex and intricate process that involves the coordination of various factors such as pH and carbon homeostasis, vesicular transport and protein translocation. Through the research conducted in this thesis, groundbreaking new insights have been gained into the mechanisms underlying cellular carbon concentration in calcifying PMCs of the sea urchin larva. The discovery of a novel cellular carbon concentration mechanism, underscored by the pivotal involvement of an extracellular carbonic anhydrase *Cara7*, alongside the identification of a proton channel *Otop2l* and an aquaporin *spAQP9* in PMCs shed light on the interaction of these enzymes and transport proteins in the calcification process. These findings provide a deeper mechanistic understanding of calcifying systems in marine organisms and offer valuable insights into their sensitivities to past and future oceanic conditions.

7 References

- Addadi, L., Raz, S., & Weiner, S. (2003). Taking advantage of disorder: Amorphous calcium carbonate and its roles in biomineralization. *Advanced Materials*, *15*(12), 959–970. <https://doi.org/10.1002/adma.200300381>
- Adonin, L., Drozdov, A., & Barlev, N. A. (2021). Sea Urchin as a Universal Model for Studies of Gene Networks. *Frontiers in Genetics*, *11*(January). <https://doi.org/10.3389/fgene.2020.627259>
- Aharon, R., & Bar-Shavit, Z. (2006). Involvement of aquaporin 9 in osteoclast differentiation. *Journal of Biological Chemistry*, *281*(28), 19305–19309. <https://doi.org/10.1074/jbc.M601728200>
- Al-Horani, F. A., Al-Moghrabi, S. M., & De Beer, D. (2003). Microsensor study of photosynthesis and calcification in the scleractinian coral, *Galaxea fascicularis*: active internal carbon cycle. *Journal of Experimental Marine Biology and Ecology*, *288*(1), 1–15. [https://doi.org/10.1016/S0022-0981\(02\)00578-6](https://doi.org/10.1016/S0022-0981(02)00578-6)
- Alvarez, B. V., Loisel, F. B., Supuran, C. T., Schwartz, G. J., & Casey, J. R. (2003). Direct Extracellular Interaction between Carbonic Anhydrase IV and the Human NBC1 Sodium/Bicarbonate Co-Transporter. *Biochemistry*, *42*(42), 12321–12329. <https://doi.org/10.1021/bi0353124>
- Bach, L. T., Riebesell, U., Gutowska, M. A., Federwisch, L., & Schulz, K. G. (2015). A unifying concept of coccolithophore sensitivity to changing carbonate chemistry embedded in an ecological framework. *Progress in Oceanography*, *135*, 125–138. <https://doi.org/10.1016/j.pocean.2015.04.012>
- Becker, H. M. (2020). Carbonic anhydrase IX and acid transport in cancer. *British Journal of Cancer*, *122*(2), 157–167. <https://doi.org/10.1038/s41416-019-0642-z>
- Beniash, E., Addadi, L., & Weiner, S. (1999). Cellular control over spicule formation in sea urchin embryos: A structural approach. *Journal of Structural Biology*, *125*(1), 50–62. <https://doi.org/10.1006/jsbi.1998.4081>
- Beniash, E., Aizenberg, J., Addadi, L., & Weiner, S. (1997). Amorphous calcium carbonate transforms into calcite during sea urchin larval spicule growth. *Proceedings of the Royal Society B: Biological Sciences*, *264*(1380), 461–465. <https://doi.org/10.1098/rspb.1997.0066>
- Benson, C. & Chow, G. (1979). Carbonic anhydrase activity in developing sea urchin embryos. *Experimental Cell Research*, *124*.
- Bentov, S., Brownlee, C., & Erez, J. (2009). The role of seawater endocytosis in the biomineralization process in calcareous foraminifera. *Proceedings of the National Academy of Sciences of the United States of America*, *106*(51), 21500–21504. <https://doi.org/10.1073/pnas.0906636106>
- Bertucci, A., Moya, A., Tambutté, S., Allemand, D., Supuran, C. T., & Zoccola, D. (2013). Carbonic anhydrases in anthozoan corals - A review. *Bioorganic and Medicinal Chemistry*, *21*(6), 1437–1450. <https://doi.org/10.1016/j.bmc.2012.10.024>
- Blair, H. C., Larrouture, Q. C., Tourkova, I. L., Liu, L., Bian, J. H., Stolz, D. B., Nelson, D. J., & Schlesinger, P. H. (2018). Support of bone mineral deposition by regulation of pH. *American Journal of Physiology - Cell Physiology*, *315*(4), C587–C597. <https://doi.org/10.1152/ajpcell.00056.2018>
- Brinkman, R. (1933). The occurrence of carbonic anhydrase in lower marine animals. *Journal of Physiology*, *80*(2), 171–173.
- Brown, D., Bouley, R., Păunescu, T. G., Breton, S., & Lu, H. A. J. (2012). New insights into the dynamic regulation of water and acid-base balance by renal epithelial cells. *American Journal of*

- Physiology - Cell Physiology*, 302(10). <https://doi.org/10.1152/ajpcell.00085.2012>
- Brownlee, C., Wheeler, G. L., & Taylor, A. R. (2015). Coccolithophore biomineralization: New questions, new answers. *Seminars in Cell & Developmental Biology*, 46, 11–16. <https://doi.org/10.1016/J.SEMCDB.2015.10.027>
- Buitenhuis, E. T., De Baar, H. J. W., & Veldhuis, M. J. W. (1999). Photosynthesis and calcification by *Emiliana huxleyi* (Prymnesiophyceae) as a function of inorganic carbon species. *Journal of Phycology*, 35(5), 949–959. <https://doi.org/10.1046/j.1529-8817.1999.3550949.x>
- Burlacot, A., Dao, O., Auroy, P., Cui n , S., Li-Beisson, Y., & Peltier, G. (2022). Alternative photosynthesis pathways drive the algal CO₂-concentrating mechanism. *Nature*, 605(7909), 366–371. <https://doi.org/10.1038/s41586-022-04662-9>
- Byrne, M., Foo, S., Soars, N. A., Wolfe, K. D. L., Nguyen, H. D., Hardy, N., & Dworjanyn, S. A. (2013). Ocean warming will mitigate the effects of acidification on calcifying sea urchin larvae (*Helicodaris tuberculata*) from the Australian global warming hot spot. *Journal of Experimental Marine Biology and Ecology*, 448, 250–257. <https://doi.org/10.1016/j.jembe.2013.07.016>
- Byrne, M., & Hern andez, J. C. (2020). Sea urchins in a high CO₂ world: Impacts of climate warming and ocean acidification across life history stages. *Developments in Aquaculture and Fisheries Science*, 43, 281–297. <https://doi.org/10.1016/B978-0-12-819570-3.00016-0>
- Caldeira, K., & Wickett, M. (2005). Ocean model predictions of chemistry changes from carbon dioxide emissions to the atmosphere and ocean. *Journal of Geophysical Research: Oceans*, 110(9), 1–12. <https://doi.org/10.1029/2004JC002671>
- Caldeira, K., & Wickett, M. E. (2003). Anthropogenic carbon and ocean pH. *Nature*, 425(6956), 365. <https://doi.org/10.1038/425365a>
- Cao, L., & Caldeira, K. (2008). Atmospheric CO₂ stabilization and ocean acidification. *Geophysical Research Letters*, 35(19), 1–5. <https://doi.org/10.1029/2008GL035072>
- Carbrey, J. M., Gorelick-Feldman, D. A., Kozono, D., Praetorius, J., Nielsen, S., & Agre, P. (2003). Aquaglyceroporin AqP9: Solute permeation and metabolic control of expression in liver. *Proceedings of the National Academy of Sciences of the United States of America*, 100(5), 2945–2950. <https://doi.org/10.1073/pnas.0437994100>
- Chang, W. W., Matt, A.-S., Schewe, M., Musinszki, M., Gr ssel, S., Brandenburg, J., Garfield, D., Bleich, M., Baukrowitz, T., & Hu, M. Y. (2021). An otopetrin family proton channel promotes cellular acid efflux critical for biomineralization in a marine calcifier. *Proceedings of the National Academy of Sciences of the United States of America*, 118(30), e2101378118. <https://doi.org/10.1073/pnas.2101378118>
- Christianson, D. W., & Fierke, C. A. (1996). Carbonic Anhydrase: Evolution of the Zinc Binding Site by Nature and by Design. *Accounts of Chemical Research*, 29(7), 331–339. <https://doi.org/10.1021/ar9501232>
- Clark, M. S. (2020). Molecular mechanisms of biomineralization in marine invertebrates. *Journal of Experimental Biology*, 223(11). <https://doi.org/10.1242/jeb.206961>
- Cohen, A. L., & Holcomb, M. (2009). Why corals care about ocean acidification uncovering the mechanism. *Oceanography*, 22(SPL.ISS. 4), 118–127. <https://doi.org/10.5670/oceanog.2009.102>
- Cooper, G. J., Occhipinti, R., & Boron, W. F. (2015). CrossTalk proposal: Physiological CO₂ exchange can depend on membrane channels. *Journal of Physiology*, 593(23), 5025–5028. <https://doi.org/10.1113/JP270059>

- Crenshaw, M. A. (1972). The Inorganic Composition of Molluscan Extrapallial Fluid. *Biological Bulletin*, 143(3), 506–512.
- Cyronak, T., Schulz, K. G., & Jokieli, P. L. (2016). The Omega myth: What really drives lower calcification rates in an acidifying ocean. *ICES Journal of Marine Science*, 73(3), 558–562. <https://doi.org/10.1093/icesjms/fsv075>
- De Goeyse, S., Webb, A. E., Reichart, G. J., & De Nooijer, L. J. (2021). Carbonic anhydrase is involved in calcification by the benthic foraminifer *Amphistegina lessonii*. *Biogeosciences*, 18(2), 393–401. <https://doi.org/10.5194/bg-18-393-2021>
- Decker, G. L., Morrill, J. B., & Lennarz, W. J. (1987). Characterization of sea urchin primary mesenchyme cells and spicules during biomineralization in vitro. *Development*, 101(2), 297–312. <https://doi.org/10.1242/dev.101.2.297>
- Denker, B. M., Smith, B. L., Kuhajda, F. P., & Agre, P. (1988). Identification, purification, and partial characterization of a novel M(r) 28,000 integral membrane protein from erythrocytes and renal tubules. *Journal of Biological Chemistry*, 263(30), 15634–15642. [https://doi.org/10.1016/s0021-9258\(19\)37635-5](https://doi.org/10.1016/s0021-9258(19)37635-5)
- Dix, J. A., & Solomon, A. K. (1984). Role of membrane proteins and lipids in water diffusion across red cell membranes. *BBA - Biomembranes*, 773(2), 219–230. [https://doi.org/10.1016/0005-2736\(84\)90085-3](https://doi.org/10.1016/0005-2736(84)90085-3)
- Dorey, N., Lançon, P., Thorndyke, M., & Dupont, S. (2013). Assessing physiological tipping point of sea urchin larvae exposed to a broad range of pH. *Global Change Biology*, 19(11), 3355–3367. <https://doi.org/10.1111/gcb.12276>
- Emllet, R. B. (1982). Echinoderm Calcite: A mechanical analysis from larval spicules. *Biological Bulletin*, 163(2), 264–275.
- Endeward, V., Musa-Aziz, R., Cooper, G. J., Chen, L. -M., Pelletier, M. F., Virkki, L. V., Supuran, C. T., King, L. S., Boron, W. F., & Gros, G. (2006). Evidence that aquaporin 1 is a major pathway for CO₂ transport across the human erythrocyte membrane. *The FASEB Journal*, 20(12), 1974–1981. <https://doi.org/10.1096/fj.04-3300com>
- Erez, J. (1978). Vital Effect on stable-isotope composition seen in Foraminifera and coral skeletons. *Nature*, 273(May), 199–202.
- Ettensohn, C. A. (2017). Sea Urchins as a Model System for Studying Embryonic Development. In *Reference Module in Biomedical Sciences*. Elsevier Inc. <https://doi.org/10.1016/b978-0-12-801238-3.99509-6>
- Fabry, V. J., Seibel, B. A., Feely, R. A., & Orr, J. C. (2008). Impacts of ocean acidification on marine biodiversity. *ICES Journal of Marine Science*, 65(3), 414–432. <https://doi.org/10.2307/j.ctv8jnz1.25>
- Fields, S., & Johnston, M. (2005). Whiter Model Organsim Research. *Science*, 307(5717), 1885–1886. <https://doi.org/10.1126/science.1110797>
- Fonseca, J. da S., Marangoni, L. F. de B., Marques, J. A., & Bianchini, A. (2017). Effects of increasing temperature alone and combined with copper exposure on biochemical and physiological parameters in the zooxanthellate scleractinian coral *Mussismilia harttii*. *Aquatic Toxicology*, 190(July), 121–132. <https://doi.org/10.1016/j.aquatox.2017.07.002>
- Frieder, C. A., Applebaum, S. L., Pan, T. C. F., Hedgecock, D., & Manahan, D. T. (2017). Metabolic cost of calcification in bivalve larvae under experimental ocean acidification. *ICES Journal of Marine Science*, 74(4), 941–954. <https://doi.org/10.1093/icesjms/fsw213>

- Furla, P., Galgani, I., Durand, I., & Allemand, D. (2000). Sources and mechanisms of inorganic carbon transport for coral calcification and photosynthesis. *Journal of Experimental Biology*, *203*(22), 3445–3457. <https://doi.org/10.1242/jeb.203.22.3445>
- Ganguly, A., Chandel, A., Turner, H., Wang, S., Liman, E. R., & Montell, C. (2021). Requirement for an Otopetrin-like protein for acid taste in *Drosophila*. *Proceedings of the National Academy of Sciences of the United States of America*, *118*(51). <https://doi.org/10.1073/pnas.2110641118>
- Geers, C., & Gros, G. (2000). Carbon dioxide transport and carbonic anhydrase in blood and muscle. *Physiological Reviews*, *80*(2), 681–715. <https://doi.org/10.1152/physrev.2000.80.2.681>
- Geyer, R. R., Musa-Aziz, R., Qin, X., & Boron, W. F. (2013). Relative CO₂/NH₃ selectivities of mammalian aquaporins 0-9. *American Journal of Physiology - Cell Physiology*, *304*(10). <https://doi.org/10.1152/ajpcell.00033.2013>
- Gilbert, P., Bergmann, K. D., Boekelheide, N., Tambutté, S., Mass, T., Marin, F., Adkins, J. F., Erez, J., Gilbert, B., Knutson, V., Cantine, M., Hernández, J. O., & Knoll, A. H. (2022). Biomineralization: Integrating mechanism and evolutionary history. *Science Advances*, *8*(10). <https://doi.org/10.1126/sciadv.abl9653>
- Gilbert, S. E. (2000). Developmental Biology 6th edition. In *Sunderland (MA): Asinauer Associates*. <https://doi.org/10.1016/B978-0-323-46294-5.00028-5>
- Goreau, T. F. (1959). THE PHYSIOLOGY OF SKELETON FORMATION IN CORALS. I. A METHOD FOR MEASURING THE RATE OF CALCIUM DEPOSITION BY CORALS UNDER DIFFERENT CONDITIONS. *The Biological Bulletin*, *116*(1).
- Graber, M., DiPaola, J., Hsiang, F., Barry, C., & Pastoriza, E. (1991). Intracellular pH in the OK cell. I. Identification of H⁺ conductance and observations on buffering capacity. *American Journal of Physiology - Cell Physiology*, *261*(6 30-6). <https://doi.org/10.1152/ajpcell.1991.261.6.c1143>
- Guss, K. A., & Etensohn, C. A. (1997). Skeletal morphogenesis in the sea urchin embryo: Regulation of primary mesenchyme gene expression and skeletal rod growth by ectoderm-derived cues. *Development*, *124*(10), 1899–1908. <https://doi.org/10.1242/dev.124.10.1899>
- Hedfalk, K., Törnroth-Horsefield, S., Nyblom, M., Johanson, U., Kjellbom, P., & Neutze, R. (2006). Aquaporin gating. *Current Opinion in Structural Biology*, *16*(4), 447–456. <https://doi.org/10.1016/j.sbi.2006.06.009>
- Hu, M. Y., Casties, I., Stumpp, M., Ortega-Martinez, O., & Dupont, S. (2014). Energy metabolism and regeneration are impaired by seawater acidification in the infaunal brittlestar *Amphiura filiformis*. *Journal of Experimental Biology*, *217*(13), 2411–2421. <https://doi.org/10.1242/jeb.100024>
- Hu, M. Y., Petersen, I., Chang, W. W., Blurton, C., & Stumpp, M. (2020). Cellular bicarbonate accumulation and vesicular proton transport promote calcification in the sea urchin larva: Mechanism of skeleton calcification. *Proceedings of the Royal Society B: Biological Sciences*, *287*(1934). <https://doi.org/10.1098/rspb.2020.1506>
- Hu, M. Y., & Stumpp, M. (2023). Surviving in an Acidifying Ocean: Acid-Base Physiology and Energetics of the Sea Urchin Larva. *Physiology (Bethesda, Md.)*, *38*(5), 0. <https://doi.org/10.1152/physiol.00007.2023>
- Hu, M. Y., Yan, J. J., Petersen, I., Himmerkus, N., Bleich, M., & Stumpp, M. (2018). A SLC4 family bicarbonate transporter is critical for intracellular pH regulation and biomineralization in sea urchin embryos. *ELife*, *7*, 1–17. <https://doi.org/10.7554/eLife.36600>
- Hub, J. S., & De Groot, B. L. (2008). Mechanism of selectivity in aquaporins and aquaglyceroporins.

- Proceedings of the National Academy of Sciences of the United States of America*, 105(4), 1198–1203. <https://doi.org/10.1073/pnas.0707662104>
- Hughes, I., Binkley, J., Hurle, B., Green, E. D., Program, C. S., Sidow, A., & Ornitz, D. M. (2008). Identification of the Otopetrin Domain, a conserved domain in vertebrate otopetrins and invertebrate otopetrin-like family members. *BMC Evolutionary Biology*, 8(41), 1–10. <https://doi.org/10.1186/1471-2148-8-41>
- Hughes, I., Blasiolo, B., Huss, D., Warchol, M. E., Rath, N. P., Hurle, B., Ignatova, E., David Dickman, J., Thalmann, R., Levenson, R., & Ornitz, D. M. (2004). Otopetrin 1 is required for otolith formation in the zebrafish *Danio rerio*. *Developmental Biology*, 276(2), 391–402. <https://doi.org/10.1016/j.ydbio.2004.09.001>
- Hurle, B., Ignatova, E., Massironi, S. M., Mashimo, T., Rios, X., Thalmann, I., Thalmann, R., & Ornitz, D. M. (2003). Non-syndromic vestibular disorder with otoconial agenesis in tilted/mergulhador mice caused by mutations in otopetrin 1. *Human Molecular Genetics*, 12(7), 777–789. <https://doi.org/10.1093/hmg/ddg087>
- Intergovernmental Panel on Climate Change IPCC. (2019). *Refinement to the 2006 IPCC Guidelines for National Greenhouse Gas Inventories; Intergovernmental Panel on Climate Change IPCC* (Vol. 2).
- Intergovernmental Panel on Climate Change IPCC. (2023). *Climate Change 2023 – The Physical Science Basis*. <https://doi.org/10.1017/9781009157896.015>
- IPCC, I. P. on C. C. (2021). *Climate Change 2021 - The Physical Science Basis*.
- Ishibashi, K. (2006). Aquaporin subfamily with unusual NPA boxes. *Biochimica et Biophysica Acta - Biomembranes*, 1758(8), 989–993. <https://doi.org/10.1016/j.bbamem.2006.02.024>
- Ishibashi, K., Kuwahara, M., Gu, Y., Kageyama, Y., Tohsaka, A., Suzuki, F., Marumo, F., & Sasaki, S. (1997). Cloning and functional expression of a new water channel abundantly expressed in the testis permeable to water, glycerol, and urea. *Journal of Biological Chemistry*, 272(33), 20782–20786. <https://doi.org/10.1074/jbc.272.33.20782>
- Ishibashi, K., Morinaga, T., Kuwahara, M., Sasaki, S., & Imai, M. (2002). Cloning and identification of a new member of water channel (AQP10) as an aquaglyceroporin. *Biochimica et Biophysica Acta - Gene Structure and Expression*, 1576(3), 335–340. [https://doi.org/10.1016/S0167-4781\(02\)00393-7](https://doi.org/10.1016/S0167-4781(02)00393-7)
- Ishibashi, K., Tanaka, Y., & Morishita, Y. (2020). Perspectives on the evolution of aquaporin superfamily. In *Vitamins and Hormones* (1st ed., Vol. 112). Elsevier Inc. <https://doi.org/10.1016/bs.vh.2019.08.001>
- Ivanov, A. I. (2008). Pharmacological Inhibition of Endocytic Pathways: Is It Specific Enough to Be Useful? In *Exocytosis and Endocytosis* (pp. 15–33).
- Jackson, D. J., Macis, L., Reitner, J., & Degnan, B. M. (2007). Sponge Paleogenomics Reveals an Ancient Role for Carbonic Anhydrase in Skeletogenesis. *Science*, 1054(June), 1893–1895.
- Jiang, L. Q., Carter, B. R., Feely, R. A., Lauvset, S. K., & Olsen, A. (2019). Surface ocean pH and buffer capacity: past, present and future. *Scientific Reports*, 9(1), 1–11. <https://doi.org/10.1038/s41598-019-55039-4>
- Johnson, D. E., & Casey, J. R. (2009). Bicarbonate Transport Metabolons. In *Drug Design of Zinc-Enzyme Inhibitors: Functional, Structural and Disease Applications* (pp. 415–418).
- Johnson, G. C., & Lyman, J. M. (2020). Warming trends increasingly dominate global ocean. *Nature Climate Change*, 10(8), 757–761. <https://doi.org/10.1038/s41558-020-0822-0>

- Jones, W. C., & Ledger, P. W. (1986). The effect of diamox and various concentrations of calcium on spicule secretion in the calcareous sponge *Sycon ciliatum*. *Comparative Biochemistry and Physiology -- Part A: Physiology*, *84*(1), 149–158. [https://doi.org/10.1016/0300-9629\(86\)90057-5](https://doi.org/10.1016/0300-9629(86)90057-5)
- Kahil, K., Kaplan-Ashiri, I., Wolf, S. G., Rechav, K., Weiner, S., & Addadi, L. (2023). Elemental compositions of sea urchin larval cell vesicles evaluated by cryo-STEM-EDS and cryo-SEM-EDS. *Acta Biomaterialia*, *155*, 482–490.
- Kahil, K., Varsano, N., Sorrentino, A., Pereiro, E., Rez, P., Weiner, S., & Addadi, L. (2020). Cellular pathways of calcium transport and concentration toward mineral formation in sea urchin larvae. *Proceedings of the National Academy of Sciences of the United States of America*, *117*(49), 30957–30965. <https://doi.org/10.1073/pnas.1918195117>
- Kahil, K., Weiner, S., Addadi, L., & Gal, A. (2021). Ion Pathways in Biomineralization: Perspectives on Uptake, Transport, and Deposition of Calcium, Carbonate, and Phosphate. *Journal of the American Chemical Society*. <https://doi.org/10.1021/jacs.1c09174>
- Karakostis, K., Costa, C., Zito, F., Brümmer, F., & Matranga, V. (2016). Characterization of an Alpha Type Carbonic Anhydrase from *Paracentrotus lividus* Sea Urchin Embryos. *Marine Biotechnology*, *18*(3), 384–395. <https://doi.org/10.1007/s10126-016-9701-0>
- Karlsson, T. (2013). *Water Fluxes and Cell Migration How Aquaporin 9 Controls Cell Shape and Motility* (Issue 1353).
- Karlsson, T., Bolshakova, A., Magalhães, M. A. O., Loitto, V. M., & Magnusson, K. E. (2013). Fluxes of Water through Aquaporin 9 Weaken Membrane-Cytoskeleton Anchorage and Promote Formation of Membrane Protrusions. *PLoS ONE*, *8*(4), 1–14. <https://doi.org/10.1371/journal.pone.0059901>
- Karp, G. C., & Solursh, M. (1985). Dynamic activity of the filopodia of sea urchin embryonic cells and their role in directed migration of the primary mesenchyme in vitro. *Developmental Biology*, *112*(2), 276–283. [https://doi.org/10.1016/0012-1606\(85\)90398-7](https://doi.org/10.1016/0012-1606(85)90398-7)
- Khajah, M. A., & Luqmani, Y. A. (2016). Involvement of Membrane Blebbing in Immunological Disorders and Cancer. *Medical Principles and Practice*, *25*(2), 18–27. <https://doi.org/10.1159/000441848>
- Kitchen, P., Salman, M. M., Abir-Awan, M., Al-Jubair, T., Törnroth-Horsefield, S., Conner, A. C., & Bill, R. M. (2020). Calcein Fluorescence Quenching to Measure Plasma Membrane Water Flux in Live Mammalian Cells. *STAR Protocols*, *1*(3). <https://doi.org/10.1016/j.xpro.2020.100157>
- Knoll, A. H. (2003). Biomineralization and Evolutionary History. *Reviews in Mineralogy and Geochemistry*, *54*(1), 329–356. <https://doi.org/10.2113/0540329>
- Knoll, A. H., Bambach, R. K., Payne, J. L., Pruss, S., & Fischer, W. W. (2007). Paleophysiology and end-Permian mass extinction. *Earth and Planetary Science Letters*, *256*(3–4), 295–313. <https://doi.org/10.1016/j.epsl.2007.02.018>
- Kottmeier, D. M., Chrachri, A., Langer, G., Helliwell, K. E., Wheeler, G. L., & Brownlee, C. (2022). Reduced H⁺ channel activity disrupts pH homeostasis and calcification in coccolithophores at low ocean pH. *Proceedings of the National Academy of Sciences of the United States of America*, *119*(19), 1–11. <https://doi.org/10.1073/pnas.2118009119>
- Lagadic-Gossmann, D., Buckler, K. J., & Vaughan-Jones, R. D. (1992). Role of bicarbonate in pH recovery from intracellular acidosis in the guinea-pig ventricular myocyte. *Journal of Physiology*, *458*(1), 361–384.

- Le Roy, N., Jackson, D. J., Marie, B., Ramos-Silva, P., & Marin, F. (2014). The evolution of metazoan α -carbonic anhydrases and their roles in calcium carbonate biomineralization. *Frontiers in Zoology*, *11*(1), 1–16. <https://doi.org/10.1186/s12983-014-0075-8>
- Le Roy, N., Jackson, D. J., Marie, B., Ramos-Silva, P., & Marin, F. (2015). Carbonic anhydrase and metazoan biocalcification: A focus on molluscs. *Key Engineering Materials*, *672*, 151–157. <https://doi.org/10.4028/www.scientific.net/KEM.672.151>
- Lee, D. J., Gutbrod, M., Ferreras, F. M., & Matthews, P. G. D. (2018). Changes in hemolymph total CO₂ content during the water-to-air respiratory transition of amphibiotic dragonflies. *Journal of Experimental Biology*, *221*(15). <https://doi.org/10.1242/jeb.181438>
- Lee, H. G., Stumpp, M., Yan, J. J., Tseng, Y. C., Heinzl, S., & Hu, M. Y. A. (2019). Tipping points of gastric pH regulation and energetics in the sea urchin larva exposed to CO₂-induced seawater acidification. *Comparative Biochemistry and Physiology -Part A : Molecular and Integrative Physiology*, *234*(March), 87–97. <https://doi.org/10.1016/j.cbpa.2019.04.018>
- Lee, S. K., Boron, W. F., & Occhipinti, R. (2023). Potential Novel Role of Membrane-Associated Carbonic Anhydrases in the Kidney. *International Journal of Molecular Sciences*, *24*(4). <https://doi.org/10.3390/ijms24044251>
- Levitus, S., Antonov, J. I., Boyer, T. P., Baranova, O. K., Garcia, H. E., Locarnini, R. A., Mishonov, A. V., Reagan, J. R., Seidov, D., Yarosh, E. S., & Zweng, M. M. (2012). World ocean heat content and thermosteric sea level change (0-2000m), 1955-2010. *Geophysical Research Letters*, *39*(10), 1–5. <https://doi.org/10.1029/2012GL051106>
- Li, S., Huang, J., Liu, C., Liu, Y., Zheng, G., Xie, L., & Zhang, R. (2016). Interactive Effects of Seawater Acidification and Elevated Temperature on the Transcriptome and Biomineralization in the Pearl Oyster *Pinctada fucata*. *Environmental Science and Technology*, *50*(3), 1157–1165. <https://doi.org/10.1021/acs.est.5b05107>
- Li, S., Li, C., & Wang, W. (2020). Molecular aspects of aquaporins. In *Vitamins and Hormones* (1st ed., Vol. 113). Elsevier Inc. <https://doi.org/10.1016/bs.vh.2019.08.019>
- Lindskog, S. (1997). Structure and mechanism of Carbonic Anhydrase. *Pharmacology and Therapeutics*, *74*(1), 1–20. [https://doi.org/10.1016/S0163-7258\(96\)00198-2](https://doi.org/10.1016/S0163-7258(96)00198-2)
- Liu, L., Schlesinger, P. H., Slack, N. M., Friedman, P. A., & Blair, H. C. (2011). High capacity Na⁺/H⁺ exchange activity in mineralizing osteoblasts. *Journal of Cellular Physiology*, *226*(6), 1702–1712. <https://doi.org/10.1002/jcp.22501>
- Livingston, B. T., Killian, C. E., Wilt, F., Cameron, A., Landrum, M. J., Ermolaeva, O., Sapojnikov, V., Maglott, D. R., Buchanan, A. M., & Etensohn, C. A. (2006). A genome-wide analysis of biomineralization-related proteins in the sea urchin *Strongylocentrotus purpuratus*. *Developmental Biology*, *300*(1), 335–348. <https://doi.org/10.1016/j.ydbio.2006.07.047>
- Loitto, V. M., Huang, C., Sigal, Y. J., & Jacobson, K. (2007). Filopodia are induced by aquaporin-9 expression. *Experimental Cell Research*, *313*(7), 1295–1306. <https://doi.org/10.1016/j.yexcr.2007.01.023>
- Lucas, J. M., & Knapp, L. W. (1997). A physiological evaluation of carbon sources for calcification in the octocoral *Leptogorgia virgulata* (Lamarck). *Journal of Experimental Biology*, *200*(20), 2653–2662. <https://doi.org/10.1242/jeb.200.20.2653>
- Maclver, B., Cutler, C. P., Yin, J., Hill, M. G., Zeidel, M. L., & Hill, W. G. (2009). Expression and functional characterization of four aquaporin water channels from the european eel (*anguilla anguilla*). *Journal of Experimental Biology*, *212*(17), 2856–2863.

<https://doi.org/10.1242/jeb.025882>

- Mann, K., Wilt, F. H., & Poustka, A. J. (2010). Proteomic analysis of sea urchin (*Strongylocentrotus purpuratus*) spicule matrix. *Proteome Science*, 8, 1–12. <https://doi.org/10.1186/1477-5956-8-33>
- Maren, T. H. (1977). Use of inhibitors in physiological studies of carbonic anhydrase. *American Journal of Physiology*, 232(4), 291–297.
- Martins Medeiros, I. P., & Souza, M. M. (2023). Acid times in physiology: A systematic review of the effects of ocean acidification on calcifying invertebrates. *Environmental Research*, 231(P1), 116019. <https://doi.org/10.1016/j.envres.2023.116019>
- Mass, T., Giuffre, A. J., Sun, C. Y., Stifler, C. A., Frazier, M. J., Neder, M., Tamura, N., Stan, C. V., Marcus, M. A., & Gilbert, P. U. P. A. (2017). Amorphous calcium carbonate particles form coral skeletons. *Proceedings of the National Academy of Sciences of the United States of America*, 114(37), E7670–E7678. <https://doi.org/10.1073/pnas.1707890114>
- Matoo, O. B., Lannig, G., Bock, C., & Sokolova, I. M. (2021). Temperature but not ocean acidification affects energy metabolism and enzyme activities in the blue mussel, *Mytilus edulis*. *Ecology and Evolution*, 11(7), 3366–3379. <https://doi.org/10.1002/ece3.7289>
- Matsui, H., Hopkinson, B. M., Nakajima, K., & Matsuda, Y. (2018). Plasma membrane-type aquaporins from marine diatoms function as CO₂/NH₃ channels and provide photoprotection. *Plant Physiology*, 178(1), 345–357. <https://doi.org/10.1104/pp.18.00453>
- Matt, A. S., Chang, W. W., & Hu, M. Y. (2022). Extracellular carbonic anhydrase activity promotes a carbon concentration mechanism in metazoan calcifying cells. *Proceedings of the National Academy of Sciences of the United States of America*, 119(40), 1–11. <https://doi.org/10.1073/pnas.2203904119>
- McClay, D. R. (2011). Evolutionary crossroads in developmental biology: Sea urchins. *Development*, 138(13), 2639–2648. <https://doi.org/10.1242/dev.048967>
- McConnaughey, T. A., & Whelan, J. F. (1997). Calcification generates protons for nutrient and bicarbonate uptake. *Earth-Science Reviews*, 42(1–2), 95–117. [https://doi.org/10.1016/S0012-8252\(96\)00036-0](https://doi.org/10.1016/S0012-8252(96)00036-0)
- Meldrum, N. U., & Roughton, F. J. W. (1933). *Physiological and Biochemical Laboratories, Cambridge*. 113–141.
- Melzner, F., Gutowska, M. A., Langenbuch, M., Dupont, S., Lucassen, M., Thorndyke, M. C., Bleich, M., & Pörtner, H. O. (2009). Physiological basis for high CO₂ tolerance in marine ectothermic animals: Pre-adaptation through lifestyle and ontogeny? *Biogeosciences*, 6(10), 2313–2331. <https://doi.org/10.5194/bg-6-2313-2009>
- Miller, W. H., Dessert, A. M., & Roblin, R. O. (1950). Heterocyclic Sulfonamides as Carbonic Anhydrase Inhibitors. *Journal of the American Chemical Society*, 72(11), 4893–4896. <https://doi.org/10.1021/ja01167a012>
- Min, Y., Li, Q., & Yu, H. (2023). Characterization of larval shell formation and CgPOU2F1, CgSox5, and CgPax6 gene expression during shell morphogenesis in *Crassostrea gigas*. *Comparative Biochemistry and Physiology Part - B: Biochemistry and Molecular Biology*, 263(July 2022), 1–9. <https://doi.org/10.1016/j.cbpb.2022.110783>
- Mitsunaga, K., Akasaka, K., Shimada, H., Fujino, Y., Yasumasu, I., & Numanoi, H. (1986). Carbonic anhydrase activity in developing sea urchin embryos with special reference to calcification of spicules. *Cell Differentiation*, 18(4), 257–262. [https://doi.org/10.1016/0045-6039\(86\)90057-6](https://doi.org/10.1016/0045-6039(86)90057-6)

- Morrill, J. B., & Marcus, L. (2005). *An Atlas of the Development of the Sea Urchin Lytechinus variegatus*.
- Mount, A. S., Wheeler, A. P., Paradkar, R. P., & Snider, D. (2004). Hemocyte-Mediated Shell Mineralization in the Eastern Oyster. *Science*, *304*(5668), 297–300. <https://doi.org/10.1126/science.1090506>
- Moya, A., Huisman, L., Ball, E. E., Hayward, D. C., Grasso, L. C., Chua, C. M., Woo, H. N., Gattuso, J. P., Forêt, S., & Miller, D. J. (2012). Whole Transcriptome Analysis of the Coral *Acropora millepora* Reveals Complex Responses to CO₂-driven Acidification during the Initiation of Calcification. *Molecular Ecology*, *21*(10), 2440–2454. <https://doi.org/10.1111/j.1365-294X.2012.05554.x>
- Nakano, E., Okazaki, K., & Iwamatsu, T. (1963). Accumulation of radioactive calcium in larvae of the sea urchin *pseudocentrotus depressus*. *Biological Bulletin, Marine Biological Laboratory*, *125*(1), 125–132.
- Newman, E. A. (1994). A Physiological Measure of Carbonic Anhydrase in Müller Cells. *GLIA*, *11*(4), 291–299.
- Oates, T. (2010). Lime and Limestone. *Kirk-Othmer Encyclopedia of Chemical Technology*, 1–53. <https://doi.org/10.1002/0471238961.1209130507212019.a01.pub3>
- Palmer, A. R. (1992). Calcification in marine molluscs: How costly is it? *Proceedings of the National Academy of Sciences of the United States of America*, *89*(4), 1379–1382. <https://doi.org/10.1073/pnas.89.4.1379>
- Pan, T. C. F., Applebaum, S. L., & Manahan, D. T. (2015). Experimental ocean acidification alters the allocation of metabolic energy. *Proceedings of the National Academy of Sciences of the United States of America*, *112*(15), 4696–4701. <https://doi.org/10.1073/pnas.1416967112>
- Paredes, E. (2016). Biobanking of a marine invertebrate model organism: The sea urchin. *Journal of Marine Science and Engineering*, *4*(1). <https://doi.org/10.3390/jmse4010007>
- Parker, M. D., Musa-Aziz, R., Rojas, J. D., Choi, I., Daly, C. M., & Boron, W. F. (2008). Characterization of human SLC4A10 as an electroneutral Na/HCO₃ cotransporter (NBCn2) with Cl⁻ self-exchange activity. *Journal of Biological Chemistry*, *283*(19), 12777–12788. <https://doi.org/10.1074/jbc.M707829200>
- Politi, Y., Levi-Kalisman, Y., Raz, S., Wilt, F., Addadi, L., Weiner, S., & Sagi, I. (2006). Structural characterization of the transient amorphous calcium carbonate precursor phase in sea urchin embryos. *Advanced Functional Materials*, *16*(10), 1289–1298. <https://doi.org/10.1002/adfm.200600134>
- Price, G. D., & Badger, M. R. (1989). Expression of Human Carbonic Anhydrase in the Cyanobacterium *Synechococcus* PCC7942 Creates a High CO₂-Requiring Phenotype. *Plant Physiology*, *91*(2), 505–513. <https://doi.org/10.1104/pp.91.2.505>
- Racki, G. (2019). Big 5 Mass Extinctions. *Encyclopedia of Geology, August*, 0–15.
- Rafiq, K., Shashikant, T., Mcmanus, C. J., Ettensohn, C. A., Rafiq, K., Shashikant, T., Mcmanus, C. J., & Ettensohn, C. A. (2014). Genome-wide analysis of the skeletogenic gene regulatory network of sea urchins (Development, (2014), 141, (950-961), 10.1242/dev.105585). *Development (Cambridge)*, *141*(12), 2542. <https://doi.org/10.1242/dev.112763>
- Ramesh, K., Hu, M. Y., Melzner, F., Bleich, M., & Himmerkus, N. (2020). Intracellular pH regulation in mantle epithelial cells of the Pacific oyster, *Crassostrea gigas*. *Journal of Comparative Physiology B: Biochemical, Systemic, and Environmental Physiology*, *190*(6), 691–700. <https://doi.org/10.1007/s00360-020-01303-3>

- Raz, S., Hamilton, P. C., Wilt, F. H., Weiner, S., & Addadi, L. (2003). The transient phase of amorphous calcium carbonate in sea urchin larval spicules: The involvement of proteins and magnesium ions in its formation and stabilization. *Advanced Functional Materials*, *13*(6), 480–486. <https://doi.org/10.1002/adfm.200304285>
- Richier, S., Fiorini, S., Kerros, M. E., von Dassow, P., & Gattuso, J. P. (2011). Response of the calcifying coccolithophore *Emiliana huxleyi* to low pH/high pCO₂: From physiology to molecular level. *Marine Biology*, *158*(3), 551–560. <https://doi.org/10.1007/s00227-010-1580-8>
- Riihonen, R., Supuran, C. T., Parkkila, S., Pastorekova, S., Väänänen, H. K., & Laitala-Leinonen, T. (2007). Membrane-bound carbonic anhydrases in osteoclasts. *Bone*, *40*(4), 1021–1031. <https://doi.org/10.1016/j.bone.2006.11.028>
- Rojek, A., Praetorius, J., Frøkiaer, J., Nielsen, S., & Fenton, R. A. (2008). A current view of the mammalian aquaglyceroporins. *Annual Review of Physiology*, *70*, 301–327. <https://doi.org/10.1146/annurev.physiol.70.113006.100452>
- Rost, B., Richter, K. U., Riebesell, U., & Hansen, P. J. (2006). Inorganic carbon acquisition in red tide dinoflagellates. *Plant, Cell and Environment*, *29*(5), 810–822. <https://doi.org/10.1111/j.1365-3040.2005.01450.x>
- Saarikoski, J., & Kaila, K. (1992). Simultaneous measurement of intracellular and extracellular carbonic anhydrase activity in intact muscle fibres. *Pflügers Archiv European Journal of Physiology*, *421*(4), 357–363. <https://doi.org/10.1007/BF00374224>
- Saotome, K., Teng, B., Tsui, C. C. (Alex), Lee, W. H., Tu, Y. H., Kaplan, J. P., Sansom, M. S. P., Liman, E. R., & Ward, A. B. (2019). Structures of the otopetrin proton channels Otop1 and Otop3. *Nature Structural and Molecular Biology*, *26*(6), 518–525. <https://doi.org/10.1038/s41594-019-0235-9>
- Sasaki, S., Lshibashi, K., Nagai, T., & Marumo, F. (1992). Regulation mechanisms of intracellular pH of *Xenopus laevis* oocyte. In *Biochimica et Biophysica Acta*, ! (Vol. 137).
- Schatzberg, D., Lawton, M., Hadyniak, S. E., Ross, E. J., Carney, T., Beane, W. S., Levin, M., & Bradham, C. A. (2015). H⁺/K⁺ ATPase activity is required for biomineralization in sea urchin embryos. *Developmental Biology*, *406*(2), 259–270. <https://doi.org/10.1016/j.ydbio.2015.08.014>
- Sevilgen, D. S., Venn, A. A., Hu, M. Y., Tambutté, E., De Beer, D., Planas-Bielsa, V., & Tambutté, S. (2019). Full in vivo characterization of carbonate chemistry at the site of calcification in corals. *Science Advances*, *5*(1), 1–9. <https://doi.org/10.1126/sciadv.aau7447>
- Sheppard Brennand, H., Soars, N., Dworjanyn, S. A., Davis, A. R., & Byrne, M. (2010). Impact of ocean warming and ocean acidification on larval development and calcification in the sea urchin *Tripneustes gratilla*. *PLoS ONE*, *5*(6), 1–7. <https://doi.org/10.1371/journal.pone.0011372>
- Sikes, C. S., Okazaki, K., & Fink, R. D. (1981). Respiratory CO₂ and the supply of inorganic carbon for calcification of sea urchin embryos. *Comparative Biochemistry and Physiology -- Part A: Physiology*, *70*(3), 285–291. [https://doi.org/10.1016/0300-9629\(81\)90181-X](https://doi.org/10.1016/0300-9629(81)90181-X)
- Smith, M. M., Smith, L. C., Cameron, R. A., & Urry, L. A. (2008). The larval stages of the sea urchin, *Strongylocentrotus purpuratus*. *Journal of Morphology*, *269*(6), 713–733. <https://doi.org/10.1002/jmor.10618>
- Soleimani, M., Grassl, S. M., & Aronson, P. S. (1987). Stoichiometry of Na⁺-HCO₃⁻ Cotransport in Basolateral Membrane Vesicles Isolated from Rabbit Renal Cortex. *The Journal of Clinical Investigation*, *79*(4), 1276–1280.
- Song, X., Liu, Z., Wang, L., & Song, L. (2019). Recent advances of shell matrix proteins and cellular orchestration in marine molluscan shell biomineralization. *Frontiers in Marine Science*, *6*(FEB).

- <https://doi.org/10.3389/fmars.2019.00041>
- Stanley, S. M. (2008). Effects of global seawater chemistry on biomineralization: Past, present, and future. *Chemical Reviews*, *108*(11), 4483–4498. <https://doi.org/10.1021/cr800233u>
- Stecher, G., Tamura, K., & Kumar, S. (2020). Molecular evolutionary genetics analysis (MEGA) for macOS. *Molecular Biology and Evolution*, *37*(4), 1237–1239. <https://doi.org/10.1093/molbev/msz312>
- Steele, A., Fries, M. D., & Pasteris, J. D. (2020). Geoscience meets biology: Raman spectroscopy in geobiology and biomineralization. *Elements*, *16*(2), 111–116. <https://doi.org/10.2138/GSELEMENTS.16.2.111>
- Stimpson, W. (1857). Crustacea and Echinodermata of the Pacific shores of north america. *Journal of the Boston Society of Natural History*, *6*.
- Stumpp, M., Dupont, S. T., Thorndyke, M. C., & Melzner, F. (2011). CO₂ induced seawater acidification impacts sea urchin larval development II: Gene expression patterns in pluteus larvae. *Comparative Biochemistry and Physiology Part A: Molecular & Integrative Physiology*, *160*(3), 320–330. <https://doi.org/10.1016/J.CBPA.2011.06.023>
- Stumpp, M., Hu, M., Casties, I., Saborowski, R., Bleich, M., Melzner, F., & Dupont, S. (2013). Digestion in sea urchin larvae impaired under ocean acidification. *Nature Climate Change*, *3*(12), 1044–1049. <https://doi.org/10.1038/nclimate2028>
- Stumpp, M., Hu, M. Y., Melzner, F., Gutowska, M. A., Dorey, N., Himmerkus, N., Holtmann, W. C., Dupont, S. T., Thorndyke, M. C., & Bleich, M. (2012). Acidified seawater impacts sea urchin larvae pH regulatory systems relevant for calcification. *Proceedings of the National Academy of Sciences of the United States of America*, *109*(44), 18192–18197. <https://doi.org/10.1073/pnas.1209174109>
- Stumpp, M., Wren, J., Melzner, F., Thorndyke, M. C., & Dupont, S. T. (2011). CO₂ induced seawater acidification impacts sea urchin larval development I: Elevated metabolic rates decrease scope for growth and induce developmental delay. *Comparative Biochemistry and Physiology Part A: Molecular & Integrative Physiology*, *160*(3), 331–340. <https://doi.org/10.1016/J.CBPA.2011.06.022>
- Suffrian, K., Schulz, K. G., Gutowska, M. A., Riebesell, U., & Bleich, M. (2011). Cellular pH measurements in *Emiliana huxleyi* reveal pronounced membrane proton permeability. *New Phytologist*, *190*(3), 595–608. <https://doi.org/10.1111/j.1469-8137.2010.03633.x>
- Sun, C. Y., Stifler, C. A., Chopdekar, R. V., Schmidt, C. A., Parida, G., Schoeppler, V., Fordyce, B. I., Brau, J. H., Mass, T., Tambutté, S., & Gilbert, P. U. P. A. (2020). From particle attachment to space-filling coral skeletons. *Proceedings of the National Academy of Sciences of the United States of America*, *117*(48), 30159–30170. <https://doi.org/10.1073/pnas.2012025117>
- Supuran, C. T. (2008). Carbonic anhydrases: An overview. *Carbonic Anhydrases: Biochemistry and Pharmacology of an Evergreen Pharmaceutical Target*, *li*, 3–16. <https://doi.org/10.1016/B978-0-12-816476-1.00001-0>
- Tambutté, S., Tambutté, E., Zoccola, D., Caminiti, N., Lotto, S., Moya, A., Allemand, D., & Adkins, J. (2007). Characterization and role of carbonic anhydrase in the calcification process of the azooxanthellate coral *Tubastrea aurea*. *Marine Biology*, *151*(1), 71–83. <https://doi.org/10.1007/s00227-006-0452-8>
- Tanhua, T., Bates, N. R., & Körtzinger, A. (2013). The marine carbon cycle and ocean carbon inventories. *International Geophysics*, *103*, 787–815. <https://doi.org/10.1016/B978-0-12->

391851-2.00030-1

- Taylor, A. R., Brownlee, C., & Wheeler, G. (2017). Coccolithophore Cell Biology: Chalking Up Progress. *Annual Review of Marine Science*, *9*(1), 283–310. <https://doi.org/10.1146/annurev-marine-122414-034032>
- Taylor, A. R., Chrachri, A., Wheeler, G., Goddard, H., & Brownlee, C. (2011). A voltage-gated H⁺ channel underlying pH homeostasis in calcifying Coccolithophores. *PLoS Biology*, *9*(6), 1–14. <https://doi.org/10.1371/journal.pbio.1001085>
- Teng, B., Kaplan, J. P., Liang, Z., Krieger, Z., Tu, Y. H., Burendei, B., Ward, A. B., & Liman, E. R. (2022). Structural motifs for subtype-specific pH-sensitive gating of vertebrate otopetrin proton channels. *eLife*, *11*, 1–19. <https://doi.org/10.7554/eLife.77946>
- Teng, B., Wilson, C. E., Tu, Y. H., Joshi, N. R., Kinnamon, S. C., & Liman, E. R. (2019). Cellular and Neural Responses to Sour Stimuli Require the Proton Channel Otop1. *Current Biology*, *29*(21), 3647–3656.e5. <https://doi.org/10.1016/j.cub.2019.08.077>
- ter Kuile, B., Erez, J., & Padan, E. (1989). Mechanisms for the uptake of inorganic carbon by two species of symbiont-bearing foraminifera. *Marine Biology*, *103*(2), 241–251. <https://doi.org/10.1007/BF00543354>
- Thies, A. B., Quijada-Rodriguez, A. R., Zhouyao, H., Weihrauch, D., & Tresguerres, M. (2022). A Rhesus channel in the coral symbiosome membrane suggests a novel mechanism to regulate NH₃ and CO₂ delivery to algal symbionts. In *Sci. Adv* (Vol. 8). <https://www.science.org>
- Thoms, S., Pahlow, M., & Wolf-Gladrow, D. A. (2001). Model of the carbon concentrating mechanism in chloroplasts of eukaryotic algae. *Journal of Theoretical Biology*, *208*(3), 295–313. <https://doi.org/10.1006/jtbi.2000.2219>
- Tian, L., Zhang, H., Yang, S., Luo, A., Kamau, P. M., Hu, J., Luo, L., & Lai, R. (2023). Vertebrate OTOP1 is also an alkali-activated channel. *Nature Communications*, *14*(1). <https://doi.org/10.1038/s41467-022-35754-9>
- Todgham, A. E., & Hofmann, G. E. (2009). Transcriptomic response of sea urchin larvae *Strongylocentrotus purpuratus* to CO₂-driven seawater acidification. *Journal of Experimental Biology*, *212*(16), 2579–2594. <https://doi.org/10.1242/jeb.032540>
- Towe, K. M. (1990). Overview of Biomineralization. *Paleobiology*, *16*(4), 521–526. <https://doi.org/10.1017/S009483730001023X>
- Trimborn, S., Lundholm, N., Thoms, S., Richter, K. U., Krock, B., Hansen, P. J., & Rost, B. (2008). Inorganic carbon acquisition in potentially toxic and non-toxic diatoms: The effect of pH-induced changes in seawater carbonate chemistry. *Physiologia Plantarum*, *133*(1), 92–105. <https://doi.org/10.1111/j.1399-3054.2007.01038.x>
- Tripp, B. C., Smith, K., & Ferry, J. G. (2001). Carbonic Anhydrase: New Insights for an Ancient Enzyme. *Journal of Biological Chemistry*, *276*(52), 48615–48618. <https://doi.org/10.1074/jbc.R100045200>
- Tsukaguchi, H., Weremowicz, S., Morton, C. C., & Hediger, M. A. (1999). Functional and molecular characterization of the human neutral solute channel aquaporin-9. *American Journal of Physiology - Renal Physiology*, *277*(5 46-5), 685–696. <https://doi.org/10.1152/ajprenal.1999.277.5.f685>
- Tu, Y.-H., Cooper, A. J., Teng, B., Chang, R. B., Artiga, D. J., Turner, H., Mulhall, E. M., Ye, W., Smith, A. D., & Liman, E. R. (2018). An evolutionarily conserved gene family encodes proton-selective ion channels. *Science*, *359*(6379), 1047–1050. <https://doi.org/10.1016/B978-0-12-801238-3.02194-2>

- Uehlein, N., Lovisolò, C., Siefritz, F., & Kaldenhoff, R. (2003). The tobacco aquaporin NtAQP1 is a membrane CO₂ pore with physiological functions. *Nature*, *425*(6959), 734–737. <https://doi.org/10.1038/nature02027>
- Van Cappellen, P. (2003). Biomineralization and Global Biogeochemical Cycles. *Reviews in Mineralogy and Geochemistry*, *54*(1), 357–381.
- Verkman, A. S. (2000). Water permeability measurement in living cells and complex tissues. *Journal of Membrane Biology*, *173*(2), 73–87. <https://doi.org/10.1007/s002320001009>
- Verkman, A. S. (2011). Aquaporins at a glance. *Journal of Cell Science*, *124*(13), 2107–2112. <https://doi.org/10.1242/jcs.079467>
- Verkman, A. S. (2013). Aquaporins. *Current Biology*, *23*(2), 52–55. <https://doi.org/10.1016/j.cub.2012.11.025>
- Verkman, A. S., & Mitra, A. K. (2000). Structure and function of aquaporin water channels. *American Journal of Physiology - Renal Physiology*, *278*, F13–F28. <https://doi.org/10.1177/153857449803200307>
- Vidavsky, N., Addadi, S., Schertel, A., Ben-Ezra, D., Shpigel, M., Addadi, L., & Weiner, S. (2016). Calcium transport into the cells of the sea urchin larva in relation to spicule formation. *Proceedings of the National Academy of Sciences of the United States of America*, *113*(45), 12637–12642. <https://doi.org/10.1073/pnas.1612017113>
- Vidavsky, N., Masic, A., Schertel, A., Weiner, S., & Addadi, L. (2015). Mineral-bearing vesicle transport in sea urchin embryos. *Journal of Structural Biology*, *192*(3), 358–365. <https://doi.org/10.1016/j.jsb.2015.09.017>
- Von Dassow, P. (2022). Voltage-gated proton channels explain coccolithophore sensitivity to ocean acidification. *Proceedings of the National Academy of Sciences of the United States of America*, *119*(25), 1–3. <https://doi.org/10.1073/pnas.2206426119>
- Wang, C. Z., Yano, H., Nagashima, K., & Seino, S. (2000). The Na⁺-driven Cl⁻/HCO₃⁻ exchanger: Cloning, tissue distribution, and functional characterization. *Journal of Biological Chemistry*, *275*(45), 35486–35490. <https://doi.org/10.1074/jbc.C000456200>
- Wang, X., & Müller, W. E. G. (2015). Involvement of aquaporin channels in water extrusion from biosilica during maturation of sponge siliceous spicules. *Biological Bulletin*, *229*(1), 24–37. <https://doi.org/10.1086/BBLv229n1p24>
- Wang, X., Wang, M., Jia, Z., Qiu, L., Wang, L., Zhang, A., & Song, L. (2017). A Carbonic Anhydrase Serves as an Important Acid-Base Regulator in Pacific Oyster *Crassostrea gigas* Exposed to Elevated CO₂: Implication for Physiological Responses of Mollusk to Ocean Acidification. *Marine Biotechnology*, *19*(1), 22–35. <https://doi.org/10.1007/s10126-017-9734-z>
- Wang, X., Wang, M., Jia, Z., Song, X., Wang, L., & Song, L. (2017). A shell-formation related carbonic anhydrase in *Crassostrea gigas* modulates intracellular calcium against CO₂ exposure: Implication for impacts of ocean acidification on mollusk calcification. *Aquatic Toxicology*, *189*, 216–228. <https://doi.org/10.1016/J.AQUATOX.2017.06.009>
- Warner, J. F., & McClay, D. R. (2014). Perturbation of the Hedgehog pathway in sea urchin embryos. In D. J. Carroll & S. A. Strickers (Eds.), *Developmental Biology of the Sea Urchin and Other Marine Invertebrates - Methods and Protocols* (Vol. 1128, pp. 211–223). Humana Press. <http://www.ncbi.nlm.nih.gov/pubmed/24567214>
- Weiner, I. D., & Verlander, J. W. (2017). Ammonia transporters and their role in acid-base balance. *Physiological Reviews*, *97*(2), 465–494. <https://doi.org/10.1152/physrev.00011.2016>

- Wheatly, M. G. (1999). Calcium homeostasis in crustacea: The evolving role of branchial, renal, digestive and hypodermal epithelia. *Journal of Experimental Zoology*, 283(7), 620–640. [https://doi.org/10.1002/\(SICI\)1097-010X\(19990601\)283:7<620::AID-JEZ2>3.0.CO;2-3](https://doi.org/10.1002/(SICI)1097-010X(19990601)283:7<620::AID-JEZ2>3.0.CO;2-3)
- Wilt, F. H. (1999). Matrix and mineral in the sea urchin larval skeleton. *Journal of Structural Biology*, 126(3), 216–226. <https://doi.org/10.1006/jsbi.1999.4105>
- Wilt, F. H. (2002). Biomineralization of the spicules of sea urchin embryos. *Zoological Science*, 19(3), 253–261. <https://doi.org/10.2108/zsj.19.253>
- Winter, M. R., Morgulis, M., Gildor, T., Cohen, A. R., & Ben-Tabou De-Leon, S. (2021). Calcium-vesicles perform active diffusion in the sea urchin embryo during larval biomineralization. *PLOS Computational Biology*. <https://doi.org/10.1371/journal.pcbi.1008780>
- Wittmann, A. C., & Pörtner, H. O. (2013). Sensitivities of extant animal taxa to ocean acidification. *Nature Climate Change*, 3(11), 995–1001. <https://doi.org/10.1038/nclimate1982>
- Wolpert, L., & Gustafson, T. (1961). Studies on the cellular basis of morphogenesis of the sea urchin embryo. *Experimental Cell Research*, 25, 311–325.
- Wu, Y., Chu, D., Tong, J., Song, H., Dal Corso, J., Wignall, P. B., Song, H., Du, Y., & Cui, Y. (2021). Six-fold increase of atmospheric pCO₂ during the Permian–Triassic mass extinction. *Nature Communications*, 12(1). <https://doi.org/10.1038/s41467-021-22298-7>
- Wu, Y., Cui, Y., Chu, D., Song, H., Tong, J., Corso, J. D., & Ridgwell, A. (2023). Volcanic CO₂ degassing postdates thermogenic carbon emission during the end-Permian mass extinction. *Science Advances*, 9(7), 1–9. <https://doi.org/10.1126/sciadv.abq4082>
- Yasumasu, I., Mitsunaga, K., & Fujino, Y. (1985). Mechanism for electrosilent Ca²⁺ transport to cause calcification of spicules in sea urchin embryos. *Experimental Cell Research*, 159(1), 80–90. [https://doi.org/10.1016/S0014-4827\(85\)80039-2](https://doi.org/10.1016/S0014-4827(85)80039-2)
- Zebreal, Y. D., Da Silva Fonseca, J., Marques, J. A., & Bianchini, A. (2019). Carbonic anhydrase as a biomarker of global and local impacts: Insights from calcifying animals. *International Journal of Molecular Sciences*, 20(12), 1–16. <https://doi.org/10.3390/ijms20123092>
- Zeziulia, M., Blin, S., Schmitt, F. W., Lehmann, M., & Jentsch, T. J. (2022). Proton-gated anion transport governs macropinosome shrinkage. *Nature Cell Biology*, 24(6), 885–895. <https://doi.org/10.1038/s41556-022-00912-0>
- Zhang, H., Blanco-Ameijeiras, S., Hopkinson, B. M., Bernasconi, S. M., Mejia, L. M., Liu, C., & Stoll, H. (2020). An isotope label method for empirical detection of carbonic anhydrase in the calcification pathway of the coccolithophore *Emiliania huxleyi*. *Geochimica et Cosmochimica Acta*, 292, 78–93. <https://doi.org/10.1016/j.gca.2020.09.008>
- Zhang, J., Jin, H., Zhang, W., Ding, C., O’Keeffe, S., Ye, M., & Zuker, C. S. (2019). Sour Sensing from the Tongue to the Brain. *Cell*, 179(2), 392–402.e15. <https://doi.org/10.1016/j.cell.2019.08.031>
- Zito, F., Koop, D., Byrne, M., & Matranga, V. (2015). Carbonic anhydrase inhibition blocks skeletogenesis and echinochrome production in *Paracentrotus lividus* and *Heliocidaris tuberculata* embryos and larvae. *Development Growth and Differentiation*, 57(7), 507–514. <https://doi.org/10.1111/dgd.12229>
- Zoccola, D., Ganot, P., Bertucci, A., Caminiti-Segonds, N., Techer, N., Voolstra, C. R., Aranda, M., Tambutté, E., Allemand, D., Casey, J. R., & Tambutté, S. (2015). Bicarbonate transporters in corals point towards a key step in the evolution of cnidarian calcification. *Scientific Reports*, 5, 1–11. <https://doi.org/10.1038/srep09983>

References

Zoccola, D., Innocenti, A., Bertucci, A., Tambutté, E., Supuran, C. T., & Tambutté, S. (2016). Coral carbonic anhydrases: Regulation by ocean acidification. *Marine Drugs*, *14*(6).
<https://doi.org/10.3390/md14060109>

Acknowledgements

First, I would like to sincerely thank Dr. Marian Hu for his great supervision throughout my whole PhD time. I appreciate his guidance, the time he took to talk through ideas and results and his availability for questions at all times. I am grateful for his support through failing experiment as well as interpreting astonishing results and to help me grow personally and career-oriented. I am very thankful for the opportunities to meet other scientists and discuss my science at various conferences. I also want to thank Dr. William Chang for his introduction into the new methods and guidance in the lab.

I am very grateful for the support of Prof. Dr. Marcus Bleich and all my colleagues in the “Physiology of Membrane Transport” department at the Institute of Physiology and for creating a warm and welcoming environment to work in. The numerous LabMeetings with fruitful discussions and talks while sharing the labs enriched my work. I also want to thank Thomas Stegman and Regina Lingg for their technical support in the lab and the care taking of the sea urchins.

Further, I want to thank Dr. Meike Stumpp and her colleagues from the Zoology department, Dr. Tyler Carrier from the GEOMAR and Dr. Marian Hu and colleagues for the monthly “Echino Meeting” including the interesting discussions about the sea urchin larva and other echinoderms.

I also thank Dr. Jonas Brandenburg from Dr. David Garfields Lab in Berlin for the provided single cell RNA sequencing data of the sea urchin larva (*Strongylocentrotus purpuratus*) and for writing the R-code to analyze out data.

Further, I want to thank Dr. Alex Quijada-Rodriguez and Prof. Dr. Dirk Weihrauch from the University of Manitoba, Canada and Dr. Marcus Schewe from the Institute of Physiology for obtaining the CO₂ conductance measurements using *Xenopus* oocytes.

This work was funded by the Emmy Noeter Programm (403529967) of the German Research Foundation, whom I thank for the financial support.

I am very grateful for the support of my family, not only during my doctorate, but my entire life. Finishing this thesis would not have been possible without my partner Marc, who supported me during my stressful times and also made life so much more fun. I am also thankful for getting to know Catrin and Femke during this doctorate and to call you now my friends. Further, I thank Leo for being by my side since school and still supporting me. Moreover, I thank Maja, Levke and Jule being a stable and important part of the last ten years, since we started our biology study together here in Kiel and also Gianni who joined the journey during the Master's.

Eidesstattliche Erklärung

Ann-Sophie Matt

Zeyestraße 30

24106 Kiel

Erklärung gem. §9 der Promotionsordnung:

Ich erkläre hiermit,

- (i) dass die Abhandlung – abgesehen von der Beratung durch die Betreuerin oder den Betreuer – nach Inhalt und Form die eigene Arbeit ist,
- (ii) dass diese Arbeit vor dem jetzigen Promotionsverfahren keinem anderen Promotionsverfahren unterzogen wurde,
- (iii) dass die Arbeit unter Einhaltung der Regeln guter wissenschaftlicher Praxis der Deutschen Forschungsgemeinschaft entstanden ist und
- (iv) dass mir kein akademischer Grad entzogen wurde.

Die vorliegende Dissertation ist eine Mischform und die aufgelisteten Manuskripte wurden in wissenschaftlichen Journalen veröffentlicht:

- I. Chang, W. W. *, **Matt, A.-S. ***, Schewe, M., Musinszki, M., Grüssel, S., Brandenburg, J., Garfield, D., Bleich, M., Baukowitz, T., & Hu, M. Y. (2021). An otopetrin family proton channel promotes cellular acid efflux critical for biomineralization in a marine calcifier. *Proceedings of the National Academy of Sciences of the United States of America*, 118(30), e2101378118. <https://doi.org/10.1073/pnas.2101378118> (*co-first authors)
- II. **Matt, A. S.**, Chang, W. W., & Hu, M. Y. (2022). Extracellular carbonic anhydrase activity promotes a carbon concentration mechanism in metazoan calcifying cells. *Proceedings of the National Academy of Sciences of the United States of America*, 119(40), 1–11. <https://doi.org/10.1073/pnas.2203904119>

Kiel, 23.05.2024

Ann-Sophie Matt